TECHNISCHE UNIVERSITÄT MÜNCHEN

Lehrstuhl für Methodik der Fernerkundung

Airborne wind lidar observations for the validation of the ADM-Aeolus instrument

Uwe Marksteiner

Vollständiger Abdruck der von der Ingenieurfakultät Bau Geo Umwelt der Technischen Universität München zur Erlangung des akademischen Grades eines Doktor-Ingenieurs genehmigten Dissertation.

Vorsitzende:		Univ.-Prof. Dr.-Ing. Liqiu Meng
Prüfer der Dissertation:		
	1.	Univ.-Prof. Dr.-Ing. Richard Bamler
	2.	Univ.-Prof. Dr. rer. nat. Markus Rapp (Ludwig-Maximilians-Universität München)

Die Dissertation wurde am 21.03.2013 bei der Technischen Universität München eingereicht und durch die Ingenieurfakultät Bau Geo Umwelt am 10.07.2013 angenommen.

Table of Contents

Abstract

The measurement of vertical wind profiles on a global scale is considered to be of highest priority with respect to numerical weather prediction and climate studies. In order to meet this demand, the European Space Agency (ESA) implemented the Atmospheric Dynamics Mission Aeolus (ADM-Aeolus) whose satellite is currently scheduled for launch in 2015. Its single payload, the Atmospheric Laser Doppler Instrument (ALADIN), operating in the UV spectral region at 355 nm will be the first wind Lidar in space. It will measure the wind speed along the line-of-sight (LOS) and demonstrate the potential of the direct-detection Doppler wind Lidar technology to globally provide wind speed observations.

As an airborne prototype of the satellite instrument, the ALADIN Airborne Demonstrator (A2D) was developed. It includes several novel technologies regarding the interferometers and detectors. The A2D aims at the pre-launch validation of the measurement principle of the ALADIN instrument, the verification of the calibration and wind measurement strategies of the ADM-Aeolus satellite and the optimisation of wind retrieval algorithms. Therefore, the A2D was deployed on the DLR Falcon aircraft and tested during an airborne campaign in the North Atlantic region in 2009. A well-established wind Lidar that uses the heterodyne technology and operates at a wavelength of 2 µm, was installed as a reference system .

Based on this unique dataset new methods and algorithms are developed in this thesis for the exploitation of the A2D observations and the results validate the ADM-Aeolus measurement strategy. The first two airborne response calibrations are evaluated for the Mie and the Rayleigh channel. A new approach of the summation of vertically distributed ground return signal results in a successful evaluation of the according response calibration function. The cross-coupling between the signals of adjacent range-gates based on the principle of the detector allows a more precise determination of the ground elevation. In combination with a Digital Elevation Model and aircraft attitude data the ground can be discriminated from clouds. Eventually, this enables the consideration of unknown instrumentally based errors by applying a Zero Wind Correction. It is found that by extending the frequency range of the calibration compared to ADM-Aeolus the non-linearity of the Rayleigh response calibration function can reliably be taken into account, thereby reducing the systematic error in the measured wind speeds. Several further corrections are introduced and quality control schemes are developed and applied to the calibrations and wind measurements. This thesis presents the first A2D wind speed profiles derived from airborne measurements. In order to facilitate the comparison between A2D and 2-µm winds, a bilinear interpolation algorithm is developed that matches the different observation resolutions. Statistical comparisons yield random errors of less than 2.5 m/s and 1.5 m/s, respectively, for the Rayleigh and the Mie channel. Moreover, the A2D and 2-µm Lidar observations are analysed in the context of ECMWF analyses, a radiosonde and recordings of the MODIS, AVHRR and QuickScat instruments, thereby highlighting wind phenomena on different spatial scales ranging from large scale jet-stream winds to local katabatic winds or cold air breakouts from the Arctic.

1. Introduction

1.1. Overview

Typically measured quantities describing the state of the atmosphere are humidity, temperature, pressure, cloud coverage, concentrations of trace gases or liquid and ice water content. However, the World Meteorological Organisation (WMO) has been stating for about a decade now, that the measurement of wind at all levels is of highest priority among the critical atmospheric variables that are not adequately measured (World Meteorological Organisation (2012)). The current capabilities of measuring wind are restricted to either fixed locations (e.g. anemometer, radiosonde, wind profiler), to preferred regions (e.g. air and ship routes, densely populated areas) or to certain altitudes (e.g. cloud motion tracking, satellite based scatterometers estimating wind speed at about sea level).

With the assumption of a geostrophic balance of the wind and mass field, wind velocities derived from radiance observations by satellites suffer from low vertical resolution and cloud cover and are limited to regions outside the tropics and to large horizontal scales (Tan and Andersson (2005)). Closing the gaps of wind information that are present over large areas of the globe would greatly contribute to improved numerical weather forecasting (Baker et al. (1995)). In turn this would not only allow the mitigation of the consequences of severe weather conditions but also ease the planning of aircraft routing or be of support regarding the variable and weather dependent amount of renewable energies. The spatial resolution of NWP models has increased in the past, which led to an increasing demand for more wind observation on smaller scales.

A data delivery in near or even quasi real time of less than 3 h or 30 minutes after sensing is required as well as an increasing observation frequency of the wind speed as a highly variable element. Whereas passive absorption line techniques cannot fulfil the strict requirements imposed onto the vertical resolution and the wind speed accuracy, active space-borne Lidar (light detection and ranging) systems can constitute the key technology to meet these needs for global wind measurements due to their small representativeness and observational errors. Thus, in 1999 the European Space Agency ESA selected the Atmospheric Dynamics Mission (ADM) Aeolus as the second Earth Explorer Core Mission of the Earth Observation Envelope Programme (ESA (1999)). ADM-Aeolus will be the first Doppler Wind Lidar (DWL) in space (ESA (2008)). The satellite carries a single instrument, ALADIN, and is expected to be launched in 2015 with a scheduled lifetime of three years. ADM-Aeolus will measure one component of the wind vector and provide vertical profiles of the components throughout the troposphere and lower stratosphere. Impact studies based on simulations were conducted that showed that wind measurements can considerably improve medium-range weather forecast (Marseille and Stoffelen

(2003), Stoffelen et al. (2005)). Taking into account the spatial distribution of wind measurements, ADM-Aeolus even provides the most information per datum due to its global observing capability (Tan and Anderson (2005)). Further insights were provided by an airborne campaign that targeted meteorologically sensitive regions (Weissmann et al. (2005)). By assimilating the obtained Lidar observations into the European Centre for Medium-Range Weather Forecasts (ECMWF) their impact onto the forecast could be demonstrated.

As ADM-Aeolus will be the first wind Lidar in space, novel technologies for the instrument hardware will be deployed, but also the retrieval algorithms for spaceborne wind Lidars is a research field without heritage from earlier missions. Thus, an airborne prototype, the ALADIN Airborne Demonstrator (A2D), was developed for pre-launch investigation and validation purposes employing the same technology as the space mission. While the ALADIN instrument is only tested under laboratory environments before launch, the A2D obtained wind speed measurements in real atmospheric conditions. In contrast to a ground based system, the viewing geometry enabled by the integration into an aircraft increases the comparability to the satellite measurements, for instance with respect to the signal dynamics or the possibility to investigate the ground return. Therefore, in 2009 an airborne campaign was conducted over Iceland, Greenland and the North Atlantic region. Two wind Lidar systems based on different measurement approaches were employed on the same aircraft for the first time worldwide and yielded an unprecedented dataset of wind measurements.

1.2. Objectives of this thesis

Ground and airborne campaigns were used to improve and characterise the overall system performance of the A2D (Reitebuch et al. (2004), Schröder et al. (2007), Li et al. (2009), Reitebuch et al. (2010)). Paffrath (2006) assessed the performance of the A2D on the basis of simulated signals. As the satellite instrument on ADM-Aeolus will only be tested in a laboratory environment, the wind retrieval algorithms could have not been validated against real atmospheric signals without the use of the airborne demonstrator. Consequently, this thesis focuses upon the development, improvement and validation of retrieval algorithms for an airborne wind Lidar as used for ADM-Aeolus. The scope of the thesis is illustrated by Fig. 1.1.

The A2D is the first airborne direct-detection wind Lidar detecting Mie and Rayleigh backscatter at the same time. A novel arrangement of a Fizeau and two Fabry-Pérot interferometers is used to analyse the backscatter from aerosol and molecules with respect to a Doppler frequency shift. In terms of viewing geometry and optical design, the A2D and the satellite instrument ALADIN show very high similarity, which is the major argument to justify a validation of the principle of the instrument and measurement procedures. Additionally, this renders algorithms, which are developed for the A2D, potentially applicable to the operational processors of the space mission. After the launch of the satellite, simultaneous measurements of ADM-Aeolus and the A2D are planned. By underflying the orbit of the satellite with the A2D integrated in an aircraft, representative observations will be obtained that are excellently suited for validation purposes.

In summary, the aims of this thesis are:

(1) the development and validation of new and the optimisation of existing retrieval algorithms

(2) the characterisation of the instrument performance

(3) the validation of the measurement principle, in particular the calibration strategy

(4) the validation of the wind measurement results

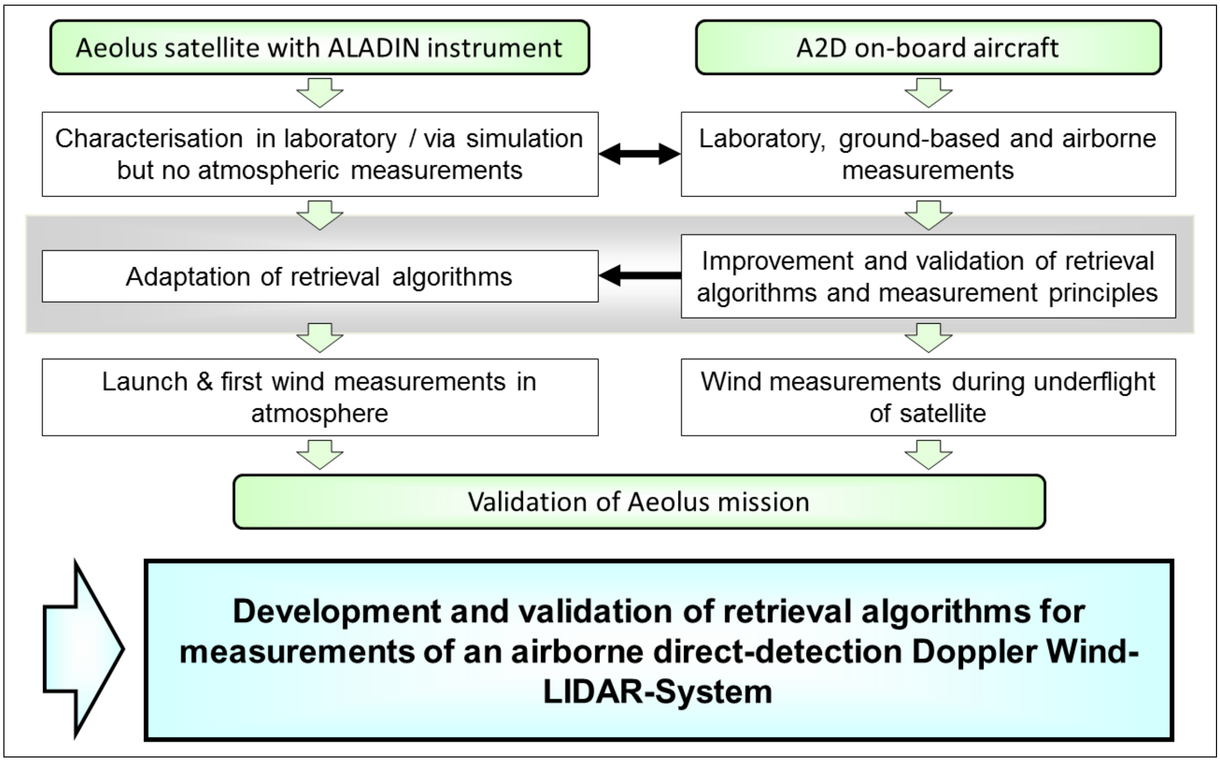

Figure 1.1.: Summary of the ADM-Aeolus programme and its relation to the airborne prototype A2D related to the development and validation of retrieval algorithms and data products before and after launch; the scope of the thesis is highlighted in grey.

Challenging requirements are posed onto the wind measurement errors for ADM-Aeolus (ESA (2008)). Therefore, in the frame of this thesis, an assessment of the A2D wind measurement errors will be performed in order to enable conclusions with respect to the satellite platform. Due to the velocities involved, regarding the moving platforms satellite and aircraft, large additional frequency offsets can be induced in the case of pointing errors. In this respect the ground echo stemming from a non-moving target can constitute a valuable measure for a zero-wind reference.

Questions that are posed within the frame of this work are:

(a) How well do the measured A2D winds compare to other independent data sources?

(b) What are the estimates of the random and systematic errors of the A2D wind measurement and how do they compare with the requirements of the ADM-Aeolus mission?

(c) Do the errors of the A2D winds exhibit any dependencies?

(d) Which parameters strongly affect the estimation of wind speed accuracy and can their influence be reduced?

(e) Can the ground return and its altitude be reliably detected, consequently allowing a distinction between clouds and ground?

(f) Can the ground return signal be used to apply the procedure of zero wind correction?

(g) Which conclusions can be drawn with respect to the ADM-Aeolus mission?

In order to answer these questions this thesis is structured as follows:

At first, the principle of the DWL is explained in chapter 2, particularly with respect to the direct-detection technique involving interferometers. The ADM-Aeolus mission and its objectives are introduced and it is discussed how these will be achieved by employing the ALADIN instrument and performing dedicated calibration and wind measurement procedures. The concept of the A2D along with its novel technologies regarding the laser transmitter, the receiver and the data acquisition sub-systems is illustrated and compared to the satellite platform.

In chapter 3 newly developed methods, which allow the exploitation of the Lidar observations obtained from an airborne campaign in 2009, are discussed and evaluated. A special focus is kept on the evaluation and assessment of the airborne calibrations of the Mie and Rayleigh channel. Several new corrections are implemented in order to reduce the present errors. In this respect the analysis of the ground return signal is of particular importance. The principle of the wind retrieval is explained in detail and quality control measures are developed to assure the reliability of the wind speed results.

The first wind profiles of A2D airborne measurements are presented in chapter 4. In the frame of statistical comparisons of the A2D winds against winds measured by the 2-µm Lidar, a new interpolation algorithm is formulated. A successive application of the corrections and quality controls illustrates the impact of different error sources onto the measured A2D wind speeds. By means of three case studies, the principle and the strategy of wind measurement by the A2D and ADM-Aeolus are validated. The wind Lidar observations are put into a meteorological context using numerical model analysis from ECMWF and satellite observations. The thesis closes with conclusions and an outlook.

2. Wind Lidar methods

2.1. State of the art

Similar to RADAR (radio detection and ranging) the LIDAR (light detection and ranging) technology is a remote sensing method that uses electromagnetic waves for the exploration of the atmospheric environment or specific targets such as land or ice surfaces. A laser (Light Amplification by Stimulated Emission of Radiation) is used as a light source emitting at wavelengths in the IR (infrared), visible or UV (ultraviolet) region. Atmospheric constituents as molecules, aerosol, ice particles or cloud droplets interact with the photons by either scattering or absorption processes. Scattered photons are collected by a telescope usually in the backscatter direction of 180°. Depending on the state of the scattering volume (temperature, pressure, velocity, shape etc.), the properties of the scattered light are changed, allowing the derivation of atmospheric quantities. For a wavelength of 355 nm the molecular backscatter coefficient β_{mol} reaches values of about $1{\cdot}10^{-5}\,\mathrm{m}^{-1}\mathrm{sr}^{-1}$ at ground level (Paffrath (2006)). Depending on the aerosol content the same values can be found for the aerosol backscatter coefficient β_{aer} (Paffrath (2006)). An aerosol climatology with an overview of measured and modelled optical properties over a wide spectral range (IR to UV) can be found in Vaughan et al. (1998). On its way through the atmosphere the laser light is attenuated by scattering and absorption and the combination of both effects is called extinction. The molecular and aerosol extinction coefficients can be derived from the backscatter coefficients.

$$\alpha_{\mathrm{mol}} = \beta_{\mathrm{mol}} \frac{8\pi}{3} sr \tag{2.1a}$$

$$\alpha_{\mathrm{aer}} = k \cdot \beta_{\mathrm{aer}} \tag{2.1b}$$

Whereas the molecular extinction coefficient α_{mol} (Eq. 2.1) can be theoretically evaluated, the determination of the aerosol extinction coefficient α_{aer} requires knowledge about the extinction-to-backscatter ratio k, also called Lidar ratio. The latter can vary within a large range depending on the type of aerosol. Both aerosols and molecules contribute to the total extinction and backscatter (Eqs. 2.2).

$$\alpha_{\mathrm{tot}} = \alpha_{\mathrm{aer}} + \alpha_{\mathrm{mol}} \tag{2.2a}$$

$$\beta_{\mathrm{tot}} = \beta_{\mathrm{aer}} + \beta_{\mathrm{mol}} \tag{2.2b}$$

The ratio of photons reaching a target point at r_t to the number of photons emitted by a Lidar at r_l is then described by the transmission $\tau(r,\lambda)$ in Eq. 2.3. As indicated, the transmission depends on the wavelength λ which is a consequence of the wavelength dependence of the scattering and absorption cross sections of the different air molecules and particles. Hence, suitable spectral regions must be selected in order to minimise the signal loss for a Lidar system.

$$\tau(r,\lambda) = e^{-\int_{r_\mathrm{l}}^{r_\mathrm{t}} \alpha_\mathrm{tot}(r,\lambda)\mathrm{d}r} \tag{2.3}$$

The energy of a single photon depends on its frequency via $E = h \cdot f$. Consequently, the number of emitted photons N_em per laser pulse can be determined from the energy of the laser pulse E_l and the laser wavelength λ_l, keeping in mind the relation $f = c/\lambda$. In Eq. 2.4 c is the speed of light of 299,792,458 m/s and h is the Planck constant with $6.62606957 \cdot 10^{-34}$ kg/(m^{2}s).

$$N_\mathrm{em} = \frac{\lambda_\mathrm{l}}{h \cdot c} \cdot E_\mathrm{l} \tag{2.4}$$

The general Lidar equation (Eq. 2.5) describes the dependency of the detected number of photons N_det with a telescope area A, the range r, the window of integration time Δt, the overlap function of the fields of view of the telescope and the laser $O(r)$, the two way transmission τ^2 and the system constant S containing, for instance, the properties of the receiver optics. The quantity $(c \cdot \Delta t)/2$ is equivalent to the length of the sampled volume.

$$N_\mathrm{det}(r,\lambda) = N_\mathrm{em} \cdot O(r) \cdot S \cdot A \cdot \frac{1}{r^2} \cdot \beta_\mathrm{tot}(r) \cdot \frac{c \cdot \Delta t}{2} \cdot \tau^2(r,\lambda) \tag{2.5}$$

Assuming a pulse energy of 60 mJ at a wavelength of 355 nm, which are both typical values used for the A2D in this thesis, the number of emitted photons is about $1.1 \cdot 10^{17}$ according to Eq. 2.4. In comparison, the number of photons reaching the A2D detector from a 600 m thick atmospheric layer at low altitudes are typically in the order of a few hundred for molecular and aerosol backscatter. An increase in signal can be obtained by integrating over several pulses or a larger range but at the expense of horizontal (for a moving platform) or vertical resolution, respectively.

The crucial characteristics of Lidar systems are the ability to provide measurements of vertical profiles with adjustable vertical resolution, the possibility to determine a random error for every observation, the low systematic errors and error correlations and the potential of data retrieval not only in clear air but also in partly cloudy conditions. Different Lidar principles, each adapted to a specific task, allow the employment on a wide field of atmospheric sciences. Range information from altimeters or ceilometers (Heese et al. (2010)) can be used for the extraction of canopy height or the terrain slope, the scanning of three dimensional structures up to the size of whole cities or the measurement of cloud bottom heights, particularly interesting for airports. On a global scale, backscatter Lidars such as CALIPSO (Cloud-Aerosol Lidar and Infrared Pathfinder Satellite Observation), LITE (Lidar In-space Technology Experiment) or

ICESat (Ice, Cloud, and land Elevation Satellite) provide information about the structure and distribution of clouds and aerosol layers or about the albedo of various ground surfaces (e.g. Zwally et al. (2002)). Rotational Raman methods and resonance fluorescence also allow deriving the temperature from the troposphere (Behrendt et al. (2002), Witschas et al. (2012a)) up to the mesosphere (Hildebrand et al. (2012)) or detecting metal species (Fricke and von Zahn (1985), Li et al. (2012))

The characterisation of micro-physical, optical and chemical properties of aerosols are wide field of application (Esselborn (2008)). Lidar technologies as the differential absorption Lidar (DIAL) or the integrated-path differential absorption (IPDA) Lidar are vital contributors to the determination of the concentration of trace gases, e.g. H_2O, CO_2, O_3 or CH_4 which will be of special interest regarding climate change or air pollution (Marksteiner (2006), Amediek et al. (2009),Vogelmann et al. (2011)).

Lidars are increasingly utilized for the measurement of wind speed (McGill et al. (1997b), Flesia and Korb (1999), Gentry et al. (2000), Reitebuch et al. (2009), Baumgarten (2010), Witschas et al. (2012a), Reitebuch (2012)). Information about turbulence (Schmitt et al. (2007)), true air speed (Rahm et al. (2001)) as well as wind shear, gusts and wake-vortices (Köpp et al. (2004)) are particularly important for the safety in aviation. Regarding renewable energy sources the ambient wind field before and in the wake of high power wind turbines can be determined (Käsler et al. (2010)). From a synergetic point of view the combined yield of all these applications leads to an improved understanding of atmospheric processes, for instance the interchange of tropospheric and stratospheric air masses and the joined effects on chemistry, weather and climate. In addition, Lidar observations contribute to completion of measurement by other instruments such as passive spectrometers, radar, balloons or sounding rockets.

After the development of the laser in the late 1950s and early 1960s, Fiocco and Smullin (1963) reported one of the first Lidar activities in 1963. With a pulsed system operated at 694 nm, they observed echoes of scattering layers in the altitude range of 60 km to 140 km, which were assumed to be caused by noctilucent clouds (Fiedler et al. (2009)) or potentially meteoric break-up. The first direct-detection (sometimes also termed incoherent) DWL was described by Benedetti-Michelangeli et al. (1972) and operated at a wavelength of 488 nm. Heterodyne wind Lidar systems were developed by Bilbro et al. (1984), Hardesty et al. (2001), Reitebuch et al. (2001)) or Rahm (2001) and Köpp et al. (2004). Many improvements enhanced the performance of ground based wind Lidar systems (Fry et al. (1991), Gentry and Korb (1994), McGill et al. (1997b), Flesia and Korb (1999), Schröder et al. (2007)), which finally enabled a successful application in the challenging environment of an aircraft (Bilbro et al. (1984), Reitebuch et al. (2001), Gentry et al. (2010), Reitebuch et al. (2012c)). The first flights of a direct-detection Doppler Lidar worldwide took place in October 2005 (Reitebuch et al. (2009)) by DLR and the first flights of a coherent and a direct-detection wind Lidar on-board the same aircraft were performed in 2007 (Reitebuch et al. (2008)). The Tropospheric Wind Lidar Technology Experiment (TWiLiTE) by NASA operating at 355 nm was the first scanning airborne Lidar employing the direct-detection method for molecular signal in a downward viewing geometry (Gentry et al. (2008)). In 2010 Gentry et al. (2010) for the first time demonstrated the capability of its fully autonomous operation.

Driven by the need for global exploration of the state of the atmosphere it was envisaged to embed Lidars on satellites. This intent was supported by simulation studies which showed the feasibility for direct-detection wind Lidar systems on space platforms such as the Space Shuttle at an orbit altitude of 250 km (Abreu (1979)) or a polar satellite at about 800 km (Rees and McDermid (1990)). Spaceborne Lidar missions were performed in the past (LITE (launched in 1994), ICESat (launched in 2003)) or are still in operation (CALIPSO (launched in 2006)). Currently the ADM-Aeolus and EarthCARE (EARTH Clouds, Aerosols and Radiation Explorer) are being prepared for launch around 2015 by ESA. They will contribute to the continuity in Lidar measurements from space furthering the understanding of the role of aerosols and clouds considering the atmospheric radiation budget and thus the climate change (Flamant et al. (2008)).

2.1.1. Principle of Doppler wind Lidar

In 1842 Christian Doppler postulated the relation between the frequency shift and the relative movement of a source with respect to a recipient of waves (Doppler (1842)). He developed his theory for light, thereby explaining effects that were observed in the light received from binary stars. A frequency f_0 emitted by the source is perceived by the observer as the initial frequency changed by the fraction v/c, the Doppler shift. Whether source and observer are approaching or receding from each other with the relative velocity v determines whether this change is positive or negative, respectively. Thus, the perceived frequency f_1 can be expressed by Eq. 2.7.

$$f_1 = f_0 \cdot (1 + \frac{v}{c}) \tag{2.6}$$

Whereas a Lidar first serves as the source emitting light towards the atmosphere it afterwards represents the observer during the act of reception. The light reflected by the atmospheric constituents exhibits the same frequency f_1 as the received light. The frequency f_2 detected by the Lidar has experienced a second Doppler shift due to the motion of the scatterers.

$$f_2 = f_1 \cdot (1 + \frac{v}{c}) \tag{2.7}$$

Combining Eq. 2.6 and Eq. 2.7 as well as neglecting the quadratic term on the basis of the approximation $v \ll c$ yields the total shift Δf between the outgoing and incoming frequency.

$$\Delta f = f_2 - f_0 = 2 \cdot f_0 \cdot \frac{v}{c} \tag{2.8}$$

Accordingly the total shift in wavelength $\Delta\lambda$ with respect to the emitted wavelength λ_0 can be derived.

$$\Delta\lambda = 2 \cdot \lambda_0 \cdot \frac{v}{c} \tag{2.9}$$

For the wavelengths of 2-µm and 355 nm, which are used for the Lidar systems in this thesis, Tab. 2.1 presents the Doppler shifts that occur for a relative velocity of 1 m/s and the relative accuracy of $\approx 7 \cdot 10^{-9}$ required for the detection.

In contrast, the Doppler shift of an acoustic wave depends on the speed of sound in air, which is approximately 343 m/s at a temperature of 293 K. The required relative accuracy for the detection of this acoustic Doppler shift is about six orders of magnitude lower than for the electromagnetic radiation.

Table 2.1.: Doppler shifts in frequency and wavelength for the electromagnetic radiation in the UV (355 nm) and IR (2-µm) and for the acoustic concert pitch (440 Hz), assuming a relative velocity of 1 m/s.

f_0 / Hz	λ_0 / m	Δf / Hz	$\Delta\lambda$ / m	ratio: $\Delta f/f_0$
$844.5 \cdot 10^{12}$	$0.355 \cdot 10^{-6}$	$5.63 \cdot 10^{6}$	$2.37 \cdot 10^{-15}$	$6.67 \cdot 10^{-9}$
$149.9 \cdot 10^{12}$	$2.0 \cdot 10^{-6}$	$1.00 \cdot 10^{6}$	$0.13 \cdot 10^{-15}$	$6.67 \cdot 10^{-9}$
440	0.78	2.57	$4.55 \cdot 10^{-3}$	$5.83 \cdot 10^{-3}$

Fig. 2.1 shows an example of a Doppler shifted atmospheric backscatter spectrum arising from a laser pulse emitted in the UV at 355 nm. The narrow spectrum of the laser is broadened in the atmosphere, resulting in a Rayleigh spectrum with a full width at half maximum (FWHM) of a few GHz. The term Rayleigh-Brillouin scattering refers to the central line shape of the scattered radiation excluding all Raman lines (Witschas et al. (2010)). Rayleigh scattering occurs in the case that the wavelength is larger than or in the order of the size of the interacting molecule. The Brownian motion of molecules, i.e. their statistical fluctuation in velocity, can be described by a Maxwell-Boltzmann distribution in which the low mass of molecules results in a wide range of velocities and hence a wide frequency spectrum. In order to determine the wind velocity with an accuracy of about 1 m/s, which is equivalent to a frequency Doppler shift of 5.635 MHz, from a spectrum that is more than 300 times broader, an exact knowledge of this line shape in real atmosphere is required. In this respect the first direct verification of Brillouin scattering and the confirmation of the accurateness of the existing line shape models was achieved by Witschas et al. (2012a).

The Mie spectrum, named after Gustav Mie (Mie (1908)), on top of the Rayleigh spectrum in Fig. 2.1 is due to backscatter from aerosols. The amplitude of the illustrated Mie peak corresponds to a very low aerosol concentration in the targeted atmospheric volume. If emanating from a typical aerosol layer, a cloud or a ground return, the amplitude of this peak would be largely increased. Describing such scattering processes with the Mie theory is valid in the case that the wavelength is approximately equal or smaller than the diametre of the encountered particles. Due to the higher mass of such particles compared to molecules, their velocity distribution within a sampled atmospheric volume is more narrow resulting in a narrowband spectrum which is smaller than but in the order of the width of the emitted laser spectrum.

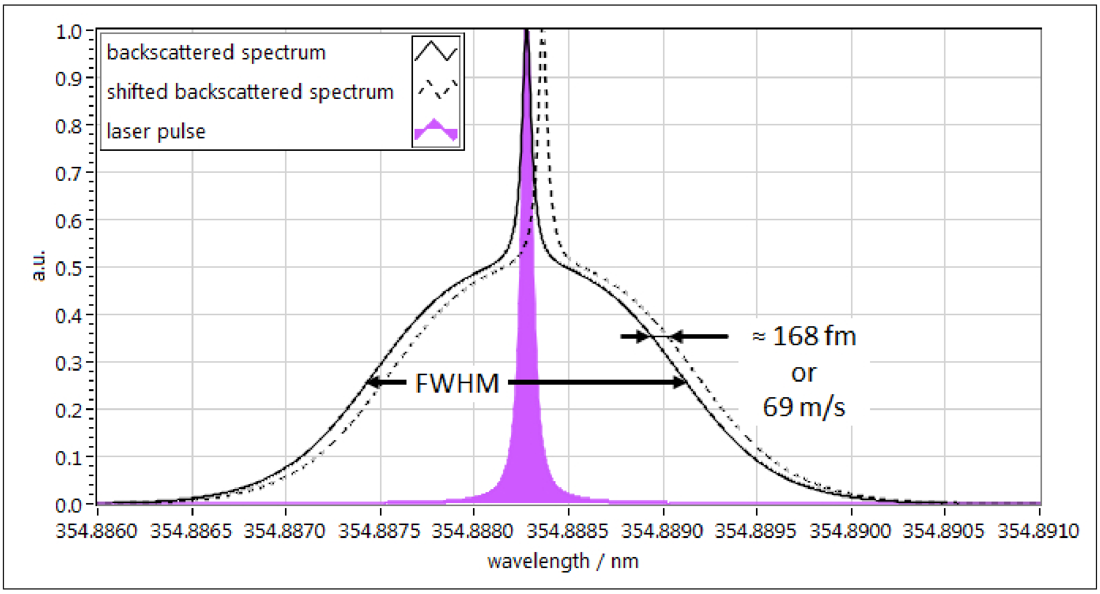

Figure 2.1.: Spectrum of a laser pulse at 354.888 nm (violet) and the atmospheric backscatter spectrum for the case that no relative velocity is present (solid). In the case of relative velocity of 69 m/s (= 250 km/h) a Doppler shift of 168 fm occurs, which is equivalent to 400 MHz. The spectral width of the laser is only slightly smaller than the width of the Mie backscatter but is much smaller than the FWHM of the broadened Rayleigh spectrum.

For the challenging task of detecting such small Doppler shifts in electromagnetic radiation as presented in Tab. 2.1 two measurement approaches proved to be of particular utility: the coherent approach using heterodyning and the direct-detection approach applying high resolution interferometry. Regarding the coherent technique the spectrally narrow Mie peak enables a heterodyning with a second laser (called local oscillator) of similar spectral width, while considering the broadband Rayleigh spectrum as a constant background. The resulting beat signal which is modulated in frequency corresponds to the observed wind speed. The restriction of the coherent technique to narrowband returns limits its application area to wind measurements in aerosol loaded regions, such as the planetary boundary layer, volcanic ash plumes or Saharan dust layers. First coherent DWL's were developed using gas lasers with CO_2 as active medium and emitting wavelengths of 10.6 µm. Such Lidars enabled the detection of aircraft wake vortices, for instance, by Huffaker et al. (1970).

The direct-detection technique likewise enables the analysis of narrowband Mie spectra by applying high resolution filters. Thereby, the Doppler frequency shift can either be related to a change in the intensity transmitted through the filters or to a position of intensity maxima on a suited detector. Similarly, the use of filters allows the detection of Doppler shifts of broadband Rayleigh spectra to which the coherent detection principle is not applicable. The major advantage of the direct-detection technique is based on its ability to analyse the molecular backscatter signal that reliably occurs in the atmosphere at all altitudes. However, in the consequence of the λ^{-4} dependence of the effective scattering cross section of molecules Lidar systems at short wavelengths, mainly UV, are favoured.

Operating a DWL at a fixed direction allows measuring only the relative velocity of the target, i.e. only one component of the velocity vector. Therefore, many DWL's relied on measurements along several azimuth directions in order to derive as well the horizontal wind direction. Applying a measurement sequence of three directions, additionally including a measurement in nadir direction, enabled the determination of vertical winds (Abreu et al. (1992), Korb et al. (1997), Souprayen et al. (1999b)). More sophisticated versions were developed by Rahm (2001) using conical scanning or by Gentry et al. (2000) and Liu et al. (2008) whose systems provide full sky access. The integration and measurements of such scanning DWL systems into aircraft were described by e.g. Bilbro et al. (1984), Reitebuch et al. (2001) or Gentry et al. (2010). Scanning operation has long been considered as an option also for spaceborne Lidars. However, the demand for a reduced risk by decreasing the complexity of the instrument as well as the fact that the measurement of single wind speed components proved to be of adequate merit in numerical models were reflected in the decision to select a fixed viewing direction for the ADM-Aeolus satellite.

2.1.2. Direct-detection Doppler wind Lidar

The measurements of atmospheric wind profiles applying a direct-detection approach are based on the analysis of the spectral content of the backscattered light using high-resolution interferometry. A wind retrieval for a direct-detection DWL necessitates an intermediate step which translates a value derived from the backscattered light, such as intensity or spatial position, into wind speed. This process requires a function describing the characteristics of the instrument which is obtained by a dedicated calibration procedure.

The direct-detection can be divided into two categories, the fringe and the edge technique, whereas the latter was used to perform the first molecular based wind measurements at 355 nm (Gentry et al. (2000)). Regarding the fringe technique the Doppler shift in frequency is estimated via a displacement of either circularly (Abreu et al. (1992), McGill et al. (1997a), McKay (1998a)) or linearly (Irgang et al. (2002), ESA (2008)) shaped fringes for both molecular and aerosol backscatter. Linear fringes can be produced by light transmitted through two plates that are arranged at a very small wedge angle, constituting a Fizeau interferometer. A Fabry-Pérot interferometer (FPI) produces concentric rings according to the interference requirement. While circular fringes are usually detected by multi ring anodes, linear fringes best match the rectangular arrangement of Charge Coupled Devices (CCD). In addition, CCD's can provide higher quantum efficiency depending on the wavelength. Alternatively, along with the edge technique, Photo Multiplier Tubes (PMT) can be used for measuring intensities (Bu et al. (2008)). The usage of an optical circle-to-line converter enabled Irgang et al. (2002) to employ a CCD as detector for the first time.

The edge technique can be further subdivided into the single-edge and the double-edge technique referring to the use of either one or two filters in the wings of the Rayleigh spectrum. Positioning the laser frequency at the point of the steepest slope of a filter, e.g. an FPI or an iodine vapour filter, results in a maximum change in transmitted intensity in the case of a present Doppler shift. However, the single edge requires an accurate energy monitoring of the outgoing laser pulses in order to distinguish between a Doppler shift or a decreased intensity of the received spectrum (Korb et al. (1997)).

This ambiguity is intrinsically avoided by employing the double-edge technique which places one FPI in the vicinity of the steepest slope of each side of the backscattered atmospheric signal and renders the energy monitoring dispensable. The wind speed can then be related to the ratio of the intensities transmitted through both filters and the measurement becomes sensitive to the sign of the wind direction. A single pair of plates that was subdivided into two sections including an additional step for shifting the transmission function of one filter constituted the first parallel double-edge (Chanin et al. (1989)). It was used to perform the first wind measurements in the stratosphere and demonstrated the possibility of detecting Doppler shifts Rayleigh spectra with a Lidar operating at 532 nm. An analytical method for retrieving the wind velocity from the ratio of the measured intensities detected on either wing of the backscattered Rayleigh spectrum was developed by Garnier and Chanin (1992). The application of the double-edge principle was successfully applied to the measurement of an aerosol peak by Korb et al. (1998). Wind measurements on the basis of broadband molecular signal become greatly desensitised to the effects of narrowband aerosol scattering by placing the filters in the wings of the backscattered spectra such that both aerosol and molecular signal change by the same fraction for a small displacement of the spectra. In addition, the change in signal per unit Doppler shift, i.e. the sensitivity, is about twice as high as for the single-edge technique. The according theory of deriving the optimal filter spacing and the first validating measurements in this configuration were presented by Flesia and Korb (1999) and Flesia et al. (2000). Analytical models for the detection of Doppler shifts from molecular and aerosol backscatter by employing the double-edge technique (McKay (1998a)) or the imaging of circular fringes with FPI's (McKay (1998b)) were developed. McKay found that in terms of the ultimate achievable measurement precision these two analytic models show only little difference for Rayleigh backscatter but regarding aerosol backscatter the fringe imaging technique is more suitable as it avoids the limitation of the wind speed dynamic range. A scanning system for the analysis of Mie spectra was designed by Sun et al. (2005) and Xia et al. (2007). It consists of one FPI which is subdivided into two semi-circles and whose plate distance can be driven by piezo-electrics. A comparison of four techniques, combining single-edge or double-edge method with FPI or iodine vapour cells, at three different wavelengths (1064 nm, 532 nm and 355 nm) was conducted by She et al. (2007) yielding recommendations for each technique regarding the most suitable field of application. Accordingly, an FPI is the best solution for probing the boundary layer in the IR and for investigating the stratosphere and mesosphere in the UV.

For a long time Doppler Wind Lidars (DWL) were limited by the restriction to make use of either molecular or aerosol backscatter due to the significant difference in spectral widths that could not be resolved by a single spectrometer simultaneously. An instrument which combines fringe imaging with a Fizeau interferometer for aerosol signal and the double-edge technique for molecular return was developed in the frame of the ADM-Aeolus mission (ESA (2008)) and is described for an airborne prototype of the Lidar on ADM-Aeolus by Paffrath (2006), Reitebuch et al. (2009) and Paffrath et al. (2009)). The application of identically constructed instrument is described by Reitebuch et al. (2009) and Paffrath et al. (2009). An FPI consists of two parallel plates with high reflective surfaces and only such light is transmitted which fulfils the interference condition depending on the wavelength and the incidence angle. For the double-edge technique beam splitters are used to distribute the incoming photons onto two or more FPI's. Thus, conventional methods in most cases lose around 90 % of the light due to reflection. In order to increase the efficiency for ADM-Aeolus, a novel sequential arrangement of the FPI's is implemented which reuses the light reflected at the first FPI for the second FPI.

The shapes of the spectral responses, i.e. the transmission functions, of an FPI or a Fizeau interferometer can be well approximated by an Airy function or a Lorentzian function, whereas the latter is given in ch. A.1. By using the Airy shape function according to Vaughan (2002) (p.91) in a modified form, the filter transmission function $T(f)$ can be described via Eq. 2.10.

$$T(f) = T_\mathrm{p} \cdot \left[1 + \left(\frac{2 \cdot \Delta f_\mathrm{FSR}}{\pi \cdot \Delta f_\mathrm{FWHM}} \right)^2 \cdot \sin^2 \left(\frac{\pi \cdot f}{\Delta f_\mathrm{FSR}} \right) \right]^{-1} \tag{2.10}$$

The constant T_p is the transmission maximum and depends on the transmittance and reflectance properties of the mirrors. Whereas Δf_FWHM is the FWHM of the transmission curve, the free spectral range (FSR) Δf_FSR is the spectral distance between two transmission maxima depending on the distance of the mirror plates. The squared term containing Δf_FWHM is also called the coefficient of finesse. With an intensity spectrum of atmospheric backscatter S_i transmitted through an FPI, that is described by the transmission function T, the intensity $I_\mathrm{A,B}$ that reaches the detector is then given by Eq. 2.11.

$$I_\mathrm{A,B}(\lambda) = \int_{\lambda_1}^{\lambda_2} T_\mathrm{A,B} \cdot S_\mathrm{i}(\lambda) \; \mathrm{d}\lambda \tag{2.11}$$

Regarding a double-edge FPI with two filters A and B, as used in this thesis, the corresponding intensities can be calculated by multiplying the respective transmission function filter $T_\mathrm{A,B}$ with the incident spectrum of the Mie and Rayleigh backscatter and integrating over the wavelength interval from λ_1 to λ_2 as indicated in Fig. 3.14.

2.2. The ADM-Aeolus mission

The ADM-Aeolus mission was selected in 1999 as the 2^{nd} Earth Explorer Core Mission (ESA (1999)) within the Living Planet Programme of the European Space Agency (ESA). After the launch, scheduled for 2015, the ADM-Aeolus satellite will bring the first DWL (Endemann et al. (2004)) and High Spectral Resolution Lidar (Flamant et al. (2008)) into space. Currently assembly and integration works as well as tests and ground segment activities are performed within the phase C/D. As a technology demonstration mission ADM-Aeolus incorporates several novel technologies (sec. 2.3) regarding the single payload ALADIN (Atmospheric Laser Doppler Instrument) with its UV laser as an active instrument (subsec. 2.2.2). The selection of a UV wavelength at 355 nm assures eye-safety for the terrestrials and an increase in the intensity of the molecular backscatter with regard to the sampling of the atmosphere above the planetary boundary layer. Thereby, the aerosol and the molecular backscatter act as complementaries in terms of vertical atmospheric coverage, i.e. providing signal from aerosol loaded and aerosol free regions.

Gallium arsenide solar arrays with a width of 13 m provide 1.4 kW average power to the subsystems of the satellite. Typical platform constraints, such as mass and volume, limit the size of the solar arrays and hence the available power for the laser. Thus, in order to maximise the yield from the limited intensity of the backscattered light, the satellite is equipped with a large 1.5 m Cassegrain telescope. ADM-Aeolus constitutes a monostatic coaxial version of a Lidar, using the same telescope for the transmission of the laser and the reception of the backscattered light. During its scheduled lifetime of three years the satellite will measure vertical profiles of the component of the wind speed vector in the LOS direction (Fig. 2.2). A projection of this component onto the horizontal plane yields the horizontal LOS (HLOS) wind component which is needed as input for NWP models. HLOS profiles will be provided from the Earth's surface up to an altitude of about 25 km, i.e. the lower stratosphere.

The satellite will revolve the Earth in a polar, sun-synchronous dawn-dusk orbit at a mean altitude of 400 km with an inclination of $\approx 97°$ and a local time of ascending node crossing at 18:00 h. This results in a nominal orbital period of 92 minutes 29 seconds and a cross-track separation of wind measurements at the equator of about 2500 km regarding two consecutive orbits. Considering a whole orbit repeat cycle of one week, which is equivalent to 109 orbits, the general spatial separation of wind measurement locations is at maximum about 370 km at the equator. Air masses move predominantly horizontally, which requires an off-nadir pointing of the satellite in order to allow the measurement of HLOS wind components. Therefore, ADM-Aeolus applies an off-nadir viewing direction of 35° towards the night side of the Earth, i.e. away from the sun, and perpendicular to the velocity direction of the satellite. However, the accuracy of the measured HLOS wind components does not only depend on the off-nadir pointing angle, involving a cosine relation due to the projection of the LOS wind component onto the horizontal plane. It also depends on the intensity of the backscattered signal, which decreases quadratically with the range from the satellite. Since about 70 % of the Earth surface is covered by clouds (Marseille and Stoffelen (2003)), wind measurements at an angle of 35° additionally constitute a compromise between the minimum range from the satellite to the atmosphere (Eq. 2.5) and a minimum obstruction by clouds. Apart from the HLOS wind components as the primary product, spin-off products, such as the backscatter and the extinction, will be derived from the measurements and used for the monitoring of aerosol and clouds layers (Flamant et al. (2008), Ansmann et al. (2007)).

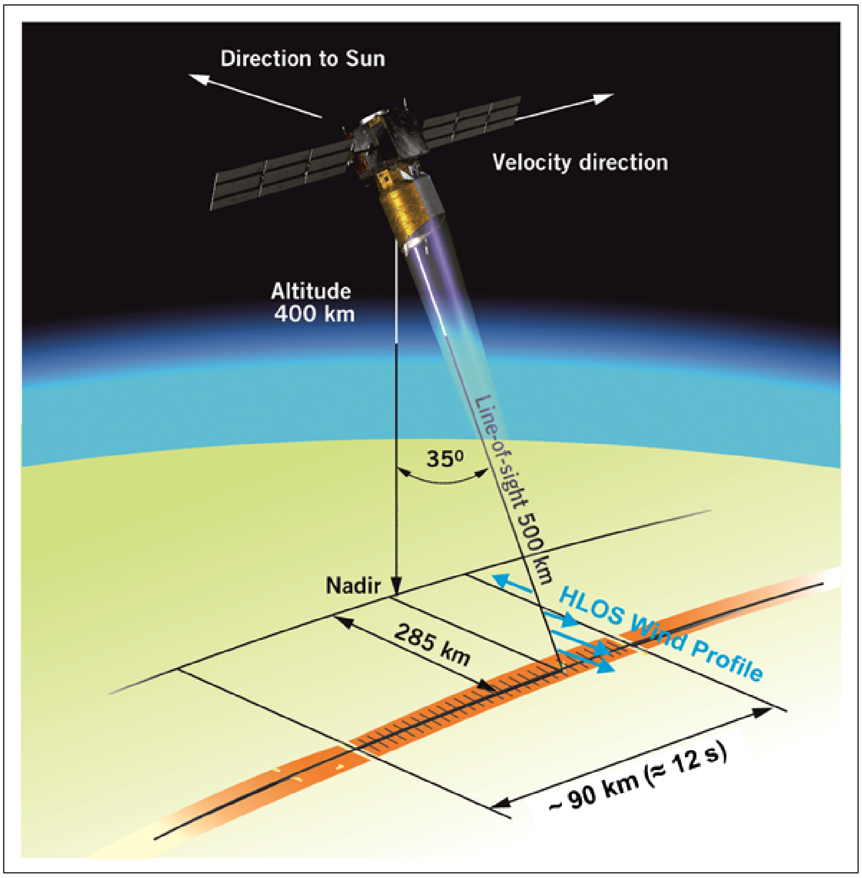

Figure 2.2.: Viewing geometry and sampling strategy of the ADM-Aeolus satellite for horizontal line-of-sight wind speeds (adapted from ESA (2008)).

2.2.1. Mission objectives

The main goal of the ADM-Aeolus mission is to demonstrate the ability to measure wind speed reliably over a long period by means of a Lidar instrument. Particular attention is paid to the accurate functioning of the laser in the space environment. The requirements for the ADM-Aeolus mission are governed by the scientific goals of the various scientific communities intending to use the provided wind products for NWP and subsequently for climate research (Tan et al. (2008)). In particular, this implies strict requirements on the random and systematic errors of the measurements as well as on the wind speed dependent error (Tab. 2.2).

The numbers given in Tab. 2.2 for the vertical resolution and for the random error regarding the HLOS component of the wind are the requirements for the ADM-Aeolus mission in terms of the impact onto meteorological forecast models (LeRille et al. (2012), ESA (2008), p.32). On which spatial scales the error requirements can be met depends on the available laser energy and hence on the energy per laser pulse (≈ 100 mJ). Thus, the required minimum uncertainty in the wind velocity affects the minimum horizontal and vertical resolution. The laser of ADM-Aeolus emits pulses at a repetition frequency of 50 Hz. In order to improve the signal-to-noise ratio, the backscatter acquired from 20 single laser pulses (≈ 3 km ground track) is accumulated on the detector to so-called *measurements* first and can be integrated over a variable horizontal length of nominally about 100 km (700 pulses) to *observations* later. Many studies, for instance by Marseille and Stoffelen (2003), Tan and Andersson (2005) and Stoffelen et al. (2006), examined and confirmed the anticipated performance and impact of ADM-Aeolus and simulated wind speed measurements making use of cloud and aerosol models (Vaughan et al. (1998)).

Requirement		PBL	troposphere	stratosphere
		0 km - 2 km	2 km - 16 km	16 km - 20 km
vertical resolution	/ km	0.5	1.0	2.0
random error (HLOS)	/ m/s	1	2	3
systematic error	/ m/s	0.4		
wind dependent error	/ %	0.7		
wind speed range	/ m/s	± 150		
horizontal integration length	/ km	100 (below 14 km) 140 (above 14 km)		
data coverage	/ -	global		
data availability	/ h	3		
measurement period	/ years	3		

Table 2.2.: Selection of requirements for the wind profile measurements by ADM-Aeolus in the planetary boundary layer (PBL), the troposphere and the stratosphere.

Finally, the ADM-Aeolus mission is to make the wind measurement data available to NWP centres and the scientific community. The ground segment is responsible for the commanding and monitoring of the spacecraft and the acquisition, processing, archiving and dissemination of data. Downlinking of the measurement data from the satellite to the receiving stations on ground is performed on the X-Band (≈ 10 GHz), whereas the housekeeping data is transmitted on the S-Band (≈ 3 GHz). The delivery of the data to various meteorological service centres is envisaged to happen in near-real time, i.e less than 3 hours after sensing, for global application or even in quasi-real time with less than 30 min for regional purposes. Several data products will be generated and provided to the public (Tab. 2.3). For instance, cloud and aerosol optical properties will be contained in the Level 2A product (Flamant et al. (2008)), whereas the Level 2B product will consist of consolidated HLOS wind profile observations after temperature and pressure correction and scene classification, which are suitable for the use in NWP systems (Tan et al. (2008)).

Table 2.3.: ADM-Aeolus data products.

Product	Content
Level 0	raw data / unprocessed instrument and platform telemetry / packet quality parameters
Level 1A	geo-located wind measurements of the satellite
Level 1B	calibrated wind velocity observations uncorrected with respect to temperature and pressure effects / parameters concerning the viewing geometry, the ground echo, the product confidence and the housekeeping
Level 2A	cloud and aerosol optical properties
Level 2B	consolidated HLOS wind profile observations after temperature and pressure correction and scene classification
Level 2C	ADM-Aeolus assisted wind product generated from Level 2B data and ECMWF analyses and forecasts

2.2.2. The ALADIN instrument

The ALADIN instrument (Morançais and Fabre (2004), ESA (2008)) is the only payload on-board the ADM-Aeolus satellite. Its major subsystems are the laser (Cosentino et al. (2012)), the telescope and receiver including the spectrometers. A reference laser system provides the frequency stability and a power laser increases the energy of the emitted laser pulses (Fig. 2.3). The transmit-receive optics shape the laser beam before emission through the telescope and subsequently guide the backscattered light towards the dual-channel receiver which comprises the Rayleigh and the Mie spectrometer. Detection units (subsec. 2.3.2) collect the photons transmitted through each of these spectrometers. Regarding the main interfaces to the satellite platform, the lasers are controlled via the transmitter laser electronics and the output from the detection units is forwarded to the data management system.

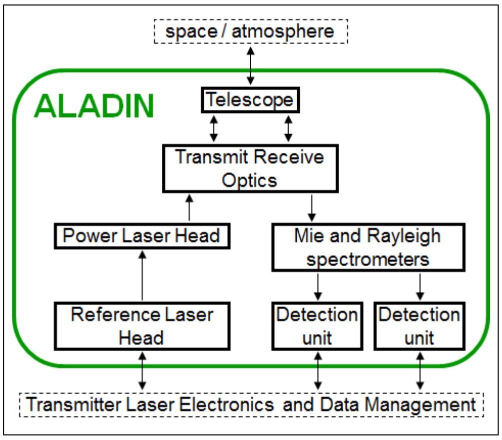

Figure 2.3.: Functional diagram of ALADIN presenting the major components and indicating the interfaces to the satellite platform and the atmosphere.

Enhancements in detector and optical technologies largely contributed to the possibility to measure wind speed by a direct-detection of the backscattered photons. A new technique with a sequential arrangement combining Mie and Rayleigh receiver was conceived to separate the signals from particle and molecular backscatter (Fig. 2.1) and hence to allow for two different ways of wind retrieval. The light backscattered by the atmosphere is conducted onto a Fizeau interferometer (FIZ) from where the reflected portion is guided towards a sequentially arranged Fabry-Pérot Interferometers (FPI). Thereby, the FIZ is used to analyse the narrowband aerosol signal and the FPI is dedicated to the broadband molecular backscatter. A heterodyne measurement, as applied for the 2-µm Lidar (ch. 3.1.4), or a Mach-Zehnder-Interferometer constitute possible alternatives for analysing the narrowband spectrum. However, the first option is not favourable at UV-wavelengths as short as the selected 355 nm and the latter would require too much space for the accommodation of the instrument on the satellite. A receiver which is almost identical to the one of ALADIN is implemented in the airborne wind Lidar system A2D (subsec. 2.3.1).

2.2.3. Calibration and wind retrieval

Calibration

A calibration procedure is needed in order to establish a relation between the measured intensities and the frequency of the backscattered light. Thus, the intention of the calibration procedure is to avoid the influence of the wind in the probed atmospheric region. This requires to keep a fixed beam direction towards nadir, thereby assuming the vertical wind speed to be negligibly small, i.e. a zero wind component in LOS direction. Nadir pointing is achieved by rolling the satellite by 35° from its nominal position, which is a unique manoeuvre regarding the class of Earth observing satellites. A slight deviation from 0° remains in order to avoid events of specular reflection which could emanate from the flat surfaces of lakes, for instance. Subsequently, the frequency of the laser is deliberately shifted in steps of 25 MHz over the required frequency range of ± 500 MHz, likewise shifting the spectrum of the backscattered light (Fig. 2.1). This procedure imitates the frequency Doppler shifts that would otherwise be caused by the wind speed in the atmospheric volume probed during the wind measurement mode. The active shifting of the frequency of the laser for calibrating the instrument constitutes another unique feature of the ADM-Aeolus mission. Assuming zero vertical wind is not valid in the tropics and in regions with strong convection, which limits the available regions for performing a calibration to the high latitudes. Consequently, the conduction of a calibration in one piece is restricted on the temporal domain by the satellite velocity of more than 7 km/s which limits the number of performable frequency steps above the suitable region. The duration of one calibration is about 20 minutes and hence takes approximately a quarter of an orbit. The ADM-Aeolus mission will use the atmospheric region between e.g. 6 and 16 km altitude for calibrating the Rayleigh channel whereas the Mie channel will be calibrated with the help of the ground return. On the basis of the A2D the calibration procedure is explained in detail in sec. 3.4.

Wind retrieval

During the wind measurement mode, which is the nominal mode of ADM-Aeolus, the satellite operates with a fixed laser frequency (except possible frequency jitter and drift) and an off-nadir angle of 35°. In order to obtain a reference measurement that relates to the frequency of the emitted laser pulse, a part of the pulse is internally diverted towards the spectrometers. Afterwards, the spectrometers are used to analyse the spectrum backscattered by the targeted atmospheric volume and provide an estimation of the mean frequency. The frequencies of both internal and atmospheric measurement are compared against the corresponding response functions which are derived from the calibration. By using the Doppler equation (Eq. 2.9) the resulting frequency difference can be converted to a wind speed component in LOS direction.

The combination of the orbital velocity of the satellite ($\approx 7000\,\mathrm{m/s}$) and the rotational velocity of the Earth ($\approx 460\,\mathrm{m/s}$ at the equator) bears the potential to induce large and varying Doppler shifts of the spectrum of the backscattered signal. From orbit prediction and attitude information these frequency shifts due to the Earth's rotation can be computed in advance. They can reach large magnitudes such that the backscatter spectrum is located outside of the frequency range of the spectrometers, which are designed for wind speed measurements of up to $\pm 150\,\mathrm{m/s}$. Thus, a corresponding adaptation of the satellite attitude, i.e. a change of pointing direction by yaw steering, is applied. A correction is required which takes into account the LOS velocity possibly induced by an unknown error in pointing direction or in orbital velocity. Therefore, the signals of the ground returns are analysed which are expected to have a zero frequency shift. Ice and snow surfaces are particularly suited, as they exhibit a large albedo in the UV. This procedure called Zero Wind Correction is employed for the first time for A2D measurements (subsec. 3.5.3).

Assuming the Lidar pointing directly into the wind direction of a strong hurricane with a maximum wind speed of about 250 km/h away from the instrument, the received backscatter spectrum would be shifted by about 400 MHz (Fig. 2.1). These velocities define to a certain extent the relevant measurement range for wind probing instruments. A shift of the backscatter spectrum by $\approx 10\,\mathrm{MHz}$, which is equivalent to about 2 m/s and in the order of the ADM-Aeolus requirements (Tab. 2.2), would not be perceivable in Fig. 2.1. The wind measurement procedure is discussed in detail in sec. 3.5 using the example of the A2D.

Unlike for many ground based systems that can afford changing between measurement modes in time frames of minutes or hours, the high satellite velocity necessitates an optimised temporal and spatial sampling strategy. The resolution of NWP models suggests an optimal length of an observation in terms of information content and error correlation. Much better than in the previously envisaged burst mode (ESA (2008)), the continuous operation of the laser enables the summation of measurements to observations of variable length. Additionally, wind measurements at an adaptable range resolution of 315 m - 2520 m, i.e. 250 m - 2000 m vertical resolution, in 25 atmospheric layers (including 1 sample for the solar background) can be performed with the ALADIN instrument. Flexible algorithms then allow a selective grouping of measurements, horizontally as well as vertically, according to the representativeness of atmospheric volumes with respect to given scenes, such as clear atmosphere or clouds. The measurement grid can be commanded differently for the Mie and the Rayleigh channel, consequently enabling to resolve different atmospheric features at different altitudes.

As a result of possible mispointing, but also due to the elevation of terrain, particularly in Greenland, the Antarctica or the Himalayas, the distance between satellite and Earth surface changes. Additionally, the eccentricity of $e = 0.0013009$ of the orbit of the ADM-Aeolus satellite (Reitebuch et al. (2012b)) corresponds to a ratio of perigee per to apogee apo of 0.997402 (where $per/apo = (1-e)/(1+e)$) and hence in a difference per - apo of roughly 18 km (considering the mean Earth radius of 6371 km). Regarding the expectable variations in the distance between the satellite and the intersection point of the laser beam and the Earth surface, major parts of the measurement grid can be lost for wind measurements below the ground, especially considering the highest vertical resolution of 250 m. Therefore, the start time of signal acquisition can be shifted accordingly for each observation (Marksteiner (2009)). Additionally, ADM-Aeolus is able to take into account geographical and meteorological variations by adapting the commanded measurement grid up to eight times per orbit.

2.3. The ALADIN Airborne Demonstrator

Up to now no wind Lidar measurements from a satellite have been performed. Thus, neither corresponding algorithms are available nor could they be tested with data from atmospheric measurements. A pre-development programme for ALADIN was implemented, which was to identify technological challenges on time (Durand et al. (2004)). In collaboration by EADS-Astrium France, EADS-Astrium Germany and the DLR the refurbished Pre-Development Model of the receiver of ALADIN together with the breadboard of the laser transmitter as well as a new and smaller telescope were used to construct the ALADIN Airborne Demonstrator (A2D) in 2003 (Reitebuch et al. (2004), Durand et al. (2005)). The A2D was intended to enable the validation of the operation modes of the satellite and the functionality of the laser and receiver of ALADIN (Durand et al. (2006)). Therefore, the A2D participated in two ground campaigns joining several other instruments including a wind-profiler, radiosondes and the 2-µm Lidar (subsec. 3.1.4) for comparative measurements in 2006 and 2007 (Reitebuch et al. (2009), Reitebuch et al. (2010)). Deployed on an aircraft, the first flights worldwide of the A2D as a direct-detection Doppler Lidar took place in 2005. During an airborne campaign in 2008 the first flights of a coherent (2-µm) and a direct-detection (A2D) wind Lidar on-board the same aircraft were used to investigate the ground return and the sea surface reflectance (Li et al. (2009)). Due to the application of the so-called *ramp-and-fire technique* for the control of the laser cavity length (Witschas (2007)), the frequency of single laser pulses proved to be stable even in the aircraft environment including vibrations (Reitebuch et al. (2009)) which constituted a crucial requirement for the first airborne wind speed measurements worldwide in a viewing geometry comparable to the one of the satellite (Marksteiner et al. (2011)). The development of the A2D was accompanied by an extensive effort in simulation and validation including the construction of an end-to-end simulator that allowed the optimisation of signal processing and comparison to first atmospheric measurements (Paffrath (2006)).

2.3.1. Instrument design

A detailed view on the subsystems of the A2D is sketched in Fig. 2.4. The laser of the A2D is set up in a master-oscillator power-amplifier configuration. Its Reference Laser Head (RLH) consists of two identical lasers, one acting as the reference laser and the other as the seed laser (Durand et al. (2005)). Both are low power lasers continuously emitting IR wavelengths at 1064 nm (281 THz) with a high frequency stability of about 234 kHz rms over 25 min (Schröder et al. (2007)). Whereas the frequency of the reference laser is kept constant via a temperature control loop, the seed laser provides tunability. The frequency difference between both lasers is controlled via a Phase Locked Loop (PLL) by optically beating the two frequencies, which allows to set the frequency of the seed laser to a user defined offset with respect to the reference laser. In turn, this capability enables the tuning of the emitted laser pulse frequency over a range of $\approx$12 GHz (UV) and thus constitutes the basis for the response calibration procedure (sec. 3.4). Additionally, the transmission curves, i.e. the spectral response, of the two FPI's can be measured with the narrowband laser signal by tuning the laser frequency (Witschas et al. (2012a)). The IR laser beam of the seed laser is injected into the resonator of the Low Power Oscillator (LPO) in order to transfer its frequency properties. This is followed by the amplification stage, where laser diodes at 808 nm are used to pump Nd:YAG (Neodymium-doped Yttrium Aluminium Garnet) crystals in order to increase the power (Power Laser Head) of the laser beam at 1064 nm. Actively controlled triggering of the laser pulse emission via the ramp-and-fire technique (Fry et al. (1991)) assures less disturbance due to aircraft vibration. Transmitting the laser pulse with a wavelength of 1064 nm through dedicated second (SHG) and third (THG) harmonic generator crystals converts the pulse to 532 nm (green) and 355 nm (UV), respectively, with a conversion efficiency of about 30 % (Schröder et al. (2007)). Preparatory work has been put into the A2D laser system, especially characterising its short term frequency stability and linewidth, yielding a jitter of about 1 MHz (rms) at 1064 nm over 14 s and a FHWM of 15 MHz at 1064 nm, which is equivalent to 3 MHz, respectively 45 MHz, at 355 nm (Reitebuch et al. (2012d)).

Although the heterodyne method of the PLL promises high precision for differential frequency measurement, it does not provide information about the absolute frequency of the laser pulse. Changes in ambient temperature and pressure may cause drifts in the frequency of the reference laser. As only the frequency difference between reference and seed laser is commanded, a drift of the reference laser frequency would be propagated to the frequency of the laser pulse which is emitted towards the atmosphere. A major impact of this fact could be the occurrence of different absolute frequencies despite the same commanded (relative) frequencies. To cancel the effect of possible long term frequency drifts onto the wind retrieval the emitted laser pulse is analysed internally by the Internal Reference (INT) in addition to the atmospheric return (sec. 3.5). Via a fiber coupler a part of the signal, which is intended for the Internal Reference, is diverted towards a wavelength meter (WM). The WM has been integrated into the A2D system in order to exactly (accuracy $\approx$2 MHz) measure the absolute frequency of the UV output. Regular calibration against a Helium-Neon laser at 632 nm ensures high frequency stability. With the help of the WM, differences between the commanded frequency steps and the resulting change in laser frequency were found during the response calibration procedure (Fig. 3.21) which can now be corrected. Additionally, the WM allows surveying the transmission properties of the FPI in dependence on temperature and pressure and hence enables the measurement of atmospheric temperature, for instance (Witschas et al. (2013)).

The laser beam with a divergence of less than 100 µrad full angle ($\pm 3\sigma$, containing $> 99\,\%$ of the energy) value is transmitted towards the atmosphere via a small piezo-electrically controlled mirror. The small mirror is attached to the frame of a Cassegrain-type telescope that consists of a 200 mm concave, aspheric primary mirror and a 75 mm convex, spherical secondary mirror collecting the backscattered light. An overlap function resulting from the structural design of the telescope, causes a range dependent reduction of the backscatter signal (Paffrath et al. (2009)). A field stop within the airborne front optics restricts the field of view of the receiver to about 100 µrad. Considering the divergence of the laser beam, this leads to a minimisation of the intensity of the solar background while avoiding a loss of backscatter signal. Furthermore, the airborne front optics include a UV camera, an electro-optical modulator (EOM), filters for the reduction of the broadband background signal and the optics for decoupling the Internal Reference signal. Unlike for the satellite, there is a strong need for the A2D to monitor and control the co-alignment of transmitted laser beam and receiver optics. For this task a part of the atmospheric backscatter signal is diverted towards the UV camera and onto an integrated CCD. Analysing the illuminated spot on the CCD provides a coordinate position of the maximum intensity which can be related to the incidence angle. This relation is used to steer the outgoing laser beam via the piezo-electrically controlled mirror at the telescope. Already small misalignments can strongly affect the wind measurement results as illustrated in subsec. 3.5.3 and sec. 4.3. After the front optics the light is conducted towards the spectrometers (subsec. 2.3.2) and the beam of the laser or backscattered light is adjusted to a diameter of 20 mm by an aperture stop, thereby matching the specifications of the FPI. The light transmitted through the spectrometers is detected by an accumulation charge coupled device (ACCD) whose signals are afterwards converted by an analogue-to-digital converter (ADC). In order to avoid saturation on the ACCD detectors, an electro-optical modulator (EOM) attenuates the intensity of the backscattered light, which is received from the near field, to the required dynamic range.

2.3.2. Interferometers and detector

Within the framework of the ADM-Aeolus mission four innovations come into operation worldwide for the first time regarding:

1. the combined configuration of two types of interferometers
2. the usage of a Fizeau interferometer
3. the sequential implementation of two FPI's
4. the use of an ACCD as detector

These novelties refer to the receiver part of the Lidar system and are implemented into the A2D as an almost exact copy of the satellite receiver (Reitebuch et al. (2009)). Within the A2D receiver the light is distributed onto two interferometers (Fig. 2.5). It is first directed onto a Fizeau

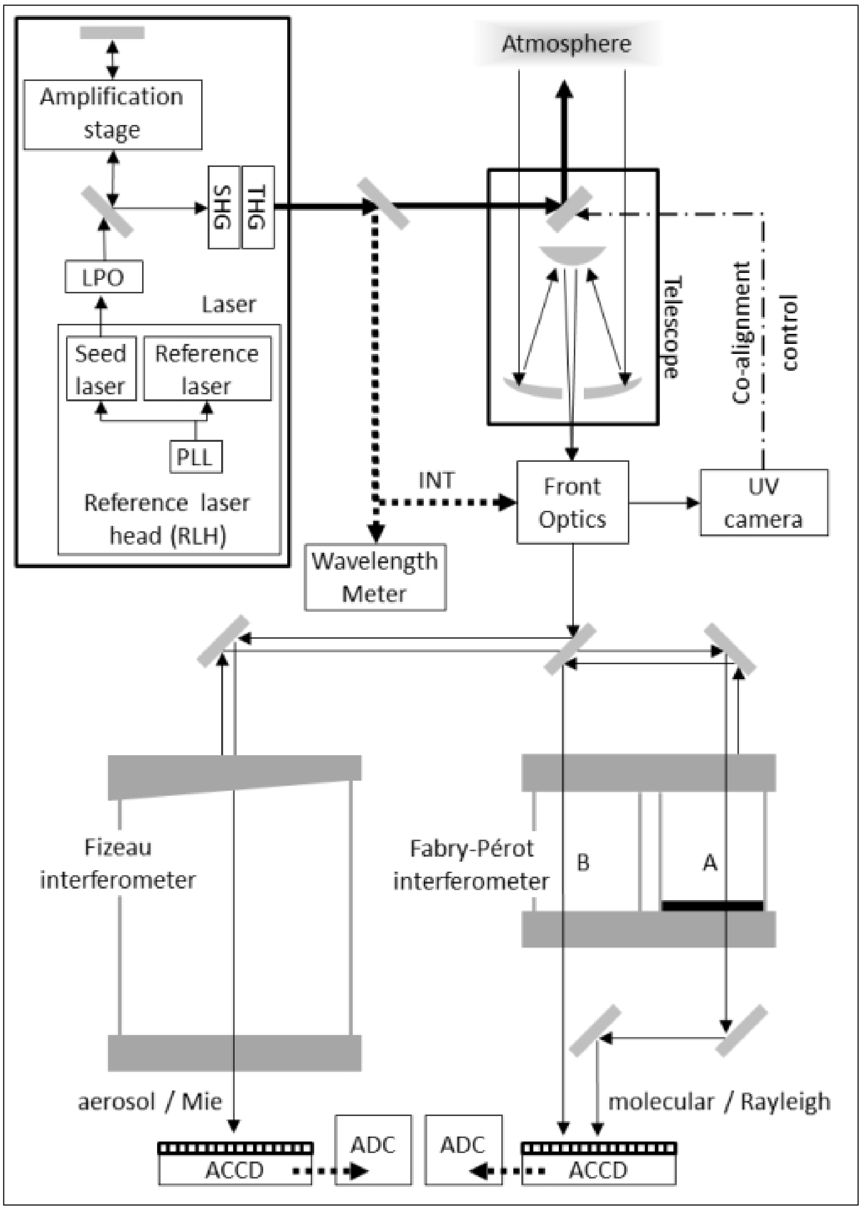

Figure 2.4.: Illustration of the subsystems of the A2D: laser, telescope, front optics and receiver including the two spectrometers and detectors. The emitted laser pulse (bold lines) is directed towards the atmosphere, the wavelength meter and spectrometers for internal reference measurement. The received backscatter signal is transmitted through the Front Optics and analysed by the spectrometers. A small part of the backscatter signal is made available to the UV-camera for the control of the co-alignment. ACCD: accumulation charge coupled device, ADC: analogue digital converter, INT: Internal Reference, LPO: low power oscillator, PLL: phase locked loop, SHG: second harmonic generation, THG: third harmonic generation.

interferometer for the detection of narrowband particle backscatter (Mie channel). Afterwards, the part of the light which is reflected at the Fizeau spectrometer is analysed by a double-edge FPI for the detection of broadband molecular backscatter (Rayleigh channel). Thus, this combined configuration of two types of interferometers allows an independent investigation of Mie and Rayleigh signals at the same time, employing two entirely different operation principles for resolving the spectrum and hence two independent wind measurement methods. Whereas narrowband aerosol signals are normally analysed with the help of heterodyning technology (subsec. 3.1.4), the usage of a Fizeau interferometer will be unique. Up to now only parallel implementations of FPI's have been used for wind measurement. This technique requires either a splitting of the incoming beam and its distribution onto two or more interferometers (Garnier and Chanin (1992), Flesia et al. (2000), Gentry et al. (2000), Sun et al. (2005)) or employs spatially closely arranged FPI's, which are illuminated simultaneously (Chanin et al. (1989), Souprayen et al. (1999b), Xia et al. (2007), Gentry et al. (2008)). The reflected light is eventually completely lost. A sequential implementation as for ADM-Aeolus firstly transmits the full beam onto one interferometer before directing the complete reflection onto the other, which improves the optical efficiency due to the reuse of the light. Furthermore, a specifically manufactured ACCD chip is utilized as the detector within the space-borne and the airborne instrument.

Fizeau interferometer

After the collection of the atmospheric backscatter by the telescope and the shaping of the beam by the front optics, a polarizing beamsplitter reflects the light towards the Mie spectrometer (Fig. 2.5). Even for a perfect Fizeau interferometer with perfect transmission at the transmission maxima only a portion of the incoming light is transmitted through the Fizeau aperture. The rest of approximately 90 % of the intensity is reflected towards the FPI (Paffrath (2006)). There is no need to cover the whole spectral width of the backscattered light, i.e. the broadband Rayleigh signal, on the detector. Thus, the physical properties of the Fizeau spectrometer can be adapted in order to only resolve the small bandwidth and Doppler frequency shift of the Mie peak. The Fizeau interferometer (Fig. 2.5) consists of two plates separated by a spacer made of Zerodur (Reitebuch et al. (2009)). The wedge angle of 4.77 µrad enclosed by the two plates governs the spectral dispersion, i.e. the width of the fringe on the detector. Whereas the transmission peak of the Fizeau of the A2D exhibits a full width half maximum (FWHM) of 137 MHz (Tab. 2.4), two adjacent peaks are separated by a free spectral range (FSR) of 2190 MHz. This results in a coefficient of finesse of 16 (Eq. 2.10). Due to the laser spectral width of about 50 MHz, which is narrow compared to the filter bandwidth of the Fizeau interferometer, the width of the Mie fringe on the detector is only marginally broadened. Additional broadening of a few MHz can be induced by the interplay of a pulse-to-pulse laser jitter and the subsequent accumulation of signals on the detector. The useful spectral range (USR) of 1596 MHz, i.e. the frequency range which is imaged onto the detector, restricts the capability of wind speed measurement to a range of about ± 145 m/s. One pixel of the detector covers the range of ≈ 100 MHz which is equivalent to 17 m/s wind speed (subsec. 3.4.2). In the absence of a Doppler shift, the backscattered aerosol spectrum is assumed to peak at the same position as the laser spectrum of the Internal Reference. The displacement of the Mie fringe on the detector is linear with the Doppler shift and observable as changes in the intensities of the few affected pixels. Considering the FWHM of the Mie fringe of 137 MHz (≈1.5 pixels), a trade-off was applied. In cases of sparse signal, the distribution of only few photons onto a higher number of pixels reduces the signal to noise ratio of the measurement. However, a reliable performance of the detection algorithm for the centroid (ch. A.1) has to be ensured with information from a minimum number of pixels.

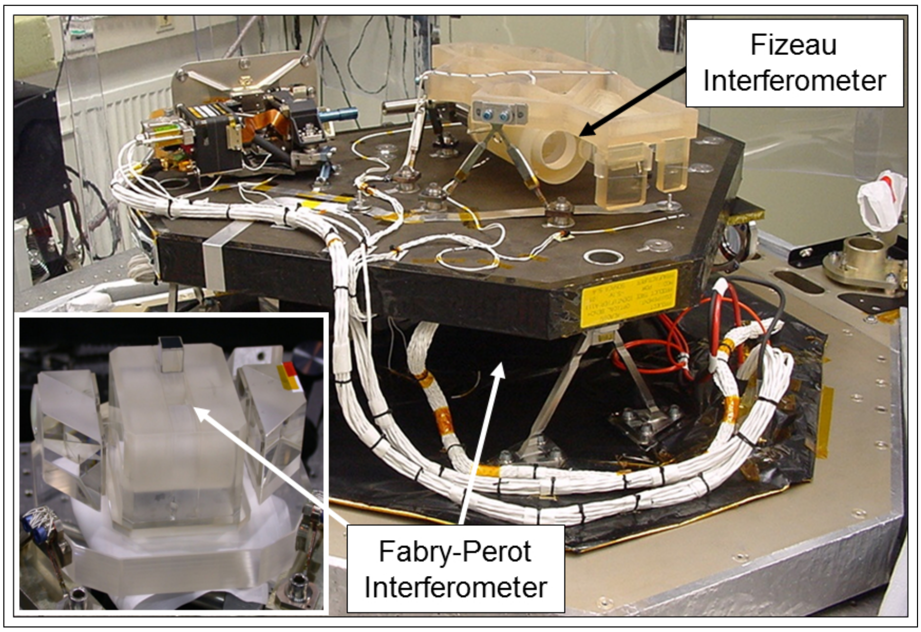

Figure 2.5.: The optical bench assembly after removal of the thermal hood including the Fabry-Pérot and the Fizeau interferometer mounted on opposite sides of the support structure. A detailed view onto the Fabry-Pérot, which is usually covered by a separate thermal casing, is given at the lower left side. The assembly to the left of the Fizeau contains the detector with the ACCD chip for the Mie channel. (Photo adapted from Reitebuch et al. (2009)).

Fabry-Pérot interferometer

The light which is not transmitted through the Fizeau interferometer is reflected towards the sequentially implemented FPI's (Fig. 2.5) employing the double-edge concept. Effects occurring due to the coupling among Fizeau wedges and FPI's are discussed by Belmonte (2008) who considers the sequential arrangement of such spectrometers an efficient way to use the incoming light. It is preferred to measure the intensities transmitted through an FPI, since the determination of a displacement (as for the Fizeau interferometer) in the order of a few MHz yields too large errors when analysing a noisy broadband molecular spectrum with a FHWM of about 1.7 GHz. As the reflection from the Fizeau may still contain signal from particle backscatter, the concept for ALADIN is to desensitise the Rayleigh channel with respect to aerosol backscatter

(Flesia and Korb (1999)). Thus, a deposited step (Fig. 2.4) of 80 nm thickness shifts the transmission curve of the direct filter (FPI) A with respect to filter (FPI) B, which ideally establishes equal spacings of 5.5 GHz, corresponding to 2.3 pm (Tab. 2.4). However, an asymmetric spacing of 6.2 GHz and 4.75 GHz is present for the A2D, which can most likely be explained by an inaccuracy in the thickness of the deposited step. Consequently, unlike for ADM-Aeolus, desensitisation does not apply to the A2D Rayleigh channel, as shown by the fact that the sensitivity is about 1/3 higher for broadband molecular signal than for narrowband signal (Fig. 3.16 and Reitebuch et al. (2009)). Using heating elements, while the FPI's are contained in a thermal hood, provides the capability of frequency fine tuning and allows a temperature stability of ± 10 mK, avoiding long term temperature drifts. The collimated beam with an incidence angle of 90° perpendicular to the surface of the plates creates an interference pattern of which only the central spot, i.e. the 0^{th} order maximum, is analysed. The mean transmission of the first (direct) filter A is about 18 % and the remaining 82 % are reflected towards the second filter B (Paffrath et al. (2009)), eventually resulting in the relation of the maximum transmissions $T_{\mathrm{B,max}} / T_{\mathrm{A,max}} = 0.748$ for the real instrument (Witschas et al. (2012b)).

Accumulation charge coupled device

In contrast to the conventional detection methods using photomultipliers, photodiodes or charge coupled devices (CCD), the registration of photons within ALADIN and the A2D system is performed by an accumulation charge coupled device (ACCD) patented by EADS Astrium (Durand et al. (2004)). Apart from a small size, further advantages of an ACCD are its high quantum efficiency of about 85 %, i.e. the conversion ratio of generated signal electrons due to incoming photons, and its capability of accumulating signals and hence reducing the impact of read-out noise contributions. Despite the different types of spectrometers, the same type of ACCD is used for both detection channels, recording the two spots of the FPI's and the single fringe formed by the Fizeau interferometer (Fig. 2.5). Simulations showed that optical efficiencies of about 0.4 % (Reitebuch et al. (2012a)) and 1.5 % (Paffrath et al. (2009)) can be expected for the whole path from the atmosphere to the detector of the Mie channel respectively the Rayleigh channel (Fig. 2.4). However, the remaining photons are sufficient to produce clearly defined signals on the light sensitive area of the ACCD of $0.4 \times 0.4\,\mathrm{mm}^2$, which is subdivided into 16 x 16 pixels (Fig. 2.6). The charges produced by the incident photons are conducted towards the ADC which converts the signal electrons to digitizer counts, the so-called least-significant bits (LSB). The conversion rate, referred to as the radiometric gain, is 0.342 LSB/electron and 0.33 LSB/electron for the Mie and the Rayleigh channel, respectively.

After the emission of a laser pulse, this so-called imaging zone integrates the signal which is received from the atmosphere during the time of a range-gate according to the pre-defined vertical resolution. In the nominal wind measurement mode the charges of each column are summed afterwards and shifted into the respective transfer row in the memory zone which is not illuminated by the spectrometers. Within the memory zone the signals of 25 range-gates can be stored and accumulated for several laser pulses, 20 of which nominally form one measurement for the A2D. However, only 18 pulses can be considered since the time needed for the transfer of the charges to the read-out register and the subsequent digitisation prevents the use of 2 pulses (Fig. 2.7). Due to a limitation to 700 pulses, the signals of 35 measurements of 18 pulses each are aggregated into one observation, which results in an observation length of 14 s keeping in mind the 50 Hz repetition frequency of the laser. The transfer of the digitised signals of the 35 measurements from the ADC to the storage computer lasts additional 4 s so that an A2D observation has a duration of 18 s (Fig. 2.6). Although the terms *measurement* and *observation* are similarly defined for the A2D as for ADM-Aeolus (subsec. 2.2.1), this subdivision into observations is a remainder of the previously envisaged operation of ALADIN in a burst-mode (ESA (2008)). An optional operation principle of a CCD, which is presented by Irgang et al. (2002), likewise allows the accumulation of the signals of several pulses and hence the reduction of noise. For this purpose, the charges on a CCD are shifted by one row every time after the signal of a range-gate has been recorded. In order to accumulate several pulses the charges are transferred back to their initial position after each pulse and the shifting procedure is repeated for every pulse. Apart from the nominal operation mode for wind measurement explained above, the ACCD of the A2D is capable of providing the actual data of the imaging zone in a 16 by 16 pixel format (Fig. 3.9), which offers the possibility of additional instrumental diagnostics.

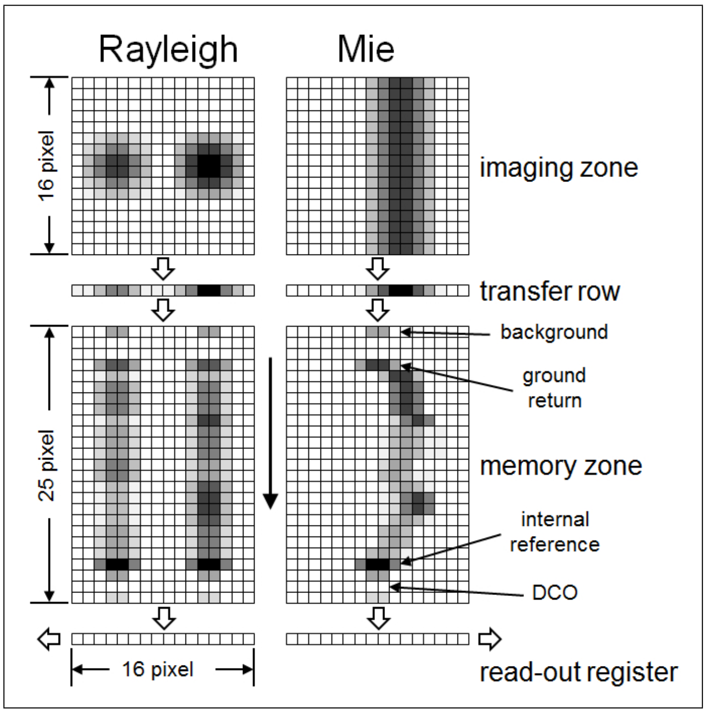

Figure 2.6.: Simplified principle of operation of the ACCD's used for the Mie and Rayleigh channel of ADM-Aeolus and the A2D. The signal is acquired by a light-sensitive imaging zone and is shifted via a transfer row to the memory zone whose 25 rows correspond to the range-gates of the atmospheric measurement. Dedicated measurements of the solar background, the Internal Reference and the detection chain offset (DCO) are performed. Intensity variations in the Rayleigh signal and shifts in the position of the Mie fringe due to the wind speed are indicated in the memory zone.

The temporal subdivision of an A2D observation is illustrated in Fig. 2.7. Equivalent to the 25 rows of the memory zone (Fig. 2.6), the recording of the signals for a single laser pulse is subdivided into 25 range-gates. A synchronisation between the laser pulse emission and the data acquisition allows the triggering of the ACCD such that the laser pulse emission is centred in range-gate #4. This range-gate records the small portion of the laser pulse which is separated from the main beam (Fig. 2.4) and is referred to as the Internal Reference signal (INT). Except for the range-gate which is dedicated to the solar background (BKG), the integration times of the range-gates can be selected from 2.1 µs to 16.8 µs (in steps of 2.1 µs), corresponding to distances of 630 m to 5040 m covered by the laser pulse.

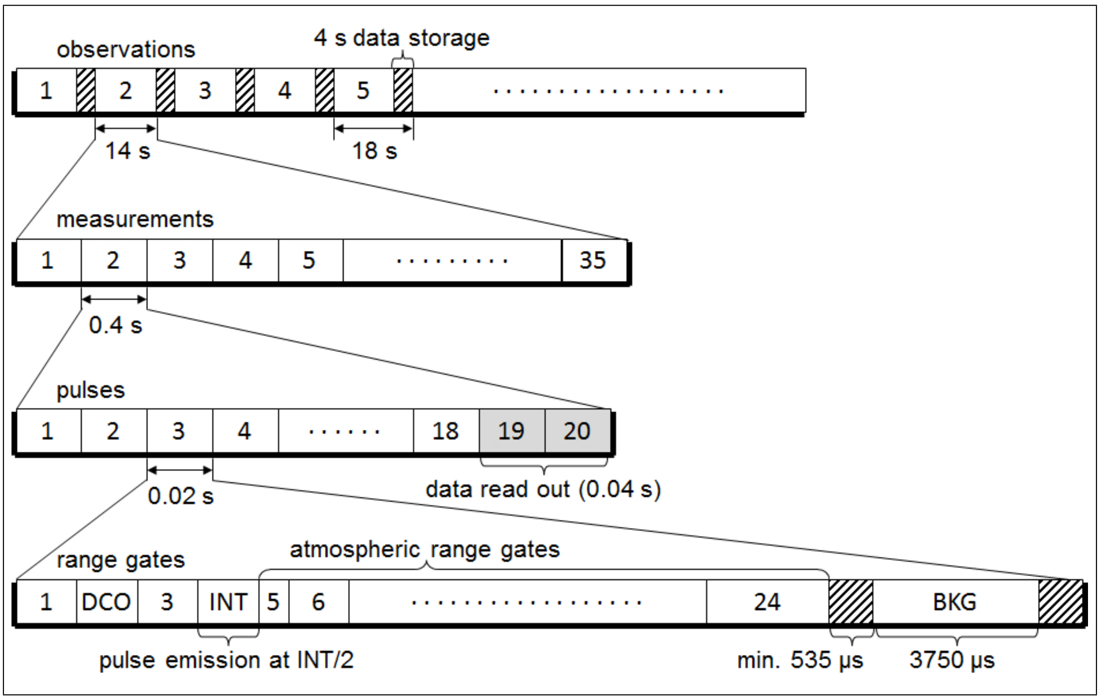

Figure 2.7.: Time sequence of the A2D signal acquisition. An observation is an aggregate of measurements which are subdivided into pulses. The vertical resolution of the atmospheric measurements is determined by the 25 range-gates whose integration times are programmable. Data read-out and storage procedures prevent the usage of 2 pulses (greyed boxes). The signal of a small portion of the emitted laser pulse is recorded in the middle of range-gate #4, which is the Internal Reference (INT). The solar background (BKG) is obtained from range-gate #25.

The read-out of the imaging zone takes at least 1 µs (ESA (2008), Reitebuch et al. (2010)). However, during the shifting procedure of charges to the transfer row, the imaging zone continues to collect light. This temporal overlap of range-gates can result in a shift of the centroid position of the fringe position (Mie channel) or a change of intensities (Rayleigh channel). Consequently, this vertical smearing of signal can lead to errors in the wind measurement in case of strong vertical wind speed gradients (subsec. 3.2). In order to assure a background signal free of contaminations by a possible ground return signal in range-gate #24, a gap is inserted. This gap between the end of the atmospheric acquisition and the start of the background acquisition is minimum 535 µs, in case that the integration time of all the 24 range-gates is set to the maximum value of 16.8 µs. The 535 µs are equivalent to a gap of 80 km. With a cruising altitude of the Falcon aircraft of maximum 13 km, this ensures a background range-gate located far below ground and hence a background signal not polluted by atmospheric contributions.

The final LSB values recorded in the data files do not exclusively result from the incoming signal photons but are also due to noise. Regarding the path of the information from the ACCD to the ADC several contributions can be associated with the noise, such as the digitisation process or the read-out noise in consequence of the conversion of the few stored charges to voltage signals in an amplifier. Although a cooling of the ACCD's to -30°C ensures a low noise level, the thermally induced dark current in the absence of light constitutes one of the main contributors. Such noise and an additional electric voltage offset, the detection chain offset (DCO), is measured by the dedicated second range-bin (Fig. 2.6). In order to avoid the influence of a possible leakage of signal from neighbouring range-gates, the range-gates #1 and #3 are considered as buffer and are not used during the wind retrieval. Placing these three range-gates before the emission of the laser pulse, and thus before the opening time of the EOM, additionally ensures an environment free of solar background radiation. By reason of statistical fluctuations, the DCO varies from pixel to pixel and is thus averaged over the 16 pixels of range-gate #2. The supposedly constant behaviour of the DCO allows a survey of the proper functioning of the ACCD and hence a quality control on the basis of measurements (sec. 3.6).

2.3.3. Comparison of A2D and ALADIN

A high degree of similarity is envisaged for the space-borne and the airborne system so as to ease the drawing of conclusions from comparisons of the measured performance of the A2D and the expected characteristics of ADM-Aeolus. Nevertheless, the different environments during operation not only require constructional amendments but also result in differences regarding the behaviour and properties of the instrument.

One of the most obvious differences is the velocity of the two platforms. With both instruments operating in a similar mode of continuously emitting laser pulses at 50 Hz, one observation of the satellite relates to a ground track of roughly 100 km, whereas the aircraft covers a distance of about 3 km. In this respect the impacts of, for instance, the atmospheric heterogeneity, the spatial resolution and the representativeness of the measurements can be studied with the A2D due to its higher horizontal resolution. In consequence of the spherical shape of the Earth surface in combination with the altitude of ADM-Aeolus of 400 km, the slant angle of the satellite of 35° translates into angles of up to 37.6° between the LOS and the local normal, decreasing with height. In contrast, a constant local incidence angle of 20° is a justifiable approximation for the A2D flying at 10 km. Simulations (Paffrath et al. (2009)) showed that the backscatter signal received by the A2D instrument from below the aircraft is always higher than the signal measured by the satellite, which is mainly due to the r^2-dynamics, i.e. the quadratic decay of the beam intensity with the distance from the laser (Eq. 2.5). The underlying radiometric performance models for the A2D Rayleigh channel, including the whole path of the photons from the emittance by the laser to the properties of the receiver optics and the detection electronics, were assessed during a ground campaign by comparing the obtained measurements to results from the A2D simulator (Paffrath et al. (2009), Reitebuch et al. (2010)). The performance of the A2D Mie channel was assessed during ground based measurements in 2011 making use of Saharan dust layers over Oberpfaffenhofen (Reitebuch et al. (2012a)).

Different dynamical range dependencies of the signal result from the fact that ADM-Aeolus and the A2D measure from space or from within the atmosphere as well as from differences in the field of view (Durand et al. (2005)). The concepts of the front optics and the telescope could not be transferred in detail from the satellite architecture to the airborne demonstrator. A new telescope had to be acquired and new routing optics had to be developed independently for the A2D. In order to protect the ACCD's of the A2D from too strong near field signal, the EOM was integrated into the front optics of the receiver. Such strong signals are a general issue for Lidar applications and were tackled for instance by Souprayen et al. (1999b) by employing two pairs of photomultiplier tubes each dedicated to the lower and upper part of the atmosphere.

The transceiver configuration of ADM-Aeolus constitutes a major difference compared to the A2D as a monostatic biaxial Lidar which requires an exact controlling of the co-alignment of the laser beam and the viewing direction. This is achieved by actively steering the piezo-electrically driven mirror at the end of the telescope (Fig. 2.4) using the information gathered by the UV camera that surveys the alignment. Therefore, an additional beam splitter is integrated into the A2D front optics for diverging a part of the backscattered signal to the camera. This signal is consequently lost for the evaluation of wind speed. The signal dynamics, the off-nadir angle and especially the high velocity pose stricter requirements to the satellite in terms of the pointing accuracy and hence to the knowledge of the attitude data. Due to volume constraints regarding the integration of the A2D into the aircraft, an off-nadir angle of only 20° could be realised. Compared to ADM-Aeolus, this results in larger errors in terms of the conversion from measured LOS wind speed to the HLOS component.

Furthermore, the allocation of the range-gates and pixels on the ACCD of ADM-Aeolus differs from that of the A2D. Since the long distance between satellite and the first atmospheric range-gate leaves enough time for the read-out of the ACCD, the Internal Reference signal is stored per pulse for ADM-Aeolus. In contrast, the Internal Reference is provided on a measurement basis for the A2D which leaves fewer options in terms of quality control for the latter. Whereas ADM-Aeolus measures the DCO on two single pixels independently for every range-gate, the A2D dedicates three range-gates (including two range-gates as buffer) to the respective measurement. Consequently, there are three more range-gates available for wind measurement to the satellite than to the airborne instrument (23 instead of 20).

According to the specifications for the spectrometers of ALADIN in vacuum, the locations of the peak transmissions of the two FPI's are almost equidistant. Regarding the A2D, a possible inaccuracy of the thickness of the deposited step in the direct filter (A) might be the cause for the different spacings (Tab. 2.4). In contrast to the specifications for the FWHM of the FPI's (1.67 GHz = 0.7 pm) of ALADIN (EADS-Astrium (2004)), the FWHM of the FPI's of the A2D was determined during a campaign in the Environmental Research Station Schneefernerhaus on Mount Zugspitze to be 1.765 GHz for the direct filter A and 1.720 GHz for the second filter B

(Witschas et al. (2012b) and Witschas et al. (2012a)). Generally, the usage of qualitatively different materials and the differences in the reception paths of both systems result in a higher total optical efficiency for the satellite (Reitebuch et al. (2012a), Reitebuch et al. (2010)). An overview of selected differences and commonalities between ADM-Aeolus and the A2D system is given in Tab. 2.4 (for spectrometer performances see also EADS-Astrium (2003), EADS-Astrium (2004) and EADS-Astrium (2012)).

Table 2.4.: Specifications and measured parameters of the airborne (A2D) and the satellite (ALADIN) wind Lidar system.

		A2D	**ADM-Aeolus**
Platform		aircraft	satellite
speed	/ m/s	≈ 200	≈ 7600
altitude	/ km	≈ 10	≈ 400
slant angle	/ °	20	35
Telescope			
configuration		coaxial	transceiver
diameter	/ m	0.2	1.5
FOV (full angle)	/ µrad	100	18.1
footprint diameter	/ m	≈ 1	≈ 8
Transmitter		Nd:YAG, tripled, diode-pumped	
operation mode		continuous	
wavelength	/ nm	354.89	354.8
repetition rate	/ Hz	50	50
tunability (UV)	/ GHz	± 6	> ± 5
laser linewidth (FWHM)	/ MHz	45	50
frequency stability	/ MHz	3	4
laser divergence (3 σ)	/ µrad	≈ 90	12
laser beam diameter	/ m	0.016	1.5
pulse energy	/ mJ	50 - 60	80 - 120
pulse duration	/ ns	25	≈ 30
output power	/ W	3.25	6
Receiver			
Fizeau			
FWHM	/ GHz	0.137	0.159
FSR	/ GHz	2.19	2.19
USR	/ GHz	1.596	1.687
finesse		> 16.1	> 16.1
wedge angle	/ µrad	4.77	4.77
plate separation	/ mm	68.5	68.5
Fabry-Pérots			
FWHM	/ GHz	1.765 (A) and 1.720 (B)	1.523 (A) and 1.594 (B)

... continued on next page

Table 2.4 – continued from previous page

		A2D	**ADM-Aeolus**
FSR	/ GHz	10.934	10.938
spacing	/ GHz	6.2 and 4.75	5.5
finesse		6.6	7
plate separation	/ mm	13.68	13.7
frequency tuning		temperature	
Detector			
ACCD		16 x 16 pixels (imaging zone)	
		25 x 16 pixels (memory zone)	
quantum efficiency	/ %	85	82
min. resolution	/ µs	2.1	2.1
Signal processing			
altitude range (nadir view)	/ km	0 - 10	0 - 30
vertical resolution	/ m	296 - 2370	250 - 2000
horizontal accumulation	/ km	0.08	7
horiz. integration length	/ km	3	100

2.4. Summary

After the invention of the laser, the Lidar technology evolved rapidly advancing various scientific fields, one of which became the measurement of wind speed using the effect of the Doppler shift. The portion of the laser pulse that is backscattered by molecules and particles in the atmosphere can be analysed by employing the edge technique with one or more Fabry-Pérot interferometers. The transmitted light is preferably imaged onto multiple ring anodes or charge coupled devices, creating moving circular fringes or spots of changing intensities on the detector, for instance. In 1999 the European Space Agency decided to launch the ADM-Aeolus satellite mission, which will contribute to the improvement of numerical weather prediction and support climate studies. Regarding the several integrated novel technologies, the single payload ALADIN currently constitutes the most sophisticated version of a wind Lidar capable of deriving wind speed from both aerosol and molecular backscatter at 355 nm at the same time. In the frame of a pre-launch risk reduction programme the ALADIN airborne demonstrator was developed, thereby aiming at a high degree of similarity between ADM-Aeolus and the A2D in terms of the system design and the wind measurement principle. The detailed discussion of the laser transmitter, the receiver and the data acquisition sub-systems provides the basis for understanding the evaluations of the airborne wind speed observations as presented in the following in ch. 3.

3. Data sets and methods

This chapter at first introduces the A2D airborne campaign conducted in September 2009 and discusses the scientific goals. An overview of the in-situ data set is given that is provided by sensors on-board the research aircraft Falcon 20 (sec. 3.1). In particular the attitude information is of importance for the retrieval of high quality wind speeds from the measured backscatter signals. A short insight is given to the measurement principle of the second Lidar on-board, the 2-µm DWL, followed by an illustration of the capability of the A2D in terms of cloud and ground detection (sec. 3.2). The main focus lies on the evaluation of the two calibrations performed over Greenland and the accuracy of the resulting response functions for the Rayleigh and the Mie channel (sec. 3.4). These functions constitute the link between wind speed and Doppler shift and are hence input to the wind speed retrieval algorithm (sec. 3.5). Several methods are developed to reduce the error on both, the obtained calibration functions and the retrieved wind profiles. Finally, a short summary of the known error sources is given, including an estimation of their impact on the wind speed accuracy.

3.1. Airborne campaign

The A2D as the airborne prototype of the ADM-Aeolus instrument was deployed in several ground and airborne campaigns, which served, among others, to verify the radiometric performance of the A2D Rayleigh channel as predicted by simulations via a comparison to measured atmospheric signals (Paffrath et al. (2009)). Several comparative wind measurement campaigns with heterodyne and direct-detection wind Lidars took place on ground, e.g. Delaval et al. (2000), Hardesty et al. (2001), Demoz et al. (2010) and Demoz et al. (2012). The first flights of a coherent and direct-detection DWL worldwide were conducted during an airborne campaign in 2007 with the A2D and the 2-µm Lidar aboard the same aircraft (Reitebuch et al. (2008), Reitebuch et al. (2012d)). This campaign led to consolidated expertise, for instance, in laser operation and yielded results in fields such as ground return and sea surface reflectance (Li et al. (2009)), but due to limited instrument performance these measurements were not suited for adequate evaluation of the wind measurement quality (Reitebuch et al. (2012d)). In 2009, for the third time, both DWL's were deployed on the Falcon 20 aircraft with the 2-µm Lidar as the reference instrument for comparison of the wind speeds measured by the A2D. Advantages of an airborne over a ground campaign in terms of a comparison to a satellite mission is the better representation of the viewing geometry, the dynamics of signal intensity and the spatial variability of clouds, amongst others. Thus, for the purpose of the validation of the ADM-Aeolus measurement strategy, a downward looking geometry was implemented for the A2D and the 2-µm Lidar. This viewing direction also allowed the acquisition of ground return echoes and hence provided the potential of pre-launch experience with ground return processing and new insights to ground and sea surface albedo properties. The A2D laser and receiver were attached to the aircraft via a dedicated frame situated on shock mounts for vibration damping. This airborne campaign in 2009 yielded an extensive amount of wind profiles and allowed an assessment of the accuracy of A2D winds measurements.

3.1.1. Objectives

The airborne campaign was expected to contribute to the validation of the ADM-Aeolus instrument concept (Reitebuch et al. (2009)) and enabled the validation and optimisation of the algorithms with real measurement data. For the first time this would allow a comparison between predicted and achieved performances. Of importance were the characterisation of the instrument and the validation of the measurement principle of the Lidar, in particular the calibration strategy. This includes, for instance, the imitation of a calibration in a geometrical configuration analogue to ADM-Aeolus. Thereby, a large albedo as that of ice surfaces would contribute to a signal to low noise ration and thus to accurate calibration, especially regarding the Mie channel. The performance of the Rayleigh channel in terms of calibration and wind retrieval calls for measurements that are preferably obtained from pure molecular signal, hence in regions with negligible aerosol content. In order to be able to assess the characteristics of the A2D over a large wind speed range, measurements in regions of high wind speeds would be supportive, e.g. in a high-altitude tropospheric jet-stream. Finally, thorough testing of the retrieval algorithms and quality-control schemes would profit the most from heterogeneous atmospheric conditions with, e.g. high vertical/horizontal wind shear or broken clouds. Besides, the investigation of the sea surface reflectance over ocean is interesting for the build-up of databases regarding the reflectance of different surface types at various wavelengths. According data sets under low and medium sea surface wind conditions and measurements with isotropic (circles) and anisotropic (straight flight) reflectance have already been acquired during the first flight of the A2D in 2007 and 2008 and analysed by Li et al. (2009). Based on this context, the region of Iceland, Greenland and the Northern Atlantic in between constitutes an adequate choice, particularly since it was shown to be a key-region for the weather development in Europe (Weissmann and Cardinali (2007)). The demands related to the objects of the airborne campaign are summarised below.

objective		demands
test performance of Rayleigh channel	⇒	pure molecular signal / low aerosol content
high wind speeds and wind speed range	⇒	jet-stream
calibration of Mie and Rayleigh channel	⇒	ice surface
validate algorithms & quality control schemes	⇒	heterogeneous atmospheric conditions (e.g. broken clouds)
albedo of sea surface	⇒	ocean

The DLR Falcon 20 aircraft (Fig. 3.1) was predestined for the task to carry the A2D to the desired locations and to allow the Lidar to execute the required measurements in a reasonable time frame. The two Lidars were installed above two windows (∅ 50 cm) that are integrated into the bottom of the fuselage and separated by about 1 m. This arrangement permits a downward viewing geometry similar to the ADM-Aeolus satellite and the probing of the same atmospheric volumes by both Lidars.

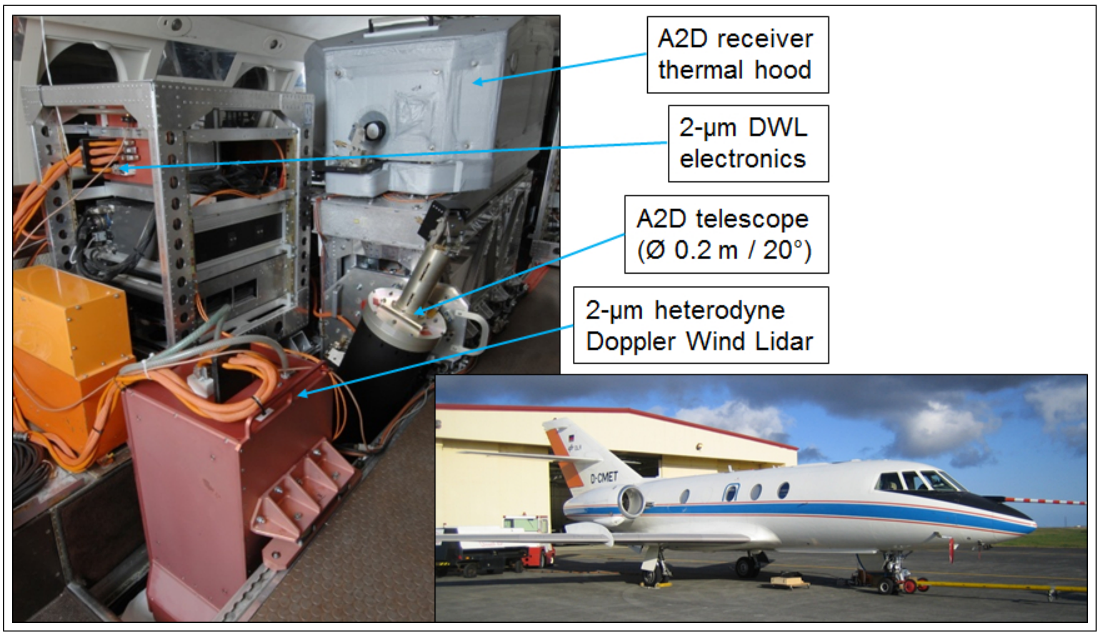

Figure 3.1.: Right: Falcon on ground in Keflavik, Iceland, with a mirror (yellowish box between the front and back wheels) positioned just below the A2D to reflect the laser beam towards the atmosphere. Left: Instrumentation within the Falcon in a viewing direction towards the back of the cabin. In the foreground the 2-µm Lidar including electronics are visible, in the background one can see the A2D telescope with the laser behind and the receiver on top.

The Falcon aircraft can reach a maximum altitude of about 13 km and allows a cruising time of more than 5 hours (Tab. 3.1)[1]. It is one of only a few research aircraft in Europe that are capable of reaching the upper troposphere and the lower stratosphere, thus enabling the measurement of pure molecular backscatter by the A2D Rayleigh channel. A maximum weight of 13.7 t allowed the presence of 5 persons on-board (2 pilots, 1 engineer, 2 scientists) together with the installed 2-µm system (≈ 215 kg) and the A2D (≈ 550 kg)(Reitebuch et al. (2009)).

In parallel to the integration of Lidar systems also aerosol sensors can be mounted at the aircraft and dropsondes can be stored on-board. Apart from the nose-boom, which enables, among others, the measurement of true airspeed, temperature, pressure and humidity, the Falcon accommodates a Global Positioning System (GPS) unit and a Honeywell Laserref Inertial Reference System[2] (IRS). The GPS and the IRS are the counterpart to the Attitude and Orbit

---

[1] `http://www.dlr.de/fb/desktopdefault.aspx/tabid-3714/5789_read-8405/`

[2] `http://www.dlr.de/fb/desktopdefault.aspx/tabid-3718/5796_read-8414/`

Control System (AOCS) of the satellite. They provide location, attitude and velocity of the aircraft and hence impact the accuracy of the retrieved wind speed.

Table 3.1.: Technical data of the DLR aircraft Falcon 20.

	maximum	typical A2D flight
length	17.2 m	
wing spread	16.3 m	
height	5.3 m	
weight	13.7 t	≈12.7 t
flight altitude	12.8 km	8.0 - 10.5 km
velocity	255 m/s (917 km/h)	≈210 m/s
flight duration	5 h 30 min	1 h 45 min - 4 h
range	3700 km	1370 - 3130 km

3.1.2. Flight tracks

The airborne campaign lasted more than 2 weeks, including a total flight time of 30 h 33 min. A summary of the various performed flights is provided in Tab. 3.2. The airport in Keflavik, Iceland, was selected as base for the airborne campaign (Fig. 3.2, next to the radiosonde station with WMO code 04018 BIKF). With two flights (flight #02 (light blue) and #03 (magenta)) from Oberpfaffenhofen via Liverpool the Falcon was transferred on September 18th.

Table 3.2.: Overview of the flights conducted during the airborne campaign 2009. CW: Cabauw, FI: Faroe Islands, KV: Keflavik, KQ: Kangerlussuaq, LP: Liverpool, NH: Nordholz, OP: Oberpfaffenhofen, SV: Stavanger. All times in UTC.

#	date	flight time	duration	routeing	comments
01	16.09.	10:06-12:46	2 h 40 min	OP-OP	test flight
02	18.09.	09:00-11:58	2 h 58 min	OP-CW-LP	transfer flight part 1
03	18.09.	13:43-16:23	2 h 40 min	LP-FI-KV	transfer flight part 2
04	21.09.	09:55-13:30	3 h 35 min	KV-KQ	2 calibrations over Greenland, radiosonde station 04360 BGAM
05	21.09.	14:30-16:14	1 h 44 min	KQ-KV	wind measurements
06	25.09.	13:51-16:10	2 h 19 min	KV-KV	very cloudy
07	26.09.	10:43-13:52	3 h 09 min	KV-KQ	wind measurement, jet-stream, 04360 BGAM, sec. 4.2
08	26.09	14:34-18:10	3 h 36 min	KQ-KV	sea surface reflectance at various angles
09	29.09.	10:57-14:55	3 h 58 min	KV-KV	wind measurement, different reference position, sec. 4.3
10	01.10.	08:56-12:50	3 h 54 min	KV-SV-NH-OP	transfer flight, broken clouds, wind measurement, sec. 4.4

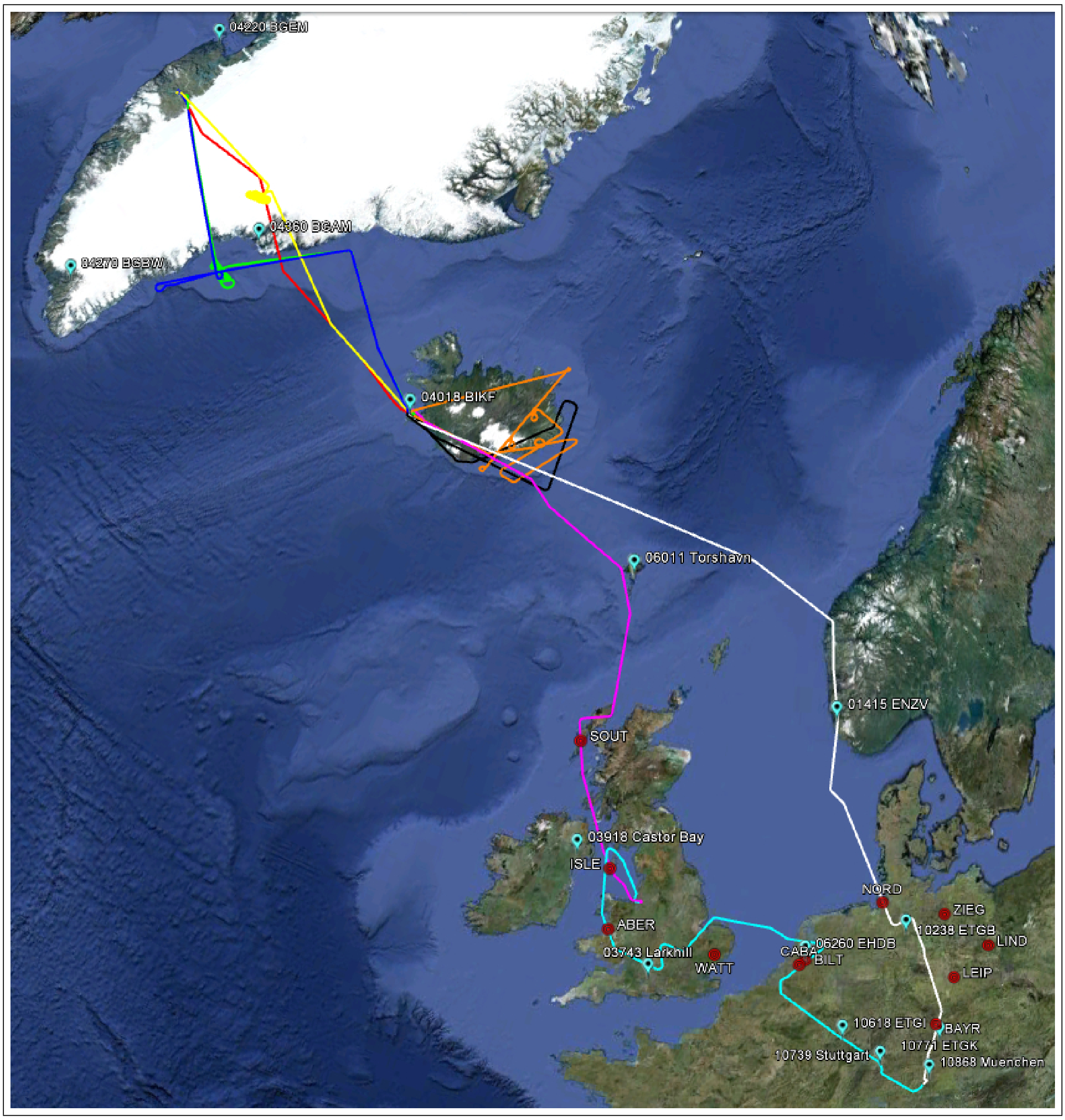

Figure 3.2.: Flight tracks of flights from Tab. 3.2: #02 light blue, #03 magenta, #04 yellow, #05 red, #06 black, #07 dark blue, #08 green, #09 orange, #10 white. Major radiosonde locations are marked as light blue balloon symbols with WMO code and wind profiler locations are represented by red circles. Google Earth was used to display this information.

On a flight over the Greenland ice shield two calibrations (subsec. 3.1.1) were performed during flight #04 (Tab. 3.2). The way back from Kangerlussuaq to Keflavik (flight #05, red) winds were measured in clear air over Greenland and over a dense blanket of clouds next to the coast. Flight#06 (black) was aborted due to unexpectedly strong cloud cover, preventing the achievement of the planned objectives. A wind measurement (subsec. 3.1.1) of about half an hour was obtained along the east coast of Greenland from flight #07 (dark blue), which is discussed in detail in sec. 4.2. During flight #08 (green) the Falcon flew circles with different roll angles in front of the coast of Greenland, which allowed measurements of the sea surface reflectance under various incidence angles (Li et al. (2010)). On September 28th the Falcon was not in operation but stayed on ground. Using a mirror below the aircraft (Fig. 3.1) several calibrations with an upward viewing direction were performed. Before flight #09 (orange) the direction of the laser beam was set to a slight tilt with respect to the telescope axis, instead of maintaining the usual parallelism. This circumstance, together with the acquisition of strong ground return over the snow and ice surfaces of Iceland, allowed the validation of the so-called Zero Wind Correction procedure (subsec. 3.5.3), whose application and results are presented in sec. 4.3. During the last flight (#10, white), the transfer from Keflavik to Oberpfaffenhofen, the 2-µm Lidar and the A2D were operated in parallel for more than one hour between Iceland and the coast of Norway. The evaluation of the data gathered in this heterogeneous atmospheric scene (subsec. 3.1.1) with broken cloud cover is discussed in sec. 4.4.

3.1.3. Aircraft data and A2D range-gates

Both the ALADIN instrument and the A2D will experience additionally induced frequency Doppler shifts according to the attitude and velocity of their space-borne and airborne platform. Thus, a posteriori knowledge of the aircraft data is essential for accurate wind measurements. Information about the attitude and velocity of the satellite are provided by the AOCS, using data from e.g. the Global Positioning System (GPS), star trackers or sun sensors (ESA (2008)). Likewise, the DLR-Falcon 20 contains a GPS receiver and an IRS. The latter is located between the two jet engines of the aircraft and slightly decentred from the origin of the Falcon coordinate system. Via the nose-boom of the Falcon measurements of, for instance, pressure, humidity, temperature as well as wind speed and direction can be provided. By combining the data from the three systems (IRS, GPS and nose-boom), further quantities can be derived such as the speed over ground or the angles of attack and sideslip. In terms of velocity the specification of the GPS receiver assures an accuracy of better than 0.1 m/s (Weissmann et al. (2005)).

The aircraft data contains 50 parameters with a time resolution of 1 second and the following data are used for A2D wind retrieval[3]:

- **a.** roll angle α_{ac} (IRS)
- **b.** pitch angle β_{ac} (IRS)
- **c.** true heading γ_{ac} (IRS)
- **d.** latitude (GPS)
- **e.** longitude (GPS)
- **f.** height above sea level h_{ac} (GPS)
- **g.** north-south velocity $v_{\mathrm{ac,NS}}$ (GPS)
- **h.** east-west velocity $v_{\mathrm{ac,EW}}$ (GPS)
- **i.** vertical velocity $v_{\mathrm{ac,V}}$ (IRS)

Attitude data (a.,b.,c.) are needed for the calculation of the pointing direction of the A2D LOS, in which the true heading corresponds to the aircraft yaw angle. Longitude and latitude (d. and e.) provide the geolocation. Amongst others, the height above sea level (f.) is used to determine the location of the A2D range-gates (sec. 3.2). The velocities (g.,h.,i.) are the components of the velocity vector of the aircraft. Considering the aircraft velocity and the A2D pointing direction, the additional LOS velocity induced to the A2D wind measurements can be calculated. Information about the accuracy of the parameters **a.** - **i.** are provided by DLR Flugexperimente[4].

The A2D is integrated into the Falcon under fixed angles. Referring to the aircraft-fixed coordinate system (COS) the downward axis and the A2D LOS enclose the angle $\alpha_{\mathrm{i}} = 20°$, while $\gamma_{\mathrm{i}} = 90°$ describes a viewing direction to the right (positive pitch axis). The projection of the A2D LOS onto the axes of the aircraft-fixed COS (forward, right, downward) yields the three components $[0\,;\sin(\alpha_{\mathrm{i}})\,;\cos(\alpha_{\mathrm{i}})]$. Usually, a small pitch angle is required to maintain the flight altitude. Thus, the A2D is additionally rotated around the pitch axis of the aircraft by $\beta_{\mathrm{i}} = \text{-}2°$, in order to approximately compensate for the additional LOS velocity that would be induced to the wind measurement otherwise. The resulting vector $\vec{p}_{\mathrm{ac}}$ is the representation of the A2D LOS in the aircraft-fixed COS.

$$\vec{p}_{\mathrm{ac}} = \begin{pmatrix} \cos(\beta_{\mathrm{i}}) & 0 & \sin(\beta_{\mathrm{i}}) \\ 0 & 1 & 0 \\ -\sin(\beta_{\mathrm{i}}) & 0 & \cos(\beta_{\mathrm{i}}) \end{pmatrix} \begin{pmatrix} 0 \\ \sin(\alpha_{\mathrm{i}}) \\ \cos(\alpha_{\mathrm{i}}) \end{pmatrix} = \begin{pmatrix} \sin(\beta_{\mathrm{i}}) \cdot \cos(\alpha_{\mathrm{i}}) \\ \sin(\alpha_{\mathrm{i}}) \\ \cos(\beta_{\mathrm{i}}) \cdot \cos(\alpha_{\mathrm{i}}) \end{pmatrix} = \begin{pmatrix} -0.033 \\ 0.342 \\ 0.939 \end{pmatrix} \tag{3.1}$$

---

[3] The aircraft data are routinely processed and provided by the DLR Flugexperimente (DLR-FX) after flights.

[4] `http://www.dlr.de/fb/desktopdefault.aspx/tabid-3718/5796_read-8414/`

Generally, right-handed coordinate systems are used (Norm (1970)) such as the geodetic COS, which is common practice in aviation. With the angles α_{ac}, β_{ac} and γ_{ac} the transformation from the aircraft-fixed COS to the geodetic COS is given by three rotary matrices, here called $\boldsymbol{R}$, $\boldsymbol{P}$ and $\boldsymbol{Y}$, which are related to the roll, pitch and yaw axis, respectively (Norm (1970)).

$$\boldsymbol{R} = \begin{pmatrix} 1 & 0 & 0 \\ 0 & \cos\,\alpha & -\sin\,\alpha \\ 0 & \sin\,\alpha & \cos\,\alpha \end{pmatrix}, \boldsymbol{P} = \begin{pmatrix} \cos\,\beta & 0 & \sin\,\beta \\ 0 & 1 & 0 \\ -\sin\,\beta & 0 & \cos\,\beta \end{pmatrix}, \boldsymbol{Y} = \begin{pmatrix} \cos\,\gamma & -\sin\,\gamma & 0 \\ \sin\,\gamma & \cos\,\gamma & 0 \\ 0 & 0 & 1 \end{pmatrix} \tag{3.2}$$

A defined sequence of rotations must be applied: 1. Roll, 2. Pitch, 3. Yaw, respecting the non-commutativity of multiplication of matrices. This yields $\vec{p}_{\mathrm{los}}$ as the representation of the A2D LOS vector $\vec{p}_{\mathrm{ac}}$ in the geodetic coordinate system.

$$\vec{p}_{\mathrm{los}} = \boldsymbol{YPR} \cdot \vec{p}_{\mathrm{ac}} \tag{3.3}$$

The velocity vector of the Falcon $\vec{v}_{\mathrm{ac}}$ is given by the north-south and the east-west velocity (g. and h.) in the North-East-Down (NED) COS. The vertical velocity (i.) is redefined in direction (from positive upwards to positive downwards) in order to comply with the right-hand rule.

$$\vec{v}_{\mathrm{ac}} = \begin{pmatrix} v_{\mathrm{ac,NS}} \\ v_{\mathrm{ac,EW}} \\ v_{\mathrm{ac,V}} \end{pmatrix} \tag{3.4}$$

By a projection of $\vec{v}_{\mathrm{ac}}$ onto the viewing direction of the A2D $\vec{p}_{\mathrm{los}}$ the aircraft induced LOS velocity $v_{\mathrm{los,ac}}$ is obtained. A correction of calibration and wind measurement data for $v_{\mathrm{los,ac}}$ must be performed, e.g. as discussed in subsec. 3.4.6.

$$v_{\mathrm{los,ac}} = \vec{v}_{\mathrm{ac}} \cdot \vec{p}_{\mathrm{los}} \tag{3.5}$$

For allowing, for instance, an assessment of the accuracy of ground elevations detected by the A2D (sec. 3.2) or a comparison of A2D wind speeds against those measured by the 2-µm Lidar (sec. 4.2), the location of the A2D range-gates must be determined. The off-nadir angle ω (in degree) is defined as the angle enclosed by the A2D LOS direction $\vec{p}_{\mathrm{los}}$ (Eq. 3.3) and the nadir direction $\vec{n} = (0,\,0,\,1)$.

$$\omega = \cos^{-1} \left| \frac{\vec{p}_{\mathrm{los}} \cdot \vec{n}}{|\vec{p}_{\mathrm{los}}|} \right| \tag{3.6}$$

Keeping in mind that, in order to gain information from the far end of a range-bin, it takes a laser pulse twice the time than just crossing the range-bin (travelling forth and back), the length d_r (index $r=$ range) of a range-gate can be determined from its integration time t and the speed of light $c = 299792458\,\mathrm{m/s}$.

$$d_\mathrm{r} = \frac{c \cdot t}{2} \tag{3.7}$$

The range r_r from the instrument to the middle of a range-bin n can be calculated by summing up the lengths of all range-gates i in between and taking into account in each case half the integration times of the Internal Reference $t(4)$ (subsec. 2.3.2, Fig. 2.7) and of the target bin $t(n)$.

$$r_\mathrm{r}(n) = \frac{1}{2} \cdot \frac{c \cdot t(4)}{2} + \sum_{i=5}^{n-1} \left[\frac{c \cdot t(i)}{2} \right] + \frac{1}{2} \cdot \frac{c \cdot t(n)}{2} = \frac{c}{4} \cdot (t(4) + t(n)) + \sum_{i=5}^{n-1} d_\mathrm{r}(i) \tag{3.8}$$

Considering the off nadir angle ω (Eq. 3.6), lengths d_r and ranges r_r can be converted to the vertical (index $v=$ vertical) axes d_v and r_v, respectively.

$$d_\mathrm{v}(n) = d_\mathrm{r}(n) \cdot \cos(\omega) \tag{3.9a}$$

$$r_\mathrm{v}(n) = r_\mathrm{r}(n) \cdot \cos(\omega) \tag{3.9b}$$

Finally, the altitude above sea level (ASL) of the middle of a range-bin is obtained by subtracting its vertical distance r_v from the flight height of the aircraft h_ac. The latter is given in the Falcon data as GPS height ASL.

$$h(n) = h_\mathrm{ac} - r_\mathrm{v}(n) \tag{3.10}$$

3.1.4. The 2-µm coherent wind Lidar

The 2-µm Lidar was deployed during several campaigns in the past, amongst others: for proving the feasibility of an active true airspeed sensor (Rahm (2001), Rahm et al. (2001)), for demonstrating the potential of characterising full-scale wake-vortices of aircraft (Köpp et al. (2004)), for targeted measurements over the Atlantic (Weissmann et al. (2005)) and for wake measurements of wind turbines (Käsler et al. (2010)). At last, the 2-µm Lidar was flown in April 2010 in order to detect ash plumes emitted by the volcano Eyjafjallajökull (Schumann et al. (2011)). For the airborne campaign in 2009 the 2-µm Lidar was deployed in the Falcon aircraft (Fig. 3.1). The wavelength of 2.022 µm is associated with low water vapour absorption, allowing a deep penetration into the atmosphere, and assures eye safety at the same time. According to Weissmann et al. (2005) the 2-µm Lidar yields best measurement results when flying at altitudes between 7 km - 12 km in regions of higher relative humidity and aerosol loads as well as in broken cloud conditions.

The Lidar system is composed of a transceiver unit developed by Coherent Technologies CTI (now Lockheed Martin Coherent Technologies[5]), a scanner and a data acquisition system that was developed at DLR (Köpp et al. (2004)). The most relevant system properties of the 2-µm Lidar are compiled in Tab. 3.3 and should be viewed in the context of the comparison of the A2D and ADM-Aeolus parameters (Tab. 2.4).

amplifying medium	Tm:LuAG
emission wavelength	2.022 µm
pulse length (FWHM)	(400 ± 40) ns $= (120 \pm 12)$ m
pulse energy	1.5 mJ - 2.0 mJ
pulse repetition rate	500 Hz
configuration	transceiver
telescope design	off-axis
telescope aperture	108 mm
scanner	rotating silicon double wedge
off-nadir angle*	20° (scan around nadir / LOS)
vertical resolution	100 m
horizontal resolution*	scan: 6.7 km ($\approx$ 32 s) LOS: 0.2 km ($\approx$ 1 s)
data acquisition	per pulse (with 500 Hz)
detection method	heterodyne
frequency offset	100 ± 3 MHz

Table 3.3.: Overview of system parameters of the 2-µm Lidar in the configuration used during the airborne campaign in 2009*.

Two lasers with diode-pumped Thulium doped Lutetium Aluminum Garnet (Tm:LuAG) crystals, i.e. a pulsed slave laser that is seeded by a continuous-wave master laser, are used to produce pulses at a repetition rate of 500 Hz. The laser beam is directed towards the atmosphere through a telescope with an aperture of 108 mm. While the transceiver configuration (monostatic coaxial Lidar) assures the alignment of the emitting and the receiving path, an off-axis design avoids the obstruction of incoming light by displacing the secondary mirror from the optical axis of the primary mirror. A rotating silicon wedge positioned after the telescope enables to steer the laser beam (Fig. 3.3). During the so-called "LOS mode", the pointing of the beam is kept fixed and provides only one component of the wind vector. The term "scan mode" describes a "step and stare" procedure with which the atmosphere is probed at several equally distributed azimuth pointing angles. The single LOS wind measurements are then averaged and analysed according to the velocity-azimuth display (VAD) technique, which has already been applied to the DWL by e.g. Chintawongvanich et al. (1989) and Reitebuch et al. (2001), both with a conically scanning 10.6 µm Lidar. Even for airborne applications where a

---

[5] `http://www.lockheedmartin.com/us/products/windtracer.html`

scan yields cycloidal instead of circular patterns the resulting observations are representative for the wind field (Weissmann and Cardinali (2007)). During the airborne campaign 2009 one scanner revolution took about 32 seconds, consisting of about 20-22 steps of 1 s accumulation time and the remaining time for moving the scanner to its positions. 500 pulses per azimuthal position are analysed and averaged to one LOS measurement. An off-nadir angle of 20° was used. With a mean aircraft ground speed of 210 m/s the horizontal resolution of an observation of 32 s in scan mode is about 6.7 km (sec. 4.2), whereas with a single LOS measurement of 1 s one obtains 0.21 km (sec. 4.4). The vertical resolution is governed by the properties of the laser pulse. Defined by the pulse length, the first and closest measurement to the aircraft is feasible in a distance of 360 m (Köpp et al. (2004)), which is equivalent to three times the FWHM of the pulse. The backscatter signal from every single laser pulse is sampled every 2 ns, corresponding to a length of 0.3 m. From 256 samples a signal power spectrum is obtained which allows the estimation of the wind speed in the respective atmospheric volume. The processed 2-µm wind speeds are finally provided at a vertical resolution of 100 m.

The measurement principle of a coherent DWL is based on the optical mixing of two optical beams (Reitebuch (2012)). One of the beams is the radiation scattered back by the atmosphere, which exhibits a frequency of f_a that is shifted with respect to the frequency of the emitted laser pulse f_p by an amount Δf_D according to the movement of the particles (aerosols/clouds). Regarding the 2-µm Lidar, the frequency of the laser pulses is determined by a continuous-wave master laser, which is also used to provide the reference beam. To enable a heterodyne detection a frequency offset Δf_off is applied with respect to f_p and the local oscillator frequency f_lo. This allows the determination of the sign of the frequency shift and, consequently, the determination of the wind direction. In the case of the 2-µm Lidar Δf_off is 100 MHz (Tab. 3.3), which is equivalent to about 100 m/s wind speed. Both low bandwidth signals, the backscattered radiation and that of the local oscillator, are combined on an optical detector. The detector measures the resulting beat frequency f_b (Eq. 3.11) that varies depending on the frequency difference, i.e. the Doppler shift Δf_D.

$$f_\mathrm{b} = |f_\mathrm{a} - f_\mathrm{lo}| = |(f_\mathrm{p} + \Delta f_\mathrm{D}) - (f_\mathrm{p} + \Delta f_\mathrm{off})| = |\Delta f_\mathrm{D} - \Delta f_\mathrm{off}| \tag{3.11}$$

Thus, the detector records a frequency modulated signal. Its mean frequency is related to the mean wind speed and the intensity of the signal is related to the intensity of the backscattered light. This heterodyne detection principle of the 2-µm Lidar sensing narrowband aerosol and cloud backscatter allows very accurate wind speed measurements and makes the 2-µm Lidar much more sensitive to such backscatter than the direct-detection method of the A2D.

The data from the 2-µm Lidar for the airborne campaign is provided in fixed formats depending on the operation mode. In the scanning mode the wind profiles are derived from 20 - 22 single LOS measurements (whereas Weissmann and Cardinali (2007) used 24 measurements). The profiles are geo-referenced, the components of the velocity vectors are given in the North-East-Down COS, and quality criteria are provided, for instance regarding the median filter algorithm (ch. A.2). In a comparison to dropsondes Weissmann et al. (2005) determined the mean observational standard deviation of the 2-µm horizontal wind speeds to less than 0.5 m/s

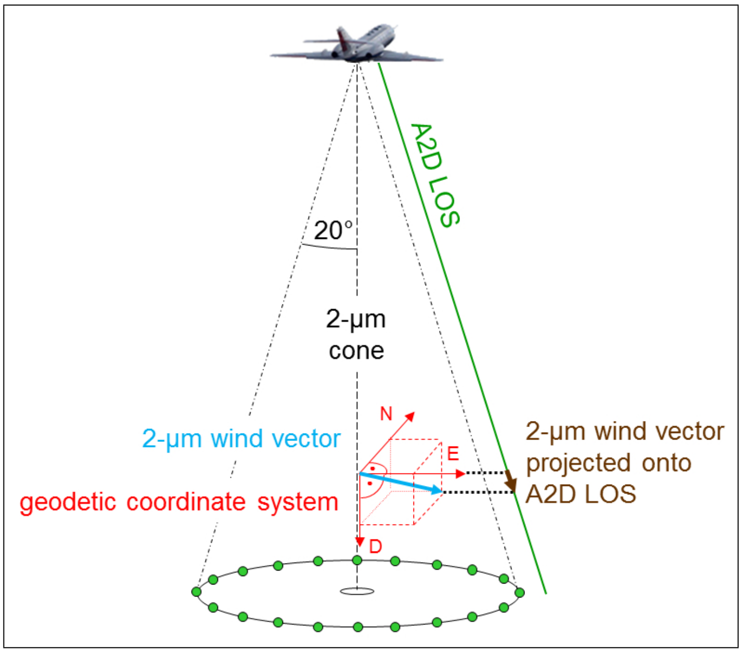

Figure 3.3.: Sketch of the measurement geometry of the 2-µm Lidar. A conical scan with a 20° angle and 20 steps (green dots) allows the retrieval of 3-D wind speed vectors (blue). The second measurement mode can be performed with a fixed LOS (green line) at an angle of 20° equal to the A2D. This yields one component of the wind vector (brown).

for high quality winds. However, for his comparison he suggested that a total error of about 1 m/s should be assigned to the 2-µm Lidar measurements. Also comparisons of the 2-µm Lidar to dropsondes in 2002 yielded low systematic and random errors for the 2-µm system with an average of 0.2 m/s and 0.4 m/s, respectively (Rahm et al. (2003)). Thus, it is to a certain degree justified to consider the 2-µm Lidar as reference with respect to the A2D wind measurements, especially to those of the Rayleigh channel that exhibit a much higher random error (subsec. 4.2.3). Examples of 2-µm wind measurements are shown, for instance, in sec. 4.2 and Fig. A.13 (from scan mode) and in sec. 4.4 (LOS mode).

The principle of the VAD scan also allows the determination of vertical wind speed. However, the accuracy of this method is rather poor for airborne measurements, because the assumption of horizontal homogeneity in the vertical wind is not fulfilled. For low vertical wind speeds it was shown that it is debatable if the retrieved wind from the 2-µm wind Lidar is real atmospheric vertical wind or an artefact (Reitebuch et al. (2012d)). Thus, the vertical winds from the 2-µm Lidar were not used to derived the 2-µm LOS wind speed.

3.2. Ground and cloud detection

Ground detection for Mie channel and comparison to a DEM

Inaccuracies in the knowledge about the position, the velocity and primarily the attitude of the platform, satellite as well as aircraft, hamper the task of precisely measuring and spatially allocating wind speeds. Owing to the large distance between the satellite and the atmospheric targets, the accuracy of the derived wind speeds is particularly sensitive in regard to attitude errors. Depending on the pointing direction, the relative velocity of the platform with respect to the target is contributing to the actual Doppler shift. This is the case if the velocity vector of the platform and the LOS direction are not perpendicular to each other. Although high precision attitude control systems are available for satellites (AOCS, star tracker) and aircraft (IRS, GPS), enabling a respective correction, they might nevertheless be subject to systematic and random errors. Resulting consequences would not only be erroneous wind speeds but also an improper localisation of the volumes within which the wind is measured and an inadequate value of the intersection height of the laser beam with the Earth's surface. To tackle these issues, the Earth's surface, assumed to be a non-moving object, is used as a so-called zero-wind reference (subsec. 3.5.3 and sec. 4.3). This approach necessitates an unambiguous discrimination between returns from the ground and moving clouds, which cause similarly high signal levels as the ground. Thus, part of the work of this thesis was driven by the intention to develop a dedicated algorithm that reliably detects ground echoes by employing a Digital Elevation Model (DEM). A distinction between different signal levels arising from different albedo values of the respective surfaces enables the discrimination between different types of ground return. Manninen (2012) demonstrated the ability of the A2D to distinguish bare ground from surfaces of ice and snow in Greenland and Iceland. Moreover, on the basis of airborne A2D measurements in 2007 and 2008, investigations by Li et al. (2009) revealed new insights on sea surface and subsurface reflectance in the ultraviolet region. Additional knowledge about the altitudes of upper and lower boundaries of cloud or aerosol layers would improve the determination of radiative properties of the atmosphere and thus have a significant impact on the accuracy of climate studies (ESA (2008)). In the case of scattering at cloud tops, the Doppler shift is induced by individual small water or ice droplets moving with the local wind velocity, providing reliable source of information due to the good SNR. Both ground and clouds generate a characteristic increase of signal intensity detected by the ACCD.

In order to obtain the actual intensity I (according to Eq. 2.11) per observation for the i^{th} range-gate (Eq. 3.12a), the raw intensity I_{raw} is corrected by the detection chain offset I_{DCO} (Eq. 3.12d) and the background signal I_{BKG} (Eq. 3.12c) before the summation over all pixels p and (optionally) measurements m. The background signal for the atmospheric range-gates is, in turn, determined by scaling the signal of the dedicated background range-gate #25 with the ratio of the integration times of the i^{th} range-gate t_{i} and the background range-gate t_0 (Eq. 3.12c). Throughout the airborne campaign the maximum number of measurements N was constantly set to 35. N is a variable and can be manually set to higher or smaller values in order to support individual scientific objectives. Eq. 3.12a - 3.12d are valid for the Mie and the Rayleigh channel.

$$I(i) = \sum_{m=1}^{N} \sum_{p=1}^{16} \left[I_{\mathrm{raw}}(p,i,m) - I_{\mathrm{DCO}}(p) - I_{\mathrm{BKG}}(p,i,m) \right] \qquad i = 5, ..., 24 \tag{3.12a}$$

$$I_{\mathrm{INT}} = \sum_{m=1}^{N} \sum_{p=1}^{16} \left[I_{\mathrm{raw}}(p,i=4,m) - I_{\mathrm{DCO}}(p) \right] \tag{3.12b}$$

$$I_{\mathrm{BKG}}(p,i,m) = \left[I_{\mathrm{raw}}(p,i=25,m) - I_{\mathrm{DCO}}(m) \right] \cdot \frac{t_{\mathrm{i}}}{t_0} \tag{3.12c}$$

$$I_{\mathrm{DCO}}(m) = \frac{1}{16} \sum_{p=1}^{16} I_{\mathrm{raw}}(p,i=2,m) \tag{3.12d}$$

The EOM blocks the backscattered light from range-gate #5 almost completely ($\approx$ 99 %) and still partially for range-gate #6. Maximum transmissivity is reached from range-gate #7. Since the background signal in range-gate #25 is recorded with the EOM fully open, the simple scaling by integration time in Eq. 3.12c is not valid for the first two atmospheric range-gates (#5; #6). This circumstance is neglected as it coincides with the strong influence of the telescope overlap function in the near field, which led to the exclusion of the first two range-gates for the evaluation of A2D measurements in ch. 4. As the Internal Reference is not affected by background light it is treated separately by just subtracting the DCO (Eq. 3.12b). Range gate #2 is dedicated to measuring the DCO, valid for a complete measurement. It is assumed that the DCO is equally high for all 16 pixels and the mean over all of these pixels is determined in order to reduce the noise. An undisturbed determination of the DCO is to be guaranteed by the placement of this range-gate between the two idle range-gates #1 and #3. Thus, signal leakage from adjacent range-gates (as found, for instance, for the Internal Reference towards range-gate #3 in Fig. 3.9) can be excluded.

An example of measured intensities according to Eq. 3.12 is given in Fig. 3.4a that shows the ascent onto Greenland including the transition from the sea surface in range-gate #22 to ice and snow covered ground up to range-gate #15. The Mie channel with its Fizeau interferometer is an inherently better detection device for narrow bandwidth spectra, which result from particle and hard target (ground) backscatter. However, the A2D Rayleigh channel is also able to provide qualitatively good ground and cloud detection as will be shown below (Fig. 3.8a). Obviously, sea and ice surfaces can be easily distinguished by their backscatter intensities reflecting the different albedo values in the UV. High intensities occur as well between range-gate #5 and #10, constituting the near field signal. Most of the intensity in this region cannot be attributed to aerosol signal, but to broadband molecular backscatter detected on the Mie channel. Determining the distribution of the molecular backscatter on the 16 pixels requires the rather complex procedure described in subsec. 3.4.6. While the background is visible in range-gate #0 and the DCO in range-gate #2, the idle range-gate #3 exhibits intensities different from zero, corresponding to the above mentioned leakage from the Internal Reference on the ACCD. The random structures in range-gates #23-24 and up to #16 in the second half of the analysed section are considered as noise among others related to the subtraction of the DCO. Around

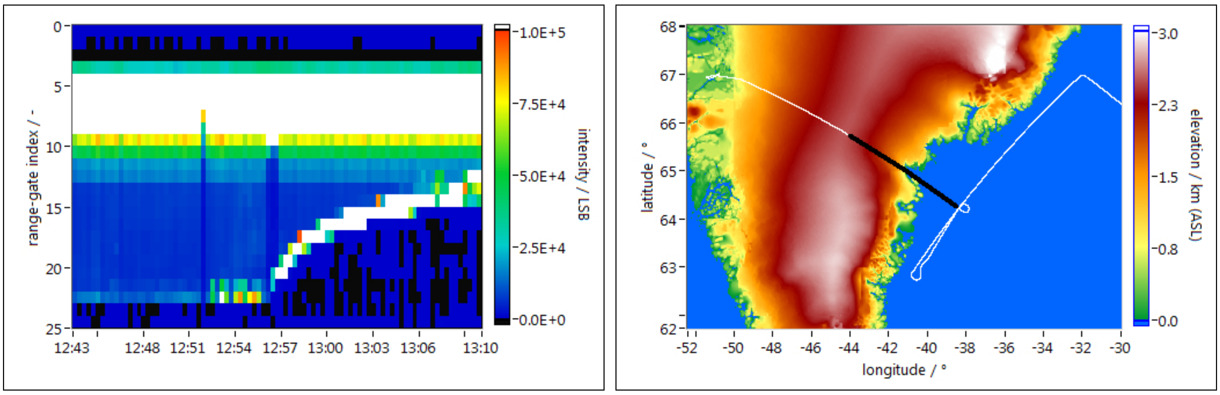

(a) *(b)*

Figure 3.4.: (a) Intensities according to Eq. 3.12a measured in the Mie channel on 2009/09/26 between 12:43 - 13:10 UTC during the ascent onto Greenland. Range-gate #4 corresponds to the Internal Reference and the flight altitude of the Falcon aircraft. The length of the flight section containing 89 observations is about 313 km. / (b) Flight track (white) of flight #7 (Tab. 3.2) and the analysed flight section (black) shown with elevations above sea level. The whole flight track of flight #07 with more details is presented in Fig. 4.4.

12:52 UTC and 12:57 UTC areas of reduced intensity are present which are either due to an undefined error source or can be traced back to an optically thin and high altitude cloud in range-gate #9. Considering the sections in the coastal region around 12:55 UTC and towards the end of the scene around 13:07 UTC, the following question arises: which signal can be attributed to a ground return and which to a possible cloud or aerosol layer?

The range-gate indexes of the ground and the corresponding altitudes found by the A2D can be verified by a comparison against a Digital Elevation Model (DEM). For the ADM-Aeolus satellite mission the Global Earth Topography and Sea Surface Elevation at a 30 arc second resolution (GETASSE30) was selected as DEM in the early phase, being the best freely available version at that time (ESA (2004)). The GETASSE30 DEM is a composite dataset of data from, amongst others, SRTM30 (Shuttle Radar Topography Mission at 30" resolution), the ground DEM ACE (Altimeter Corrected Elevation) and the mean sea surface height. It provides surface heights with respect to the ellipsoidal reference body of the World Geodetic System of 1984 (WGS84), which in turn approximately describes the shape of the Earth. Inhomogeneities in density result in an irregular form of the Earth, called geoid, that can be approximated by a spherical harmonic model of the Earth's gravitational potential, here the EGM96[6]. Geoid heights N (EGM96) have to be used to convert from heights above the ellipsoid h (DEM) to orthometric heights H (approx. height above sea level (ASL)) according to $H = h - N$. The DEM is mainly employed for ground detection and verification purposes within the operational L1B processor of ADM-Aeolus. However, it is used on-board the satellite as well, although in a much more reduced version of a so-called Look-Up-Table containing mean elevation values over defined areas (Marksteiner (2009)). The Look-Up-Table triggers the vertical shifting of

---

[6] `http://cddis.nasa.gov/926/egm96/egm96.html`

the measurement grid accordingly, in order to optimise the number of wind measurements and ensure reliable ground echo detection. Based on these facts it was decided to employ the GETASSE30 DEM for the evaluation of the data from the A2D airborne campaign. Apart from a few extreme outliers, further types of error sources contributing to the uncertainty of the ACE ground DEM in elevation are discussed in Johnson et al. (2001). Regarding the future measurements of ADM-Aeolus and A2D, it is also questionable if the chosen DEM version can still be considered reliable or whether it should be replaced by a more accurate one with higher horizontal resolution, e.g. the freely available G-DEM with 1 arc second resolution introduced in Hayakawa et al. (2008). This could enable successful investigations of a possible relationship between surface albedo and laser beam incidence angle (Manninen (2012)).

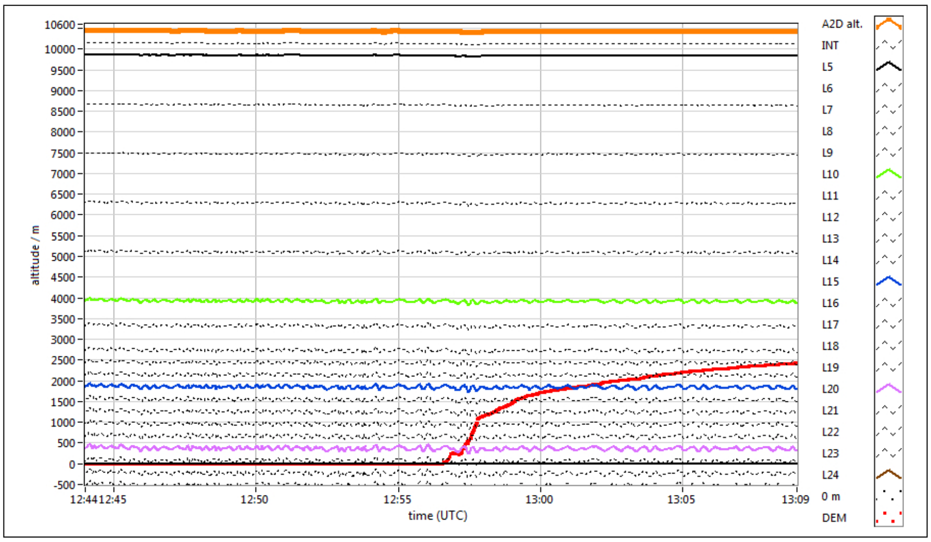

Figure 3.5.: Altitudes of the intersection of the DEM (red) and the A2D laser LOS for the flight section 12:44 - 13:09 UTC of flight #07. The 0 m altitude level and the Falcon flight height at 10.4 km are indicated in black and orange, respectively. The altitudes of the lower borders of the atmospheric range-gates are also shown (thin black dashed lines and coloured lines for range-gates #5, #15, #20 and #24). The maximum elevation over Greenland reaches almost 2500 m and would be detected by the A2D range-gate #13 and #14 (L13, L14).

Whereas the flight track is indicated on top of the DEM in Fig. 3.4b, Fig. 3.5 shows a comparison of the DEM with the altitudes of the A2D range-gates, giving the indexes at which the A2D ground return is expected. The intersection point of the A2D LOS with the DEM is determined by the measurement geometry, taking into account information about the attitude and flight altitude of the Falcon as well as its longitude and latitude coordinates (ch. 3.1.3) and, additionally, the mounting geometry of the A2D within the aircraft. By propagating along the LOS (considering potential blocking of mountains under extreme off-nadir angles) and thereby approaching the surface, a search algorithm selects the point of the DEM that is closest to the intersection coordinates (longitude and latitude) that are calculated from LOS pointing data. The indexes found from measured intensities and from calculated DEM intersections agree very well (Fig. 3.4a and Fig. 3.5). The sea surface is located in range-gate #22 and the maximum elevations encountered in Greenland reach range-gate #14 and #13. Thus, for instance, it can be concluded that the high intensities measured in range-gate #12 at 13:09 UTC towards the very end of the section (Fig. 3.4a) must be the result of strong cloud backscatter. Despite only minimal variations in off-nadir angle (less than ± 1°), the vertical position of the range-gates can easily change by 100 m. The oscillations present in the vertical position are directly linked to oscillations in aircraft attitude and are more pronounced at lower altitudes due to the linear dependence on the distance to the instrument (Fig. 3.5 and Fig. 3.7).

Weighted ground detection for Mie channel

A single wind observation of the A2D lasts 14 seconds, within which the Falcon covers a distance of about 3 km. Therein the ground surface can easily be moving within 2 - 3 range-gates (≈ 600 m), particularly in steep, mountainous terrain as it is present in Iceland and in the coastal regions of Greenland. So far the ground return was assigned to the centre altitude of the single range-gate with the highest intensity, which allows a resolution of only about 300 m according to the range-gate settings. In order to improve the accuracy of elevation estimation h_{GR}, a simple weighting method can be applied which weighs the centre altitudes h (Eq. 3.10) of the range-gates g presumed to contain the ground signal $I(g)$ (Eq. 3.12a) according to their fractional contribution to the signal sum. Here g is counting the involved ground return range-gates, starting at 1 and normally not exceeding the value of 3 within one observation.

$$h_{\mathrm{GR}} = \frac{\sum_g h(g) \cdot I(g)}{\sum_g I(g)} \tag{3.13}$$

Inherent to the principle of the ACCD's used for the A2D and ALADIN, a temporal overlap exists between adjacent range-gates (Reitebuch et al. (2010)). The ACCD is continuously acquiring a signal. Since the readout of the 16 lines of the imaging zone to the transfer row (Fig. 2.6) takes about 1 µs, a fraction of the received photons per pulse of one range-gate are assigned to the following range-gate and the other way round. This circumstance would enable a weighting procedure already on pulse basis. Due to the summation of pulses to measurements and, further, to observations, a spatial dimension of overlap is added. Regarding varying elevation of the target along flight distances of about 85 m per measurement and 3 km per observation the latter would be proportionately less affected by the temporal overlap. The effect of the overlap is apparent in the simplified sketch of Fig. 3.6, which shows an excerpt from the 2$^{\mathrm{nd}}$ response calibration during flight #04. In case of nadir pointing the 2.1 µs integration time of the smallest range-gate and the 1 µs overlap are equivalent to altitudes of 315 m and 150 m, respectively. Very good agreement is found between the location of the calculated ground intersection elevation from the DEM (black line) and the detected number of range-gates containing ground signal (blue line). As soon as the altitude of the ground is not anymore located within the height interval defined by the overlap, the hard target backscatter signal is solely assigned to a single range-gate (here #20).

The impact of the new method of weighted signal summation across several range-gates is visualised in Fig. 3.7. In the upper figure the intersection height is set to the centre altitude

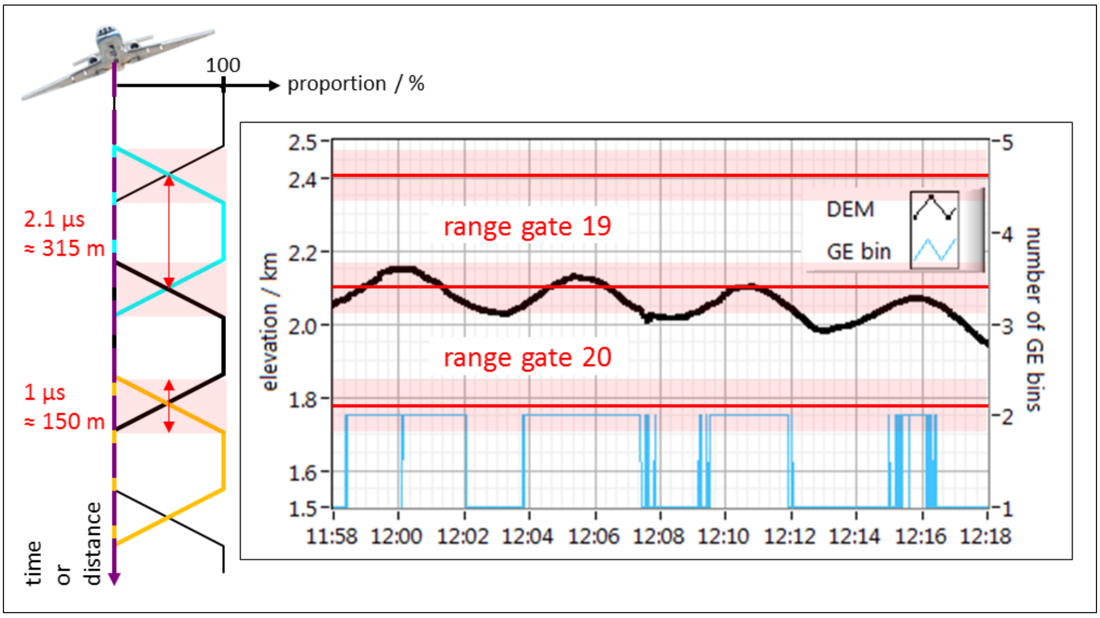

Figure 3.6.: In contrast to assumed fixed range-gate borders (red lines) a temporal overlap of 1 µs (= 150 m) exists between range-gates (red shaded). If the elevation of the ground intersection from the DEM (black) is located within the height interval of the overlap, the backscatter signal of the hard target is sensed by both neighbouring range-gates (blue indicating no. of ground echo (GE) range-bins from A2D). The presented section is an excerpt from flight #04 when the Falcon flew circles ensuring nadir pointing during calibration.

of the single A2D range-gate with the highest intensity on the Mie channel. The influence of the A2D resolution grid is visible as steps of about 300 m in the intersection heights, which correspond to 2.1 µs range-gate integration time. The oscillations in centre altitude of the range-gates, due to the correlation with the off-nadir angle (green), are expected and are also present for the range-gate borders in Fig. 3.5. While for the analysed section the maximum intensity method yields a mean absolute difference between DEM and A2D of 87 m, an improved elevation estimation, in cases where the ground return signal is spread over two range-gates, is achieved with a mean absolute difference of only 55 m (lower figure). Also the standard deviation decreases from 98 m to 53 m. Consequently, signal spread between two or more layers provides the ability to determine the altitude of ground, cloud or sea surface with higher accuracy than the vertical resolution of 296 m (with 20° off-nadir pointing) might suggest. Both the mean absolute difference and the standard deviation obviously depend on the variation in elevation of the sampled terrain. Thus, the derived values are only valid for the discussed example, but nevertheless give a very good indication of the overall performance improvement. Another option to verify the determined elevation of ground and cloud returns would be a comparison against the 2-µm Lidar (in case that the ground return signals were available) with its capability of locating these high intensity signals with a precision of only a few metres. The error of elevations determined within the non-overlap region (2.1 µs - 1 µs = 1.1 µs which is equivalent to 155 m) is half its vertical thickness, i.e. 155/2 m ≈ 77.5 m for a 2.1 µs range-gate and 20° off nadir pointing. Likewise the uncertainties in the overlap region can be roughly estimated. The maximum variation of the backscatter intensity of a single ground bin is generally assumed to be about ± 40 % (as can be found from flight #04 over Greenland). Applying this value to a split signal in the case of a ground return distributed over two range-bins, the variation of the ratio of the signals can be calculated. Thus, for a fraction of 50 %-50 % among the signal of two range-gates an uncertainty of ± 20 % (yielding 70 % -30 %) has to be attributed, while for a fraction of 90 % - 10 % one obtains only 5.5 %. Under the above assumption of a 2.1 µs range-gate and 20° off nadir pointing, these uncertainties translate into vertical uncertainties of ± 31 m and ± 9 m, respectively, keeping in mind the vertical extent of the overlap region of 140 m.

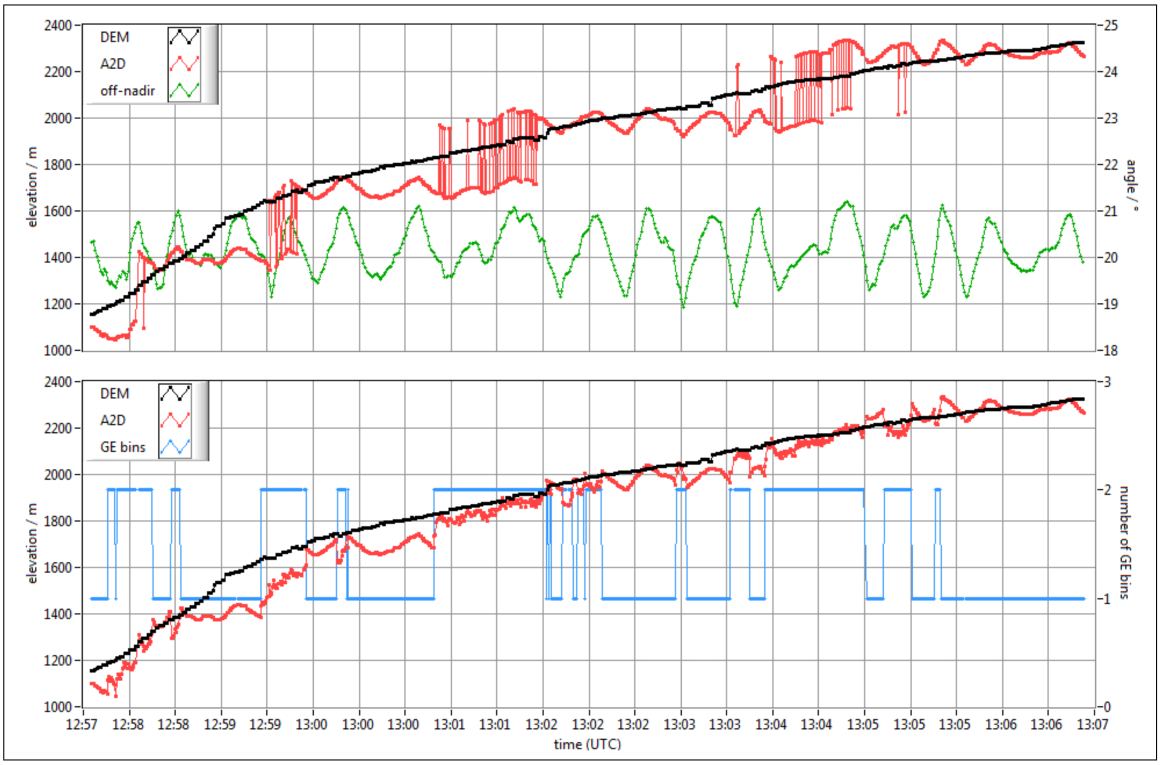

Figure 3.7.: Top: Elevation of calculated intersection points of the DEM and the A2D LOS (black) compared with the elevation of the ground return derived from A2D intensities on the Mie channel (red) per measurement for flight #07. A2D ground return indexes are allocated to the range-gates with maximum intensity. The mean absolute deviation of DEM and A2D ground elevation is 87 m (standard deviation 98 m). The off-nadir angle, varying between 19°-21°, is indicated in green. / Bottom: Elevations compared for the weighted averaging method. The ground return signals detected are all spread within 1 or 2 range-gates (blue). The mean absolute deviation of DEM and A2D ground elevation for this section is 55 m (standard deviation 53 m).

Owing to the new weighting method, the ground detection algorithm follows even more complex terrain with much lower albedo than the ice sheet on Greenland as it can be seen in Fig. A.8

with an example section over Iceland. The analysis of data from the 2009 airborne campaign revealed the improvement in ground elevation determination for the A2D and the ADM-Aeolus mission.

Cloud detection for Rayleigh channel

Since the Fizeau interferometer does not filter the complete narrowband aerosol signal, a reflected portion reaches the FPI. Despite the low transmission around the crosspoint of the two filters, the Mie signal significantly contributes to the intensities measured on the Rayleigh channel. With this information in hand, the method introduced above constitutes one possible way to enable a distinction between a ground signal and a cloud signal, not only for the Mie but also for the Rayleigh channel. Selecting a very illustrative example section with high variability in clouds from flight #10 on October 1$^{\mathrm{st}}$, a Ground-Cloud-Mask can be derived (Fig. 3.8a). The ground (white) is determined per measurement by locating the calculated DEM intersection point within the A2D grid. Shortly after measurement 5000 the ground index is shifted from range-gate #22 to #21, due to a right hand bend flown by the Falcon. An algorithm that makes use of signal gradients is applied in order to decide whether or not a cloud is present within a single range-bin. The Rayleigh signal intensity on measurement level I_{m}, according to Eq. 3.12a, is corrected for range r and normalised with the ratio of the range-gate integration time $t(i)$ to the minimum integration time of 2.1 µs.

$$I_{\mathrm{m,scaled}}(i) = I_{\mathrm{m}}(i) \cdot r(i)^2 \cdot \frac{t(i)}{2.1\mu s} \tag{3.14}$$

After deriving the signal gradient $\Delta I(i)/\Delta r(i)$, according to Eq. 3.15 a threshold can be applied to check for the existence of backscatter increase and decrease.

$$\frac{\Delta I(i)}{\Delta r(i)} = \frac{I_{\mathrm{m,scaled}}(i+1) - I_{\mathrm{m,scaled}}(i)}{r(i+1) - r(i)} \tag{3.15}$$

Depending on the measured intensity distribution throughout the range-gates, these manually provided thresholds yield a simple signature of flags (increase, decrease, constant) which is afterwards matched to predefined cases, including multilayer detection, and which finally results in a cloud mask. This algorithm certainly still exhibits some deficiencies, but performs well enough for its current purpose of detecting the uppermost range-bin affected by a cloud or aerosol layer. It is preferred here to keep the separation between Mie and Rayleigh channel. Consequently, wind speeds derived from the pure molecular signal are used for the assessment of the accuracy of the Rayleigh channel (sec. 4.4). Thus, the range-bin containing the cloud top and all range-bins below are excluded (Fig. A.18) and flagged as invalid. The same holds for cases where the signal reaches the ground in between the broken cloud cover. Kox (2008) successfully developed a multilayer cloud detection algorithm dedicated to A2D observations from ground, which was validated with co-located measurements of a second aerosol Lidar. This multilayer algorithm could replace the simpler algorithm described above.

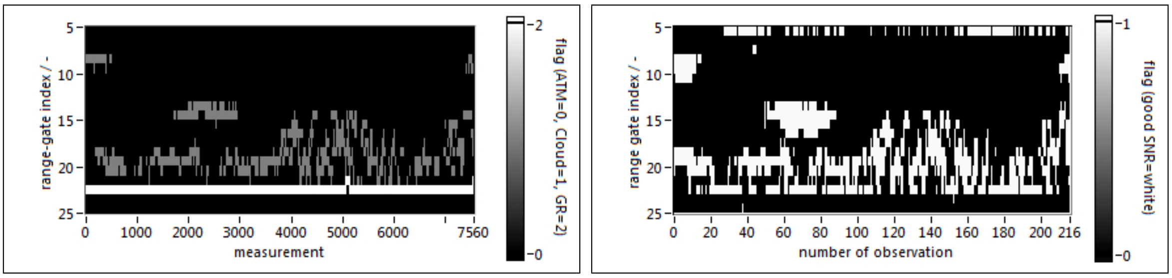

(a) *(b)*

Figure 3.8.: (a) A Ground-Cloud-Mask derived from Rayleigh channel intensities. The ground (white, flag = 2) in range-gate #22, clouds (grey, flag = 1) and assumed clean atmosphere (black, flag = 0) are shown. The 7560 measurements were recorded during flight #10 on 2009/10/01 between 09:35 and 10:40 UTC. / (b) An SNR mask derived from the Mie channel for the same flight section. The 216 observations are equivalent to the number of measurements for the Rayleigh mask. Values that exceed an SNR threshold of 5 are depicted in white (1), otherwise in black (0). Only atmospheric range-gates #5 - #24 are shown.

The cloud mask derived from the Rayleigh channel is in good agreement with the Signal-to-Noise-Ratio (SNR) mask determined from the Mie channel (Fig. 3.8b, sec. 3.6). The most obvious differences occur in the very first 10 observations and the lower part of the cloud between observation 50 - 90 in range-gate #15,- #16. For both the Mie and the Rayleigh channel it is not possible to detect the ground continuously by looking at the intensities, due to partial coverage by optically thick or opaque clouds. The validity mask derived from the Ground-Cloud-Mask in Fig. 3.8a is used in sec. 4.4 for the analysis of wind measurements.

3.3. Mie and Rayleigh response

The two different techniques of a direct-detection wind Lidar implemented for the A2D rely on different principles of resolving the frequency spectra of the backscattered light. Whereas, for the Rayleigh channel, the FPI's each create a simple fixed spot on the ACCD, the light passing through the Fizeau interferometer is displayed as a single fringe (subsec. 2.1.2), potentially moving if wind speed is present. The key characteristics are the respective intensities of the spots on the Rayleigh channel and the location of the peak on the Mie channel. The signals detected on the ACCD's show a dependence on frequency, distance from the receiver as well as on backscattering and extinction coefficient among others. Referring to the operation principle of the ACCD (Fig. 2.6), examples of signals measured during the airborne campaign are shown in Fig. 3.9.

The imaging zones reveal the positions and sizes of the spots and the fringe within the 16 by 16 pixel areas. After integration, transfer and storage a range resolved view onto the measurements is possible, showing the brightest signal at range-gate #4, the Internal Reference. Additionally, for both, Mie and Rayleigh channel, the details of range-gate #13 and #22 are extracted, containing an optically thin cloud and the ground return signal, respectively. These

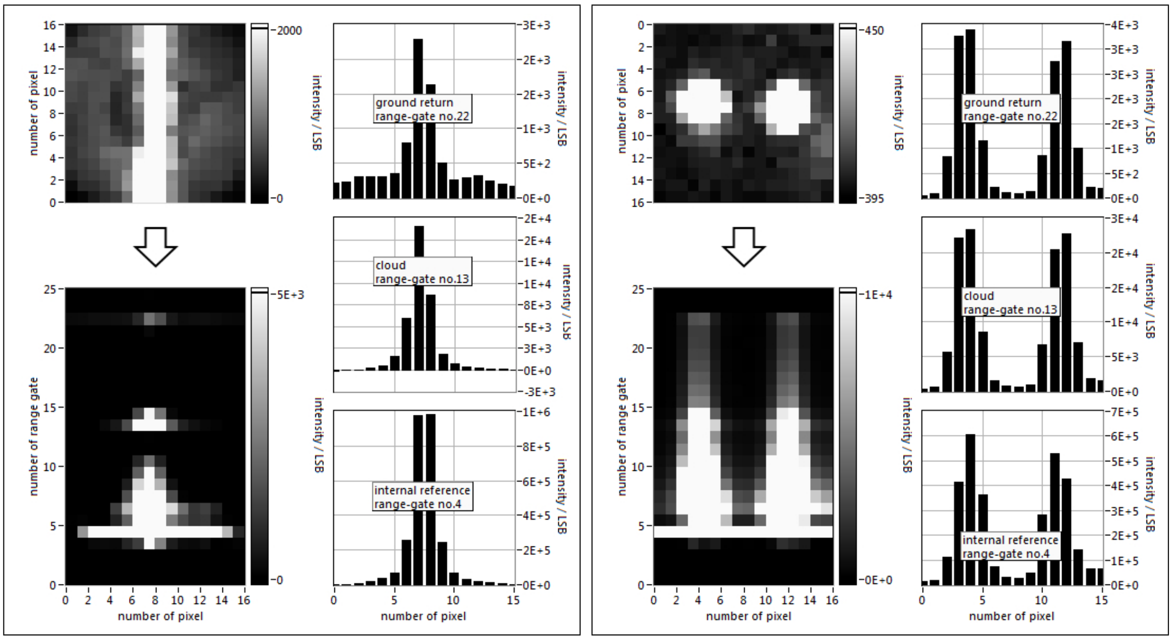

(a) (b)

Figure 3.9.: Examples of intensities measured on the Mie (a) and Rayleigh channel (b) during the airborne campaign on 2009/09/26. For both cases the imaging zone of the ACCD is shown on the top left and a recording of all 25 range-gates (from the memory zone) below. Exemplarily, three range-gates are extracted and presented in detail for the ground return (top), a cloud (middle) and the Internal Reference (bottom). The illustrations of the imaging and memory zone are related to different measurements, because it is not possible to acquire these measurements simultaneously.

examples clearly illustrate the relative signal magnitudes which are important in terms of the cloud and ground detection algorithm previously introduced (sec. 3.1). In range-gate #3 the above mentioned leakage of signal from adjacent range-gates is visible (Fig. 3.9a and Fig. 3.9b). Although the concept of operation does not foresee the reception of signal in this range-gate, it apparently contains charges that have to be attributed to the Internal Reference. It is worth noting that the presented examples of imaging zone and memory zone are not obtained from the same measurement, since the concept of the detection electronics only allows data storage in either imaging mode (16 by 16 pixel, top) or Lidar mode (16 x 25 pixel, bottom). The unit of Least Significant Bit (LSB), in which the intensity I is given (also in Fig. 3.4a), is proportional to the number of electrons created on the ACCD by the incoming photons, taking into account a conversion rate g (radiometric gain) of 0.33 and 0.342 LSB/electron for the Rayleigh (index R) and the Mie (index M) channel, respectively (EADS-Astrium (2006)). Via the quantum efficiency q_{eff} of the detector this unit is thus directly related to the number of photons N_{ACCD} illuminating the ACCD.

$$I_{\text{M,R}} = N_{\text{ACCD}} \cdot q_{\text{eff}} \cdot g_{\text{M,R}} \tag{3.16}$$

Mie channel

In the past, several dedicated algorithms have been developed for the analysis of Mie signals using different approaches and focussing on different key aspects, mainly the accuracy (Paffrath (2006), EADS-Astrium (2011), Reitebuch et al. (2012b)). A short explanation of the Downhill Simplex Algorithm (DSA) that is applied for the evaluations presented in this thesis, is given in ch. A.1. Four characteristics of the signal shape are determined: peak height h_p, peak position x_p, spectral width w_p and offset h_0. The peak height provides information about the intensity of the Mie-type backscatter (aerosol, water and ice clouds, ground return, narrowband Internal Reference) and can hence be used in the formulation of an SNR and quality criterion. The peak position is proportional to the frequency shift and thus to the LOS wind speed. The spectral width can experience a broadening by either laser frequency jitter or wind speed differences within a range-gate. The determination of such broadening would allow the definition of an additional quality control parameter. The offset is composed of several contributors, mainly broadband Rayleigh signal and to a lesser extent the solar background and the cloud or ground albedo. As found from response calibrations (subsec. 3.4.3) a wind speed of 1 m/s would approximately be equivalent to $\Delta x_\mathrm{p} = 0.06$ pixel on the ACCD. Keeping in mind the wind speed requirements defined for the ADM-Aeolus satellite mission (sec. 2.2), the value of about 0.06 pixel demonstrates the accuracy to which the DSA is demanded to provide reliable results of the determination of the centroid position of the fringe. Examples of signals from the Internal Reference, cloud and ground return are shown in Fig. 3.9a. Reliable evaluation is only possible in range-gates containing sufficiently high backscatter signal from either the near field (≈ range-gates #5 - #10) or cloud/aerosol layers (range-gates #13 - #14) or ground return (range-gate #22). The received intensities can cover several orders of magnitude, due to signal loss, depending on the transmissivity of the atmosphere, the optical thickness of respective layers, varying albedo and backscatter coefficients. Exemplarily, the peak intensities of the ground and the cloud return given in Fig. 3.9a differ by about one order of magnitude. Highest intensities of up to 10^6 LSB are obtained for the Internal Reference signal, which is well centred on the ACCD around pixel value of 7.5. The illumination of several (at least two) channels (pixel columns) in the imaging zone by the fringe is needed to assure an accurate determination of the centroid of the backscatter spectrum by the DSA. However, this requirement on the distribution of signal demands a higher number of detected photons in order to stand out of the background noise, which in the example reaches a level of about 10 % of the ground return peak height. Apart from other minor noise sources, the background noise consists mainly of broadband Rayleigh backscatter which is assumed constant in frequency over the small USR of the Fizeau spectrometer for the determination of the centroid of the Mie fringe.

The width of the Mie fringe as experienced from airborne measurements is slightly broadened. Regarding a single laser pulse return, the broadening is caused by a small tilt of the fringe when mapped onto the imaging zone (Fig. 3.9a) and the subsequent signal summation to the transfer row (Fig. 2.6). The tilt is supposedly related to irregularities in the surface of the Fizeau wedge and investigations are under way. In terms of a measurement where the signal of P pulses is accumulated the broadening can also be induced by laser frequency jitter or high wind speed gradients either horizontally along the flight path or vertically within a range-gate.

Rayleigh channel

The function of the Fabry-Pérot interferometer used for the Rayleigh channel was introduced in subsec. 2.3.2. An example for typical Rayleigh signal intensities measured on the ACCD is presented in Fig. 3.9b. In contrast to the imaging zone, the background (Eq. 3.12c) and the DCO (Eq. 3.12d) are already subtracted for the memory zone and the extracted range-gates. The imaging zone contains the two spots produced by the two FPI's and, as indicated in Fig. 2.6, all charges are summed vertically by transfer to a single row. Unlike in Eq. 3.12 the signal of a single range-gate, as stored in the memory zone, is not summed over all 16 pixel but, on the basis of Eq. 2.11, split into two halves in order to determine the intensity of the two spots separately. However, so-called "ghosts images" can occur, which are frequency dependent artefacts, and which supposedly originate from parasitic reflections of the light at one or more of the various optical surfaces within the system. An example is visible in the imaging zone in Fig. 3.9b in the region around the 16th horizontal and 11th vertical pixel (#15 and #11 when start counting from zero). Pixels that contain these signal artefacts should be excluded from evaluation of the actual signals (Reitebuch et al. (2010)). Thus, instead of 8 pixel, the signal intensity of each spot (based on Eq. 3.16) created by the two FPI's is obtained by summing over 6 pixel p only, according to Eqs. 3.17.

$$R(f) = \frac{I_{\mathrm{A}}(f) - I_{\mathrm{B}}(f)}{I_{\mathrm{A}}(f) + I_{\mathrm{B}}(f)} \tag{3.17a}$$

$$I_{\mathrm{A}} = \sum_{p=1}^{6} [I_{\mathrm{raw}}(p) - I_{\mathrm{DCO}}(p) - I_{\mathrm{BKG}}(p)] \tag{3.17b}$$

$$I_{\mathrm{B}} = \sum_{p=9}^{14} [I_{\mathrm{raw}}(p) - I_{\mathrm{DCO}}(p) - I_{\mathrm{BKG}}(p)] \tag{3.17c}$$

The major portion of the signal of the single spots is concentrated within 3 to 4 pixels, rendering the summation over 6 pixel sufficient. A contrast function is used to define the Rayleigh response R via the intensities I_{A} and I_{B} (Reitebuch et al. (2012b)). The intensities, and thus the response, change with frequency and give a unique value within one FSR. Apart from using a contrast function, the response could also be defined via a simple ratio $I_{\mathrm{A}}/I_{\mathrm{B}}$. However, since it was decided to use the contrast function within the frame of the ADM-Aeolus mission, the same procedure is chosen for the A2D in order to maintain comparability. The use of the contrast function is historically based (for instance used by Chanin et al. (1989), Garnier and Chanin (1992) and Souprayen et al. (1999a)) and should not differ fundamentally from the simple ratio (used e.g. by Korb et al. (1998), Flesia and Korb (1999) and Gentry et al. (2000)) in terms of wind speed accuracy. In fact, the contrast function rather avoids too large/small numbers (as obtained from the simple ratio), is easier to linearise regarding the response calibration function (ch.3.4.3) and exhibits a slightly different behaviour in terms of error sources (subsec. 3.4.5).

Fig. 3.9b exemplarily also shows signals summed to observations for the Internal Reference (range-gate #4), a cloud return (range-gate #13) and a ground echo (range-gate #22). The highest intensities are found for the Internal Reference. The cloud must be rather optically thin, since it still allows the laser beam to penetrate and to detect a ground return. Compared to the Internal Reference the peak intensity of the ground echo is more than two orders of magnitude weaker.

3.4. Response calibration

This chapter discusses the response calibrations performed for the Mie and the Rayleigh channel. At first the question arises: Why is a calibration necessary for a direct-detection wind Lidar and especially for ADM-Aeolus and the A2D? Regarding the 2-µm DWL, the coherent wind Lidar principle does not require a calibration, since it obtains the Doppler frequency shift, and hence the wind speed, directly by a heterodyne process and a subsequent frequency analysis of the signal (subsec. 3.1.4). In contrast, the A2D applies the direct-detection method whose measured quantities (e.g. lateral position or intensity) cannot be directly related to a frequency without further knowledge. Therefore, an intermediate step is necessary, in order to obtain a relation between these quantities and the wind speed. A calibration is then a way to determine the response of an instrument in respect of a reference signal without being subject to the actual measurement variable of interest, here the wind.

In this respect, Fig. 3.10 shows the principle and two approaches for the wind retrieval. For a direct-detection Lidar the relation between the instrument response R and the frequency is the missing link, that allows to deduce the wind speed from the measured quantity. Two types of responses are provided by the A2D: a ratio determined by the measured intensities for the Rayleigh channel and the position of the centroid of the fringe for the Mie channel. The A2D and the Lidar on ADM-Aeolus are the only systems worldwide, which change the laser frequency in steps of Δf to simulate a Doppler frequency shift of the light backscattered from the atmosphere. This procedure yields respective response functions $R(f)$ for the Rayleigh and the Mie channel. In order to avoid the influence of wind speed on these reference measurements, a LOS velocity of zero must be assured, which requires the nadir pointing by turning the satellite or the aircraft. Within a certain interval of the response function a frequency can be unambiguously assigned to a given response value, considering the respective sensitivities (derivatives) $\delta R/\delta f$. Via the Doppler equation the LOS wind speed v_{los} can then be calculated from a determined frequency shift Δf. Strictly speaking, the Rayleigh response varies according to changes in atmospheric pressure and temperature, which in fact renders a wind measurement valid only for the time and in the area of the calibration. Apart from the measurement approach in a real atmosphere (not in a laboratory atmosphere) used for the A2D and ADM-Aeolus, also a simulation (dashed boxes) is a feasible solution. Taking into account the lineshapes of the laser and the broadened Rayleigh-Brillouin backscatter spectrum as well as the instrument functions of the interferometers, the response function can be simulated (Dabas et al. (2008)). The required vertical profiles of temperature and pressure can be obtained from NWP models, e.g. ECMWF. For the ADM-Aeolus mission a mixture of both the measurement and the simulation approach will be used.

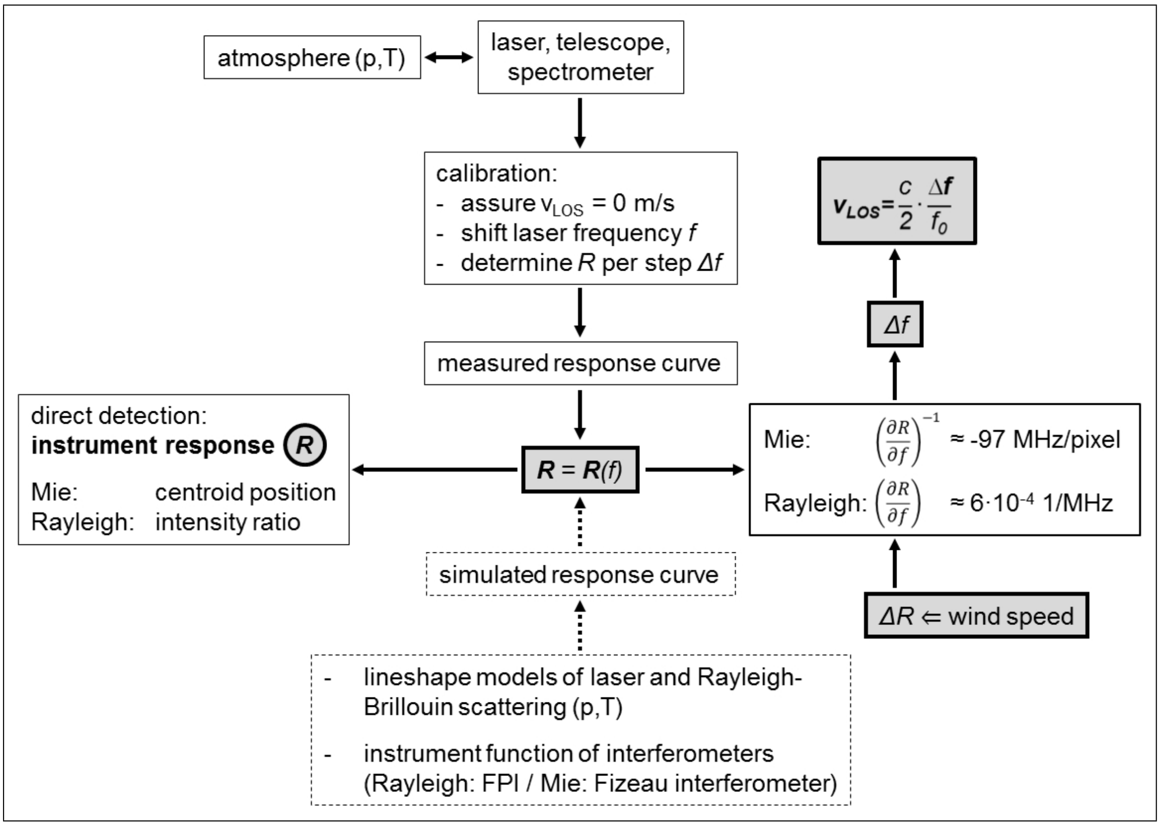

Figure 3.10.: Concept of calibration for the A2D and ADM-Aeolus direct-detection Doppler wind Lidar.

A calibration for a Rayleigh Doppler Lidar that is based on a simulation approach is applied by Baumgarten (2010), who compares measured signal ratios against a model that is calculated by convolving the transmission spectrum of the (iodine) filter and the Doppler and temperature broadened Rayleigh-Brillouin line. Similarly Garnier and Chanin (1992), Gentry and Korb (1994) and McGill et al. (1997a) rely on a simulated response function. In contrast to the A2D and the ADM-Aeolus approach, where the laser frequency is changed, Gentry and Korb (1994) keep the laser frequency stable and obtain an instrument function by scanning the FPI itself. This is achieved by commanding piezo-actuators that change the distance between the two interferometer plates accordingly to the applied voltage. A related procedure is described by McGill et al. (1997a), who increased the density of the gas inside a sealed FPI canister using a stepper motor. In this case, a special optic converts the ring of transmitted light to a fringe, which is then caused to move across a detector according to the changing pressure.

3.4.1. A2D calibrations over Greenland

The calibration approach of the ADM-Aeolus mission (subsec. 2.2.3) is to rotate to a nadir viewing position and consequently exclude the influence of horizontal wind speed, while additionally neglecting vertical wind speeds (subsec. 2.2.3). From this viewing geometry well defined Doppler frequency offsets are simulated by deliberately changing the laser frequency itself through a specified range. As the A2D is a non-scanning device and its integration angles within the aircraft are fixed, the only way to mimic this procedure with the A2D on-board the Falcon, is to fly right circles with a 20° roll angle (as indicated in Fig. 3.6), hence enabling approximate nadir pointing. The velocity of earth surface is assumed to be zero, which is valid in particular for solid ground. Due to nadir pointing during the calibration procedure, zero velocity is also a good approximation for ocean surface. In fact, a slight off-nadir pointing is necessary to avoid specular reflections from smooth surfaces (e.g. lakes). Concerning the satellite, this pointing offset (a few mrad) is intentionally commanded and has to be kept very small in order to hold the return signal within the USR of the interferometers, keeping in mind the velocity of the satellite of more than 7 km/s. For the A2D a much larger mean off-nadir angle of about 3.5° mainly originates from the aircraft pitch angle which is necessary to maintain an angle of attack and hence a constant flight altitude. The induced LOS velocity is corrected afterwards (subsec. 3.4.6) via the knowledge about the aircraft attitude (subsec. 3.1.3) and the installation angles of the A2D within the Falcon. For a response calibration the laser frequency is tuned (subsec. 2.3.1) in steps of 25 MHz (corresponding to 4.5 m/s) over a sufficiently large interval of the USR that enables a reliable determination of the relation between Doppler shift and response. Thereby, for the A2D one step equals one observation including 700 laser pulses, i.e. the frequency is changed before the start of each observation and kept constant throughout the measurement time of the next 14 seconds. The two calibrations performed with the A2D comprise a much wider frequency range than the ± 500 MHz envisaged for the ADM-Aeolus mission. 72 frequency steps were commanded, which would allow a maximum analysis range of ± 900 MHz. However, by approaching the edges of the ACCD with the Mie fringe, part of the signal is lost for the determination of the centroid position, which gives erroneous results and hence prevents the usage of the complete frequency range (subsec. 3.4.3). In contrast, the fixed position of the Rayleigh spots allows exploiting the full frequency range of the calibrations (subsec. 3.4.3).

Fig. 3.11 shows the flight track of flight #04 during the two calibrations over Greenland, which can also be seen in Fig. 3.2 on the lower left next to the radiosonde station 04360 BGAM. The 1$^{\text{st}}$ calibration was performed during the top row (higher latitudes) of the circles, the 2$^{\text{nd}}$ one during the bottom row, connected by a straight flight path. The actual flight pattern does not resemble exact circles but is distorted to a cycloidal shape due to a prevailing westerly wind constantly shifting the Falcon towards the east. Temporally, the flight section extends over more than one hour in time and spatially about 76 km in longitudinal and 43 km in latitudinal direction. On the one hand, the circling can be seen as an advantage, enabling the aircraft to stay within a confined region and preventing heterogeneities that might otherwise be inferred by, for instance, atmospheric features like clouds or large variations in ground elevation along a straight flight path. On the other hand, these idealised calibrations partly lack in realism compared to expected calibrations from the space-borne platform, since they exhibit much less variation in temperature and pressure profiles or ground albedo values. A calibration, as performed by the ADM-Aeolus satellite, lasts about 20 - 25 min, which is roughly equivalent to 1/4 orbit. In contrast, it takes only 12 minutes for the A2D, which equals 150 km in straight flight at an aircraft velocity of 210 m/s.

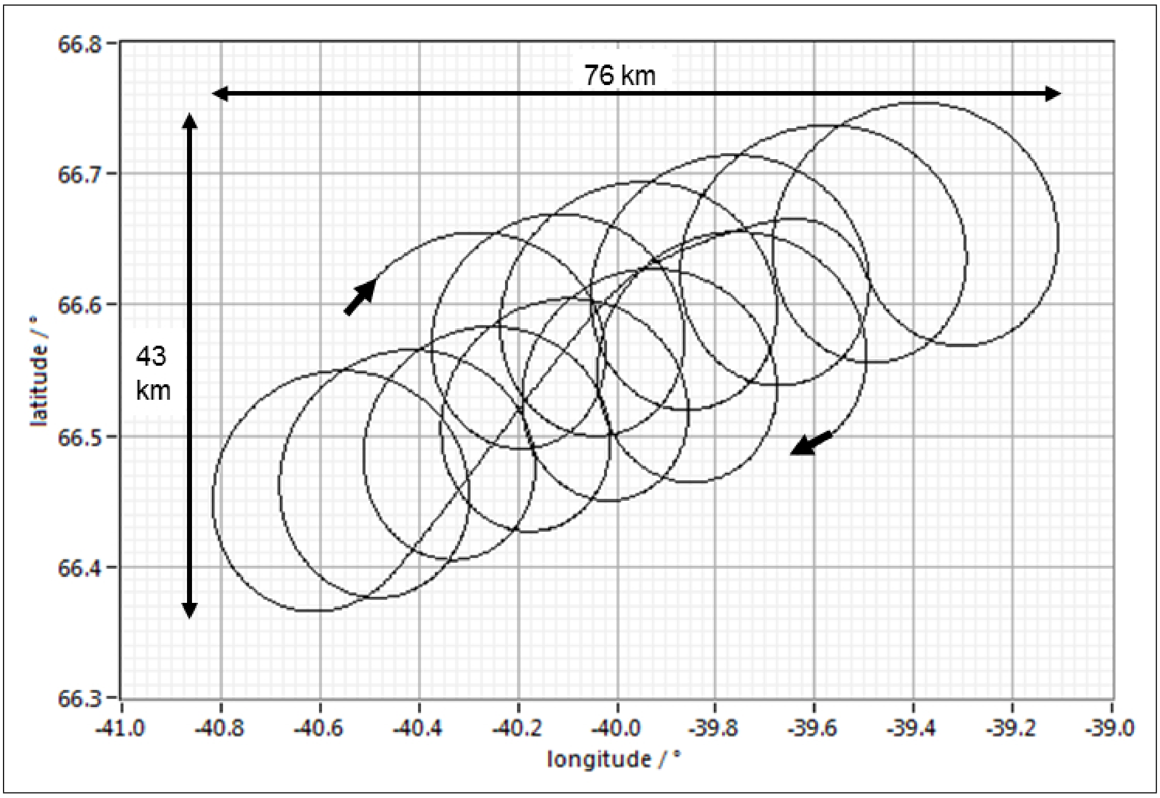

Figure 3.11.: Flight track of the Falcon (black) during the two calibrations between 11:20 - 12:30 UTC (flight #04). Arrows mark the start and the end of the track.

The two calibrations from the A2D airborne campaign were obtained under homogeneous atmospheric conditions, allowing a focussed investigation of error sources. As expected (subsec. 3.1.1) strong ground return intensities were obtained from the highly reflective ice surface in the UV yielding good signal to noise ratios. Generally, the highest attention has to be paid to the minimisation of all unknown contributions to the LOS velocity during calibration, such as biases in pointing knowledge or incorrect assignment of a moving cloud as ground return (sec. 3.2). But also the stability of the optical properties of the interferometers and the optical alignment of the instrument are factors that strongly influence the performance of the A2D (Paffrath et al. (2009), Witschas et al. (2012b)). Slight discrepancies of interferometer properties during a wind measurement or the applied calibration can yield big errors in retrieved wind speed.

3.4.2. Mie calibration

Unlike for molecular scattering, the scattering process of the emitted laser light on aerosols, cloud particles or hard targets does not induce a significant spectral broadening, which depends on temperature and pressure, and hence on altitude. Consequently, it is deemed sufficient for the calibration of the Mie channel, to utilise for example only the ground return signal. The resulting response function is assumed to be valid for all atmospheric range-gates. A calibration of the Mie channel could in principle also be performed at aerosol or cloud layers but the ground return from the ice surface over Greenland with a good albedo provides the higher signal to noise ratio.

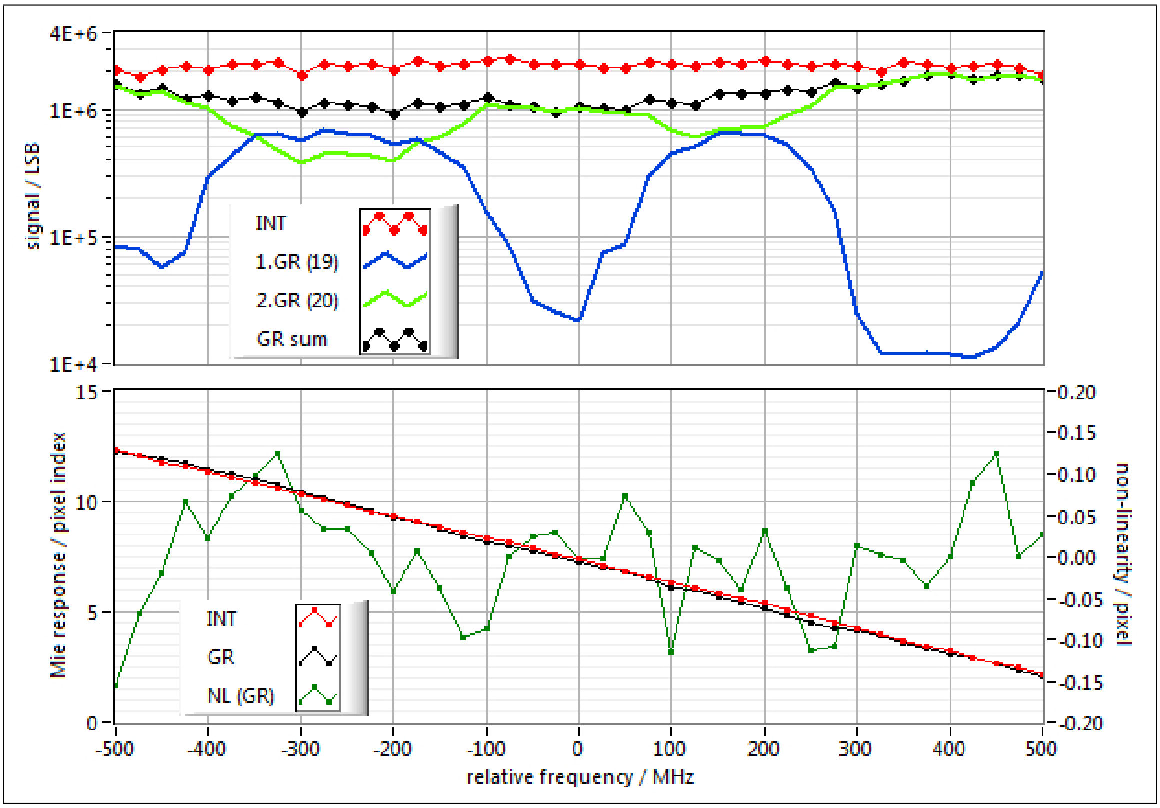

Figure 3.12.: Response calibration of the Mie channel for the 2^{nd} calibration of flight #04 for a frequency interval of ± 500 MHz with respect to the Rayleigh crosspoint (ch. 3.4.3). Top: Signal intensity of the Internal Reference (red, INT), the 1^{st} ground return range-gate (blue, 19), the 2^{nd} ground return range-gate (green, 20) and the sum of both ground return range-gates. Bottom: The response calibration function for the Internal Reference (INT, red) and the summed ground return signal (GR, black) together with the non-linearity $\gamma_{\text{M,GR}}$ (NL, Eq. 3.18) of the ground return response function.

As foreseen for ADM-Aeolus, the frequency range of ± 500 MHz was also selected for the analysis of the A2D Mie calibration. This range corresponds to 41 observations, during a period of approximately 12 minutes (11:29.30 - 11:41.44 UTC) and a flight path of slightly more than two complete circles (Fig. 3.11). The top of Fig. 3.12 shows the intensities measured for the Internal Reference and the ground return during the 2^{nd} calibration according to Eqs. 3.12. It is evident that the ground return signal is split between the range-gates #19 and #20 (compared to #20 and #21 for the 1^{st} calibration (Tab. 3.4)). The two regions between -400 MHz to -100 MHz and 100 MHz to 300 MHz (Fig. 3.12 top), where ground return signal is distributed between two range-gates, can be explained in relation to the two circles flown by the aircraft and an according adaptation of the pitch angle in order to compensate for the westerly wind at flight level. Similar distributions of ground signal are present in the 1st calibration. Since the analysis of the signal of each of the two range-gates does not lead to a continuous response calibration function, the signals of both have been summed (subsec. 3.4.6) yielding the black curve (GR sum). With a comparison of measured ground elevation and DEM (sec. 3.2) it was verified for both calibrations that only ground return signal is present in range-gates #19 and #20. The conclusion is additionally supported by e.g. MODIS (MODerate resolution Imaging Spectroradiometer) data which does not show cloud cover in the respective region and by the simultaneous measurements of the 2-µm DWL on-board the Falcon aircraft. Similar to the Internal Reference with about ± 16 % ($1.8 - 2.5 \cdot 10^6$ LSB, regarding the maximum and minimum values), the summed intensity of the ground return exhibits relatively small variations within approximately ± 35 % ($0.9 - 1.9 \cdot 10^6$ LSB). For the Internal Reference an almost constant value of signal intensity is expected. However, regarding the ground return, this seems to point to a rather homogeneous albedo value of the ice surface and especially to an independence of the LOS azimuth angle. The intensities obtained from the ground return are almost as high as those for the Internal Reference and only about 1 % of this intensity can be attributed to the Rayleigh background, which is not subtracted here (subsec. 3.4.6). On the bottom of Fig. 3.12 the two response calibration functions for the Internal Reference and the ground return are shown, constituting the shift of the respective centroids of the Mie peak with frequency. From a least squares fit through these functions, applying a linear function without weights, the parameters sensitivity β_M and offset α_M (index M referring to the Mie channel) are obtained according to Eq. 3.18.

$$R_{\mathrm{M}}(f) = \alpha_{\mathrm{M}} + \beta_{\mathrm{M}} \cdot f + \gamma_{\mathrm{M}}(f) \tag{3.18}$$

Additionally, for the ground return the residual between fit and measured function, called non-linearity (NL) $\gamma_{\mathrm{M,GR}}$, is displayed. While the frequency range of the analysed part of the calibration is ± 500 MHz (≈ 10 pixel), the NL ranges between ± 0.13 pixel, corresponding to ± 13 MHz. Taking into account $\beta_{\mathrm{M,GR}}$ from Tab. 3.4 the 13 MHz equals 2.6 m/s.

In Tab. 3.4 the main results of the two Mie calibrations are compiled. As expected, a linear behaviour (Fig. 3.12, bottom), i.e. proportionality between Doppler frequency shift and pixel position of the fringe centroid on the ACCD, is found. A shift of 1 pixel equals roughly 100 MHz or 18 m/s. Keeping in mind the requirement of 0.6 m/s accuracy in LOS direction (subsec. 2.2.1) imposed on the ADM-Aeolus mission, the accuracy of the determination of the centroid of the peak by the DSA (ch. A.1) must be in the order of 0.03 pixel. Due to very similar signal shape characteristics (particularly the spectral width) of both, Internal Reference signal and the hard target signal of the ground return, the same results for the parameters describing the response functions could be expected. Instead a slight difference of 2 MHz/pixel in sensitivity is present for both calibrations which might be due to the different optical paths, and hence different illumination of the Fizeau interferometer, used for the Internal Reference and the atmospheric signal. The frequency range in Tab. 3.4 and in Fig. 3.12 is given with respect to the Rayleigh reference frequencies (subsec. 3.4.3), which explains the difference in the Mie offsets of 0.3 pixel between the two calibrations corresponding to about 25 MHz, i.e. one frequency step. In fact, this particular difference can be disregarded, since the actually relevant quantity for the wind retrieval is the difference in offset between the Internal Reference and the ground ($\alpha_{\mathrm{M,INT}}$ - $\alpha_{\mathrm{M,GR}}$) which is the same for both calibrations ($\approx$0.05 pixel).

Table 3.4.: Sensitivity and offset for the Mie channel are derived from a linear fit through the response calibration functions of the Internal Reference and the ground return. The errors of γ_{M} refer to the 1 σ interval and are given in units of pixel and MHz (taking into account the respective sensitivities).

			1	2
calibration number			1	2
time		/ UTC	11:29.30 - 11:41.30	12:02.35 - 12:14.35
frequency range		/ MHz	± 500	± 500
summed GR		/ range-gates	20 / 21	19 / 20
INT:	sensitivity $\beta_{\mathrm{M,INT}}$	/ MHz/pix	-98.7 ± 0.3	-98.6 ± 0.3
GR:	sensitivity $\beta_{\mathrm{M,GR}}$	/ MHz/pix	-97.0 ± 0.3	-96.6 ± 0.3
INT:	offset $\alpha_{\mathrm{M,INT}}$	/ pixel	7.00 ± 0.01	7.30 ± 0.01
GR:	offset $\alpha_{\mathrm{M,GR}}$	/ pixel	6.96 ± 0.01	7.25 ± 0.01
INT:	std. dev. of $\gamma_{\mathrm{M,INT}}$	/ pixel	0.081	0.057
		/ MHz	8.00	5.62
GR:	std. dev. of $\gamma_{\mathrm{M,GR}}$	/ pixel	0.058	0.064
		/ MHz	5.62	6.18

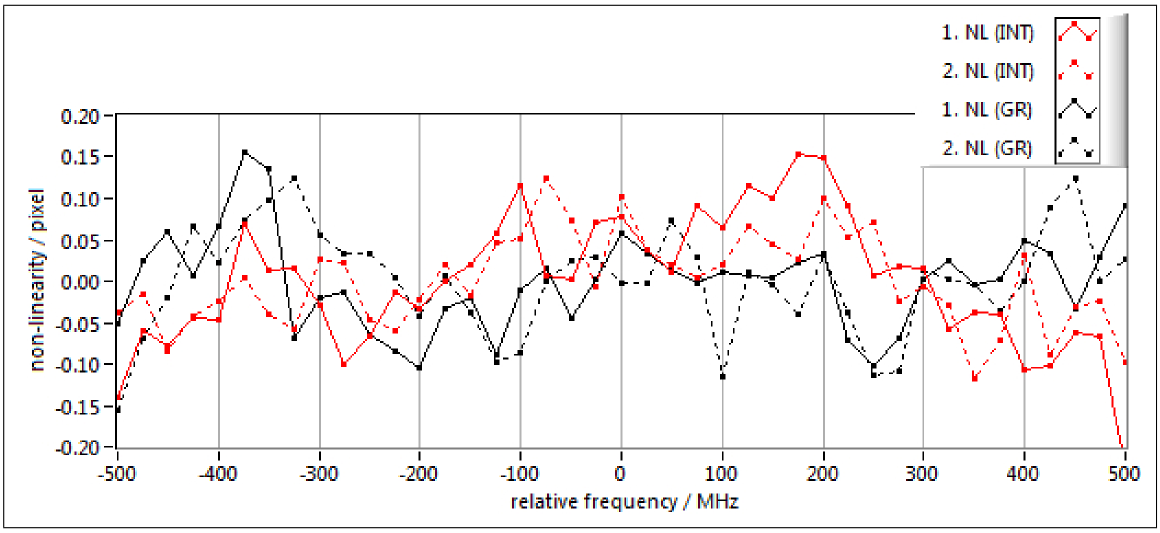

Figure 3.13.: The non-linearities (NL) of the Mie response functions from the 1st (solid) and 2nd (dashed) response calibration. Non-linearities from response functions of the Internal Reference (INT) $\gamma_{\mathrm{M,INT}}$ and the summed ground return signal (GR) $\gamma_{\mathrm{M,GR}}$ are plotted in red and black.

The non-linearities of the four response functions (Internal Reference and ground return for both calibrations) are presented in Fig. 3.13. Simulations (Paffrath (2006)) showed that non-linearities with a distinctive and repetitive pattern on a scale of pixel-to-pixel are expected from the Mie response calibration functions. Keeping in mind that 1 pixel corresponds to about 100 MHz, the measured response functions in Fig. 3.13 obviously do not show such a behaviour. Despite the very high signal levels (even for the Internal Reference) the measurements of the airborne campaign seem to be too noisy for the expected non-linearity pattern to be doubtlessly detected. Tab. 3.4 contains the standard deviation values for the four γ_{M}. The small difference between the two $\gamma_{\mathrm{M,GR}}$ (0.058 / 0.064) could potentially be explained by the difference in the distribution of ground return and the subsequent process of signal summation. No such reason can be consulted to explain the seemingly significant difference in the two $\gamma_{\mathrm{M,INT}}$ (0.081 / 0.057) with a remarkably higher value for the 1st calibration. The variances of the measured response values, and hence in the non-linearity, express themselves in uncertainties of the parameters for sensitivity and offset derived from the linear fits. Assuming exactness in the frequency axis, these uncertainties can be calculated according to Press et al. (1992) (p.663):

$$\sigma_\alpha = \sqrt{\frac{\sum\limits_{i=1}^{n} \frac{{x_i}^2}{\sigma_{\mathrm{NL}}^2}}{\sum\limits_{i=1}^{n} \frac{{x_i}^2}{\sigma_{\mathrm{NL}}^2} \cdot \sum\limits_{i=1}^{n} \frac{1}{\sigma_{\mathrm{NL}}^2} - \left(\sum\limits_{i=1}^{n} \frac{x_i}{\sigma_{\mathrm{NL}}^2}\right)^2}} \tag{3.19a}$$

$$\sigma_\beta = \sqrt{\frac{\sum\limits_{i=1}^{n} \frac{1}{\sigma_{\mathrm{NL}}^2}}{\sum\limits_{i=1}^{n} \frac{{x_i}^2}{\sigma_{\mathrm{NL}}^2} \cdot \sum\limits_{i=1}^{n} \frac{1}{\sigma_{\mathrm{NL}}^2} - \left(\sum\limits_{i=1}^{n} \frac{x_i}{\sigma_{\mathrm{NL}}^2}\right)^2}} \tag{3.19b}$$

with n as the number of considered calibration steps, σ_{NL}^2 as the standard deviation of the respective NL γ_{M} (Tab. 3.4) and x_{i} as the single NL values. While a value of about ± 0.3 MHz/pixel (Tab. 3.4) for one standard deviation regarding the sensitivities corresponds to 0.3 %, the ± 0.01 pixels for the offsets equal 1 MHz. Comparing the ± 0.3 MHz/pixel to the difference of 2 MHz/pixel between the sensitivities $\beta_{\mathrm{M,GR}}$ and $\beta_{\mathrm{M,INT}}$ found for each calibration, one might very well assume a significant difference between the sensitivity of the Internal Reference and the ground return. This fact additionally supports the decision to chose the response function of the ground return, instead of the Internal Reference, to be representative for atmospheric signals in general. Due to the obviously random behaviour of the non-linearity γ_{M} (Fig. 3.13) in the Mie channel, a modelling of a non-linearity function and the application of a reliable correction method is prevented. In contrast, a correction for the non-linearity is developed for the Rayleigh channel in subsec. 3.4.4.

In order to obtain the ground return response function in Fig. 3.12 several corrections had to be applied which are more extensively discussed in subsec. 3.4.6. For example a correction of the LOS velocity induced by the aircraft speed and attitude is necessary as well as the exclusion of measurements that are associated with outliers. Rayleigh backscatter from the fraction of the range-gate that is located above the ground, the so-called atmospheric contamination, is contributing to the measured total intensity of the Mie ground return signal by about 1 %.

A respective correction would be inaccurate due to the imprecise knowledge of the actual altitude of the earth surface (sec. 3.2). However, the albedo of the ice surface is large enough to yield a clearly detectable peak, making a correction dispensable.

3.4.3. Rayleigh calibration

A response function for atmospheric signals (blue dots) has been simulated for 130 steps à 50 MHz starting at 844.7485 THz (Fig. 3.14). The indicated laser pulse (magenta) is shaped according to a Lorentz function and features a spectral width of 45 MHz and is emitted at a frequency of 844.75145 THz. The spectral shape of the molecular Rayleigh-Brillouin line (light blue) is calculated according to the model of Witschas (2011a) taking into account a temperature of $\mathrm{T} = 270\,\mathrm{K}$ and a pressure of $\mathrm{p} = 700\,\mathrm{hPa}$. The shapes of the transmission curves of the FPI's (red, black) are determined from the properties in Tab. 2.4, additionally including the effect of defects (Witschas (2011b)). Knowing the molecular backscatter spectrum and the filter properties, one can compute the transmitted intensities through the FPI's (pink and gray). By integrating these intensities over the frequency, the signal on the ACCD can be obtained, corresponding to $I_\mathrm{A}(f)$ and $I_\mathrm{B}(f)$ in Eq. 3.17. Regarding the calibration and wind measurement, the region of interest lies between two opposite steep edges and around the crossing point of the transmission curves of the two FPI's. Here the gradient of the response function reaches its maximum and the function itself can be approximated by a straight line.

Within the ground-segment algorithms of the ADM-Aeolus mission only three response calibration functions are envisaged for the Rayleigh channel: Internal Reference, atmosphere and ground return. A single response function for the atmosphere will be derived for the altitude range between 6 km and 16 km. The actual shape of the response calibration function depends on the atmospheric conditions, i.e. pressure and in particular temperature. Therefore, a temperature and pressure correction (Dabas et al. (2008)) is necessary to avoid errors of up to several meters per second.

In contrast to the smooth simulated response function, real atmospheric measurements from the A2D affected by noise are shown in Fig. 3.15. Relative frequencies are used here instead of absolute frequencies. The reference frequency of 0 MHz is derived from the responses of the Internal Reference. The commanded frequency of the calibration step, which yields the difference $I_\mathrm{A}(f) - I_\mathrm{B}(f)$ closest to zero, is defined as the reference frequency. This frequency is located close to the crosspoint of the two filter transmissions curves. Fig. 3.15 shows a frequency interval of 1.7 GHz (corresponding to 69 calibration steps of 25 MHz) around the reference frequency for the two A2D airborne calibrations. The interval of 1.0 GHz that is nominally used for ADM-Aeolus is also indicated in Fig. 3.14. Due to the high signal levels and the homogeneous atmosphere without clouds encountered during the airborne calibrations over Greenland, the A2D was capable of resolving the atmosphere per range-gate. Apart from the response function of the Internal Reference, functions have also been obtained for 14 atmospheric range-gates (L5-L18) and the ground return. The latter is derived from the summed ground return signals (subsec. 3.4.6) of the range-gates #20 and #21 for the 1^st calibration as well as range-gates #19 and #20 for the 2^nd calibration.

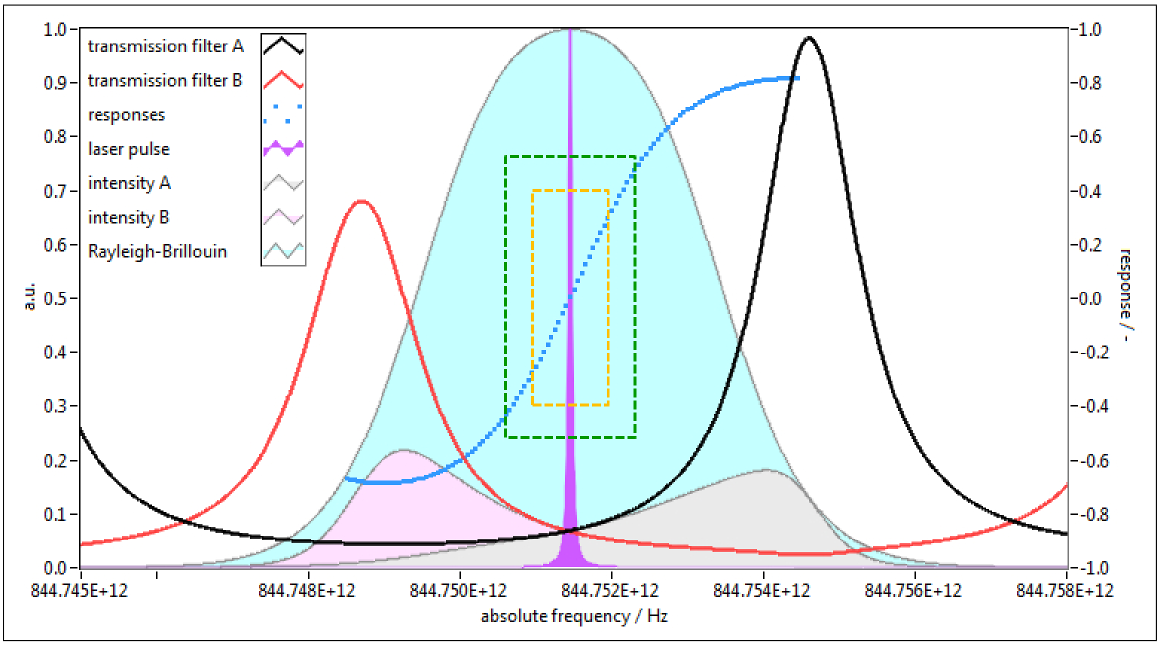

Figure 3.14.: Simulated response function (blue dots) for 130 steps in intervals of 50 MHz (range: 6500 MHz). The simulated laser pulse (magenta), the Rayleigh-Brillouin backscatter spectrum (light blue) and the transmission curves of the filters A (black) and B (red) determine the transmitted intensities through filter A (gray) and B (pink). The responses refer to the y-axis on the right, the other quantities are shown in arbitrary units (left y-axis). The dashed orange box indicates a frequency interval of 1 GHz as foreseen for the response calibrations of ADM-Aeolus, whereas the dashed green box indicates a frequency interval of 1.7 GHz as used for the A2D wind retrieval.

Just as for the Mie response calibration (subsec. 3.4.2) and similar to the algorithms for the ADM-Aeolus mission, a linear least squares fit without weights is applied to the Rayleigh response. According to Eq. 3.18 the parameters offset α_{R} and sensitivity β_{R} (index R referring to the Rayleigh channel) are obtained. The non-linearity γ_{R} is the residual to the straight line.

$$R_R(f) \;=\; \alpha_R + \beta_R \cdot f + \gamma_R(f) \tag{3.20}$$

The response function of the ground return yields very similar values in terms of offset and sensitivity (slope) compared to the Internal Reference (Fig. 3.16), which is expected due to the spectrally narrow bandwidth of both signals. In turn the atmospheric responses lead to lower offsets and higher sensitivities. Particularly the offset changes with altitude, whereas the sensitivity stays almost constant. Differences between both calibrations in the sensitivity and especially in the offset can be observed. While these differences do not reach more than about 0.5 m/s at 100 m/s wind speed regarding the sensitivity, the differences in offset lead to almost 2.5 m/s below 6 km. The strong deviations of range-gates #5 and #6 (L5 and L6, dashed lines) in terms of offset are very likely related to the telescope overlap and thus to

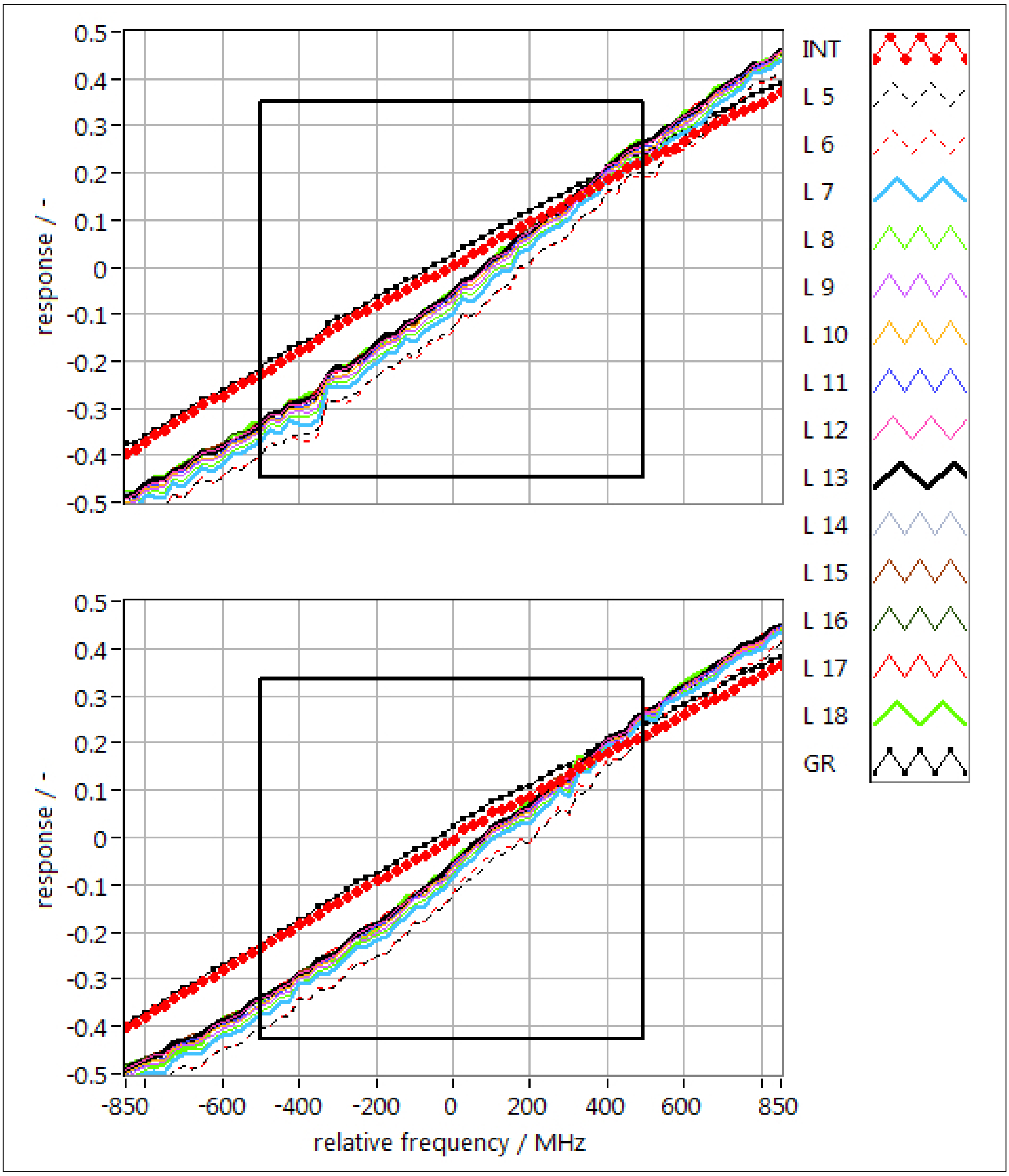

Figure 3.15.: Measured response calibration functions from the 1st (top) and 2nd (bottom) calibration for a frequency interval of ± 850 MHz. Response functions for the Internal Reference (INT, red), the atmospheric range-gates (L5 - L18, coloured) and the summed ground return (GR, black) are shown. The black box indicates a frequency interval of ± 500 MHz, which is used for the ADM-Aeolus mission.

the angular susceptibility of the FPI regarding the incident light. In the region where the calibrations were performed, the ice surface of Greenland has an elevation of more than 2 km. Thus, no response functions could be obtained below this altitude which would be necessary for the wind retrieval at other geographical locations. However, in particular the profiles of the offset show an asymptotic behaviour that is used for an extrapolation of the profiles. The mean values of the lowest (with respect to altitude) four/three ($1^{st}/2^{nd}$ calibration) offsets and sensitivities from the atmospheric response functions are assigned to range-gates below 2.5 km (range-gate #15/#14) for wind retrievals. Differences occur in the profiles regarding the two frequency analysis intervals, most noticeably a shift by approximately 0.01 ($\approx$16 MHz with a sensitivity of about $6.2 \cdot 10^{-4}$/MHz) regarding the offset and by approximately $3 \cdot 10^{-5}$/MHz ($\approx$0.3 % wind speed dependent error) in terms of sensitivity. Also the sensitivity profiles for 1.7 GHz are closer than for 1 GHz. In particular the shifts suggest that the linear fit does not exactly describe the behaviour of the response functions at least in the interval of 1.7 GHz.

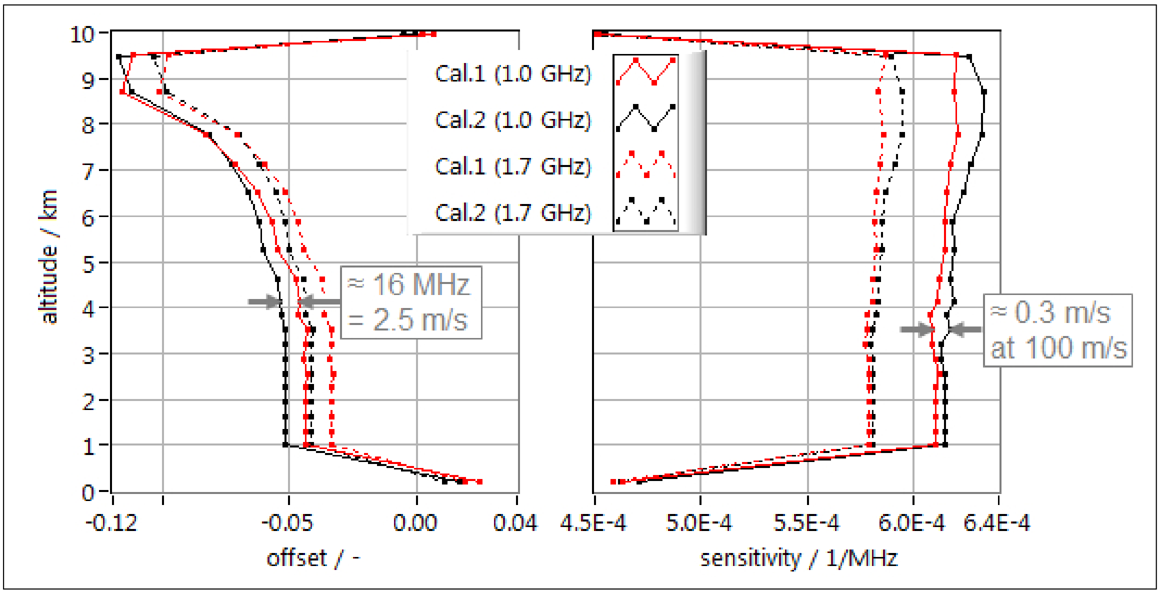

Figure 3.16.: The parameters offset α_R (left) and sensitivity β_R (right) are derived from linear fits through the response functions of the 1^{st} (red) and 2^{nd} (black) airborne calibration for frequency intervals of ± 850 MHz (dashed lines) and ± 500 MHz (solid lines). The parameters are displayed versus the altitude of the corresponding range-gates with the Internal Reference (INT) at 10 km, the ground return (GR) at 0 km and the atmospheric range-gates in between.

3.4.4. Non-linearity of Rayleigh response calibration functions

The non-linear behaviour of the atmospheric response functions is clearly visible in Fig. 3.15 and the corresponding measured non-linearities (NL) are shown in Fig. 3.17. The analysis of the two airborne calibrations yielded the first insight into the properties of the NL, which was not taken into account for ADM-Aeolus so far. Up to now it was foreseen for the ADM-Aeolus mission to correct measured responses with the measured value of the non-linearity using a next-neighbour approach (EADS-Astrium (2011)) for the wind retrieval (subsec. 3.5.1). If doing so, large errors in the derived wind speed will result if the noise is of similar magnitude as during the airborne calibrations. Regarding the interval of ± 200 MHz around the reference frequency, which corresponds to about ± 35 m/s, the atmospheric NL can easily reach absolute values up to 0.02. Assuming an approximate sensitivity β_R of $6.0 \cdot 10^{-4}$/MHz from a linear fit for an atmospheric response function (Fig. 3.16), this is equivalent to magnitudes of up to 33 MHz ($= 0.02/\beta_\mathrm{R}$) or about 6 m/s when taking into account the Doppler shift conversion factor (Tab. 2.1) of 5.63 MHz/(m/s). Thus, when using calibrations on intervals as large as ± 850 MHz the NL cannot be neglected. Theoretically, a description of noise free calibration response functions could be derived, considering modelled filter transmission functions and atmospheric conditions. This approach would, for instance, require exact prior knowledge of atmospheric pressure and temperature profiles. Thus, for the sake of simplicity, a polynomial fit is selected to model the NL instead. The seemingly point-symmetric shape of the response function with a single inflection point suggests the approximation by a polynomial of odd order. Describing the non-linearity $\gamma_\mathrm{R}(f)$ with a 5th order polynomial yields the response calibration functions following Eq. 3.20:

$$R_\mathrm{R}(f) = \alpha_\mathrm{R} + \beta_\mathrm{R} \cdot f + \sum_{i=0}^{5} \left(\gamma_\mathrm{R,i} \cdot f^i\right) \tag{3.21a}$$

$$= \underbrace{(\alpha_\mathrm{R} + \gamma_\mathrm{R,0})}_{c_0} + \underbrace{(\beta_\mathrm{R} + \gamma_\mathrm{R,1})}_{c_1} \cdot f + \underbrace{\gamma_\mathrm{R,2}}_{c_2} \cdot f^2 + \underbrace{\gamma_\mathrm{R,3}}_{c_3} \cdot f^3 + \underbrace{\gamma_\mathrm{R,4}}_{c_4} \cdot f^4 + \underbrace{\gamma_\mathrm{R,5}}_{c_5} \cdot f^5 \tag{3.21b}$$

In Fig. 3.17 a well pronounced shape of the fits is obvious and consistent between the two calibrations. This simplifies the detection of outliers, which might be present, for example, at -400 MHz in the 1st calibration and at 200 MHz and 300 MHz in the 2nd calibration.

The polynomial coefficients c_i from Eq. 3.21 are compiled in Tab. 3.5. Each set of coefficients specifically describes only the response function of one of the two airborne calibrations within the frequency interval of ± 850 MHz and around the respective reference frequency. The standard deviations $\sigma_\mathrm{c,INT}$, $\sigma_\mathrm{c,ATM}$ and $\sigma_\mathrm{c,GR}$ of the measured NLs with respect to the corresponding polynomial fits over the frequency range of 1.7 GHz (Fig. 3.17) are given in Tab. 3.5 and certainly constitute a measure of quality for the response functions. The exemplarily selected atmospheric range-gate #15 is located at 3.5 km altitude. It is found that $\sigma_\mathrm{c,ATM}$ is more than twice as high as $\sigma_\mathrm{c,INT}$ and $\sigma_\mathrm{c,GR}$, which can to a certain degree be attributed to the lower signal level received from the molecular backscatter. The residuals from which the respective σ_c are determined are shown in Fig. 3.19 (Internal Reference), Fig. A.4 (range-gate #15) and Fig. A.7 (ground return). An analysis about the similarity of the two response calibration functions is performed in subsec. 3.4.5.

The decision to use a 5th order polynomial instead of a 3rd, 7th or even higher order polynomial was additionally supported by the results of simulations without instrument noise for the satel-

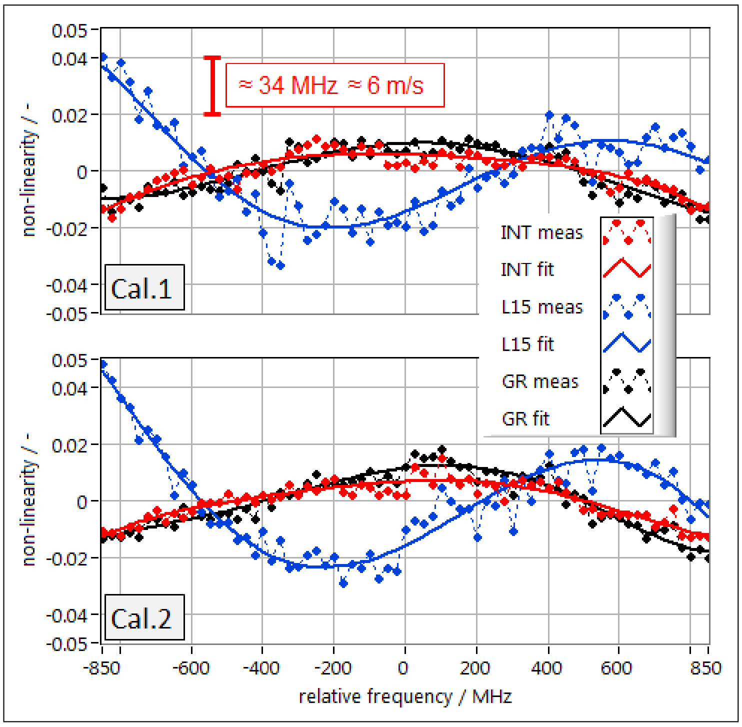

Figure 3.17.: The non-linearities of the measured (dots) and fitted (lines, Eqs. 3.21) Rayleigh response functions from the 1st (top) and 2nd (bottom) response calibration for a frequency interval of ± 850 MHz. Non-linearities from response functions of the Internal Reference (INT, red) $\gamma_{\mathrm{R,INT}}$, the atmospheric range-gate (L15, blue) $\gamma_{\mathrm{R,i}}$ and the summed ground return (GR, black) $\gamma_{\mathrm{R,GR}}$ are shown. The red marker indicates the magnitude of the equivalent wind speed errors.

lite instrument on ADM-Aeolus (Nikolaus (2012)). A 3rd order polynomial fit leaves a structure in the remaining residual, which indicates that this order is not sufficient to represent the NL. In contrast, a 5th order polynomial seems to be sufficient, since the residual of the fit does not show any remaining structure and can hence be regarded as noise. Consequentially, applying a 7th order polynomial fit would yield no significant improvement and the fit is more affected by outliers. The higher the order the more prone is the fit to mimic small scale modes that are not present in the FPI transmissions and the Rayleigh-Brillouin lineshape (Fig. 3.14).

When looking at Tab. 3.5 a systematic pattern of the signs of the coefficients seem to be present. While the signs of the coefficients for the ground return and the atmospheric layers each match for both calibrations, this is not the case for the Internal Reference. Since the response functions of the ground return and the Internal Reference exhibit almost the same shape, one could speculate that the signs of the coefficients should agree. However, the signs of the coefficients for the Internal Reference of the 1st calibration deviate from the expected pattern. Although, this might not be a criteria for direct exclusion, this fact contributes to a number of indications, which finally lead to the decision to prefer the 2nd calibration for the wind retrieval and successive wind speed comparisons (ch. 4). As soon as more airborne calibrations are available, the quality

Table 3.5.: Fit coefficients c derived from a linear and subsequent 5th order polynomial fit through the response calibration functions of the Rayleigh channel for the Internal Reference (INT), atmospheric (ATM) range-gate #15 (L15) and the ground return (GR). The corresponding standard deviations σ_c of the residuals are given in units of both response and frequency (assuming the sensitivities according to Fig. 3.16 (right)).

calibration number			1	2
time		/ UTC	11:25.36 - 11:46.14	11:58.23 - 12:19.01
frequency range		/ MHz	± 850	± 850
summed GR		/ range-gates	20 / 21	19 / 20
INT:	$c_{\mathrm{INT},0}$	/ 10^{-3}	5.75	6.69
	$c_{\mathrm{INT},1}$	/ $10^{-6} \cdot \mathrm{MHz}^{-1}$	- 3.58	6.09
	$c_{\mathrm{INT},2}$	/ $10^{-8} \cdot \mathrm{MHz}^{-2}$	- 1.67	- 2.76
	$c_{\mathrm{INT},3}$	/ $10^{-11} \cdot \mathrm{MHz}^{-3}$	1.63	- 2.91
	$c_{\mathrm{INT},4}$	/ $10^{-14} \cdot \mathrm{MHz}^{-4}$	- 1.45	0.14
	$c_{\mathrm{INT},5}$	/ $10^{-17} \cdot \mathrm{MHz}^{-5}$	- 1.56	2.91
	$\sigma_{\mathrm{c,INT}}$	/ 10^{-3}	2.56	2.33
		/ MHz	5.69	5.18
ATM:	$c_{\mathrm{ATM},0}$	/ 10^{-2}	- 1.44	- 1.57
	$c_{\mathrm{ATM},1}$	/ $10^{-5} \cdot \mathrm{MHz}^{-1}$	4.91	6.19
	$c_{\mathrm{ATM},2}$	/ $10^{-8} \cdot \mathrm{MHz}^{-2}$	7.50	8.58
	$c_{\mathrm{ATM},3}$	/ $10^{-10} \cdot \mathrm{MHz}^{-3}$	- 1.50	- 1.69
	$c_{\mathrm{ATM},4}$	/ $10^{-14} \cdot \mathrm{MHz}^{-4}$	- 3.81	- 5.05
	$c_{\mathrm{ATM},5}$	/ $10^{-17} \cdot \mathrm{MHz}^{-5}$	7.52	5.68
	$\sigma_{\mathrm{c,ATM}}$	/ 10^{-3}	5.45	5.43
		/ MHz	9.40	9.36
GR:	$c_{\mathrm{GR},0}$	/ 10^{-2}	0.97	1.15
	$c_{\mathrm{GR},1}$	/ $10^{-5} \cdot \mathrm{MHz}^{-1}$	0.55	1.50
	$c_{\mathrm{GR},2}$	/ $10^{-8} \cdot \mathrm{MHz}^{-2}$	- 5.32	- 6.17
	$c_{\mathrm{GR},3}$	/ $10^{-11} \cdot \mathrm{MHz}^{-3}$	- 1.43	- 5.83
	$c_{\mathrm{GR},4}$	/ $10^{-14} \cdot \mathrm{MHz}^{-4}$	3.18	3.41
	$c_{\mathrm{GR},5}$	/ $10^{-17} \cdot \mathrm{MHz}^{-5}$	0.38	4.64
	$\sigma_{\mathrm{c,GR}}$	/ 10^{-3}	3.20	2.54
		/ MHz	6.96	5.52

control approach for calibration selection can be verified. The polynomial coefficients might also be applicable as monitoring parameters with respect to the stability of the instrument. The similar spectral properties of the Internal Reference and the ground return signal, suggested an examination of the strong noise and the possible outliers that obviously affect $\gamma_{\mathrm{R}}(f)$, but no correlation was found. Also no distinct result was obtained from a spectral Fourier coefficient analysis of the measured $\gamma_{\mathrm{R}}(f)$.

The approach to consider the NL as a function of frequency and to describe it with a polynomial of 5th order, as presented above, is newly introduced in this thesis. If pursuing the current approach of the ADM-Aeolus algorithms (EADS-Astrium (2011)) ambiguities can occur as it is explained in ch. A.3. Therefore, it is preferred in the wind retrieval to account for the non-linearity as a function of frequency.

Fig. 3.18 presents the non-linearities $\gamma_\mathrm{R}(f)$ of the response functions from Fig. 3.15 if considered for a frequency interval of 1 GHz (black box) as used for ADM-Aeolus. From Fig. 3.18 it is apparent that the NLs of the atmospheric range-gates are highly correlated in terms of shape. Nevertheless, on this smaller frequency interval the behaviour of $\gamma_\mathrm{R}(f)$ looks rather random, in particular for the atmospheric range-gates. Also extreme values of the measured $\gamma_\mathrm{R}(f)$ have a great impact onto the results of the polynomial fit (Tab. 3.6) especially for a small number of frequency steps. The analysis of a larger frequency range, including more calibration steps, reduces the uncertainty in the derived fit parameters. Thus, for the two A2D airborne calibrations the enlarged interval of 1700 MHz was used for the analyses and the wind retrieval.

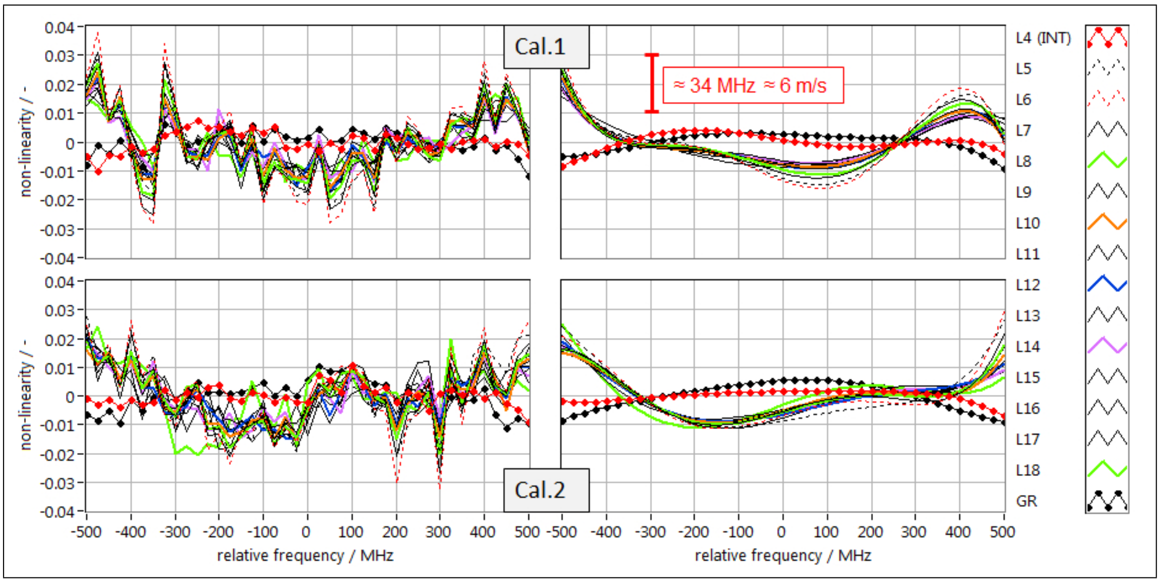

Figure 3.18.: The non-linearities (NL) of the measured (left) and fitted (right, Eqs. 3.21) Rayleigh response functions from the 1st (top) and 2nd (bottom) response calibration for a frequency interval of ± 500 MHz. NLs from response functions of the Internal Reference (INT) $\gamma_\mathrm{R,INT}$, the atmospheric range-gates $\gamma_\mathrm{R,i}$ and the summed ground return (GR) $\gamma_\mathrm{R,GR}$ are shown. The red marker indicates the magnitude of the equivalent wind speed errors.

The standard deviations $\sigma(\gamma_\mathrm{R}(f))$ of the measured NLs over the frequency range of 1 GHz (Fig. 3.18, left) are also given in Tab. 3.6 and certainly constitute a measure of quality for the response functions. It is found that $\sigma(\gamma_\mathrm{R,L15})$ is more than twice as high as $\sigma(\gamma_\mathrm{R})$ for the Internal Reference and the ground return, which can to a certain degree be attributed to the lower signal level received from the molecular backscatter. Consequently, these higher standard deviations also lead to larger errors for the sensitivity and the offset, which are calculated according to Eq. 3.19. The higher difference in standard deviation of $\gamma_\mathrm{R,GR}$ between the two calibrations might be an artefact from the summation of the ground signal. Compared to the 2nd, the 1st calibration exhibits a higher standard deviation in γ_R for the Internal Reference and for the range-gates #5 to #12 (L5-L12). The standard deviation of the non-linearity of the atmospheric range-gates shows an asymptotic behaviour (similar to the offset profiles) with decreasing values towards the ground.

Table 3.6.: Sensitivity and offset are derived from a linear fit through the response calibration functions of the Rayleigh channel for the Internal Reference (INT), the ground return (GR) and the atmospheric (ATM) range-gate #15 (L15). Errors refer to the 1σ-interval. The corresponding standard deviations $\sigma(\gamma_\mathrm{R})$ of the residuals are given in units of both response and frequency (assuming the respective sensitivities β_R).

calibration number			1	2
time		/ UTC	11:29.30 - 11:41.30	12:02.35 - 12:14.35
frequency range		/ MHz	± 500	± 500
summed GR		/ range-gates	20 / 21	19 / 20
INT:	sensitivity $\beta_\mathrm{R,INT}$	/ 10^{-4}/MHz	4.52 ± 0.02	4.55 ± 0.02
ATM:	sensitivity $\beta_\mathrm{R,L15}$	/ 10^{-4}/MHz	6.09 ± 0.05	6.18 ± 0.05
GR:	sensitivity $\beta_\mathrm{R,GR}$	/ 10^{-4}/MHz	4.63 ± 0.02	4.71 ± 0.03
INT:	offset $\alpha_\mathrm{R,INT}$	/ 10^{-2}	0.70 ± 0.06	0.02 ± 0.05
ATM:	offset $\alpha_\mathrm{R,L15}$	/ 10^{-2}	-4.30 ± 0.14	-5.18 ± 0.15
GR:	offset $\alpha_\mathrm{R,GR}$	/ 10^{-2}	2.54 ± 0.07	1.75 ± 0.09
INT:	std. dev. $\sigma(\gamma_\mathrm{R,INT})$	/ 10^{-2}	0.36	0.35
		/ MHz	7.96	7.69
ATM:	std. dev. $\sigma(\gamma_\mathrm{R,L15})$	/ 10^{-2}	0.90	0.98
		/ MHz	14.79	15.86
GR:	std. dev. $\sigma(\gamma_\mathrm{R,GR})$	/ 10^{-2}	0.43	0.55
		/ MHz	9.29	11.68

Comparing the fits for the two calibrations (Fig. 3.18, right), it is obvious that, in particular for the atmospheric range-gates, the slope and the curvature on both ends differ as well as the location of minima and maxima. No consistent shape of $\gamma_\mathrm{R}(f)$ seems to be deducible on an interval of 1 GHz, neither for the atmospheric range-gates nor for the Internal Reference and the ground return. Directly considering $\gamma_\mathrm{R}(f)$, according to the next-neighbour approach, could induce errors of up to almost 10 m/s, regarding the measured NL value of almost 0.04 for the 1st calibration in Fig. 3.18. Hence, it is preferred to neglect the $\gamma_\mathrm{R}(f)$ for the wind retrieval, when using a calibration with a frequency interval of 1 GHz (or less) and similar noise levels.

3.4.5. Error analysis for the calibrations

As shown in Fig. 3.16, the two airborne calibrations yielded different values for the describing fit parameters offset and sensitivity. Translated into wind speed, the difference in the offset can reach magnitudes of 2.5 m/s regarding the lower atmospheric range-gates. The availability of only two calibrations hinders the attempt to assess the similarity of the calibrations. However, making use of the residual of the fits for the response functions (Fig. 3.17), some indications can be drawn. To make the response functions of the two calibrations comparable, absolute frequencies from WM measurements must be used as in Fig. 3.19. The relative frequencies of the x-axis are related to the reference frequency of $844.75 \cdot 10^{12}$ Hz which is different to the relative frequencies used in subsec. 3.4.3, e.g. in Fig. 3.15. Thus, the fit coefficients in Tab. 3.5 differ from those in Fig. 3.20.

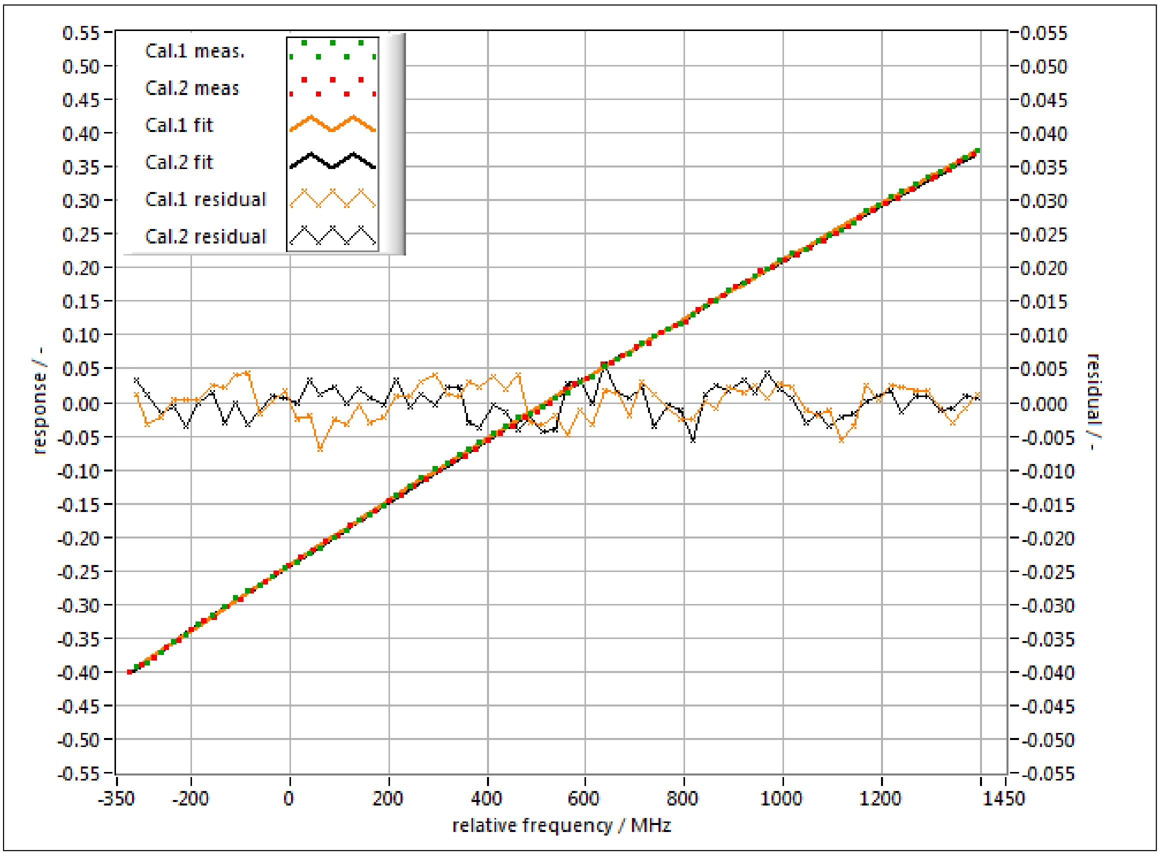

Figure 3.19.: The responses of the Internal Reference for the 1st (green dots) and the 2nd (red dots) calibration, the respective 5th order polynomial fits (bold solid orange and bold solid black line, left y-axis) and the corresponding residuals (thin orange and black line with crosses, right y-axis). The frequencies are relative to $844.750000 \cdot 10^{12}$ Hz.

Apart from some minor indications no argument can be given that strongly suggests a better quality and hence the preference of one of the two calibrations, neither regarding the Internal Reference nor the atmospheric path of the light. According to Tab. 3.5, the standard deviations $\sigma_{\mathrm{c,INT}}$ for the Internal Reference are $2.56 \cdot 10^{-3}$ (1st calibration) and $2.33 \cdot 10^{-3}$ (2nd calibration). Since all corrections described above (subsec. 3.4.6 and sec. 3.6) are applied to the calibrations, the residuals of the two calibrations are assumed to be free of systematic errors and to exhibit a random behaviour. The question is, whether the difference of the two response functions can be explained within this random behaviour. One approach is to simulate random response functions by taking the 5th order polynomial fit of the response function for the 2nd calibration and add Gaussian distributed random noise in order to mimic the residual. The standard deviation of $2.44 \cdot 10^{-3}$ for the Gaussian noise is derived from the residuals of both calibrations. Subsequently, the coefficients of a 5th order polynomial fit through each of the 10^6 realisations of such noisy response functions are determined. The histograms in Fig. 3.20 show the distribution (grey) of the coefficients. The coefficients of the 1st calibration (blue) are far out of the intervals of ± 1 standard deviation (black) around the coefficients of the 2nd calibration (red). Thus, it is unlikely that the difference between the two calibrations is exclusively due to statistical processes regarding the response. Similar results are obtained for the atmospheric range-gates of which those for range-gate #15 are shown as an example in Fig. A.4 and Fig. A.5. Despite almost the same time, the same location of the aircraft (temperature and pressure) and the same off-nadir angle ω (altitude of range-gates), the shapes of the atmospheric response functions differ. To a certain extent this difference can be ascribed to the difference found for the Internal Reference. However, the fact that the difference is more pronounced for range-gates closer to the aircraft may suggest a relation, for instance, to the telescope overlap or a misalignment of laser beam and telescope viewing direction. Fig. A.7 and Fig. A.6 present the results for the response calibration functions of the ground return.

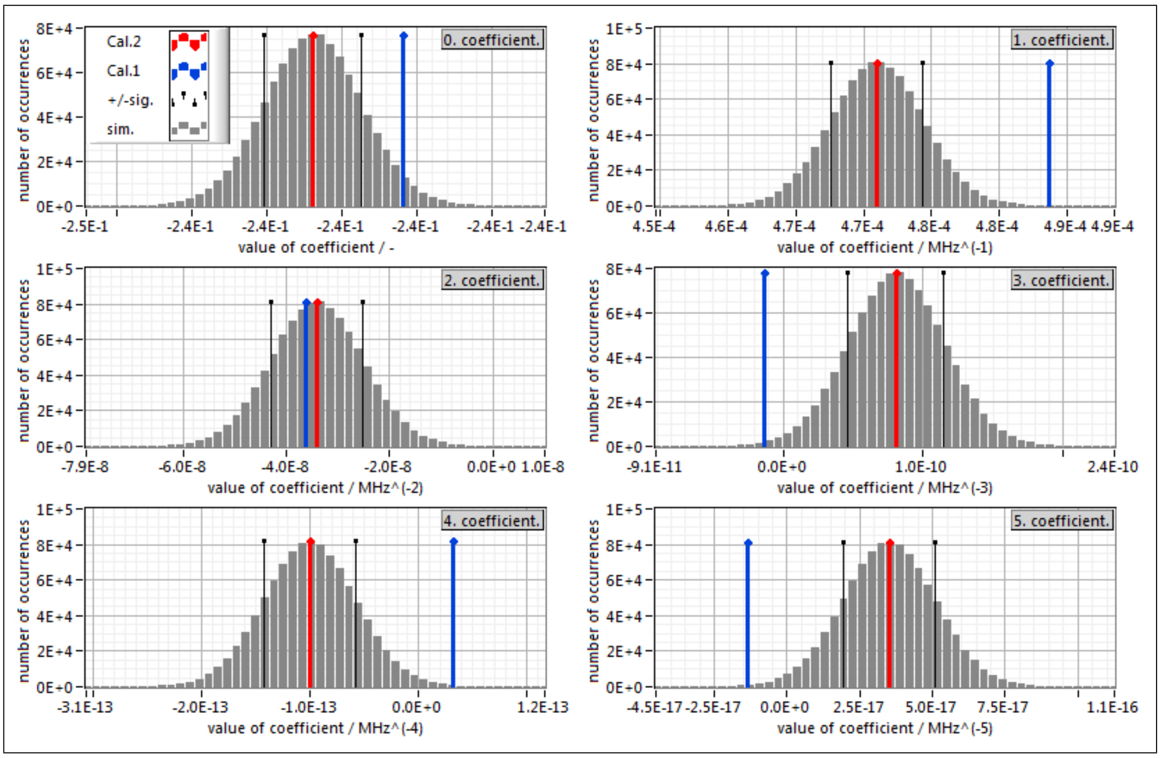

Figure 3.20.: Distribution of the six coefficients (grey, according to Eq. 3.21b) obtained from 10^6 simulations of a response function using random noise according to σ_c and the coefficients derived from the 5th order polynomial fit for the 2nd calibration (red) of the Internal Reference. The intervals of ± 1 standard deviation of the coefficients of the 2nd calibration are marked in black. The coefficients derived from the 5th order polynomial fit for the 1st calibration are indicated in blue.

Additionally to the evaluation with the A2D algorithms, the data of the two airborne Mie and Rayleigh response calibrations was used as input to the operational L1B processor of the ADM-Aeolus mission. Good agreement was found in a comparison of the two processors regarding the resulting sensitivities and offsets[7]. Thus, the developed A2D algorithms are assumed to be free of major deficiencies.

3.4.6. Corrections

This chapter describes several methods that were applied in order to reduce the systematic and random errors of the calibration and wind speed measurements. Considered are the aircraft induced LOS velocity, the summation of ground return signal, which is distributed over several range-gates, and the implementation of more precise measurements of the frequency of the outgoing laser pulse.

Laser frequency measurements from a wavelength meter

The laser frequency is commanded as an offset to the frequency of the seed laser (Fig. 2.4) relative to the reference laser, automatically in steps of 25 MHz during calibration or manually for adjustments during wind measurement mode. This differential frequency offset, the so-called TLE (Transmit Laser Electronics) frequency, is stored per observation together with other housekeeping data. The usable range of the frequency offset is up to 12 GHz, restricted by the capability of the control electronics. This is a much wider range than the 1 GHz to 1.7 GHz needed for the response calibration, in particular wider than one FSR of the FPI (Tab. 2.4), and it thus permits the determination of the FP filter parameters (Witschas et al. (2012a)). A commercial wavelength meter (High Finesse WS Ultimate) measures the absolute UV frequency of every emitted laser pulse with an accuracy of about 1 MHz - 2 MHz (Witschas (2007)). The wavelength meter (WM) is calibrated against a frequency-stabilized He-Ne laser every 100 s, which prevents long-term frequency drifts. A mean value from four frequency measurements per second is calculated and a single value of the absolute mean frequency of the laser pulses per observation is obtained from an average over 14 s.

Fig. 3.21 presents the absolute frequencies and the frequency increments per observation for the two calibrations. Taking into account the 14 s observation time and the WM sampling the frequency four times per second, the accuracy of a frequency measurement for a calibration step is about 0.2 MHz. Regarding the commanded frequency steps of 25 MHz, most of the increments measured by the WM are within a range of 25 MHz ± 2 MHz. However, during both calibrations outliers occur which reach increment values of 10 MHz and 40 MHz (e.g. at step 64 and 65 of the 2nd calibration). This relative deviation of up to 15 MHz with respect to the expected 25 MHz hence corresponds to almost 3 m/s LOS velocity for a single observation. Mean increment values of 25.14 MHz and 25.07 MHz are found for the 1st and the 2nd calibration, respectively. Depending on whether an inaccurate frequency step occurs towards the start/end or in the

---

[7] Dorit Huber, Personal communication, 2012/09/04

middle of the calibration it will more strongly affect either the sensitivity or the offset that are both derived from the response function. The effect using the measured frequency from the WM instead of the commanded frequency steps is discussed in subsec. 4.2.3. A comparison of the position within the calibrations (number of observation (Fig. 3.21) and relative frequency (Fig. 3.18)) reveals that the outliers in frequency steps are not correlated with the outliers in non-linearity. Moreover, the magnitude of the non-linearity outliers (up to about 10 m/s) cannot be completely explained by the frequency outliers (max. 15 MHz is equivalent to max. 3 m/s).

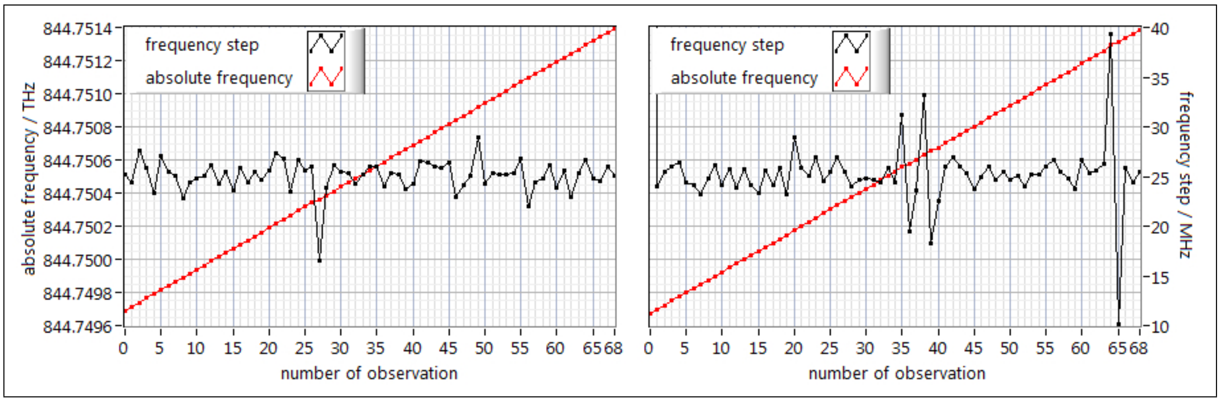

Figure 3.21.: Absolute frequencies (red, left y-axis) of the emitted laser pulses measured by the WM for 1.7 GHz intervals of the 1st (left) and 2nd (right) calibration. The frequency increments (black, right y-axis) vary between 10 MHz and 40 MHz with a mean of about 25 MHz.

Summation of distributed ground return signal

With a view to the zero-wind correction (subsec. 3.5.3) a correct response function for the ground return is of interest. The response functions for the ground return given for the 1st and 2nd calibration in Fig. 3.15 are both obtained after the summation of the ground return signal. Fig. 3.22 (top) shows the distribution of the ground return signal between range-gate #19 and #20. Neither of the two range-gates yields a practical response function (blue and green). So far such signal distributions in several range-gates were not expected for the ADM-Aeolus mission and hence no accordant algorithm was foreseen that retrieves an appropriate response function.

The solution provided in this thesis is a summation of the signal of the involved range-gates per pixel p and all valid measurements N according to Eqs. 3.22. The range-gate i is chosen to be 20 and 19 for the 1st and the 2nd calibration, respectively, i.e. a summation over two range-gates. The improved response function (black) that is achieved for the 2nd calibration is illustrated in Fig. 3.22 (bottom).

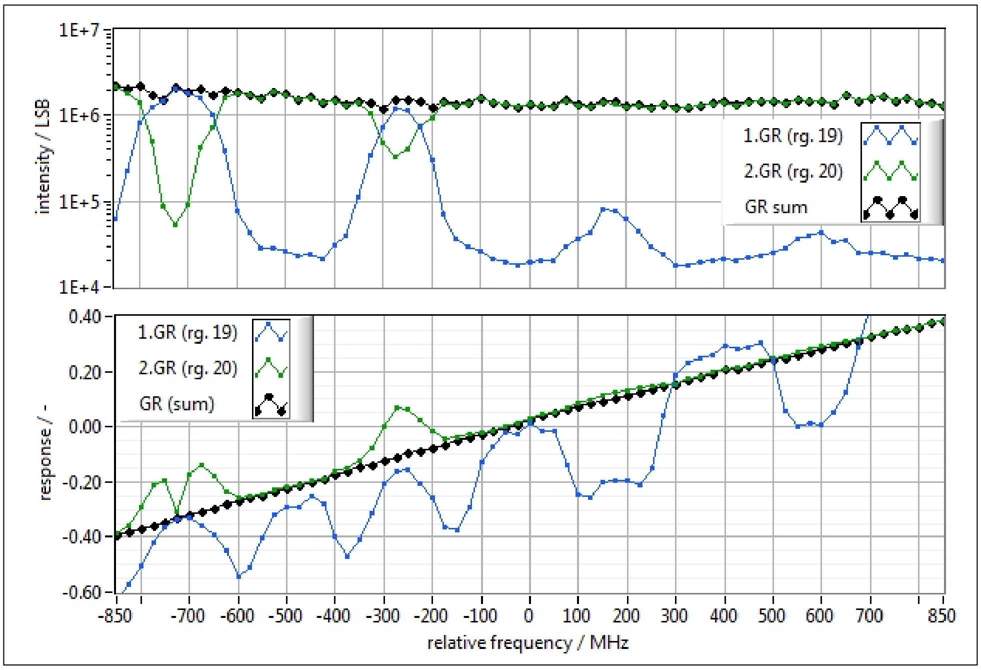

Figure 3.22.: 2^{nd} calibration: intensities (top) of the range-gates containing ground return signal and the responses functions (bottom) calculated per single range-gate (green and blue) and after summation (black).

$$I(p,i) = \sum_{m=1}^{N} [I_{\mathrm{raw}}(p,i,m) - I_{\mathrm{DCO}}(p) - I_{\mathrm{BKG}}(p,i,m)] \tag{3.22a}$$

$$I_{\mathrm{GR}}(p) = I(p,i) + I(p,i+1) \tag{3.22b}$$

The distribution of signal for the Mie channel is presented in Fig. 3.12. Also for the Mie channel a summation of signal must be performed in order to obtain a usable response function. However, due to the ACCD operation principle (Fig. 2.6) together with the definition of the response, the Mie channel is less sensitive to distributed signal than the Rayleigh channel. A reasonable centroid position can still be determined from a fringe with low SNR. In contrast, the read-out of the Rayleigh spots cannot maintain the actual intensity ratio $I_{\mathrm{A}}/I_{\mathrm{B}}$ (and hence the response value) of a single range-gate, since the line through the centres of the Rayleigh spots is not exactly aligned with the corresponding ACCD axis.

The importance of the detection of a distributed ground return signal has also been shown with respect to the determination of the ground intersection altitude in sec. 3.2 (Fig. 3.6). Although the read-out of the Rayleigh spots actually leads to an S-shaped (Reitebuch et al. (2010)) range-gate overlap function, a linear weighting for the determination of ground elevation (subsec. 3.4.2) is used as approximation so far.

Aircraft induced LOS velocity

In case the viewing direction of the wind Lidar is not perpendicular to its velocity direction a frequency Doppler shift is induced, which requires a correction of the retrieved Rayleigh and Mie wind speeds. Such corrections for aircraft induced LOS velocity have been performed, for instance, by Bilbro et al. (1984) and Reitebuch et al. (2001) for coherent DWL. For the A2D the aircraft induced LOS velocity $v_{\mathrm{los,ac}}$ is determined from posterior calculations involving the attitude data of the Falcon (subsec. 3.1.3). Subsequently, Eq. 3.23 converts this velocity to an according correction $\Delta R_{\mathrm{los,ac}}$ in the response domain, using k_{c} as the conversion factor of 5.636 MHz/(m/s) at 354.89 nm and $\beta_{\mathrm{R/M,a/g}}$ as the sensitivity obtained from the uncorrected Rayleigh (index R) or Mie (index M) response function for the respective atmospheric (index a) or ground return (index g) range-gate.

$$\Delta R_{\mathrm{los,ac}} = v_{\mathrm{los,ac}} \cdot k_{\mathrm{c}} \cdot \beta_{\mathrm{R/M,a/g}} \tag{3.23}$$

$\Delta R_{\mathrm{los,ac}}$ is calculated by use of a first guess of the sensitivity $\beta_{\mathrm{R/M,a/g}}$ (which still contains the aircraft induced LOS velocity). Thus, it could be argued that an iterative approach is necessary but for the case of the two calibrations of the airborne campaign the obtained corrections ΔR were small and hence the influence on the sensitivity $\beta_{\mathrm{R,M}}$ is negligible. For the 2nd calibration Fig. 3.23 presents the induced LOS velocity, the according response correction and the Rayleigh response function of an atmospheric range-gate before and after correction.

Rayleigh background on Mie channel

The broadband (Tab. 2.4) Rayleigh backscatter signal is also transmitted through the Fizeau interferometer. Due to the small USR of the Mie spectrometer the molecular return acts as an almost constant background signal. However, since the Fizeau interferometer constitutes an imaging device, the opto-mechanical construction of the telescope influences the distribution of the light onto the ACCD of the Mie channel. Operating the A2D in imaging mode allows the recording of this distribution on the array of 16 x 16 pixels (Fig. 3.24a), which are usually summed to a single array of 16 pixels (Fig. 3.24b) during wind measurement mode.

As can be seen in Fig. 3.24a the primary mirror of the telescope is not completely imaged but the major part of the ring of high intensity is visible. The low intensity in the middle corresponds to the central obscuration by the secondary mirror of the telescope. Also the radial obscuration by the three supporting struts are present in intervals of 120°. The intensity of this Rayleigh background signal decreases with increasing distance from the A2D and hence only affects measurements significantly up to about 4 km from the aircraft. Dedicated measurements have to be performed in order to obtain the information about the Rayleigh background per range-gate. The laser frequency is tuned in such a way that the Mie signal fringe is not contained in the USR (Mie Out Of Useful Spectral Range (MOUSR)) and is hence not detected by the ACCD. During these measurements the range-gate setting must be the same as for the wind measurements to which the correction will be applied later. Additionally, also the aircraft

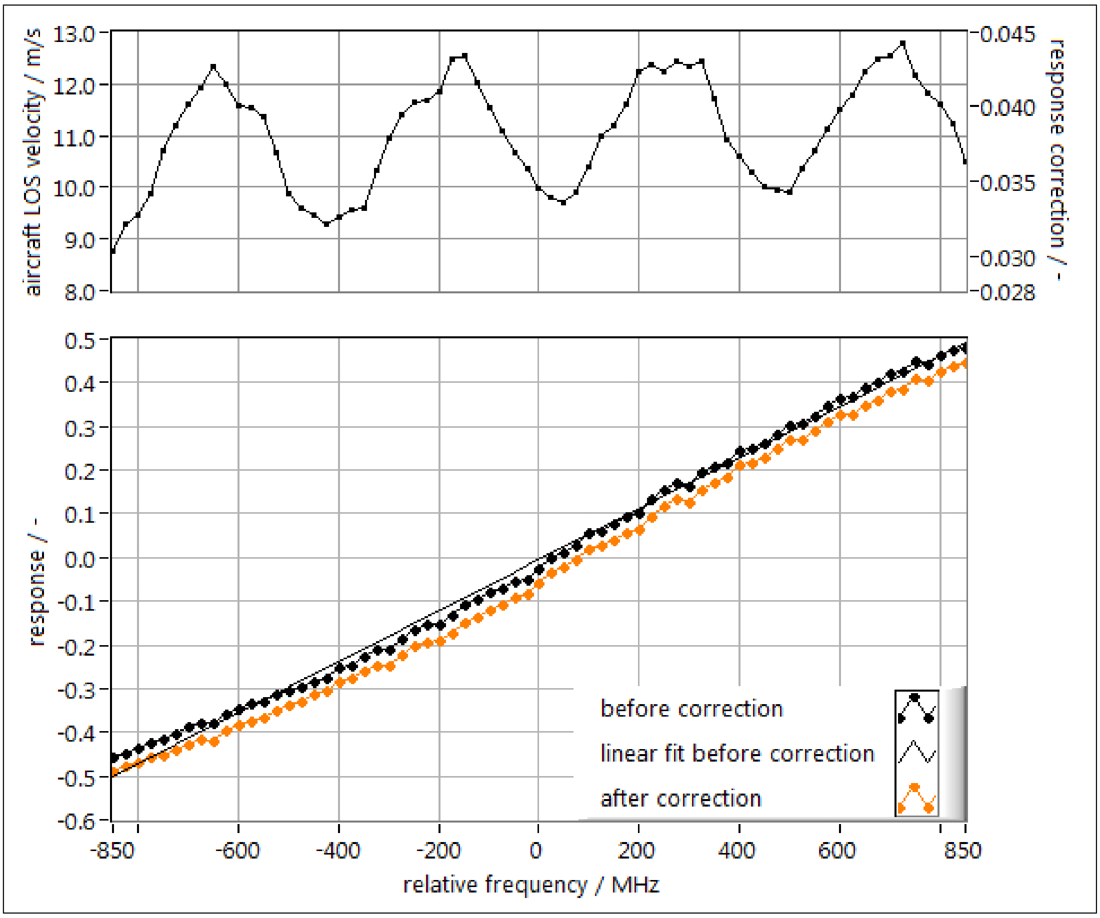

Figure 3.23.: Top: Calculated aircraft induced LOS velocity $v_{\mathrm{los,ac}}$ and the corresponding response correction $\Delta R_{\mathrm{los,ac}}$ for the 2^{nd} calibration. Bottom: Rayleigh response function of the atmospheric range-gate #15 before and after correction including the linear fit through the uncorrected response function which provides $\beta_{\mathrm{R,a}}$ for correction according to Eq. 3.23.

attitude and the pointing of the laser beam should not be varied, neither between wind measurement and MOUSR procedure nor during the single periods themselves. Strong variations in intensity and distribution from measurement to measurement prevent a successful modelling of the Rayleigh background. The typical magnitude of the intensity variation on a pixel during one observation is displayed in Fig. 3.24b and maximum deviations from the mean can still reach more than 10 %. Apart from the DCO and the nominal background intensity, the mean value of the Rayleigh background $I_{\mathrm{Ray}}(p,i)$ of one observation is additionally subtracted from the raw Mie signal for all 16 pixels p (Eq. 3.24). The centroid for all atmospheric range-gates i is determined from the corrected Mie signal $I_{\mathrm{M,corr}}(p,i)$.

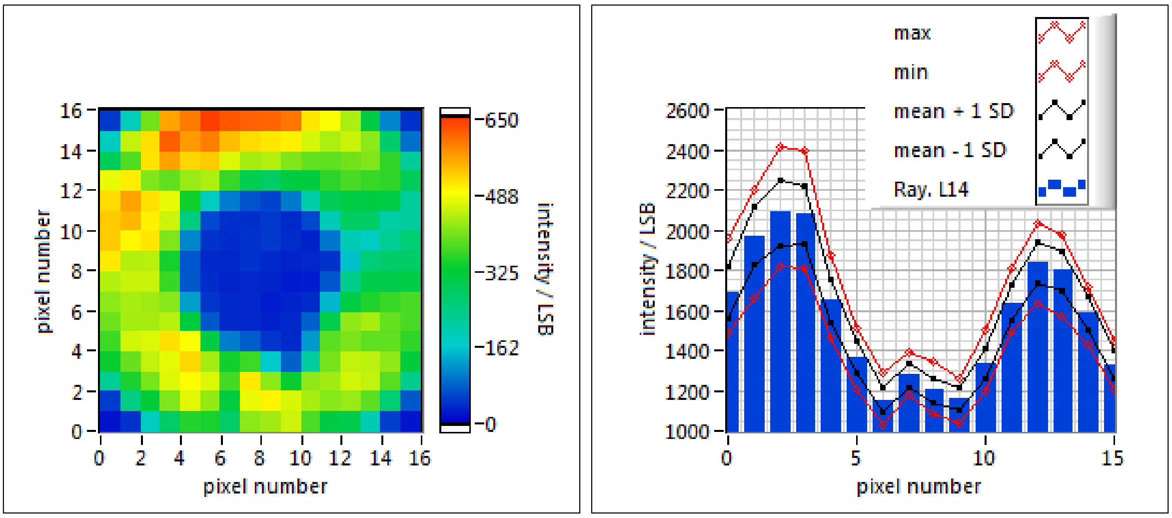

(a) *(b)*

Figure 3.24.: (a) Example for a total column measurement of the Rayleigh background on the Mie channel recorded from ground in imaging mode on 2010/09/06 between 13:05.10 - 13:12.58 UTC. / (b) Rayleigh background (blue) from 2009/09/26 taken as a mean over 20 observation (between 11:34.12 - 11:40.08 UTC) for range-gate #14 (L14). The minimum and maximum values (red) from the corresponding 700 measurements are indicated for each pixel. Accordingly the standard deviation (black) is derived per pixel.

$$I_{\mathrm{M,corr}}(p,i) \;=\; \sum_{m=1}^{N} \left[I_{\mathrm{raw}}(p,i,m) - I_{\mathrm{DCO}}(p) - I_{\mathrm{BKG}}(p,i,m)\right] - I_{\mathrm{Ray}}(p,i) \qquad i \;=\; 5, ..., 24 \tag{3.24}$$

Correcting wind measurements for the Rayleigh background can yield more precise wind speeds for low aerosol concentrations for range-gates close to the A2D, for which the determination of the centroid would be less accurate otherwise. Presumably, similar intensity ratios between the molecular return on the Mie channel and aerosol backscatter will be present for the A2D and for the ADM-Aeolus satellite. However, for the measurements from space no temporal intensity variations (Fig. 3.24b) of the molecular background are expected. Consequently, a constant correction can be applied, instead of repeating a MOUSR procedure. This so-called TOBS correction does not vary with height and only takes into account the effect of telescope tripod obscuration EADS-Astrium (2011). Compared to the A2D the central obscuration of the telescope of the ADM-Aeolus satellite is much smaller (≈ 5.2 %) due to the larger primary mirror, which also results in a smaller loss of intensity regarding the Mie signal. Whereas the secondary mirror of the A2D can obscure about 50 % of the fringe, it is only ≈ 15 % for ADM-Aeolus.

3.5. Wind retrieval

The relative velocity v_{meas} between the aircraft and the sampled atmospheric volume in LOS direction is determined according to Eq. 3.25.

$$v_{\text{meas}} = \frac{c}{2}\frac{\Delta f}{f_0} = (f_{\text{ATM}} - f_{\text{INT}}) \cdot \frac{\lambda_0}{2} \tag{3.25}$$

Mie responses (centroid position) and Rayleigh responses (Eq. 3.17a) are obtained during the wind measurement mode for the Internal Reference and the atmospheric range-gates. The respective frequencies are retrieved by inverting the corresponding Mie (Eq. 3.18) and the Rayleigh response function (Eq. 3.21) derived from a calibration. The difference of the resulting frequencies f_{ATM} (atmospheric) and f_{INT} (internal) is equivalent to the Doppler shift induced by the relative motion. For the Rayleigh channel the frequencies are determined from Eqs. 3.27, whereas Eqs. 3.28 yields the frequencies for the Mie channel. The emitted laser wavelength λ_0 and frequency f_0 are given in Tab. 2.1.

$$v_{\text{los}} = v_{\text{meas}} - v_{\text{los,ac}} - v_{\text{ZWC}} \tag{3.26}$$

However, v_{meas} must be corrected for the aircraft induced LOS velocity $v_{\text{los,ac}}$ (Eq. 3.5) in order to obtain the LOS wind speed v_{los} (Eq. 3.26). Additionally, a Zero Wind Correction (ZWC) v_{ZWC} can be necessary as discussed in subsec. 3.5.3.

3.5.1. Rayleigh wind retrieval

From the intensities obtained during the wind measurement the responses for the Internal Reference $R_{\text{R,INT}}$ and the atmospheric range-gates $R_{\text{R,ATM}}$ are determined per observation according to Eq. 3.17. The internal and atmospheric response functions are defined by the respective polynomial coefficients (Eq. 3.21). After subtracting the measured responses from the response function (Eq. 3.27), the resulting function is resolved for the frequencies $f_{\text{R,INT}}$ and $f_{\text{R,ATM}}$.

$$\left[\sum_{i=0}^{5} \left(c_{\text{ATM,i}} \cdot f^i\right)\right] - R_{\text{R,ATM}}(f_{R,ATM}) = 0 \tag{3.27a}$$

$$\left[\sum_{i=0}^{5} \left(c_{\text{INT,i}} \cdot f^i\right)\right] - R_{\text{R,INT}}(f_{R,INT}) = 0 \tag{3.27b}$$

The determination of the polynomial roots results in a number of intersection points with the frequency axis equivalent to the order i of the polynomial. From these frequencies the one within the 1700 MHz interval of the calibration is selected and defined as f_{ATM} and f_{INT}, respectively, for Eq. 3.25. Fig. 3.25 summarises the principle of the wind retrieval. In addition to the approach that considers the non-linearity in dependence on the frequency as presented here, the alternative approach using the non-linearity in relation to the response is discussed in A.3.

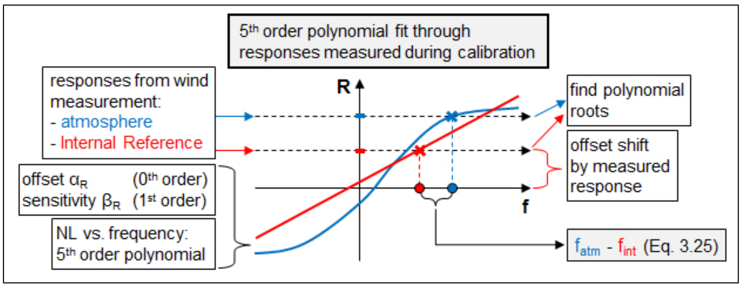

Figure 3.25.: Sketch of the wind retrieval scheme incorporating the NL as a function of the frequency.

From the calibrations it was found that the shapes of the Rayleigh response functions show an altitude dependency. However, the altitudes $h(n)$ of the range-gates during wind measurement differ from those during the calibration due to the different off-nadir angle ω and aircraft flight altitude. Additionally, the ADM-Aeolus satellite and the A2D allow the commanding of user defined range-gate grids, which can also differ between the Mie and the Rayleigh channel. Throughout the airborne campaign the range-gate grids were adapted according to the purpose of the current measurement, (e.g. high ground elevation of Greenland, high altitude jet-stream or calibration) but were kept equal for the Rayleigh and the Mie channel at the same time. The Falcon flew at 10432 m during the wind measurement on 2009/09/26 around 12:00 UTC (sec. 4.2), whereas the flight altitude was 9968 m and 9965 m during the two calibrations on 2009/09/21. Consequently, a linear interpolation is performed between the coefficients c_i from the calibration to obtain the response function for the according altitude of the wind measurement. In the case that range-gates during wind measurement are located above the highest altitude for which the calibration provides a response curve, the coefficients of the highest range-gate (#5) are taken into account. Just as for the profiles of offset and sensitivity (Fig. 3.16) also an extrapolation of the polynomial coefficients (subsec. 3.4.4) is performed for the range-gates below the 2.5 km (ground elevation during calibration). The obvious difference in the offset profiles between the 1^{st} and the 2^{nd} calibration results in significant differences in the retrieved wind speeds. ADM-Aeolus will perform a calibration once a week over suitable areas of the whole globe, which results in a wide geographical spread of the single observations and hence a corresponding spread in the probed atmospheric conditions. Since mainly polar regions will be used for calibration, large differences in atmospheric temperature will occur with respect to wind measurements, particularly at lower latitudes. Additionally, the derivation of a single response function for the whole atmosphere contributes to a mismatch between the response function and to the majority of wind measurements. However, unlike for the ADM-Aeolus mission no temperature correction (Dabas et al. (2008)) is applied to winds retrieved from A2D measurements. Simulations of Rayleigh response calibration functions, including Rayleigh-Brillouin scattering, showed that only a minor portion of the shifts in offset (Fig. 3.16) depends on the atmospheric temperature profile, because the temperature differences between calibration (2009/09/21) and wind measurements (e.g. 2009/09/26, sec. 4.2) were only in the order of 10 K. The offset rather seems to depend on the distance from the aircraft than on the altitude of the sampled range-gate.

3.5.2. Mie wind retrieval

The response calibration functions of both the Ground Return and the Internal Reference yield almost the same sensitivity and offset (Tab. 3.4). However, the Internal Reference signal is received via a different optical path through the telescope and the front optics of the receiver than the Ground Return and the atmospheric signal. Based on this fact it was decided to use the response calibration function of the Ground Return for the wind retrieval from the atmospheric range-gates, hence applying the parameters $\alpha_{\mathrm{M,GR}}$ and $\beta_{\mathrm{M,GR}}$. Additionally, the optional usage of the parameters $\alpha_{\mathrm{M,INT}}$ and $\beta_{\mathrm{M,INT}}$ of the Internal Reference would result in a systematic difference of the retrieved wind speed of 0.7 m/s considering the offset and in a wind speed dependent difference of 1 m/s per 50 m/s regarding the sensitivity. Inverting Eq. 3.18 results in Eq. 3.28. Its evaluation with the Mie responses $R_{\mathrm{M,INT}}$ for the Internal Reference and $R_{\mathrm{M,ATM}}$ for the atmospheric signal obtained during the wind measurement mode yields the corresponding frequencies. $f_{\mathrm{M,ATM}}$ and $f_{\mathrm{M,INT}}$ are input to Eq. 3.25.

$$f_{\mathrm{M,INT}} = \frac{R_{\mathrm{M,INT}} - \alpha_{\mathrm{M,INT}}}{\beta_{\mathrm{M,INT}}} \tag{3.28a}$$

$$f_{\mathrm{M,ATM}} = \frac{R_{\mathrm{M,ATM}} - \alpha_{\mathrm{M,GR}}}{\beta_{\mathrm{M,GR}}} \tag{3.28b}$$

Before the determination of the centroid positions of the Mie peak ($R_{\mathrm{M,INT}}$ and $R_{\mathrm{M,ATM}}$) with the DSA (ch. A.1), summation of signals per pixel from measurements to observations is performed according to Eq. 3.12a in order to increase the signal to noise ratio. Subsequently, the Rayleigh background is subtracted according to Eq. 3.24. Therefore, the MOUSR procedure is taken into account which is closest in time to the wind measurements to be evaluated and which fulfils the criteria mentioned in subsec. 3.4.6.

3.5.3. Zero wind correction

A zero wind is defined as the wind speed that is measured in an atmospheric volume which in fact does not exhibit any relative velocity towards the A2D or the ADM-Aeolus satellite. For the ADM-Aeolus satellite the AOCS maintains a LOS at a position which is to be constantly ensuring a relative velocity of zero at the intersection point with the Earth, hence compensating for the speed of the satellite and the earth rotation by yaw-steering. Regarding the A2D the aircraft attitude data (subsec. 3.1.3) is used to correct for the aircraft induced LOS velocity $v_{\mathrm{los,ac}}$. Considering the three rotation axes, the measured Doppler shift is most sensitive to a rotation around the yaw axis. An error in the determination of the yaw angle will result in a corresponding error of the retrieved wind speed. The acquisition of ground return signal can provide a reference for the correction of unknown contributions to the measured LOS velocity v_{meas} (Eq. 3.26). Thus, the ground detection (sec. 3.2) and the summation of ground signal (subsec. 3.4.6) constitute essential parts of the ZWC scheme of the A2D and can be similarly valuable for the ADM-Aeolus mission. Since solid ground is not moving, the resulting speed v_{los} for the range-gate containing the ground return should be zero after subtraction of the aircraft induced velocity $v_{\text{los,ac}}$. In the case that the obtained value for the ground speed v_{GR} deviates from $v_{\text{los,ac}}$ the respective difference is defined as the Zero Wind v_{ZWC} (Fig. 3.26).

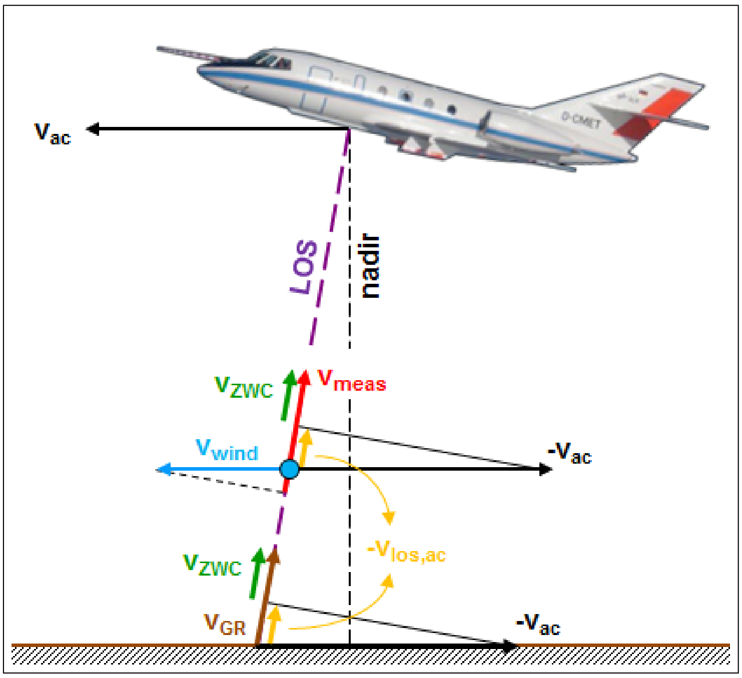

Figure 3.26.: Illustration of the determination of the Zero Wind Correction (ZWC) value v_{ZWC} (green), which is given as the difference between $v_{\text{los,ac}}$ (orange) and the measured velocity of the ground v_{GR} (brown). The velocity of the aircraft v_{ac} (black), the wind speed v_{wind} (blue) and unknown contributions, which are combined in v_{ZWC}, contribute to the measured LOS wind speed v_{meas} (red).

In order to reduce the effect of noise, v_{ZWC} is determined from the mean over many observations. Fig. 3.27 presents two periods from the 2009/09/26 and the 2009/09/29 for each of which a ZWC value was derived from the ground returns observations marked in red. These are observations for which all measurements contain the ground return within the same range-gate and which exhibit a high signal level due to reflection at ice surfaces. The ground return elevation was determined according to the ground detection algorithms introduced in sec. 3.2. For the Rayleigh channel the obtained values for v_{ZWC} are $\approx$5.4 m/s (2009/09/29) and -0.2 m/s (2009/09/26). Such a big difference of 5.6 m/s cannot be explained by errors in the aircraft attitude or velocity data (subsec. 3.1.3). Thus, the large ZWC value v_{ZWC} found on the 2009/09/29 (sec. 4.3) likely arises from other causes, for instance, from instrumental errors such as a misalignment between the transmit and the receive path. This kind of error is specific to the A2D since the corresponding telescope of the ADM-Aeolus satellite is used for both the transmit and the receive path. For the A2D the difference in v_{ZWC} can be traced back to a modification of the mirror that controls the steering of the laser beam (Fig. 2.4) which was performed on 2009/09/28 and which changed the alignment with respect to the telescope axis. These findings agree with the high sensitivity of the Rayleigh spectrometer to the incident angle of the light (Witschas et al. (2012b)). Consequently the Rayleigh winds retrieved during the airborne campaign after 2009/09/28 need a correction. A value of $v_{\mathrm{ZWC}} = 5.4\,\mathrm{m/s}$ was applied to the winds presented in sec. 4.4 and sec. 4.3.

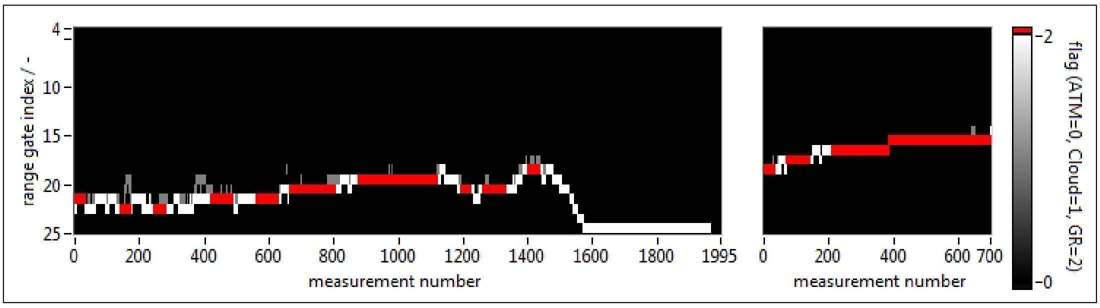

Figure 3.27.: Ground returns used (red) for the determination of the ZWC value over Iceland on the 2009/09/29 between 12:07.15 - 12:24.24 UTC (left) and over Greenland on the 2009/09/26 between 12:57.49 - 13:03.47 UTC (right). Ground returns not used (white) and range-gates which are identified to contain aerosol or clouds (grey) are shown, too. Atmosphere and range-gates below ground are marked in black. The internal reference corresponds to range-gate #4.

Different ZWC values were found for the Mie and the Rayleigh channel. Thus, in the future the range-gate grids of the A2D must be selected such that ground return signal is provided also for the Rayleigh channel to allow the determination of a respective ZWC value. Especially for the ADM-Aeolus mission, this fact results in a trade-off between several high resolution ground bins in order to avoid atmospheric contamination and the expansion of the wind measurements as far as possible into the higher atmosphere. Additionally, if the zero wind offset stays constant over a long enough period, it could also be corrected via the bias found from comparison against Weather Forecast models. For the ADM-Aeolus mission another approach of determining the zero wind offset caused by an unknown mispointing is the Harmonic Bias Estimation discussed in Marksteiner (2009). Distortions within the satellite structure can be generated, for instance, by thermal stress due to eclipse phases. This may result in a change of the relative angles between the star trackers and the telescope, eventually yielding a mispointing. Considering the satellite revolving the earth on a circular orbit, a sinusoidal behaviour of the ZWC values can be expected.

3.6. Quality control measures

Quality control is necessary to distinguish which data are more reliable than others. For example, indicators such as the monotony of the measured response calibration functions or the FWHM of the detected Mie signal are derived that allow a respective classification. Some of the quality control measures that are applied to the A2D calibrations and wind measurements are presented in this chapter. During the airborne campaign over Greenland on 2009/09/26 between 11:00 - 13:00 UTC unusually many corrupted measurements occurred which are detected and excluded from the evaluation of the two calibrations for the Rayleigh and the Mie channel. Applying a threshold to the Signal to Noise Ratio regarding the Mie channel assures the exclusion of outliers, which is especially important for the statistical comparisons in ch. 4. The signal intensities retrieved on the Rayleigh channel per measurement also provide information for quality control.

Detection of corrupted measurements

The DCO value (subsec. 2.3.2 and Eq. 3.12d) is supposed to vary within a small range, a circumstance which enables the detection of certain instrument malfunctions. From plausibility checks of the recorded ACCD data it was noticed that the DCO value exceeds the expected margins from time to time. Mostly this happens rather sporadically showing only minor impact on the measurement results, but during the two airborne calibrations a strong increase in the rate of occurrence of outliers was detected (Fig. 3.28).

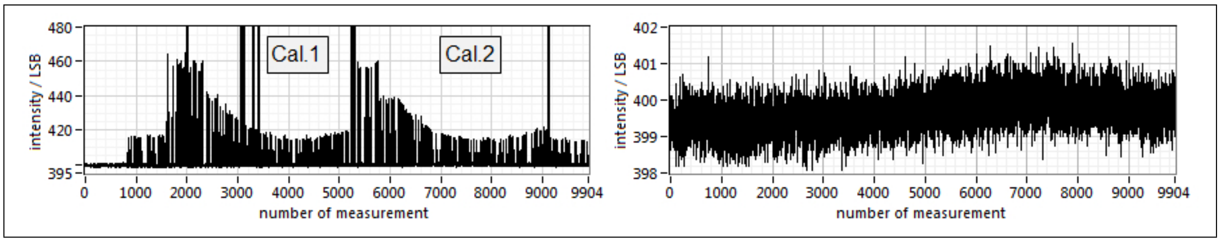

Figure 3.28.: Mean pixel intensity of the Rayleigh DCO channel per measurement from 11:00.08 to 12:30.03 UTC on 2009/09/21, comprising the two airborne calibrations. The DCO values are shown including (left) and excluding (right) outliers.

In the presented case single outliers reach values of more than 12,000 LSB, but in the majority of the cases the DCO value is below 470 LSB. Due to the strong variability of the magnitude of the intensity of the DCO values, simple thresholds are applied as validity criteria (Tab. 3.7). For Mie and Rayleigh channel almost all outliers occur at the same measurements, which suggests that the outliers are due to the same instrumental fault in the detection chain. Both channels exhibit a similar proportion of outliers with about 5 % and the outliers seem to be randomly distributed. The impact of the exclusion of such corrupted measurements from the analysis of the Rayleigh calibrations can be seen in Tab. 4.2. Assuming homogeneous atmospheric conditions throughout an observation, a reduced number of valid measurements does not change the value of the response. Nevertheless, the resulting responses would be more strongly affected by noise due to the lower signal level.

Table 3.7.: Thresholds applied to the DCO values in order to detect corrupted measurements (outliers) within the two airborne calibrations.

calibration number	1		2	
time / UTC	11:25.36 - 11:46.14		11:58.23 - 12:19.01	
channel	Mie	Rayleigh	Mie	Rayleigh
threshold / LSB	308 - 312	398 - 402	309 - 313	398 - 402
no. of outliers / %	5.6	5.1	5.6	5.2
DCO (incl. outliers) / LSB	313.8	401.1	313.3	401.00
DCO (excl. outliers) / LSB	310.1	399.6	310.8	400.00

Several causes were identified that lead to DCO outliers. Three of these causes, of which an incorrect assignment of the signal to the range-gates is the most frequent one, are presented in Fig. 3.29. The corrupted assignment results in the location of the Internal Reference at range-gate #3 instead of the nominal range-gate #4. From this range-gate part of the signal of the Internal Reference leaks into range-gate #2 and is hence detected as an increase in the DCO value.

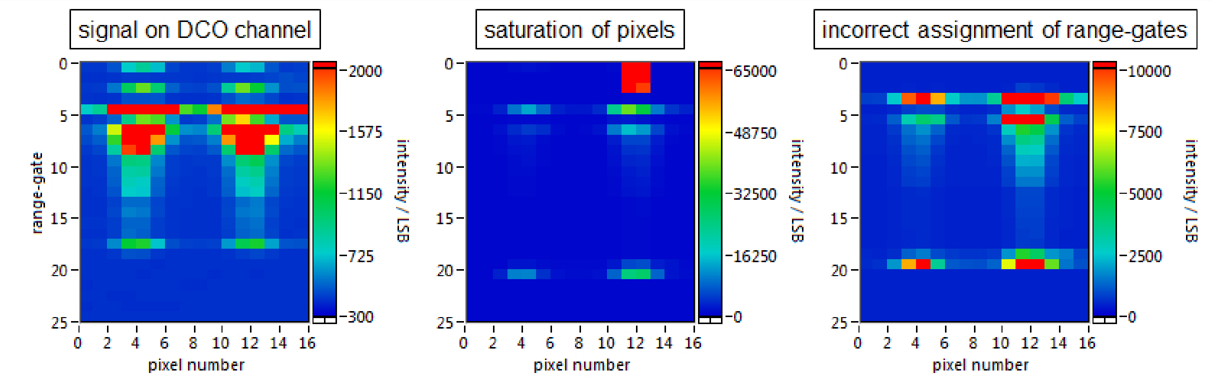

Figure 3.29.: Three examples of malfunctions that were detected via the monitoring of the DCO value. Left: The DCO channel (range-gate #2) contains signal. Middle: Occasionally saturations of single pixels or pixel areas occur. Right: The DCO channel contains signal due to an incorrect assignment of range-gates with an index shift of -1.

The occurrence of the first DCO outliers (around measurement 800) coincides with the restart of the ACCD signal data acquisition. No DCO outliers were found for measurements with the A2D instrument on ground, which suggests that at least part of their occurrence is related to airborne measurements, possibly to turbulences, vibrations or shocks. The incorrect assignment could then be introduced by a timing jitter of the laser pulse transmission, which is affected by vibration. Indeed outliers were found more often during phases of clear air turbulence rather than in calm atmospheric conditions. However, the rate of occurrence was much lower than during the phase of the two calibrations.

Applying a Signal-to-Noise-Ratio threshold to signals from aerosol backscatter

Additionally to the detection of corrupted measurements (sec. 3.6), the quality control for the Mie channel consists of the application of an SNR threshold. Already a few erroneous wind speeds would otherwise result in flawed parameters derived from statistical comparisons (sec. 4.2). However, providing a high number of reliable wind speed measurements likewise in heterogeneous atmospheric conditions (sec. 4.4) with high wind speed gradients (sec. 4.2) and broken clouds (sec. 4.3) is one of the main goals. Various definitions of a respective SNR exist, for instance, suggested by Rees and McDermid (1990), Marseille and Stoffelen (2003) or Reitebuch et al. (2010). However, a derived SNR parameter (Eq. 3.29) showed the best performance regarding A2D airborne wind measurements and was consequently used for the evaluations presented in ch. 4.

$$SNR = \frac{I_{\max}}{\frac{1}{11}\left(\sum_{i=0}^{15} I(i) - \sum_{i(I_{\max})-2}^{i(I_{\max})+2} I(i)\right)} \tag{3.29}$$

Fig. 3.30 presents a Mie signal from a wind measurement on 2009/09/26 at 12:00 UTC in order to illustrate the parameters of Eq. 3.29. The signal emanates from a sub-visible cirrus located at observation #33 in range-gate #14 (Fig. 3.31) and the solar background, the DCO and the Rayleigh background are subtracted. The maximum intensity $I_{\max}$ at pixel #7 is about 3500 LSB. A comparison to the magnitude of the Rayleigh background on the Mie channel in Fig. 3.24b of 2,100 LSB illustrates the necessity of subtracting this background before determining the centroid position of the Mie peak and the SNR.

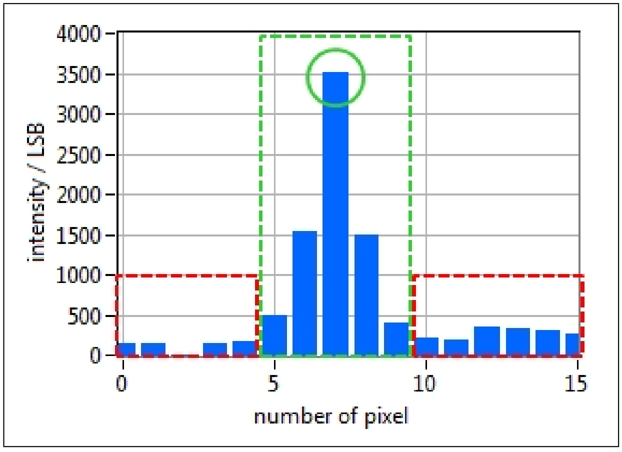

Figure 3.30.: Illustration of the SNR definition of Eq. 3.29 on a Mie signal from a wind measurement on 2009/09/26. The maximum intensity $I_{\max}$ is recorded on pixel #7 (green circle). The interval of pixel #5 to #9 (green box) is defined as the signal. The mean of the intensities measured on the remaining pixels (red boxes) is defined as noise.

The effectiveness of the quality control by an SNR threshold is illustrated in Fig. 3.31. On the top it presents the SNR values per range-gate and observation for the wind measurement scene discussed in sec. 4.2. Regions of higher SNR are visible that correlate with the proximity to the aircraft (range-gates #5 to #9), an orographic cloud (range-gates #13 and #14), enhanced aerosol concentration from a katabatic flow (range-gates #19 to #21) and the sea surface (range-gate #22). The SNR values higher than 60 in range-gate #3 are due to a leakage of signal from the Internal Reference (range-gate #4). Applying an SNR threshold of 3.0., which resulted from manual adjustment, yields the mask that is presented in the middle of Fig. 3.31. The shape of the cloud, the regions of higher aerosol content below the aircraft and at low altitudes as well as the sea surface return are recognisable. Most of the range-bins exhibiting an SNR value smaller than 3.0 yield unrealistic wind speeds (Fig. 3.31, bottom).

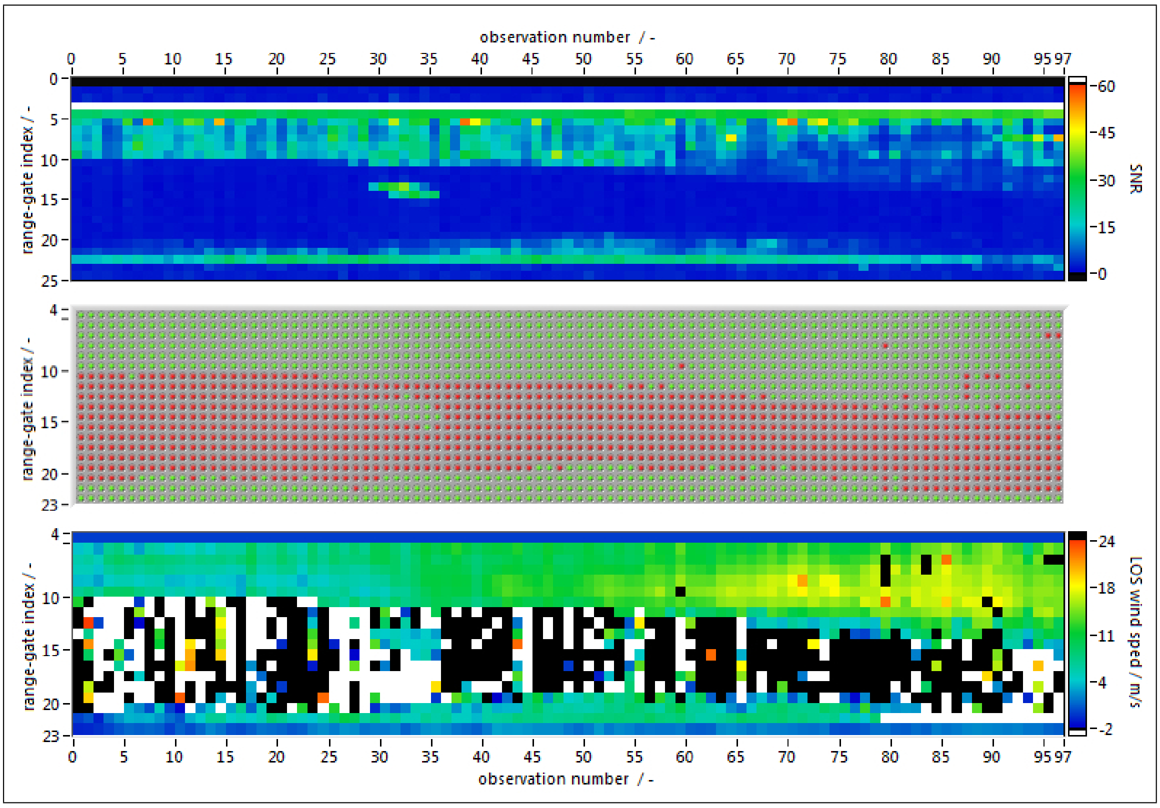

Figure 3.31.: Top: Signal to noise ratio obtained from measurements of the A2D Mie channel on 2009/09/26 between 11:50 - 12:19 UTC (observation 1 - 97). Range-gate index #4 corresponds to the Internal Reference. / Middle: SNR mask obtained by applying a threshold of 3.0, with higher and lower values represented by green and red colour, respectively. The vertical axis starts with the Internal Reference on top and ends with range-gate #22 (containing the sea surface echo) on the bottom. / Bottom: Wind speeds (before application of the SNR-mask) measured on 2009/09/26 (sec. 4.2).

Variation of measured intensities on the Rayleigh channel

The evaluation of the signals of the Rayleigh channel on measurement basis allows creating a new quality criterion on observation level. Eqs. 3.30 defines the signal intensity I_{m} per measurement m and range-gate i. The mean value of the intensity $\mu(I_{\mathrm{m}})$ is derived on measurement basis as well as the standard deviation $\sigma(I_{\mathrm{m}})$. Thus, the expression $\sigma(I_{\mathrm{m}})/\mu(I_{\mathrm{m}})$ refers to the intensity variation within an observation. It is used as an individual weight for a linear fit per range-bin in Eq. 4.11 on an observational scale in subsec. 4.2.3.

$$I_{\mathrm{m}}(i,m) = \sum_{p=1}^{16} \left[I_{\mathrm{raw}}(p,i,m) - I_{\mathrm{DCO}}(p) - I_{\mathrm{BKG}}(p,i,m) \right] \tag{3.30a}$$

$$\mu(I_{\mathrm{m}}) = \frac{\sum_{m=1}^{N}(I_{\mathrm{m}}(i,m))}{N} = \frac{I(i)}{N} \tag{3.30b}$$

$$\sigma(I_{\mathrm{m}}) = \sqrt{\frac{1}{N-1}\sum_{m=1}^{N}\left(I_{\mathrm{m}}(i,m) - \mu(I_{\mathrm{m}}(i,m))\right)^2} \tag{3.30c}$$

The ratio of the standard deviation to the mean of the intensities is shown in Fig. 3.32. It is visible that especially the range-gates below the cloud between observation #32 - #35 exhibit a high signal variation. This fact is interpreted as a lower wind measurement quality regarding the respective range-bins. Therefore, higher values of $\sigma(I_{\mathrm{m}})/\mu(I_{\mathrm{m}})$ are translated into a lower weight in Eq. 4.11. The low values in range-gates #5 to #7 show the influence of the telescope overlap and are not used in the evaluation of the wind measurements in sec. 4.2.

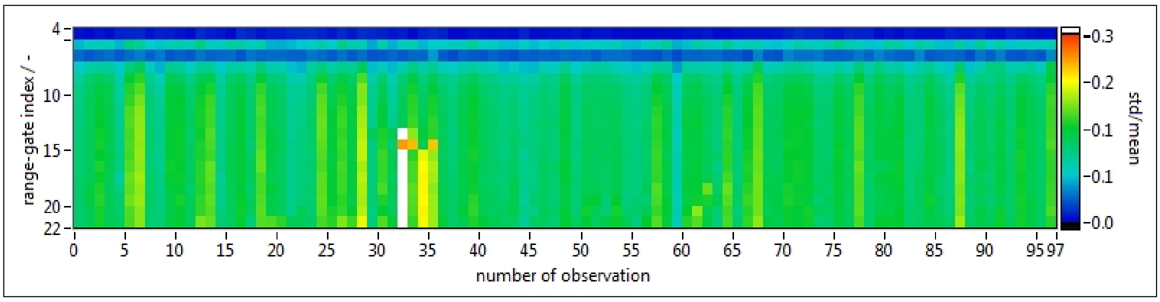

Figure 3.32.: Quality criterion derived from the intensity variation on the Rayleigh channel during wind measurements on 2009/09/26 from 11:50 - 12:19 UTC. Range-gate index #4 corresponds to the Internal Reference. Range-gates #5 to #22 correspond to the atmosphere.

Detailed quality control algorithms and scene selection schemes tailored to simulated ADM-Aeolus data are presented in Tan et al. (2008). However, these algorithms are tested on simulated data and idealized cases, in contrast to the quality control performed on real measurements within the framework of this thesis. The L2A processor (Flamant et al. (2008)) of the ADM-Aeolus mission contains an advanced quality control scheme that will allow identifying aerosol stratification in many cases.

3.7. Summary

This chapter gave an introduction to the airborne campaign in 2009 with the Falcon aircraft on which the A2D and the 2-µm Lidar were deployed in parallel. The exploitation of the range-gate overlap allows a more precise determination of the ground return elevation. Combining a DEM and the knowledge from the available aircraft data, the ground return signal can be discriminated from clouds. Whereas for the Mie channel the two airborne calibrations yield very similar response functions, those of the Rayleigh channel exhibit a difference in the offset. A new approach of the summation of ground return signal, which is distributed over several range-gates, results in a successful evaluation of the ground return response functions of the two calibrations. In order to enable a reliable consideration of the non-linearity of the Rayleigh calibration response function, the analysis interval must be enlarged. A polynomial of 5^{th} order is recommended to fit the non-linearity. Correction for calibrations and wind measurements were discussed such as the usage of WM frequencies and the consideration of the aircraft induced LOS velocity as well as a Zero Wind Correction. Quality control measures were introduced for the detection of corrupted and the exclusion of low SNR measurements, which assures reliable results from the statistical comparisons performed in ch. 4.

4. Validation of A2D wind observations and retrieval

The main goal of this thesis is to support of the pre-launch validation of the measurement and calibration strategy of the ADM-Aeolus satellite (subsec. 2.2.3), keeping in mind the novel technologies implemented (subsec. 2.3.2). This shall be achieved by comparing A2D wind measurements against other sources and thereby implicitly validating the measurement principle, the function of the instrument and the retrieval algorithm. The airborne campaign in 2009 for the first time enabled evaluation of wind Lidar measurements over the whole range from aircraft to ground with a viewing geometry similar to the ADM-Aeolus satellite. The coherent 2-µm Lidar on-board the Falcon, NWP models and radiosondes all rely on measurement principles different to the A2D one and thus constitute valuable and independent sources of wind measurements. The methods and optimized retrieval algorithms presented in ch. 3, such as the correction of LOS velocity (subsec. 3.1.3), the simulation of the non-linearity (subsec. 3.4.4) and the application of the developed quality indicators (sec. 3.6), were considered for the A2D winds presented here. Furthermore, the reliable detection of the ground return (sec. 3.2) now allows a zero wind correction (subsec. 3.5.3).

This chapter presents a detailed analysis of three selected wind measurement sections of flights on September 26th, 29th and October 1st. Each analysis is dedicated to a specific situation, allowing a better assessment of the performance of the A2D (e.g. in complex atmospheric scenes) and emphasising the main improvements achieved by the developed algorithms. As mentioned in ch. 1, the ADM error requirements (2 m/s HLOS) are an extreme challenge. The statistical comparisons of wind fields presented within the current chapter yield, among others, an estimation of the random and systematic error of A2D wind measurements. In order to avoid the introduction of errors in a subsequent statistical comparison of winds, a dedicated aerial interpolation algorithm was developed to map 2-µm winds from their present measurement grid onto the A2D grid. Comparing A2D Rayleigh and Mie winds to the 2-µm winds statistical parameters, such as random error, systematic error and correlation coefficient, are derived that allow an assessment of the A2D wind measurement performance. The 2-µm Lidar can provide reliable wind measurements only in regions with sufficient aerosol content, which regularly leads to extensive gaps in the middle atmosphere. For low aerosol loads this restriction hardly allows a comparison of A2D Mie and Rayleigh winds to 2-µm winds on a significantly large database resulting in valuable Rayleigh winds not contributing to the validation. To close this gap, wind speeds from ECMWF analyses are used for a comparison against these Rayleigh winds. As ECMWF winds are provided on a different grid than 2-µm winds, modifications on the preceding aerial interpolation algorithm are necessary and will be described below. The validity of A2D measurements is supported by the common identification of features, such as clouds or confined sea surface winds, in other sources (2-µm Lidar, ECMWF, radiosonde).

4.1. Spatial and temporal matching and statistics

4.1.1. Aerial interpolation of 2-µm winds onto the A2D grid

The fact that both, the A2D and the 2-µm Lidar, were sensing the same atmospheric volumes at the same time strongly suggests drawing advantage of a direct range-gate to range-gate comparison of their measured wind speeds. The measurement grids of the two Lidars are visualised in Fig. 4.1.

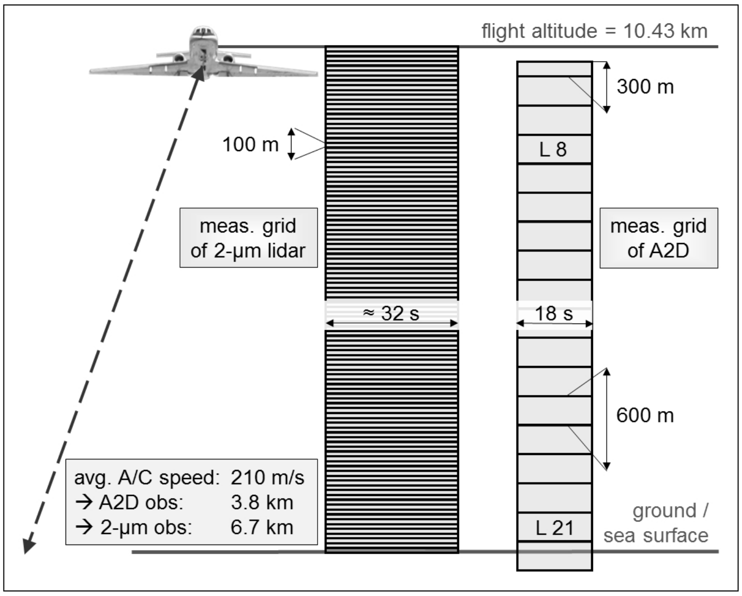

Figure 4.1.: Sketch of the measurement grids of the A2D (right) and the 2-µm Lidar (left). Also indicated are aircraft flight altitude, sea/ground surface, laser LOS with 20° off-nadir pointing, A2D range-gate numbering (e.g. L8, L21) and range-bin dimensions. The relative sizes of A2D and 2-µm range-bins are true to scale.

The presented information and sketches are based on the section flown on September 26th between 11:50 - 12:19, which is analysed in sec. 4.3. For an average aircraft velocity of 210 m/s a single A2D observation of 18 s and a 2-µm observation of 32 s spreads horizontally over 3.8 km and 6.7 km, respectively. One should keep in mind that within the interpolation algorithm the subdivision of an A2D observation (subsec. 2.3.2) into two parts of 14 s (actual measurement) and 4 s (e.g. read-out) is accounted for. Neglecting the latter this leads to a horizontal length of 2.9 km. The A2D grid along the laser LOS depends on the commanded vertical resolution with varying integration times and thus range-gate thicknesses. For the presented case, the Internal Reference corresponding to range-gate #4 and range-gates #23 and #24, located below the sea surface, are not shown. Range-gate #5 with 2.1 µs integration time, i.e. 315 m range, is followed by range-gates with 4.2 µs, i.e. 630 m, down to range-gate #22. Regarding an off-nadir angle of 20° as indicated, this translates into 296 m and 592 m vertical thickness, respectively. In contrast to the A2D, the 2-µm winds are provided at a constant vertical resolution of 100 m per range-gate. For a comparison of A2D and 2-µm winds, a very simple realisation to overcome the difference in vertical and temporal (horizontal) resolution of the two Lidars, would be a next-neighbour comparison, considering the shortest distance between the centre of an A2D range-gate and the surrounding 2-µm range-gates. In order to avoid the consequential introduction of a representativeness error, an algorithm was developed which interpolates the wind speeds of the 2-µm Lidar onto the A2D measurement grid.

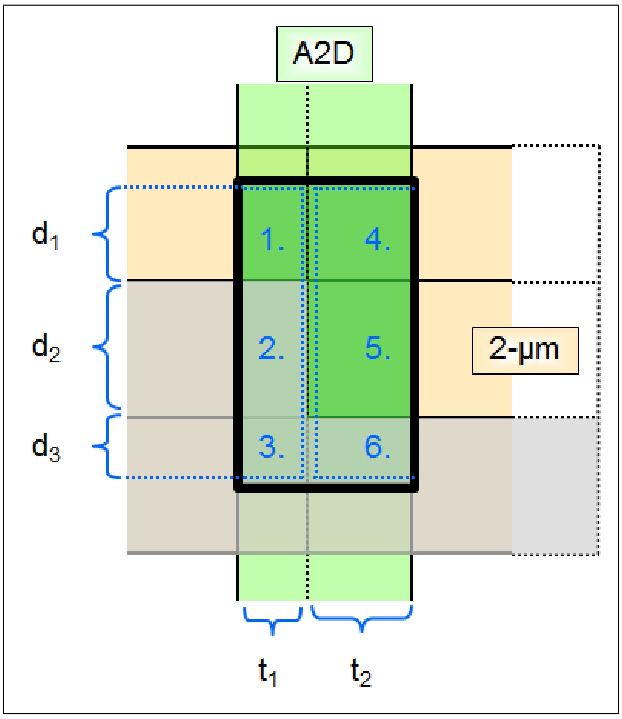

Figure 4.2.: Sketch of the A2D - 2-µm aerial interpolation scheme: Every section of a 2-µm range-bin (beige) covering the selected A2D range-bin (dark green, bold frame) is allocated a weight depending on its respective aerial contribution. The weights are determined by the product of the corresponding relative vertical and temporal (horizontal) extents d_i and t_i, respectively. Situations can occur where an A2D range-bin is only partly covered by valid 2-µm data and leaves an uncovered area (grey).

Fig. 4.2 shows a sketch of the interpolation scheme. It illustrates three A2D range-bins (green): the main one in the centre, surrounded by a bold black frame, and two range-bins indicated above and below. In this simplified sketch six 2-µm range-gates (beige) completely cover the main A2D range-gate. The relative size of the aerial contribution of each 2-µm range-gate to the area of the A2D range-gate depends on the proportions of the lengths d_i (vertical scale) and the times t_j (horizontal scale), determined by the current A2D measurement grid, time and aircraft attitude. Defining a vector of vertical weights $\vec{d}$, a vector of horizontal weights $\vec{t}$ and a matrix **V** containing the 2-µm wind velocities of the respective range-bins

$$\vec{d} = [d_1, d_2, d_3, ..., d_i], \qquad \vec{t} = [t_1, t_2, ..., t_j], \qquad \mathbf{V} = \begin{pmatrix} v_{1,1} & v_{1,2} & \cdots & v_{1,\mathrm{j}} \\ v_{2,1} & v_{2,2} & \cdots & v_{2,\mathrm{j}} \\ \vdots & \vdots & \ddots & \vdots \\ v_{\mathrm{i},1} & v_{\mathrm{i},2} & \cdots & v_{\mathrm{i},\mathrm{j}} \end{pmatrix}$$

and fulfilling $\sum d_i = 1$ and $\sum t_j = 1$, we obtain a single 2-µm wind speed valid for the area of the A2D range-gate.

$$v_{2\mu\mathrm{m}} = \vec{d} \cdot \mathbf{V} \cdot \vec{t}^T \tag{4.1}$$

By the use of this interpolation algorithm the information content of every single 2-µm range-bin has an impact on the overall result, unlike e.g. for the simple next-neighbour comparison mentioned above, where under certain conditions whole range-bins would be completely neglected.

It often occurs that no valid 2-µm winds are available to cover the whole area of an A2D range-bin, indicated in Fig. 4.2 by the shaded area affecting the contributions 2., 3. and 6. In this case the resulting 2-µm wind speed must be determined from the remaining contributions (here 1., 4. and 5.). Therefore, the wind speed obtained from these valid contributions has to be divided (scaled) by the percentage of their area on the whole area of the A2D range-bin, which is equal to the sum of the respective aerial weights $d_\mathrm{i} \cdot t_\mathrm{j}$. Now the question arises at which coverage ratio $r_{\mathrm{cvg,i}}$ an interpolated 2-µm wind speed should still be declared as valid, i.e. representative for the equivalent A2D range-bin. Mismatches would for instance occur in cases of strong vertical or horizontal wind shear on spatial scales comparable to the size of an A2D range-gate, usually 3000 m · 600 m. Conceivable circumstances could comprise measurements at the edge of jet-streams or zones of intense convection. Imagining an A2D range-bin of 600 m vertical extent probing a region of strong vertical wind shear that is covered by 2-µm winds only at the upper 200 m of its area, this would obviously introduce an error into the statistical comparison. Thus, the coverage ratio can be utilised as a measure of quality control, setting an empirically determined minimum threshold of 85 % throughout all comparisons presented in this thesis. Hence, every pair of A2D and 2-µm wind speeds, where valid 2-µm winds cover at least 85 % of the area of the respective A2D range-bin, is used in the statistical comparison. An example of coverage ratios resulting from the analysis of the flight section discussed in sec. 4.2 is provided in Fig. A.9.

Whereas the altitude of the provided 2-µm range-bins is given with respect to the geodetic coordinate system and the mean sea level is used as fixed height reference, the altitudes of the A2D range-bins are bound to the aircraft coordinate system. Consequently, the shift of the A2D grid (along with the aircraft flight altitude) with respect to the 2-µm grid is considered by using the mean aircraft altitude per 14 s observation time during the interpolation process. Depending on whether the 2-µm Lidar was operated in LOS or in VAD mode (subsec. 3.1.4), the 2-µm wind vectors must also be projected onto the A2D LOS before the comparison of the single component LOS winds. During three of the four sections selected for comparison here (Tab.4.1), the 2-µm Lidar was operated in scan mode. Thus, compared to the LOS winds of the A2D measured at a constant 20° slant angle, the 2-µm Lidar provided three dimensional wind vectors. These had to be projected onto the A2D LOS by firstly displaying all components in the same geodetic coordinate system making use of the aircraft attitude data and secondly by taking the vector product of the 2-µm wind vector ($\vec{v}_{2\mu\mathrm{m}}$) and the temporal mean of the A2D LOS unit vector ($\vec{v}_{\mathrm{A2D,LOS,u}}$):

$$v_{2\mu\mathrm{m,LOS}} = \vec{v}^{\,T}_{2\mu\mathrm{m}} \cdot \vec{v}_{\mathrm{A2D,LOS,u}} = \begin{pmatrix} v_{2\mu\mathrm{m,N}} \\ v_{2\mu\mathrm{m,E}} \\ v_{2\mu\mathrm{m,Z}} \end{pmatrix}^{T} \cdot \begin{pmatrix} v_{\mathrm{A2D,Nu}} \\ v_{\mathrm{A2D,Eu}} \\ v_{\mathrm{A2D,Zu}} \end{pmatrix} \tag{4.2}$$

with the subscripts N, E and Z referring to northerly, easterly and zenith direction, respectively. Significant vertical wind is often associated with regions of strong convection (e.g. tropics), severe weather or orographic characteristics. Thus, considering the conditions during the wind measurement on September 26^{th}, it is a reasonable assumption that the vertical wind speed is small compared to the horizontal one ($v_{2\mu\mathrm{m,Z}} = 0\,\mathrm{m/s}$). Similarly, based on this assumption, also Abreu et al. (1992) neglected the vertical wind speed for the wind retrieval from Doppler Lidar measurements performed in Michigan. Investigations of the vertical component of the 2-µm winds and their properties shown during this measurement period revealed a random distribution and justified the assumption above. This interpolation strategy could also be adapted during the ADM-Aeolus validation phase regarding satellite overpasses of well scheduled airplane trajectories.

4.1.2. Aerial interpolation of ECMWF winds onto the A2D grid

Based on its measurement technique and the frequency with which it is sensing the atmosphere, the 2-µm Lidar is not capable of extracting wind speed information from regions without aerosols, i.e. molecular backscatter only. This fact leaves behind a considerable number of A2D Rayleigh wind measurements that have not been compared to the 2-µm winds. To close this gap and enable a coarse assessment of the validity of A2D winds in aerosol free regions, wind fields of NWP models can be used. For this study the data was obtained from the ECMWF Integrated Forecast System (IFS) containing T799L91 products (799 points horizontally on 91 height levels with varying vertical resolution). Interpolation from the respective surrounding points of the resulting 0.25° grid onto the Falcon flight track yielded the wind speed to be compared to the A2D measurements. Unlike the 2-µm winds, ECMWF data is provided according to pressure levels and not to constant altitudes. Since also the A2D winds depends on the aircraft flight height (Fig. A.14), an adapted interpolation algorithm is necessary, taking into account two data fields both based on differently varying altitude. The ECMWF winds that are input to the aerial interpolation have already been subject to a preceding interpolation. The original ECMWF wind fields resulting from the analyses are provided on a grid scale of 0.25°, leading to approximate distances of 12 km in east-west and 28 km in north-south direction. From this coarse grid ECWMF wind speeds are interpolated onto the much finer grid of longitude and latitude values per second available from the Falcon flight data (subsec. 3.1.3). This results in A2D observations with an extent of 14 s now covered with ECWMF wind speeds on a second by second grid, Fig. 4.3 shows a simplified sketch of the A2D-ECMWF interpolation scheme. Each dot represents an ECWMF data point on the respective pressure level (dashed line). The density of the ECWMF model levels varies with altitude due to the link to pressure levels. It becomes obvious that an ordinary averaging just over the points contained in an A2D range-bin (bold frame) does not lead to a correct ECWMF wind representative for the A2D area and can introduce a systematic error by predominantly accounting for the impact of lower (denser) levels. Thus, paying attention to a balanced aerial contribution, the construction of artificial ECMWF range-bins is necessary. Therefore, the size of a single ECMWF range-bin is determined by four neighbouring points, defining the upper and lower borders as the mean altitudes (crosses) of each of two of these points, while the horizontal borders are fixed by the respective time. After allocating the mean wind speed value of the four corner points to the constructed ECMWF range-bin as well as computing the corresponding aerial contribution to the A2D area, the algorithm follows the structure as described for the A2D - 2-µm comparison above.

A case which has not been considered yet by the current algorithm is an A2D range-bin fully comprised by only two ECMWF model levels. By allocating a mean value of all respective upper and lower ECMWF points, disregarding a potential shift of the A2D range-bin towards one of the two ECWMF levels, a systematic error would be induced. For a vertical A2D range-gate thickness of 600 m this can become relevant only far above 10 km altitude, hence, does not affect the present evaluation. Note that for wind measurement cases where A2D range-gates of 300 m vertical thickness are commanded, the effect can occur already above 3 km. A quality control using the coverage criterion, as for the comparison against 2-µm winds above, is applied here, too. Since ECMWF analyses do not exhibit data gaps as for the 2-µm Lidar, this control only affects the boundaries of the whole measurement section, where either ground topography or simply a too short comparison range selected by the user might influence the availability of ECMWF winds. A third and very similar aerial interpolation algorithm was developed also for 2-µm and ECMWF data so as to enable a comparison of horizontal wind speeds and wind directions.

4.1.3. Accuracy of A2D wind measurements

In order to obtain more information about the accuracy and characteristics of A2D wind measurements, a statistical comparison is performed in which the 2-µm Lidar is taken as the truth, due to its proven small bias and random error (subsec. 3.1.4 and Weissmann et al. (2005)). As illustrated in subsec. 4.1.1 the aerial interpolation algorithm was used to match the 2-µm grid temporally and spatially with the A2D grid. Defining the mean values $\overline{v}_{2\mu\mathrm{m}}$ and $\overline{v}_{\mathrm{A2D}}$ for the n therefrom resulting 2-µm and A2D wind speeds $v_{2\mu\mathrm{m,i}}$ and $v_{\mathrm{A2D,i}}$, respectively:

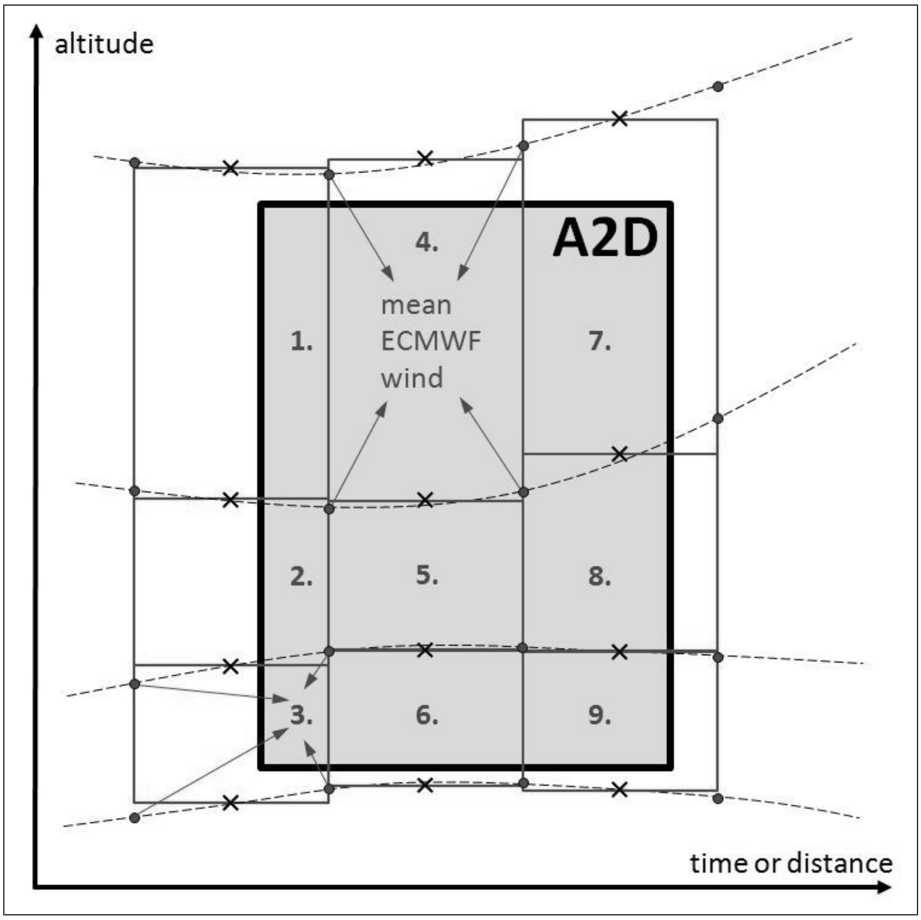

Figure 4.3.: Simplified sketch of the A2D - ECMWF interpolation scheme: Artificial ECMWF range-bins (thin frames) are constructed and wind speeds allocated from four neighbouring ECMWF data points (dots) each using the mean altitude of the respective two points belonging to different ECWMF levels (dashed lines) as the upper and lower range-bin border (cross). In order to obtain an ECMWF wind speed representative for the A2D area (bold frame) an aerial weighting over all numbered contributions is performed.

$$\overline{v}_{2\mu\mathrm{m}} = \frac{1}{n}\sum_{i=1}^{n} v_{2\mu\mathrm{m,i}} \tag{4.3a}$$

$$\overline{v}_{\mathrm{A2D}} = \frac{1}{n}\sum_{i=1}^{n} v_{\mathrm{A2D,i}} \tag{4.3b}$$

allows the calculation of the systematic error (or bias) μ. The standard deviation σ is chosen as a measure to characterise the variability of the differences between single A2D and 2-µm measurements around their corresponding mean value. The linear correlation coefficient r describes the strength and direction of the linear relationship between the wind measurements of the two Lidar systems.

$$\mu = \frac{1}{n}\sum_{i=1}^{n}(v_{\mathrm{A2D,i}} - v_{2\mu\mathrm{m,i}}) \qquad = \overline{v}_{\mathrm{A2D}} - \overline{v}_{2\mu\mathrm{m}} \tag{4.4a}$$

$$\sigma = \sqrt{\frac{1}{n-1}\sum_{i=1}^{n}\left[(v_{\mathrm{A2D,i}} - v_{2\mu\mathrm{m,i}}) - \frac{1}{n}\sum_{i=1}^{n}(v_{\mathrm{A2D,i}} - v_{2\mu\mathrm{m,i}})\right]^2} \qquad = \sqrt{\frac{1}{n-1}\sum_{i=1}^{n}(\Delta v_{\mathrm{i}} - \mu)^2} \tag{4.4b}$$

$$r = \frac{\sum_{i=1}^{n}(v_{2\mu\mathrm{m,i}} - \overline{v}_{2\mu\mathrm{m}})\cdot(v_{\mathrm{A2D,i}} - \overline{v}_{\mathrm{A2D}})}{\sqrt{\sum_{i=1}^{n}(v_{2\mu\mathrm{m,i}} - \overline{v}_{2\mu\mathrm{m}})^2}\sqrt{\sum_{i=1}^{n}(v_{\mathrm{A2D,i}} - \overline{v}_{\mathrm{A2D}})^2}} \qquad = \frac{\sigma_{2\mu\mathrm{m,A2D}}}{\sigma_{2\mu\mathrm{m}}\cdot\sigma_{\mathrm{A2D}}} \tag{4.4c}$$

The correlation coefficient is thus the ratio of the cross correlation $\sigma_{2\mu\mathrm{m,A2D}}$ to the product of $\sigma_{2\mu\mathrm{m}}$ and σ_{A2D}, which are the standard deviations of the 2-µm and A2D winds, respectively. The two possible extreme values for r are $r = 0$, where the 2-µm and A2D wind measurements would be completely uncorrelated and $r = 1$ indicating perfect correlation with all points located on a straight line. The case of a negative r would point to an oppositional definition of the wind speed direction of the two Lidar systems. $r = 1$ does not mean that the A2D is measuring exactly the same wind speed as the 2-µm Lidar but the relation could also be following any straight line definition involving a simple additional scaling factor and offset. It is reasonable to expect a linear dependence between A2D and 2-µm winds and consequentially to look for an optimal straight fitting line. Therefore, a least squares procedure is applied to the data to determine mainly the unknown slope of the fitting line which will serve as an estimate for the wind speed dependent error of the A2D measurements. Although they inherently are supposed to have the same meaning, it is distinguished here between the terms *sensitivity* and *offset*, (mainly) used with respect to the calibration (sec. 3.4), and *slope* and *intercept* for the parameters obtained from the linear fits in the statistical comparisons of the current chapter. This is in order to avoid ambiguities within the framework of this thesis. Referring to the Chi-Square Fitting in Press et al. (1992), we can consider each wind speed contributing to the overall cost χ^2 with the squared value of its (vertical) deviation $\Delta v_{\mathrm{A2D,i}}$ from the assumed straight line. Therefore, we assume the 2-µm winds as perfect measurements free of errors and assign the same uncertainty to every single A2D wind for the time being.

$$\chi^2 = \sum_{i}^{n}(\Delta v_{\mathrm{A2D,i}})^2 = \sum_{i}^{n}(v_{\mathrm{A2D,i}} - a - b\cdot v_{2\mu\mathrm{m,i}})^2 \tag{4.5}$$

Here χ^2 is a measure of the fit quality, a is the intercept and b the slope of the straight line equation. The best fit is considered the one which minimises this sum of squared deviations. Local extrema of a function can be determined via its first derivative:

$$\frac{\delta\chi^2}{\delta a} = -2\sum_i^n \left(v_{\mathrm{A2D,i}} - a - b \cdot v_{2\mu\mathrm{m,i}}\right) \tag{4.6a}$$

$$\frac{\delta\chi^2}{\delta b} = -2\sum_i^n \left(v_{\mathrm{A2D,i}} - a - b \cdot v_{2\mu\mathrm{m,i}}\right) \cdot v_{2\mu\mathrm{m,i}} \tag{4.6b}$$

A second derivative is not necessary since only one minimum is expected for this quadratic function. In order to fulfil the requirement for a minimum, both expressions on the right hand side must be equal to zero, which yields:

$$0 = \sum_i^n v_{\mathrm{A2D,i}} \qquad - a \cdot n \qquad - b\sum_i^n v_{2\mu\mathrm{m,i}} \tag{4.7a}$$

$$0 = \sum_i^n v_{\mathrm{A2D,i}} \cdot v_{2\mu\mathrm{m,i}} \qquad - a\sum_i^n v_{2\mu\mathrm{m,i}} \qquad - b\sum_i^n v_{2\mu\mathrm{m,i}}^2 \tag{4.7b}$$

This set of equations can then be solved for the two unknowns to:

$$a = \frac{\sum_i^n v_{2\mu\mathrm{m,i}}^2 \sum_i^n v_{\mathrm{A2D,i}} - \sum_i^n v_{2\mu\mathrm{m,i}} \sum_i^n v_{2\mu\mathrm{m,i}} \cdot v_{\mathrm{A2D,i}}}{n\sum_i^n v_{2\mu\mathrm{m,i}}^2 - \left(\sum_i^n v_{2\mu\mathrm{m,i}}\right)^2} \tag{4.8a}$$

$$b = \frac{n\sum_i^n v_{2\mu\mathrm{m,i}} \cdot v_{\mathrm{A2D,i}} - \sum_i^n v_{2\mu\mathrm{m,i}} \sum_i^n v_{\mathrm{A2D,i}}}{n\sum_i^n v_{2\mu\mathrm{m,i}}^2 - \left(\sum_i^n v_{2\mu\mathrm{m,i}}\right)^2} \tag{4.8b}$$

The parameters, such as systematic difference (bias), standard deviation and slope especially in terms of linear fits, are commonly used for statistical comparison. Examples can be found, for instance, in Chintawongvanich et al. (1989) whose study showed very good agreements of wind velocity and wind direction measured by Lidar, acoustic Doppler sodar and a tower instrumented with anemometers. Similar assessments have been performed in Reitebuch et al. (2001) where comparisons to radiosonde, wind profiler and NWP model revealed an excellent capability of the 10-µm WIND (Wind Infrared Doppler lidar) Lidar system in measuring whole wind profiles.

So far all wind measurements are considered as equally valuable. As a refined version a weighted fit is implemented. By reproducing the calculations for Eq. 4.5 to Eq. 4.8 including weights w_i for each wind measurement according to:

$$\chi^2_\mathrm{w} = \sum_i^n \left[\Delta v^2_\mathrm{A2D,i} \cdot w_\mathrm{i}\right] = \sum_i^n \left[\left(v_\mathrm{A2D,i} - a - b \cdot v_{2\mu\mathrm{m,i}}\right)^2 \cdot w_\mathrm{i}\right] \tag{4.9}$$

we get the following solutions:

$$a_\mathrm{w} = \frac{\sum_i^n w_\mathrm{i} \cdot v^2_{2\mu\mathrm{m,i}} \sum_i^n w_\mathrm{i} \cdot v_\mathrm{A2D,i} - \sum_i^n w_\mathrm{i} \cdot v_{2\mu\mathrm{m,i}} \sum_i^n w_\mathrm{i} \cdot v_{2\mu\mathrm{m,i}} \cdot v_\mathrm{A2D,i}}{\sum_i^n w_\mathrm{i} \sum_i^n w_\mathrm{i} \cdot v^2_{2\mu\mathrm{m,i}} - \left(\sum_i^n w_\mathrm{i} \cdot v_{2\mu\mathrm{m,i}}\right)^2} \tag{4.10a}$$

$$b_\mathrm{w} = \frac{\sum_i^n w_\mathrm{i} \sum_i^n w_\mathrm{i} \cdot v_{2\mu\mathrm{m,i}} \cdot v_\mathrm{A2D,i} - \sum_i^n w_\mathrm{i} \cdot v_{2\mu\mathrm{m,i}} \sum_i^n w_\mathrm{i} \cdot v_\mathrm{A2D,i}}{\sum_i^n w_\mathrm{i} \sum_i^n w_\mathrm{i} \cdot v^2_{2\mu\mathrm{m,i}} - \left(\sum_i^n w_\mathrm{i} \cdot v_{2\mu\mathrm{m,i}}\right)^2} \tag{4.10b}$$

with a_w and b_w being the slope and intercept of the weighted linear fit through the available data points.

The weights w_i can be defined differently, depending on the user's intention on how strong the individual deviations are to be penalised. However, it is very common to weight each measurement by the inverse of its standard deviation, if available, which means: the better the accuracy of a measurement the higher its influence onto the fit. This procedure has, for instance, been applied by Abreu et al. (1992) for smoothing wind measurement data in time and altitude by fitting a 3rd-degree polynomial. In the present study A2D winds are compared on observation level, which allows the derivation of quality criteria from the measurement level as described in sec. 3.6. These quality criteria are combined and used to form individual weights for the Rayleigh channel (Eq. 4.11a), which include the influence of DCO validity with P_valid as the fraction of valid measurements within the current observation and $r_\mathrm{cvg,i}$ as the coverage ratio discussed in sec. 4.1. $\sigma_\mathrm{i}(I_\mathrm{m})$ and $\mu_\mathrm{i}(I_\mathrm{m})$ are the standard deviation respectively the mean of the signal intensities of the valid measurements (index m) per range-gate. The standard deviation is scaled with the mean value in order to reflect the range dependence of the detected intensity and not to broadly underestimate measurements at distances closer to the instrument, i.e. at higher altitudes. An example for weights as they were used for the analysis of a wind measurement section on September 26th is given in Fig. 4.8, showing only the contribution of the part that is derived from the intensity variations.

$$w_{\mathrm{i,Ray}} = \left(\frac{\sigma_{\mathrm{i}}(I_{\mathrm{m}})}{\mu_{\mathrm{i}}(I_{\mathrm{m}})}\right)^{-1} \cdot P_{\mathrm{valid,i}} \cdot r_{\mathrm{cvg,i}} \tag{4.11a}$$

$$w_{\mathrm{i,Mie}} = \sqrt{SNR} \cdot P_{\mathrm{valid,i}} \cdot r_{\mathrm{cvg,i}} \tag{4.11b}$$

Unlike for the Rayleigh channel, this quality criterion is not applicable for the Mie channel due to the influence of the strongly varying intensity of the Rayleigh background (telescope image). Nevertheless, the fraction of valid measurements and the coverage ratio can still be applied for the Mie channel. Additionally, also the SNR (Fig. 3.31) constitutes a very practical criterion which is used here in the definition for a respective weight (Eq. 4.11b).

Based on Eq. 4.5 the parameters slope (b or b_{w}) and intercept (a or a_{w}) for a linear fit were derived allowing variation only for A2D winds and assuming 2-µm winds as perfectly measured. A more sophisticated version is the allocation of errors in both (index B) coordinates leading to the χ^2 merit function as in Eq. 4.12. Whereas a_{B} and b_{B} are again the intercept and slope, $\sigma_{\mathrm{A2D,i}}$ and $\sigma_{2\mu\mathrm{m,i}}$ stand for the standard deviations for the i$^{\mathrm{th}}$ point referring to the A2D and 2-µm Lidar. Eq. 4.12 has to be minimized with respect to a_{B} and b_{B}, which is complicated by the occurrence of b_{B} in the denominator causing the first derivative of χ^2 with respect to b_{B} (compare to Eq. 4.6b) to become a non-linear equation.

$$\chi^2(a_{\mathrm{B}},b_{\mathrm{B}}) = \sum_{i}^{n} \frac{(v_{\mathrm{A2D,i}} - a_{\mathrm{B}} - b_{\mathrm{B}} \cdot x_{\mathrm{i}})^2}{\sigma^2_{\mathrm{A2D,i}} + b^2_{\mathrm{B}} \cdot \sigma^2_{2\mu\mathrm{m,i}}} \tag{4.12}$$

The resulting extensive procedure including an iterative approach is adapted from Press et al. (1992).

4.2. Case study for observations during a high altitude jet

Three wind measurement periods have been selected from the airborne campaign and are analysed in the chapters below in order to illustrate the successful implementation of the developed retrieval algorithms and to validate both the A2D instrument and the measurement and calibration procedure by:

- taking into account both calibrations (sec. 3.4)
- including frequency correction (subsec. 3.4.6)
- correcting the non-linearity (subsec. 3.4.4)
- applying Mie and Rayleigh quality control (sec. 3.6)
- proving the ability of A2D to measure wind
  - over a longer period of time
  - under conditions of strong wind shear
  - over a large wind speed range
  - under varying aerosol loads
  - below optically thin clouds
  - in complex broken cloud conditions
  - with small random and systematic errors
- applying a Ground Cloud Atmosphere mask (sec. 3.2)
- validating of the principle of Zero Wind Correction (subsec. 3.5.3)

An overview of dates, times and aircraft data of the selected periods used for the processing of the A2D winds is given in Tab. 4.1. As mentioned in subsec. 3.4.5 mean altitudes as well as the mean off-nadir angles were used for processing the A2D winds of the selected flight sections. For the retrieval of wind speeds from the A2D Mie channel, telescope images from dedicated MOUSR procedures close in time to the wind measurements and consistent with the commanded range-gate resolution were applied for correction.

Table 4.1.: Overview of three flights comprising four selected wind measurement periods. All times in UTC.

date	2009/09/26	2009/09/29		2009/10/01
flight time	10:43 - 13:52	10:57 - 14:55		09:24 - 12:50
takeoff location	Keflavik	Keflavik		Keflavik
landing location	Kangerlussuaq	Keflavik		Oberpfaffenhofen
measurement time	11:50 - 12:19	13:09 - 13:27	13:33 - 13:49	09:35 - 10:40
mean altitude / m	10432	8091		10307
altitude range / m	10360 - 10530	8050 - 8135		10235 - 10460
off-nadir angle / °	20.28	20.12		20.04
MOUSR time	11:34 - 11:40	13:28 - 13:32		10:40 - 10:45
2-µm operation	scan mode	scan mode	LOS mode	scan mode

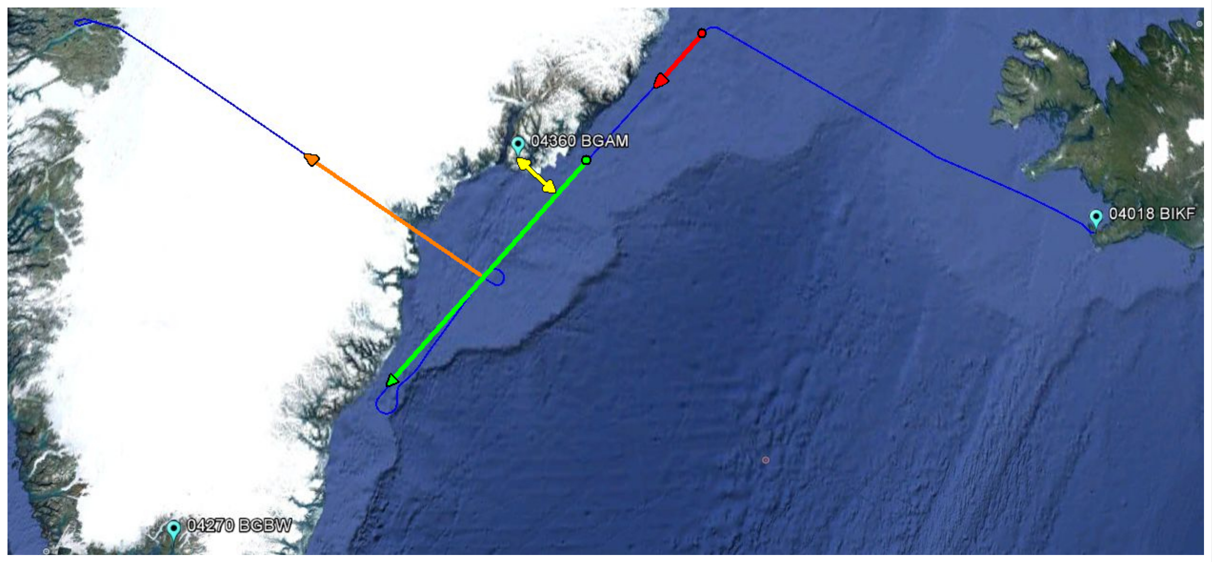

Figure 4.4.: Flight track of 2009/09/26 (blue) starting in Keflavik, Iceland (right) and ending in Kangerlussuaq, Greenland (left). Wind measurements (green, orange) and MOUSR (red) section are indicated along with the flight direction (arrows). Shortest distance to radiosonde station 04360 BGAM is 74 km (yellow). Google Earth was used to display this information.

The flight on 2009/09/26 took place between 10:43 (takeoff) - 13:52 UTC (landing). Fig. 4.4 shows the flight track starting in Keflavik, Iceland and ending in Kangerlussuaq, Greenland (left). Two major wind measurement sections were identified that overlap with 2-µm measurements and provide reasonable amounts of valid winds for a statistical comparison. The second section (orange) between 12:43 - 13:10 UTC was analysed with respect to ground and cloud return in sec. 3.2. The longer wind measurement section (green) between 11:50 - 12:29 UTC along the east coast of Greenland will be analysed in the following. Two MOUSR (subsec. 3.4.6) measurements were performed during that flight under which only the indicated one (red) between 11:34 - 11:40 UTC matches the range-gate setting of this wind measurement period and is of acceptable quality. Also indicated are the locations of three radiosonde stations on southern and eastern Greenland as well as on Iceland. During the first wind measurement section the shortest distance to the station 04360 BGAM (WMO code), which is used here for comparisons of wind speed and wind direction, was 74 km (yellow). An evaluation of this wind measurement period not yet including corrections, such as compensation for non-linearity or WM frequencies, can be found in Marksteiner et al. (2011).

4.2.1. Meteorological situation

In order to improve the interpretation of the A2D and 2-µm wind measurement results, a discussion of the meteorological situation is helpful. Fig. 4.5a shows a view on the North-Atlantic region recorded on 2009/09/26 at 13:22 UTC in the near infrared between 1628 – 1652 nm by the MODIS instrument on the NASA (National Aeronautics and Space Administration) satellite

Terra (Günther et al. (2002), King et al. (2003)).This frequency range is advantageous for the discrimination between snow and clouds. It reveals broken low level cloud cover reaching from the south-west of Iceland (65°N, 20°W) to the southern tip of Greenland. But also a band of high level clouds is present between 62°N and 38°-43°W which is almost at the end of the A2D measurements (green line). A smaller cloudy region formed at the coast of Greenland nearby the first part of the A2D measurement period (65°N, 39°W). From this region a narrow part extends to the flight track in westerly direction. The impact of both cloudy regions will be visible in the wind measurement results below (subsec. 4.2.2).

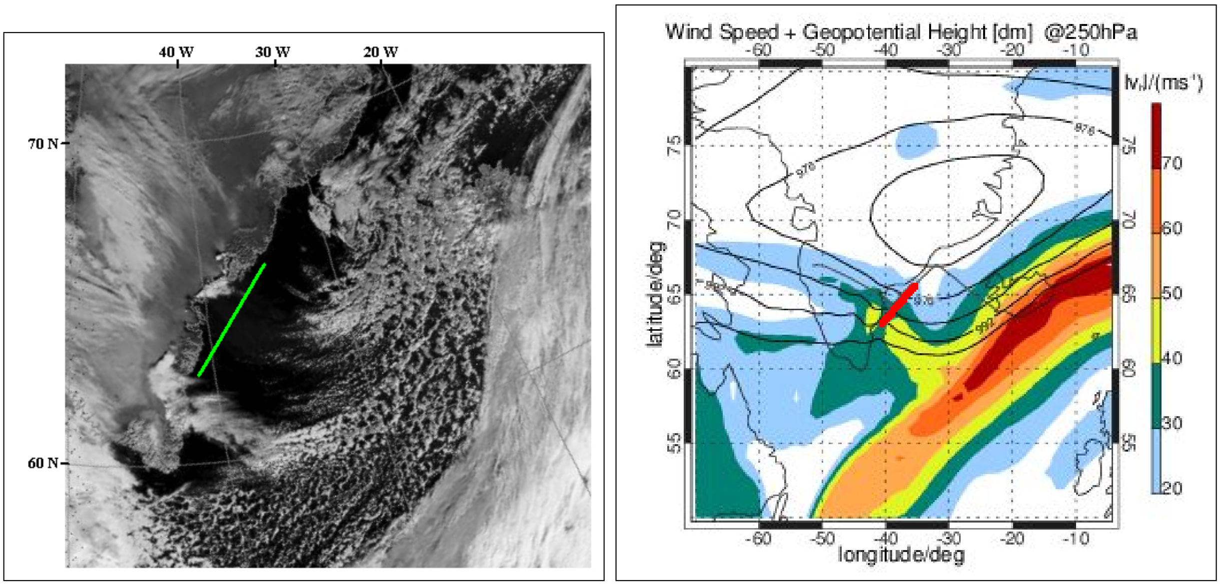

(a) *(b)*

Figure 4.5.: (a) MODIS image from the IR channel of the North Atlantic region on 2009/09/26. Snow and clouds appearing in dark grey and light grey to white, respectively. Greenland and Iceland are visible on the left and upper right side, respectively. The A2D wind measurement section is indicated as a green line along the coast of Greenland. The measurements took place in an almost cloud free (black) area. (MODIS image adapted from NERC Satellite Receiving Station, Dundee University, Scotland, `http://www.sat.dundee.ac.uk`) / (b) Horizontal wind speed (colour coded) from an ECMWF analysis for 12:00 UTC at pressure level 250 hPa (≈ 10.5 km = Falcon flight height). Greenland is covered by a low pressure area with geopotential height indicated as black isolines. The whole flight track from Keflavik to Kangerlussuaq is plotted as a blue line. The wind measurement section is indicated on top in red, next to the coast line of Greenland.

Fig. 4.5b presents horizontal wind speeds taken from an ECMWF analysis for 2009/09/26 at 12:00 UTC for a 250 hPa pressure level (≈ 10.5 km). The A2D wind measurement section is indicated as a red line crossing regions of 20 m/s at the beginning and around 40 m/s towards the end. The regions of high horizontal wind speed correlate with the existence of the Southern Greenland tip jet (Doyle and Shapiro (1999)). The intersection of the flight track and the lines of the same geopotential height agrees with the fact that the Falcon was also flying at a constant pressure level, thereby increasing flight altitude from 10360 - 10530 m (Tab. 4.1). Combining the information of Fig. 4.5b & 4.5a one notices that the low pressure system with its centre located at 70°N and 30°W is causing the formation of low level broken clouds in its southern region (around 63° and 35°W), shuffling them towards Iceland by its anti-clockwise turning. Also the location of the jet-stream and the intensity of the wind speed within the jet-stream seem to be associated with the low pressure system. Being aligned along the front of the steepest pressure gradient the wind direction is almost perpendicular to the Falcon flight path and thus advantageous for A2D wind measurements.

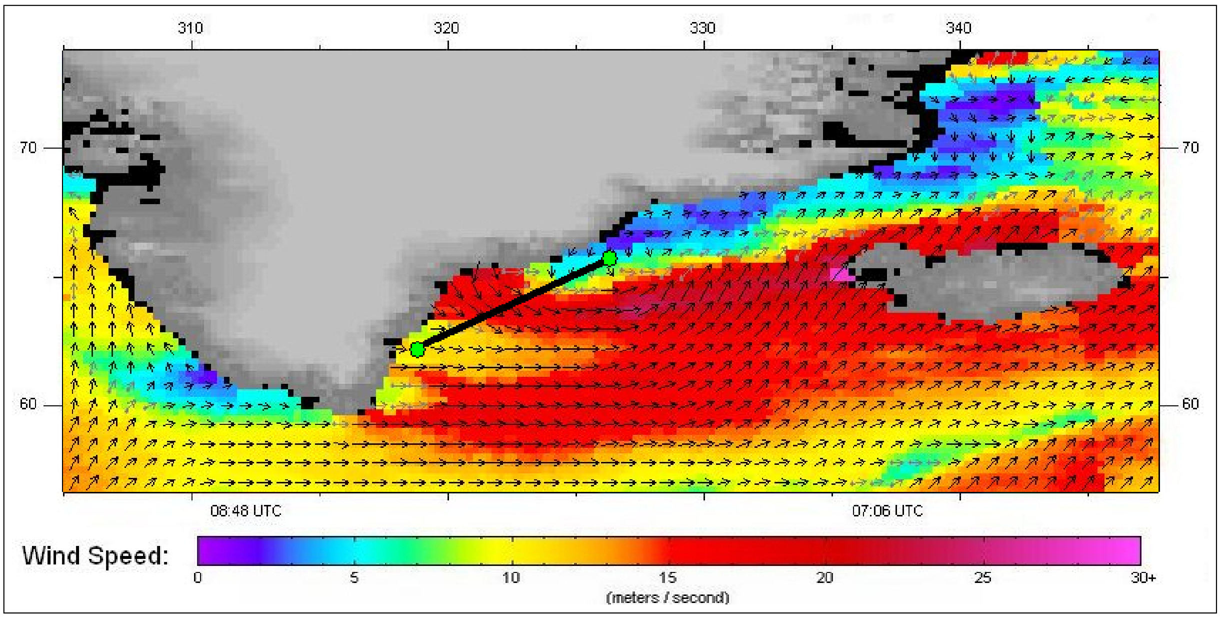

Figure 4.6.: Wind direction (arrows) and wind speed (arrow length) at 10 m above sea level measured over the North Atlantic on 2009/09/26 by the scatterometer QuikSCAT for morning passes around 07:00 UTC. Greenland on the top left and Iceland on the right side are shown in grey colours according to terrain elevation whereas the black colour symbolises areas with no data. The A2D wind measurement section is indicated by black a line with start and end marked by green dots. Wind speeds in the whole region occur from 0 m/s (violet) up to 30 m/s (pink). Figure adapted from Remote Sensing Systems (`http://www.remss.com/qscat/qscat_description.html`).

An overview of the wind situation at sea level with measurements from NASA's earth observation satellite QuikSCAT is shown in Fig. 4.6. The QuikSCAT satellite (Hoffman and Leidner (2005)) constitutes a scatterometer operating at microwave frequencies (approx. 14 GHz) and providing wind speed and wind direction right above the sea surface by making use of a relation to backscattered intensity, intensity distribution and sea surface roughness. The wind directions and speeds presented were measured during the morning passes over the North Atlantic on 2009/09/26 around 07:00 UTC, i.e. approximately five hours before the A2D wind measurement. A striking feature around 320°E and 65°N is the strong and aligned wind region of 15 - 20 m/s related to a katabatic wind (Heinemann and Klein (2002)). This katabatic wind originates from air masses cooled atop the Greenland ice shield. Due to its higher density in combination with the slope of the terrain, the air flows down to the sea surface. On the Greenland ice shield higher terrain elevations towards north and south create a valley which constitutes an orographic characteristic that accelerates the wind on its downward way due to a generated drainage effect. The katabatic wind is blowing almost perpendicularly into the LOS direction of the A2D in the middle of the wind measurement section. Fortunately the QuikScat data could be used for interpretation since QuikSCAT stopped recording data on 2009/11/23, three weeks after the airborne campaign.

4.2.2. A2D wind observations

Fig. 4.7 shows the A2D and 2-µm wind measurement on 2009/09/26 between 11:50 - 12:19 UTC along the east coast of Greenland, comprising 97 A2D and 55 2-µm observations. The LOS wind fields are displayed in an altitude range from 300 m up to 9.4 km and a horizontal extent of 368 km corresponding to 29 minutes flight of the Falcon with a mean ground speed of 210 m/s. The A2D grid has been vertically interpolated from the irregular A2D grid onto a grid of 100 m, matching the resolution of the 2-µm data. For the region presented in Fig. 4.7 the original A2D grid consisted of range-gates with a vertical thickness of ≈ 600 m. With the Falcon at a mean flight altitude of 10.4 km, the ground/sea surface return was constantly and completely (no ACCD range-gate overlap) detected in range-gate #22 which was proven by a comparison to the DEM model. Because the sea surface return in range-gate #22 affects the results of the interpolation of the A2D grid onto the 100 m vertical resolution, the LOS wind fields are not shown below 300 m. Also due to the influence of the A2D telescope overlap function mainly above 9.4 km, wind measurements in these regions are assumed to be invalid.

When comparing the A2D Mie winds and the 2-µm winds, obvious similarities in wind field pattern and characteristics are visible, which are based on the fact that both are targeting aerosol backscatter. High altitude measurements range down to 7 km at the beginning and 5 km towards the end, while low altitude measurements range from the sea surface partly up to about 2 km. White areas in between mark invalid wind measurements due to low SNR, i.e. low aerosol content and hence low particle backscatter. In cases of clean atmosphere solely the Rayleigh channel, with its sensitivity to molecular backscatter, is able to close this gap and provide valid full vertical wind profiles. For all three wind measurements strong winds with up to 24 m/s LOS velocity are indicating a part of the jet-stream on the upper right region between 6 km - 10 km and from 12:05 to 12:19. The wind zone between 12:00 and 12:15 reaching from the sea surface up to 2 km exhibits LOS wind speeds of up to 12 m/s being related to the katabatic flow (Fig. 4.6) streaming down from the Greenland ice shield. Generally, changes in the magnitude of the measured LOS winds in Fig. 4.7 can not only be attributed to the magnitude of the horizontal wind speed, but also to an azimuthal turning of the wind direction with altitude. As the horizontal projection of the A2D LOS is almost aligned with the direction of the katabatic flow, the HLOS winds can be estimated to about $(12\,\mathrm{m/s}) / (\sin 20°) = 35\,\mathrm{m/s}$. This velocity is higher compared to the about ≈ 20 m/s measured by the QuikScat instrument (Fig. 4.6). However, it is known that QuikScat is underestimating higher wind speeds. Furthermore, another fact might contribute to the observed difference, i.e. wind speeds from QuikScat are

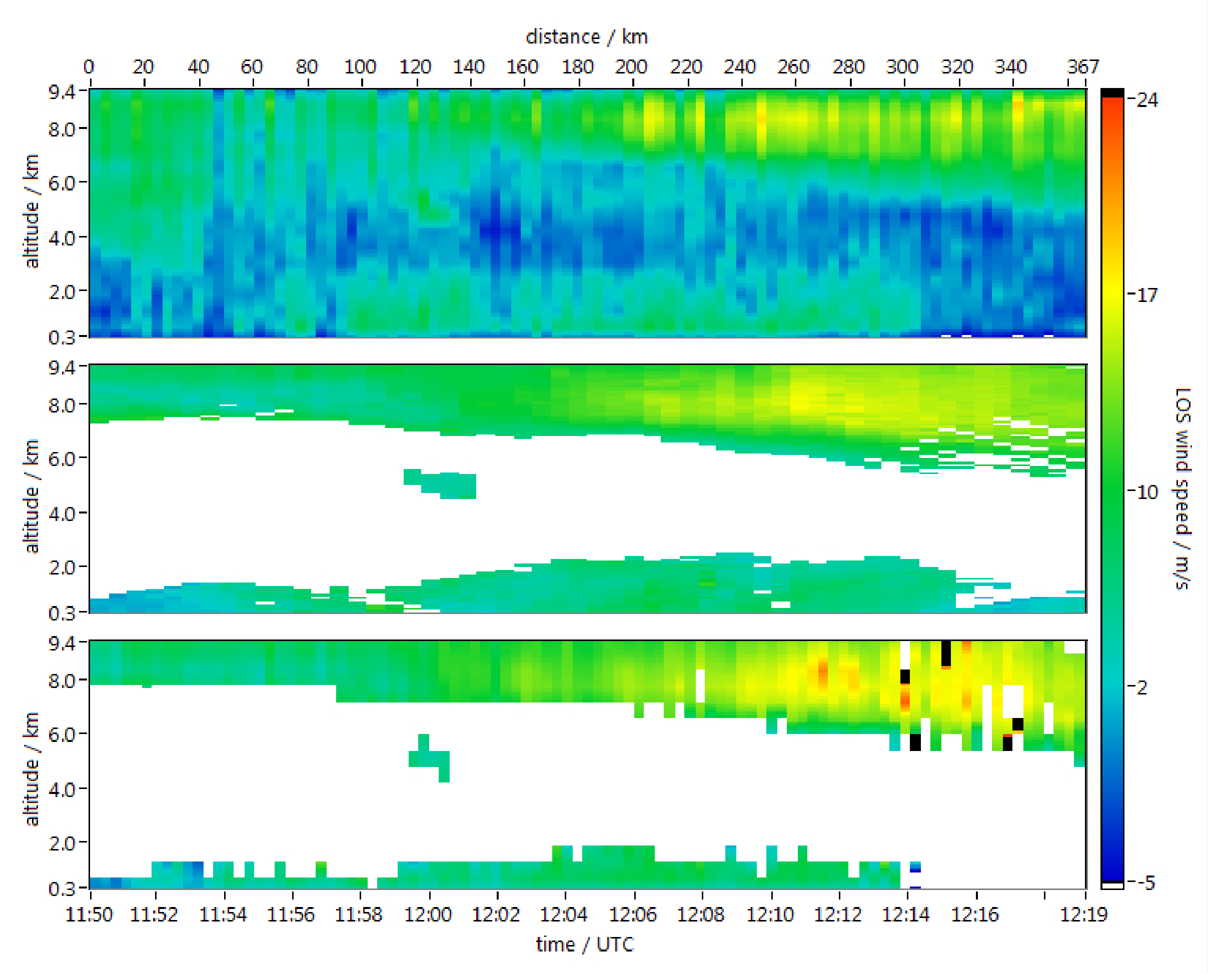

Figure 4.7.: LOS wind speed as measured on 2009/09/26 between 11:50 - 12:19 UTC from A2D Rayleigh channel (top), A2D Mie channel (bottom) and 2-µm Lidar (middle). A2D winds are interpolated onto a 100 m vertical grid. Valid Mie and 2-µm winds are present between 2 km to ground and 6 km - 10 km. White colour and black bins represent invalid winds due to low aerosol signal. Measured LOS wind speed ranges from minimum -5 m/s to maximum 24 m/s.

obtained from an extrapolation to a height of 10 m above sea level compared to A2D winds which are here determined at a higher altitude of about 300 m and from an integration over a range-gate of up to several hundred meters vertical thickness. Additionally, QuikScat data is only available for the morning (≈ 07:00 UTC) and the evening pass (≈ 22:40 UTC) of the satellite, which can not exclude possible transitional phases of the wind field with stronger wind during the day. The fact that valid signal from particle backscatter is present up to 2 km can rather be explained by the katabatic wind carrying ice crystals and snow from Greenland, instead of assuming a dispersion of marine aerosols, which usually does not reach further up than a few 100 m. The small region measurements around 12:00 UTC at about 5 km, which shows valid winds also for the Mie channel and the 2-µm Lidar, corresponds to the cloud mentioned above along with Fig. 4.5a. This stationary cloud can be considered as an orographic phenomenon induced by the katabatic flow. Regarding the length of the total A2D measurement period of 367 km, it would comprise 3 to 4 observations by the ADM-Aeolus satellite of 100 km each. Considering the whole region from right below the aircraft down to the sea surface as potential measurement volume, the 2-µm Lidar delivered 2630 valid winds out of 5720 maximum possible, which corresponds to a relative fraction of about 46 %. This is higher than the average of about 36 % derived by Weissmann et al. (2005) during nine days of the A-TReC campaign over the North Atlantic in 2003 and makes the period on the 2009/09/26 a very valuable case for a comparison to A2D wind measurements.

4.2.3. Statistical comparison

Applying the equations derived in subsec. 4.1.3 for comparisons of wind fields obtained from the A2D, the 2-µm Lidar and NWP yield results presented in this section. Appropriate weights for the Mie (Fig. 3.31, Eq. 4.11b) and Rayleigh channel were deduced. Fig. 4.8 shows the weights for the Rayleigh channel calculated from Eq. 4.11a. Except from a few single range-bins and the whole 59th observation, for whose discrepancy no explanation could be found, values vary between 5 and 10, hence, underlining the qualitatively rather homogeneous measurements during this flight section.

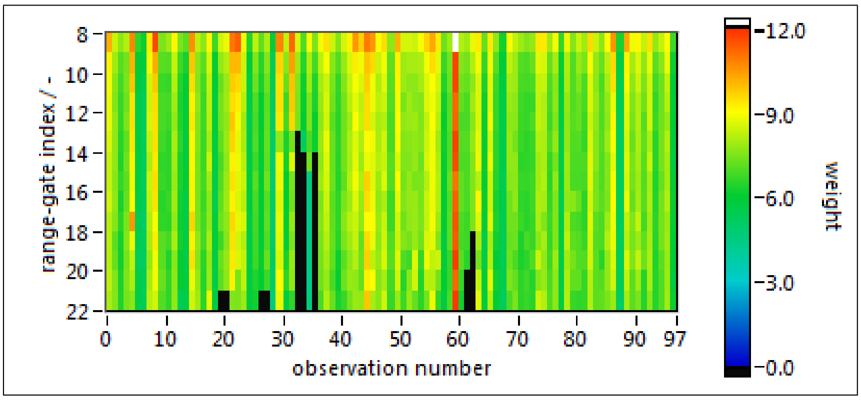

Figure 4.8.: Weights for the A2D Rayleigh wind measurements on 2009/09/26 from 11:50 - 12:19 UTC calculated from Eq. 4.11a and shown from range-gate #8 to #21. Values vary roughly between 5 and 10 with maxima up to 12. Black colour indicates measurements that were identified as being located under optically thick clouds or aerosol layers and were excluded from the comparison.

As mentioned in sec. 3.6 the Rayleigh wind measurements below clouds are excluded from the statistical comparison. A cloud mask has been derived as explained in sec. 3.2 and applied to the present case, thereby excluding the measurements now marked in black (Fig. 4.8). The intensity threshold for the cloud recognition was set relatively low, making the algorithm very sensitive and resulting in the exclusion not only of the area below the stationary cloud (around observation 35), but also below some stronger aerosol layers (e.g. observation 61 and 62).

Rayleigh channel and 2-µm Lidar

Tab. 4.2 contains the results of the statistical comparison for different versions of the Rayleigh wind retrieval evolving from a basic case towards the latest retrieval including all types of corrections presented throughout this thesis. The quantities given are the slope (Eq. 4.4) and the slope error with respect to the ideal slope of 1.0 together with the intercept for the complete definition of the linear fit line. In contrast to the mean (Eq. 4.4), the median is the more robust estimator for the central value and a considerable difference of both could in our case indicate the existence of outliers. But for the results presented in Tab. 4.2 the difference can be attributed to the fragmentation of the wind field by the occurrence of the jet-stream.

Apart from the standard deviation also the correlation coefficient (Eq. 4.4) and the number of compared winds change by application of the various corrections and quality controls. The seven cases of Tab. 4.2 are defined as follows:

- a) basic case: ± 500 MHz calibration interval, LOSV correction
- b) as a) but range-gates #5 & #6 excluded from comparison
- c) as b) but all measurements with DCO out of range are excluded from wind retrieval
- d) as c) but frequencies measured by wavemeter instead of commanded frequencies used
- e) as d) but calibration interval ± 850 MHz and non-linearity correction applied
- f) as e) but all measurements from below clouds are excluded from comparison
- g) as f) but weighting of measurements via quality criteria
- h) as f) but different errors assumed for A2D and 2-µm winds in linear fit procedure
- i) as f) but processed with 1st calibration (Fig. A.10)

The basic case a) corresponds to a wind retrieval using a calibration interval of ± 500 MHz (as ADM-Aeolus) followed by a correction of the LOS velocity induced by the relative movement of the platform. The calibration response curve is assumed to be linear and no non-linearity correction took place. While the slope (Eq. 4.8) of 0.93 deviates by about 7 % from the ideal value of 1.0, also the bias of -1.5 m/s and the standard deviation of more than 3.1 m/s in LOS direction are higher than the requirements for the ADM-Aeolus mission. The correlation coefficient of 0.74 supports the assumption of a linear relation between A2D and 2-µm wind measurements. A fact that will certainly contribute to the observed systematic and random error is the procedure of extrapolation involved in the creation of sensitivity and offset profiles (subsec. 3.4.3) or the coefficients of the non-linear fit (subsec. 3.4.4) from the calibrations. However, the influence is not considered very significant since the sensitivity and offset profiles show a "saturation effect" yielding more similar values with increasing distance from the instrument and, thus, the values from the lowest available range-gates should in good approximation be valid for the missing range-gates. Except for case g) which refers to Eq. 4.10 and 4.11a and case h) which uses the theory derived from Eq. 4.12, the statistical values are calculated from Eq. 4.8 to 4.4.

Table 4.2.: Overview of the evolution of results of the statistical comparisons of A2D Rayleigh winds and 2-µm winds for the 2009/09/26 between 11:50 - 12:19. Rayleigh winds calculated with 2nd calibration (except case i)) and removal of various error sources step by step. Cases: a) basic, b) two range gates excluded, c) corrupted measurements considered, d) wavelength meter frequencies used, e) extended frequency interval, f) cloud masked, g) weighting via quality criteria, h) different errors for A2D and 2-µm , i) 2ndcalibration used.

	a)	b)	c)	d)	e)	f)	g)	h)	i)
slope	0.93	0.99	1.00	1.01	0.96	0.97	0.96	1.05	1.18
slope error / %	-7	-1	0	1	-4	-3	-4	5	18
intercept / m/s	-0.85	-0.64	-0.79	-0.85	-0.21	-0.28	0.04	-1.00	0.31
µ(mean bias) / m/s	-1.48	-0.71	-0.74	-0.76	-0.54	-0.57	-0.57	-0.57	2.02
median / m/s	-1.43	-1.03	-0.74	-1.08	-0.88	-0.89	-0.89	-0.89	1.65
σ(std. dev.) / m/s	3.13	2.41	2.41	2.43	2.33	2.34	2.34	2.34	3.12
r (correlation coeff.)	0.74	0.84	0.85	0.85	0.85	0.85	0.85	0.85	0.83
# of compared winds	612	526	526	526	526	511	511	511	511

Due to a very high noise level caused by the combined influence of telescope overlap, pointing jitter and possible other errors it was decided for measurements from ground to exclude about the first 2 km in order to overcome the high uncertainties connected with the transmit-receive path overlap function for the A2D (Paffrath et al. (2009)). Also, in the A2D measurements from the airborne campaign it became obvious that the winds measured in range-gates #5 and #6 (Internal Reference = range-gate #4) are not reliable and, amongst others, are strongly influenced and biased by the overlap function of telescope and laser beam. With the aircraft flying at 10.4 km, the upper border of range-gate #7 is located at 9.23 km altitude and in this case only the highest measurements of the 2-µm Lidar reach up to 10.1 km. Therefore, excluding these two range-gates as done for case b), reduced the number of compared winds by 86, corresponding to about 14 %, at most of the winds can be attributed to range-gate #6. Compared to case a) the statistical values improve without exception for all given parameters.

If, as in subsec. 3.4.6, for case c) all measurements exhibiting DCO outliers are excluded from both, the calibration and the wind retrieval, no significant improvement can be achieved, apart from minor improvements regarding slope and correlation coefficient. Applying an additional correction by using the frequencies measured by the wavelength meter instead of the commanded ones (case (d) and subsec. 3.4.6), minor increases in the systematic and random error can be observed.

Further improvement can be obtained in case e) by evaluating the response calibration over the extended frequency interval of ± 850 MHz, including a polynomial fit of 5th order (subsec. 3.4.4) and the respective non-linearity correction during the wind retrieval. The slope now slightly deviates again from the ideal value of 1.0 by -4 % but reductions of the systematic error from

-0.76 m/s to -0.54 m/s and the standard deviation from 2.43 m/s to 2.33 m/s are achieved. Also, the standard deviation reaches its minimum with 2.35 m/s and the correlation coefficient stays close to its maximum value.

Case f) excludes all wind measurements from the statistical comparison that are located in and below clouds as marked in black and mentioned along with Fig. 4.8. For the measurement of 2009/09/26 only 15 winds fall into this category. The fact that no significant changes in the statistical values are present actually implies a nevertheless good quality of the excluded range-bins. Therefore, an increase of the threshold values for cloud recognition could be reasonable and gain more useful winds from within and below optically thin clouds as sub-visible cirrus for the comparison. Case g) weights all measurements individually according to Eq. 4.10 and Eq. 4.11a. As could be expected from the rather homogeneous atmospheric measurement scene, only minor corrections of slope and intercept are resulting.

As introduced with Eq. 4.12, the assumption that the 2-µm Lidar delivers perfect wind speed measurements can be replaced by assigning a worst case random error of $\sigma_{2\mu\mathrm{m,i}} = 1\,\mathrm{m/s}$ to the 2-µm winds (Weissmann et al. (2005)) and performing a linear fit with errors in both directions according to Press et al. (1992) (case h). 2 m/s is considered a plausible value for the A2D random error $\sigma_{\mathrm{A2D,i}}$, which is in fact supported by the estimation made below in Eq. 4.13. The random errors on both coordinates were each assumed to be the same for every ith range-bin, i.e. independent of wind speed and not including weights as in Eq. 4.11. The slope $b_{\mathrm{B}} = 1.05$ and the intercept $a_{\mathrm{B}} = 1.0\,\mathrm{m/s}$ deviate significantly from case f), however, both parameters depend strongly on the ratio of the assumed random errors allocated to the 2-µm and A2D winds. Additionally, the procedure adapted from Press et al. (1992) allows the calculation of the uncertainties in the estimates of a_{B} and b_{B}. Thereby, $\sigma_{\mathrm{a}} = 0.25\,\mathrm{m/s}$ and $\sigma_{\mathrm{b}} = 0.03$ express the fact that the uncertainty in the measurement points introduces an uncertainty in the estimation of the parameters a_{B} and b_{B} and the slope of the linear fit will therefore be found most likely in a region between 1.02 and 1.08. A minimum χ^2 of 554.2 resulted from Eq. 4.12, keeping in mind the number of 511 considered points.

Finally case i) is included to illustrate the enormous influence of the quality of different calibrations. The numbers obtained from a wind retrieval involving the 1st instead of the 2nd calibration differ significantly, particularly in slope, bias and standard deviation. The decision to regard the 2nd calibration as the better one and, therefore, to present the major part of the results in this thesis with respect to this calibration, is particularly based on the higher standard deviation of the 1st calibration. From the wind fields along with their differences presented in Fig. 4.10 it can be concluded that the difference does not depend on the magnitude of the wind speed but is rather associated with the range-gate number and, thus, the distance from the instrument. In summary, Tab. 4.2, whose values are to a certain extent specific for the wind measurements regarded in the current chapter, reveals that the most efficient corrections are thus the exclusion of range-gates within the overlap region of the A2D and the application of the non-linearity correction.

Fig. 4.9 shows a scatterplot of the winds measured by the A2D and the 2-µm Lidar, illustrating the results emanating from case g) in Tab. 4.2. It seems that the rather good and stable values, obtained from the statistical comparison, are based on the consideration of the atmospheric

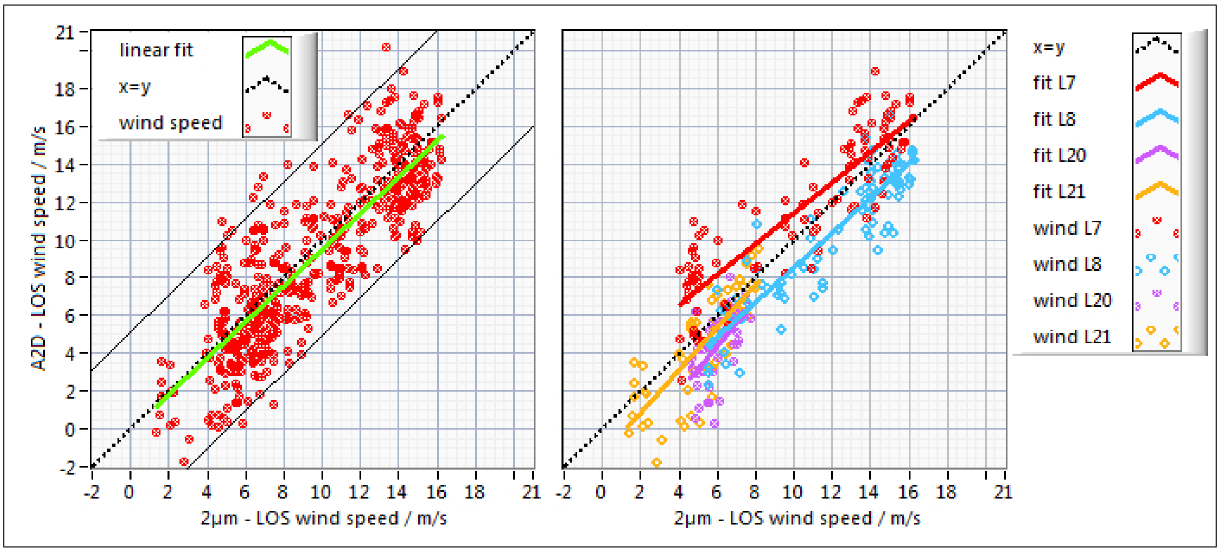

Figure 4.9.: Left: Scatterplot for all Rayleigh winds (red dots) available for comparison within range-gates #7 - #21 processed with the 2nd calibration from 2009/09/21, using a coverage ratio of 85 % and the correction scheme of case g) from Tab. 4.2. The linear fit line (green) and the ideal x = y line (dashed, black) are also indicated together with a ± 5 m/s-interval (black lines). Right: Scatterplots for four selected range-gates #7 (8.95 km altitude), #8 (8.36 km), #20 (1.26 km) and #21 (0.67 km) with individual linear fit lines and the ideal x = y line (dashed, black). 2-µm winds on x-axis and A2D winds on y-axis.

scene in a whole, providing a high number of winds (Fig. 4.9 left). A comparison of single range-gates (Fig. 4.9 right) reveals discrepancies presumably originating from both, the distance of the wind measurement to the aircraft and from a pure altitude dependence. Four example range-gates are selected, two located close to the aircraft and to the ground, respectively, and distinguished by colour. Focussing on the linear fit lines only, one could interpret the range-gates #8, #20 and #21 to match very well but excluding range-gate #7, the closest one to the aircraft, which might still be influenced by the effects mentioned above. Values for standard deviation can be attributed to each of the single range-gates and a range dependency was found in such a way that the highest value still occurs in the range-gate closest to the aircraft (2.6 m/s) but low values of almost 1 m/s (range-gate #11) can be reached, too. Also, the systematic error shows a range dependency with positive values (≈ 1 m/s) close to the aircraft and negative values (up to -2 m/s) in the mid and lower atmosphere. A small part of the random error might be traced back to the influence of the aerial interpolation algorithm onto the 2-µm wind speed values used for the comparison. In the case of stationary measurements from ground a significant part of the ≈ 2 m/s random error could potentially be explained by wind gusts, but becomes less probable regarding the spatial relations with respect to the 2.9 km flown by the Falcon in 14 s of an observation during the airborne measurements. A respective scatterplot as in Fig. 4.9 (left) employing the 2nd calibration (case i))is illustrated in Fig. A.10.

As introduced in subsec. 3.1.4 the 2-µm Lidar can be operated in two different measurement modes, at constant LOS or using a VAD scan. If the 2-µm Lidar is operated in LOS mode, the resulting comparison of A2D and 2-µm winds is much more reliable. Assuming perfect parallel alignment of 2-µm and A2D LOS and neglecting the axis offset between both as well as the different laser divergences, one obtains an almost perfect match of the sampled atmospheric volumes of the two Lidars. However, during the current measurement scene the 2-µm Lidar was executing VAD scans with 20° off-axis angle. Regarding a flight height of about 10 km, the maximum horizontal distance between the exact A2D and 2-µm measurement locations is about 7 km ($10\,\mathrm{km} \cdot \sin(20°) \cdot 2$) at ground level. For the mean distance one has to consider the chord length $s = 2r \cdot \sin(\phi/2)$ (with radius r and horizontal angle ϕ between A2D and 2-µm measurement location) changing with VAD scan angle and linearly with the distance from the aircraft. The calculation of the average length (centre of gravity method) of this chord considering a 360° scan of the 2-µm Lidar fails due to an undefined primitive, but simulation gives a value of 0.64 for the unit circle. For a flight altitude of 10 km this results in a horizontal mean distance of the measurement locations of 2.2 km at a distance of 5 km from the aircraft, linearly increasing. The mean distance of 2.2 km is even less than the horizontal averaging length per observation of the A2D (2.9 km) and 2-µm Lidar (6.7 km) and much less than the maximum 11 km (subsec. 3.1.4) that needed to be considered by Weissmann et al. (2005). Keeping this result in mind, one can assume that the A2D and the 2-µm Lidar were sensing almost the same atmospheric volumes and write for the standard deviation (random errors) of the difference (Eq. 4.4b):

$$\sigma = \sqrt{\sigma^2_{\mathrm{A2D}} + \sigma^2_{2\mu\mathrm{m}}} \tag{4.13}$$

under neglect of the representativeness error. Assuming the maximum proposed value of 1 m/s random error for the 2-µm Lidar, a (minimum) random error of about 2.12 m/s (which is in good agreement with the assumption of 2 m/s random error made for case h)) has to be attributed to the A2D Rayleigh measurements and thus the main fraction of the standard deviation of about 2.34 m/s (Tab. 4.2).

One of the most striking results is the rather poor agreement of the two calibrations for the Rayleigh channel, while very good agreement was found for the Mie channel (subsec. 4.2.3). From differences in slope and intercept (Fig.3.16) follows a difference in the evaluated wind speeds as it is illustrated in Fig.4.10. Clearly, the discrepancy is related to the region close to the aircraft with a peak at range-gate #8 (8360 m altitude, i.e. ≈ 2 km below the Falcon) in this case. This fact pertains to the interpretation of the results presented in Tab. 4.2 for the cases h) and i) inasmuch as the magnitude of present wind speeds in combination with the altitude of their occurrence should be taken into account for statistical comparisons as done in Fig. 4.9, for instance. Detailed investigations have been performed in order to clarify the difference in the Rayleigh calibrations. Neither the noise present in the response functions (subsec. 3.4.5) nor deviations of temperature concerning the spectrometers or outliers in data recording or wrong frequency steps could give a sufficient explanation. However, the properties of the observed difference most likely hint at the aspect of the alignment sensitivity of the FPI.

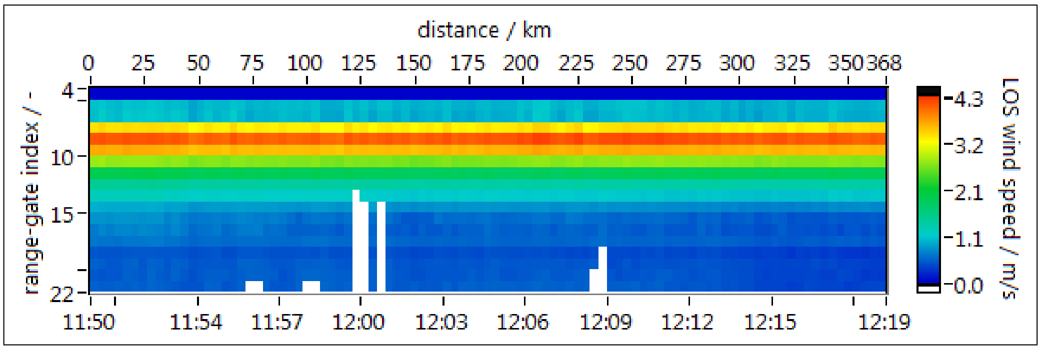

Figure 4.10.: The difference of wind speeds retrieved for the A2D Rayleigh channel using the 1st and 2nd calibration is displayed for the flight section between 11:50 - 12:19 UTC on 2009/09/26. The correction scheme of case f) from Tab.4.2 was applied. The uppermost range-gate #4 corresponds to the internal reference.

Mie channel and 2-µm Lidar

As for the Rayleigh channel (Fig. 4.9) the comparison of the winds measured by the A2D Mie channel and the 2-µm Lidar are illustrated as a scatterplot (Fig. 4.11). The respective differences in wind speed mainly range from about -2 to 2 m/s. Occasionally higher values occur up to -6 or 6 m/s that are also visible in the scatterplot. A threshold on the wind speed difference of 10 m/s was set, which excluded three outliers exhibiting values of -16 m/s, 30 m/s and 33 m/s that had a strong influence especially onto the slope of the linear fit line. The number of points (488) used for the statistical comparison is slightly less than for the Rayleigh channel (511). Referring to Tab. 4.2 the most obvious and most important difference to the Rayleigh comparison is the very low standard deviation of the Mie comparison of only 1.36 m/s, which also improves the correlation coefficient to 0.95. Both, bias and slope values are slightly worse than for the Rayleigh comparison.

The most important results obtained from the statistical comparisons for the flight section on 2009/09/26 between 11:50 - 12:19 UTC are summarized in Tab. 4.3 comprising the Rayleigh case h) from Tab. 4.2 and the Mie case presented in Fig. 4.11. Unlike for the Rayleigh channel, the comparisons for the Mie channel do not show such an enormous difference from 1st to 2nd calibration (Fig. A.11). Furthermore, the table contains from comparisons involving wind speed and wind direction modelled by the ECWMF and measured by the 2-µm Lidar that are discussed below.

In contrast to the Rayleigh winds, the Mie winds hardly show any range dependency in the systematic error, which might point to a very high sensitivity of the Rayleigh spectrometer with respect to the angle of the incoming backscattered light as already suggested and investigated in Witschas et al. (2012b). This might be a reason why the A2D wind measurements of the Rayleigh channel are not reliable in the near-field, i.e. close to the instrument, and range-gates #5 and #6 had to be excluded from the respective statistical comparison. In contrast, the Mie wind speeds of these two range-gates seem to be of likewise good quality as the rest and do not have a worsening influence on the statistical values.

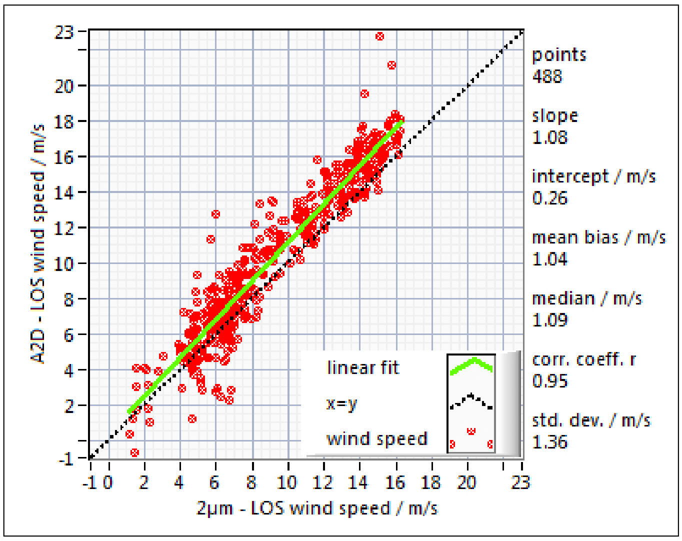

Figure 4.11.: Scatterplot for winds measured by the A2D Mie channel and the 2-µm Lidar (red dots) within range-gates #7 - #21 (Internal Reference = #4) processed with the 2^{nd} calibration from 2009/09/21, using a coverage ratio of 85 %. The linear fit line (green) and the ideal x = y line (dashed, black) are also indicated.

Table 4.3.: Overview of the results of the statistical comparisons of winds measured or modelled by the A2D, the 2-µm Lidar and ECMWF. Comparisons involving Rayleigh and Mie channel refer to the A2D LOS, whereas the comparison of ECMWF and 2-µm Lidar are for horizontal wind and wind direction.

	Rayl. / 2-µm	Mie / 2-µm	Rayl. / ECMWF	Mie / ECMWF	2-µm / ECMWF	2-µm (dir.) / ECMWF
slope	1.05	1.08	1.29	1.25	1.16	1.17
slope error / %	5	8	29	25	16	17
intercept / m/s	-1.00	0.33	-4.33	-1.36	-4.02	-52.65°
µ(mean bias) / m/s	-0.57	1.04	-2.31	0.93	0.38	-0.88°
median / m/s	-0.89	1.09	-2.54	1.10	0.69	-2.45°
σ(std. dev.) / m/s	2.34	1.36	2.52	1.96	2.78	7.22°
r (correlation coeff.)	0.85	0.95	0.85	0.91	0.98	0.91
# of compared winds	511	488	1405	593	473	473

ECMWF analysis

It is visible in Fig. 4.7 that, unlike for the molecular scattering, the aerosol backscatter allows wind measurements only in confined regions, mainly in the boundary layer and below the aircraft or wherever good signal to noise ratio can be achieved. This partly selective character may lead to a wrong or at least distorted interpretation of the quality of the Rayleigh winds and the derived values from the statistical comparison against the 2-µm winds. Thus, wind speed data from ECWMF analyses can constitute a valuable source to close this gap and a statistical comparison can give at least indications about the reasonableness of the A2D Rayleigh winds.

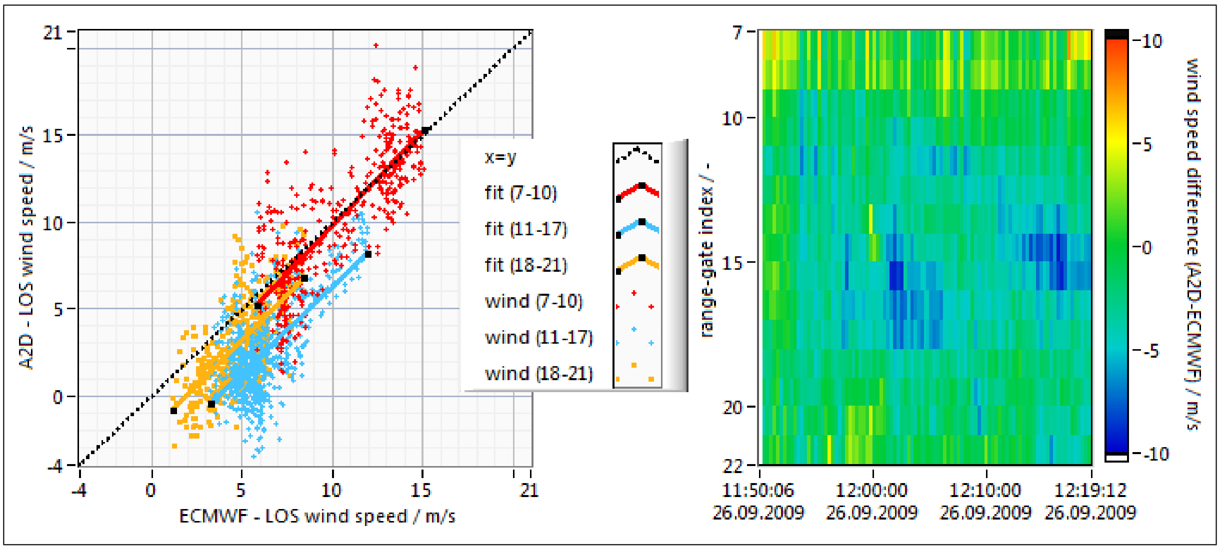

Figure 4.12.: Left: Scatterplot of winds measured by the A2D Rayleigh channel (case f)) and modelled by the ECMWF analysis within range-gates #7 - #21 (Internal Reference = #4) processed with the 2$^{\text{nd}}$ calibration from 2009/09/21. The wind field is divided into three sections including individual linear fit lines: range-gates #7 - #10 (upper section, 6.9 km - 9.2 km, red), range-gates #11 - #17 (middle section, 2.7 km - 6.9 km, blue),range-gates #18 - #21 (lower section, 0.0 km - 2.7 km, yellow). The ideal x = y line (dashed, black) is also indicated. Right: Wind speed differences between ECMWF analysis and A2D Rayleigh channel.

For better distinction of the aerosol free and aerosol loaded regions, the scatterplot in Fig. 4.12 is divided into three sections each illustrated in its own colour. It clearly shows a large systematic error of about 4 m/s in the middle atmosphere (blue), whereas the aerosol loaded sections show either no (upper part, red) or a smaller bias (lower part, yellow) of less than 2 m/s. The statistical comparison between the Rayleigh and the ECMWF winds was additionally performed without the division into sections, yielding a single linear fit. The respective results are contained in Tab. 4.3. The ECMWF analysis was taken for 12:00 UTC, which is almost exactly the middle of the measurement period, and the data was first projected onto the A2D LOS and then interpolated as discussed in subsec. 4.1.2. There was no need to apply a coverage ratio since ECMWF analyses provide continuous data fields in the domain of the A2D measurements, a fact which, as well, leads to the high number of comparable winds ($1405 = 96$ A2D obs $\cdot$ 15 range-gates excluding the range-bins according to case f)). The ECMWF wind field generally matches very well the coarse structure found by the A2D and 2-µm Lidar with the jet-stream at high altitudes towards the end of the section and the katabatic flow above the sea surface (Fig. 4.7 and Fig. A.12). Nevertheless, a rather big slope error of 29 % is apparent. While the higher wind speeds between 12 m/s - 15 m/s (7 km - 9 km altitude) are well represented, lower wind speeds between -2 m/s to -8 m/s (A2D) and 1.5 km - 8 km show a higher systematic error, leading to the mean bias value of -2.3 m/s. The slight increase in standard deviation in contrast to the comparison with the 2-µm winds might be explainable due to the ECMWF model resolution of -0.25°, which in the region of the presented measurement section leads to a horizontal sampling grid of about 12 km in east-west and 28 km north-south direction, and hence required a spatial interpolation of the wind field onto the Falcon flight track. The right part of Fig. 4.12 presents the wind speed differences (A2D Rayleigh - ECMWF). Obviously, the existence of large regions of negative values (blue) between range-gates #13 and #18 in the free troposphere does not support the deductions in terms of the relatively small systematic error inferred by the comparison of A2D Rayleigh and 2-µm winds (Fig. 4.9 and Fig. 4.2). However, the negative differences are restricted to certain areas and appear throughout the whole mid atmosphere, which raises the assumption that the mismatch might be based on analysed ECMWF wind direction locally deviating from the reality. This assumption cannot be proven since the 2-µm Lidar did not provide wind measurements in the respective region but again a comparison of ECMWF and 2-µm wind directions for the available parts might provide an indication of the general accordance of measurement and model.

A comparison of horizontal wind speed for ECMWF analysis and 2-µm Lidar (Fig. 4.13, right) yields an intermediate outcome, resulting in a rather high slope error of 16 %, contrasted by a good mean bias of 0.38 m/s and an excellent correlation coefficient of 0.98 (Tab. 4.3). The higher standard deviation of 2.78 m/s seems to support the conclusion about the connection of increasing standard deviation and model resolution just mentioned above.

The equivalent statistical comparison of the wind directions derived from 2-µm and ECWMF data leads to a linear fit of similar quality (Fig. 4.13). Apart from the high slope error of 17 % and some minor features, measurement and model seem to be in good agreement with a correlation coefficient of 0.91, a mean bias of -0.88° and a standard deviation of 7.22°. Further investigations of the differences in wind direction, show that the region around the katabatic flow exhibits the biggest deviations, both in terms of maximum and average. Nevertheless, not even the occurring magnitudes of up to 25° could explain the maximum differences in wind speed found from the comparison of Rayleigh and 2-µm winds (Fig. 4.12). The fact that the wind directions measured by the 2-µm Lidar and modelled by the ECMWF are in reasonable accordance for the region available for comparison, entails only two possible explanations for the discrepancy of wind speeds between the A2D Rayleigh channel and the ECWMF appearing in the free troposphere. Either the ECMWF model is overestimating or the A2D is accordingly underestimating the wind speed in the respective aerosol free region. All comparisons performed for the present case involving ECMWF data (e.g. Tab. 4.3, Fig. 4.14) are based on the horizontal wind speed and wind direction from the ECMWF analysis for 12:00 UTC on 2009/09/26 as

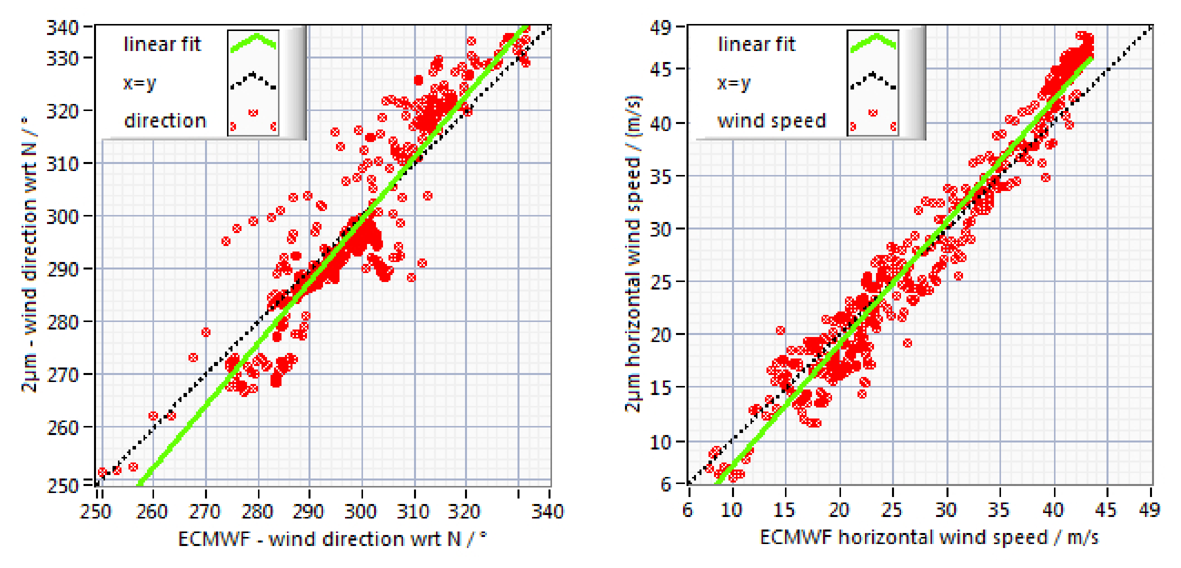

Figure 4.13.: Left: Scatterplot of wind directions retrieved from 2-µm Lidar (y-axis) and the ECMWF analysis (x-axis) for 2009/09/26 at 12 UTC (red dots) within an altitude range from the sea surface to 10 km. The linear fit line (green) and the ideal x = y line (dashed, black) are also indicated. Right: Scatterplot as on the left, but for wind speed.

shown in Fig. A.12. The respective measurements of the 2-µm Lidar for the same period can be viewed in Fig. A.13.

From this single example measurement section presented in the current chapter it is difficult to draw a final conclusion related to the ECMWF, but, regarding the A2D, an influence of Mie cross-talk on the Rayleigh channel seems possible, i.e. the part of the backscattered light which is reflected at the Mie spectrometer (aerosol) towards the Rayleigh spectrometer (molecules) has a significant impact on the intensities on channel A and B, and hence on the evaluation of the Rayleigh response. Regarding especially the upper range-gates (red) in Fig. 4.12, this would infer that the part of the aerosol signal reflected on the Fizeau interferometer acts in a way that it (more or less by chance) cancels the systematic error present in the middle, aerosol free part of the atmosphere (blue). It is noted that a comparison of Lidar data to operational analyses by Weissmann et al. (2005) also revealed differences of up to ± 15 m/s, which to the authors' opinion emphasises the need for more representative and higher resolved wind measurements in data sparse regions above the Atlantic Ocean. The obvious discrepancies found from the comparison of the ECMWF analysis with the measurements of the A2D and 2-µm Lidar emphasise this need for additional high quality winds measurements.

Radiosonde measurements

The presence of a radiosonde station (04360 BGAM) at the east coast of Greenland allows further comparisons to the wind speed and direction. As indicated in yellow in Fig. 4.4 the shortest distance between station and the Falcon flight track adds up to 74 km. For Fig. 4.14 the first 24 A2D observations and the first 14 2-µm observations were taken into account, which are the closest to the radiosonde station. The length of both sections is about 90 km and corresponds, on the one hand, to roughly a quarter of the whole measurement period ($\approx$ 7 min) and, on the other hand, to the approximate length of one ADM-Aeolus observation. The fact that the 2-µm Lidar was operating in scan mode allows additional comparisons of horizontal wind speed and direction with measurements of the radiosonde and the modelled values from the ECMWF analysis. The radiosonde was launched at 12:00 UTC, i.e. at the middle of the A2D measurement period.

Regarding the middle and right plot of Fig. 4.14 the ECMWF analysis was additionally considered for the same time and at the single location of the radiosonde station. For the left plot the ECMWF data is only taken into account along the Falcon flight track. A2D LOS winds as well as the respective ECMWF and radiosonde winds projected onto the A2D LOS agree roughly within an interval of 5 m/s. From sea surface up to an altitude of about 7 km the same coarse tendency of increasing wind speed is visible for all three. The slight bend towards lower wind speed for ECMWF between 7 km - 10 km, might be connected to the assimilation of the radiosonde data, exhibiting the same feature but even more pronounced. Each A2D range-gate and ECMWF model level is provided with bars of minimum and maximum values illustrating the respective uncertainties. At most of the range-gates the ECMWF and radiosonde wind speeds are located within the A2D bars. While the A2D bars clearly show the highest variation without a dependence on altitude, the ECMWF uncertainty is generally lower and decreases with height. With a pronounced peak at 1.3 km the radiosonde measurement exhibits a feature not found in the A2D data. Due to its small scale, the peak might be smoothed out by the Lidar inherent property to average data over a larger area. Indeed, the Lidar measurements are more representative for the wind in a region than point measurements of a radiosonde which might be subject to local influences (Weissmann and Cardinali (2007)). The right plot of Fig. 4.14 compares the horizontal wind speed found from the ECMWF (along flight track and at radiosonde location), the 2-µm Lidar and the radiosonde. In general all three sources agree in the overall shape of predicted and measured profiles. While the ECMWF winds along the flight track show the same wave like modulation the radiosonde and 2-µm winds between 7 km and 10 km, the ECMWF winds at the radiosonde location do rather not. Also up to 1 km above sea level the ECMWF at the station deviates largely. These differences of up to 15 m/s with respect to the 2-µm Lidar are supposed to be related to the turning of wind direction during the transition of the air from land to sea. This assumption is supported by the findings from the respective comparison in Fig. 4.14 middle, where the 2-µm and ECMWF (station) wind directions differ by 50°. Also the peak in radiosonde wind speeds at 1.3 km altitude is associated with a change in wind direction and it is similarly present in the ECMWF analysis and, inverted, in the 2-µm measurements. Due to the modelling nature of ECMWF small features are likely to be smoothed. In terms of the modulation above 7 km, the 2-µm and the radiosonde agree much

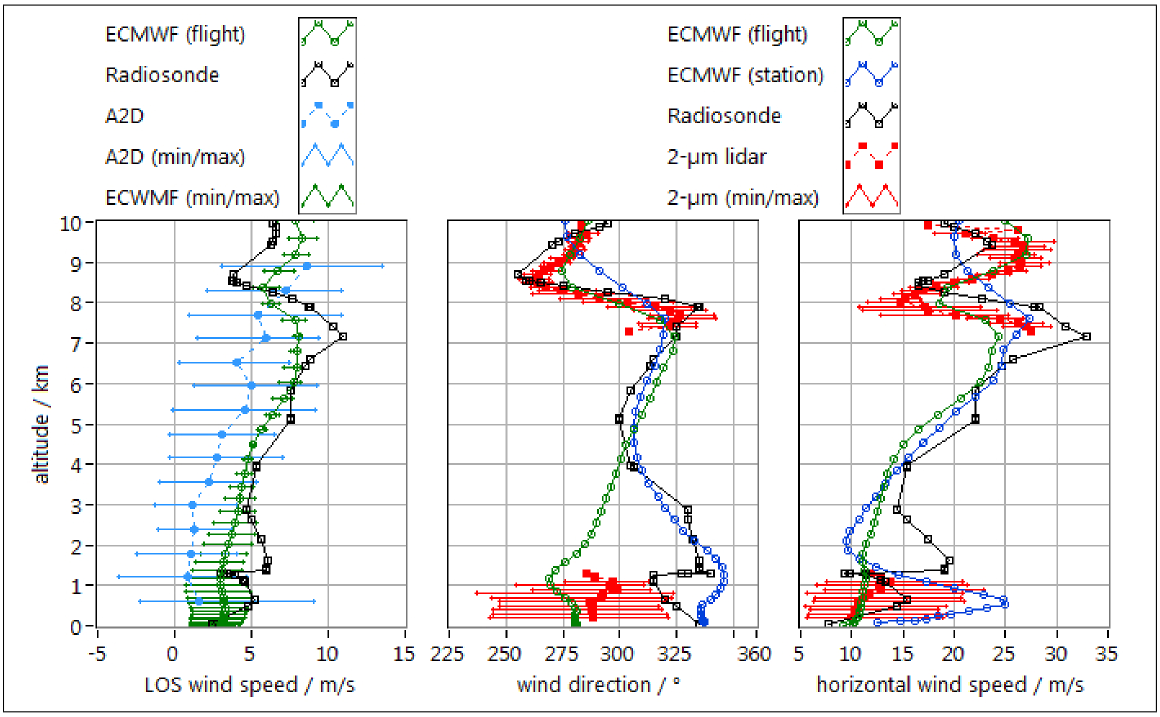

Figure 4.14.: Comparison of LOS wind speed (left), horizontal wind speed (right) and wind direction (middle) from A2D, ECMWF analysis (12:00 UTC), 2-µm Lidar and radiosonde at radiosonde location 04360 BGAM 12:00 UTC for 2009/09/26. A2D and 2-µm data are averaged over the first 24 and 14 observations, respectively. ECMWF (flight) data is averaged along the flight track of the first 24 A2D observation (11:50.06 - 11:57.18 UTC). Horizontal bars for A2D, 2-µm and ECMWF (flight) data refer to the minimum and maximum value occurring per layer within the averaging period. Left: Mean A2D LOS wind speed (light blue, dashed line, circles) compared to winds measured by the radiosonde (black, solid line, squares) and predicted by the ECMWF, both projected onto the A2D LOS. Middle and right: Wind direction and horizontal wind speed from radiosonde, 2-µm Lidar (red, dashed line, squares) and ECMWF analysis considered along the flight track (green, solid line, circles) and at the radiosonde location (ECMWF(station)) (dark blue, solid line, circles).

better than for the horizontal wind speed, whereas now at low altitudes a large offset up to 45° is present. However, the included minimum-maximum bars for the 2-µm measurements point to much bigger uncertainties at low than at high altitudes and the turning of wind direction during the land-sea transition might contribute to explain the present differences. The mismatches between ECMWF (station) and radiosonde, though related to the same location, might relativise the conclusion found from the statistical A2D-ECMWF comparison (Fig. 4.12) and increase the confidence in the Rayleigh A2D measurements. Certainly, also radiosonde drifting contributes to the encountered differences. The above mentioned discrepancies between A2D and 2-µm Lidar on one side and ECMWF and the radiosonde on the other, despite the rather small distance of 74 km, consolidate the point of view that two Lidar systems deployed on the same aircraft are preferred with respect to a comparative analysis of wind measurements.

4.3. Validation of zero wind correction

In order to illustrate the application and the correctness of the ZWC procedure presented in subsec. 3.5.3, an exemplary measurement section is discussed here. Since the atmosphere was very clear yielding only small SNR values and hence few valid measurements for the A2D Mie channel, the focus for the wind retrieval and the comparison lies on the Rayleigh channel in the current section. Fig. 4.15a shows the flight track of the Falcon on 2009/09/29 with the start and the landing in Keflavik at 10:57 UTC and 14:55 UTC (flight #09, Tab. 3.2). From the measurement section over Iceland (see also Fig. A.8) between 11:54 - 12:20 UTC a ZWC value was determined. Two wind measurement sections of about 16 minutes and 19 minutes length are located in front of the east-coast of Iceland. During the first section the 2-µm Lidar was operating in scanning mode and during the second section with a fixed LOS, viewing into the same direction as the A2D. Fig. 4.15b gives a basic overview of the meteorological situation in the region of the wind measurements. The image was recorded by a MODIS instrument in the near infrared. While clouds were covering the western part of Iceland as well as the ocean in the north and the south, the three measurement sections were located in a cloud free area. Snow and ice surfaces appear in the south of Iceland yielding beneficial, strong ground return signals for the zero wind measurements.

A median filter (ch. A.2) had to be applied to the data obtained from the 2-µm measurements in LOS mode during the second wind measurement section, resulting in the wind field as presented in Fig. 4.16a (top). The A2D Rayleigh winds shown in Fig. 4.16a (bottom) are processed according to case f) in subsec. 4.2.3 and corrected for zero wind. With a mean flight height of the Falcon of 8091 m, the altitude range from 0.2 to 6.4 km comprises the A2D range-gates #7 to #21. During the measurement period of 971 s the Falcon covered a horizontal distance of 205 km with an average ground speed of 211 m/s. 54 observations were obtained from the A2D, whereas the 2-µm Lidar provided one wind profile per second in the LOS mode. Due to the low aerosol content only few valid 2-µm measurements are available for this short measurement period. Thus, the coverage ratio is reduced to 50 % in order to increase the number of range-bins for the statistical comparison. A reduction is tolerable as no strong wind speed gradients are present.

Between the 2009/09/26 (sec. 4.2) and the 2009/09/29 the pointing direction of the laser beam of the A2D was slightly changed by applying a new reference position to the steerable mirror attached to the telescope (Fig. 2.4). On 2009/09/28 four ground based response calibrations on Iceland were conducted using two different reference positions (Reitebuch et al. (2012d)). The observed differences in the calibration results regarding offset and sensitivity suggest that every change in the pointing direction of the laser beam with respect to the telescope axis requires a new calibration. Since no additional airborne response calibration was performed using the new pointing direction, the response calibrations available from the 2009/09/21 above Greenland must be applied, although they are principally not suitable for wind retrieval after 2009/09/29. However, in this respect the changed pointing direction can be interpreted as a change in incidence angle onto the FPI's, consequently introducing an error into the retrieved wind speed. As it can be assumed that the pointing stays constant over time, a ZWC should be applicable using a single value, which can even be determined from a separate measurement

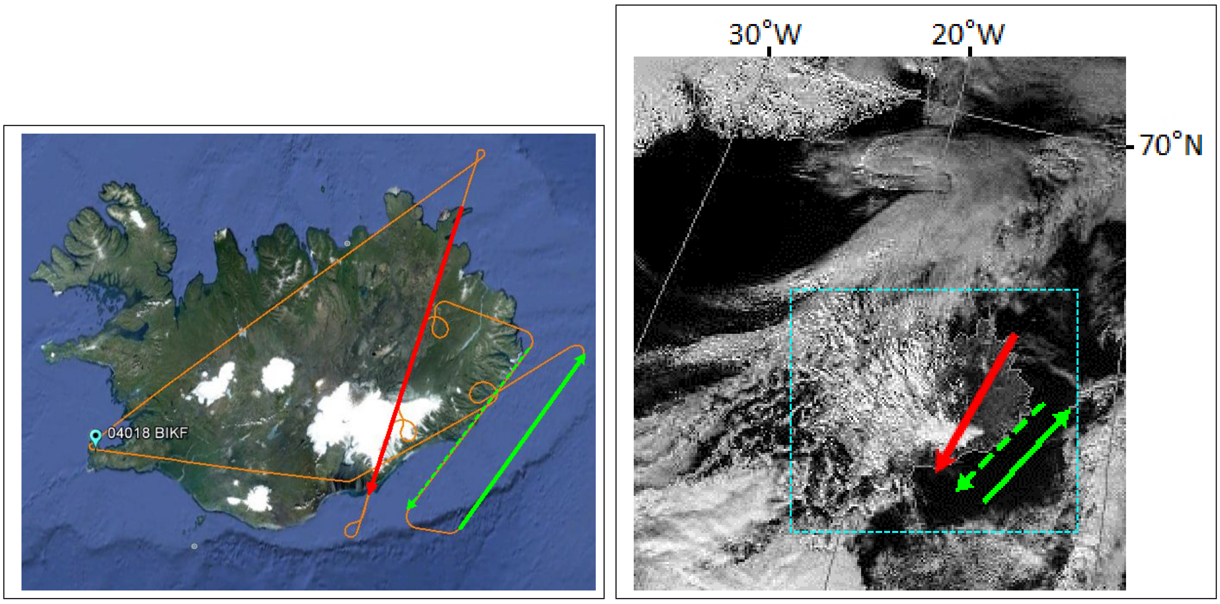

(a) (b)

Figure 4.15.: (a) Flight track of the Falcon on 2009/09/29 (orange) including a flight section over Iceland from which a ZWC value for the A2D was obtained (red). Two wind measurement periods are indicated in green, during which the 2-µm Lidar was operating in scanning mode (dashed) and with a fixed LOS (solid). The radiosonde station marked with the WMO code 04018 BIKF is located at Keflavik. (Google Earth was used to display this information.) / (b) This image from channel 2 (841 - 867 nm) of the MODIS instrument on the TERRA satellite was taken at 13:52 UTC on 2009/09/29 and shows the North Atlantic region around Iceland. The dashed rectangle frames the region shown in figure (a). Snow and ice surfaces appear in white, as present in the mountainous regions in the south-east of Iceland. Clouds are associated with light grey to white colour and cover the western half of Iceland and large parts of the ocean (black). The bare ground of the eastern part of Iceland (dark grey) is visible. The measurement period over Iceland from which the ZWC values were obtained (red) and the A2D wind measurement section (green) along the east coast of Iceland took place in an almost cloud free area. The arrows indicate the flight direction of the Falcon. (MODIS image from NERC Satellite Receiving Station, Dundee University, Scotland, `http://www.sat.dundee.ac.uk`)

under the same pointing conditions. Such a ZWC value was obtained between 11:54 - 12:20 UTC over Iceland (Fig. 4.15) from strong ground return signals of snow and ice surfaces (Fig. 3.27 (left)). The mean over 21 A2D observations yielded a velocity offset of 5.4 m/s for the Rayleigh channel (Fig. A.17). For check of consistency an additional ZWC value was determined from measurements on the 2009/09/26 before the laser beam pointing was modified (Fig. 3.27 (right) and Fig. 3.4) yielding in a velocity offset of -0.2 m/s (Fig. A.16). Considering the difference of both ZWC values of more than 5 m/s, this illustrates the high sensitivity of the Fabry-Pérot spectrometer with respect to the incidence angle of the light (Witschas et al. (2012b)).

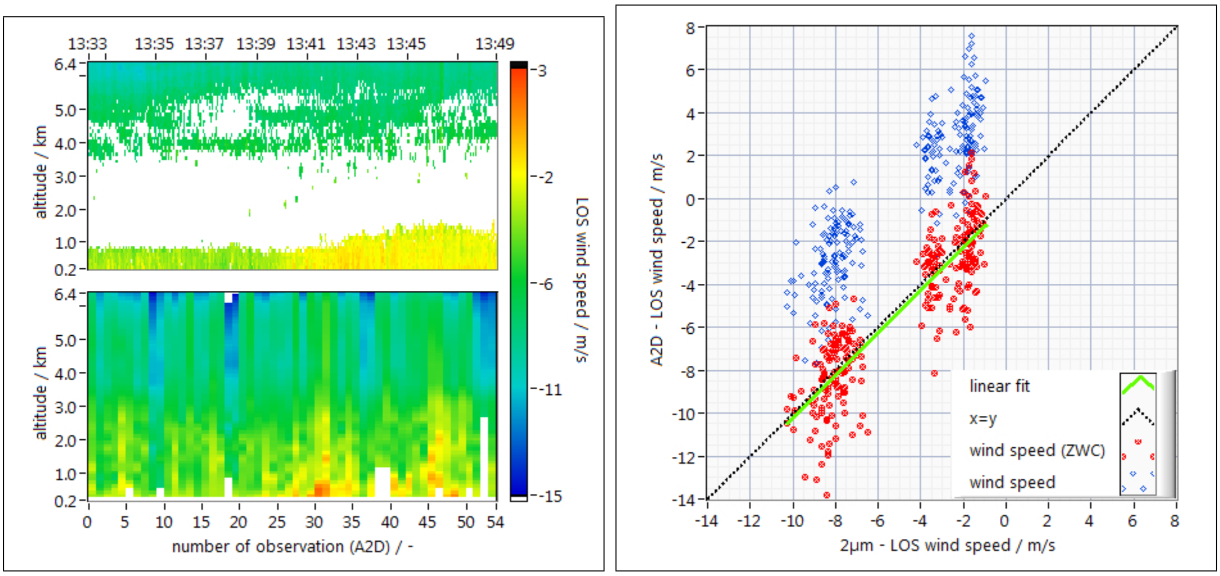

(a) *(b)*

Figure 4.16.: (a) LOS wind speeds obtained from the A2D Rayleigh channel (bottom) and the 2-µm Lidar (top) on 2009/09/29. The A2D winds are corrected with a ZWC value of 5.4 m/s. The 54 observations correspond to 205 km horizontal distance. / (b) Scatterplot for the winds as measured by the 2-µm Lidar and the A2D Rayleigh channel (blue dots, uncorrected) within range-gates #7 to #21 (Internal Reference in range-gate #4) processed with the 2$^{\text{nd}}$ calibration from 2009/09/21, using a coverage ratio of 50 % and the correction scheme of case f) from Tab. 4.2. Red dots refer to the zero wind corrected A2D winds. The linear fit line (green) and the ideal x=y line (dashed, black) are indicated.

Two conglomerations of wind speeds are visible in Fig. 4.16b. They correspond to the two areas in which valid measurements are provided by the 2-µm Lidar, with the lower and higher LOS wind speeds close to the aircraft and to the sea surface, respectively. Red colour denotes the zero wind corrected LOS wind speeds obtained from the A2D Rayleigh channel as displayed in Fig. 4.16a, whereas the blue colour refers to the uncorrected wind speeds. The bias of the wind speeds measured with the changed pointing direction is almost exactly compensated by the ZWC.

An analyses of the second measurement period (Fig. A.15) of the flight between 13:08 UTC and 13:28 UTC (Fig. 4.15a (green dashed)) yielded LOS wind speeds that show the opposite sign compared to the ones presented in Fig. 4.16. This fact can be explained by the difference of 180° in heading angle of the aircraft and a corresponding viewing direction of the two Lidars. As presented in Tab. 4.4, very similar results are obtained from a statistical comparison for both measurement sections which constitutes further evidence in terms of the correctness of the applied ZWC. With the 2-µm Lidar operating in LOS mode during the second wind measurement section, both Lidars were sampling the same atmospheric volumes. Consequently, the error associated with spatial representativeness can be assumed negligible.

Table 4.4.: Results of the statistical comparisons of A2D Rayleigh winds and 2-µm winds for two evaluation periods on the 2009/09/29. The Rayleigh winds were calculated with the 2nd calibration according to case f) (subsection 4.2.3) but with a coverage ratio of 50%.

time (UTC)		13:08.47 - 13:27.23	13:33.05 - 13:49.15
slope		1.05	0.95
slope error	/ %	5	-5
intercept	/ m/s	-0.61	-0.46
µ (mean bias)	/ m/s	-0.38	-0.20
median	/ m/s	-0.44	-0.07
σ (std. dev.)	/ m/s	1.71	1.82
r (correlation coeff.)		0.86	0.84
# of compared winds		341	276

4.4. Case study for observations during cloudy conditions

A wind measurement section on 2009/10/01 allows the effective application of several methods introduced in this thesis, including the ZWC (subsec. 3.5.3) and the cloud detection algorithm (subsec. 3.2) at the same time. Fig. 4.17 shows the flight track of the Falcon with the start in Keflavik at 08:56 UTC (Fig. 3.2). Wind measurements were performed during 09:35 - 10:39 UTC with the 2-µm Lidar operating in LOS mode. Information about the Rayleigh background on the Mie channel (ch. 3.4.6) was obtained from a dedicated MOUSR procedure between 10:40 - 10:45 UTC. An overview of the cloud coverage over the North Atlantic at 11:15 UTC, i.e. about one hour after the wind measurements, is given in Fig. 4.18. The image was recorded by the AVHRR/3 (Advanced Very High Resolution Radiometer) instrument (Pavolonis and Heidinger (2004), Thomas et al. (2004)) on the NOAA-17 (National Oceanographic and Atmospheric Administration) satellite . A high-altitude jet-stream (Fig. 4.19) was present elongating from Greenland over Iceland to Scotland and further to Denmark. This jet-stream was associated with the bands of cirrus clouds visible at the bottom of Fig. 4.18. At the time a high pressure area was present above Greenland and a low pressure area above Northern Norway causing a low level flow of arctic air masses towards the South. This cold air along with the warm surface of the ocean leads to the isolated convection cells, i.e. the broken cloud scenery, whose structure is visible in the A2D and 2-µm wind measurements (Fig. 4.19).

Fig. 4.19 presents the wind speeds along the A2D LOS as measured by the A2D Rayleigh and Mie channel as well as the 2-µm Lidar. Corresponding LOS wind speeds from the ECMWF model were computed taking into account the horizontal wind speed and the wind direction as provided by the analyses for 06:00 UTC and 12:00 UTC (Fig. A.19). A linear interpolation between these two analyses, considering the respective time of measurement of each profile, resulted in the wind field shown in Fig. 4.19 (top). During the measurement time of more than one hour the Falcon aircraft covered a distance of 943 km with a mean ground speed of 242 m/s. Regarding the mean flight height of 10307 m, the altitude range from 0.2 km to 9.7 km comprises the A2D range-gates #6 to #21, each with a vertical thickness of about 596 m (4.2 µs). As the ECMWF analyses are provided according to non-equidistant pressure heights, the data is interpolated onto the regular 2-µm measurement grid with the displayed maximum altitude of 9.7 km about corresponding to the ECMWF model level #39. 216 observations were obtained from the A2D, whereas the 2-µm Lidar provided one wind profile per second in the LOS mode, i.e. 3800 profiles. Before interpolation onto the A2D measurement grid, a median filter was applied (sec. A.2) to the 2-µm data. Several quality control measures are applied to the A2D winds.

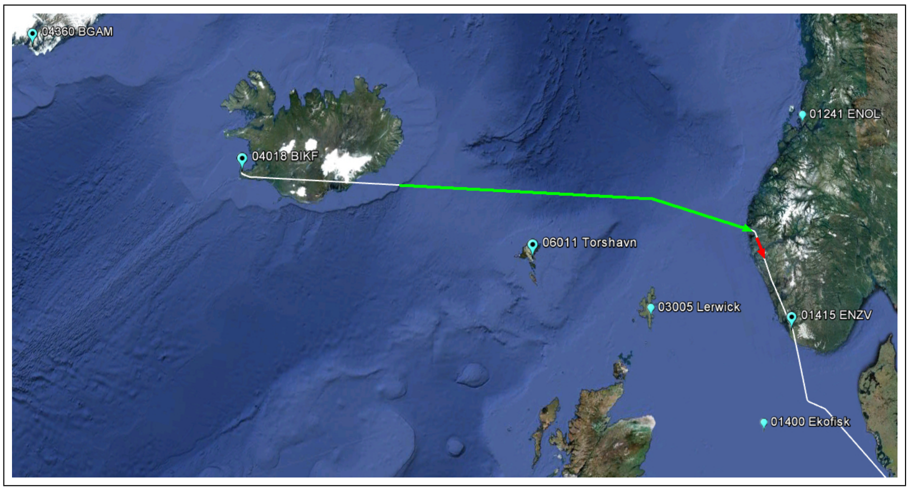

Figure 4.17.: Flight track of the Falcon on 2009/10/01 (white) starting in Keflavik (Iceland) and crossing the North Sea towards Norway and Denmark. The analysed wind measurement section and the period of the MOUSR measurement (subsec. 3.4.6) are marked in green and red, respectively. The locations of various radiosonde stations (light blue) are marked with their WMO codes. (Google Earth was used to display this information.)

As discussed in subsec. 2.3.2, the sensitivity for the molecular signal is about 1/3 higher than for the aerosol signal (Fig. 3.16). Moreover, no correction of Mie contamination according to Dabas et al. (2008) is performed. Thus, Rayleigh wind measurements within and below optically thicker clouds or aerosol layers are not considered reliable and are excluded by applying a cloud mask (see sec. 3.2, Fig. 3.8a). Thereby, a worst-case scenario is applied, defining every range-bin on observation level as invalid if it contains one or more measurements flagged as contaminated by a cloud. The Rayleigh winds presented in Fig. 4.19 are corrected with a ZWC value of 5.4 m/s gained from a dedicated measurement section over Iceland (sec. 4.3, Fig 4.15). Wind speeds obtained from the Mie channel are accepted if the signal exceeds an SNR threshold of 5 (Eq. 3.29, Fig. 3.8b, Fig. A.18). Regarding both, Mie and Rayleigh channel, weights according to Eq. 4.11 (Fig. A.18) were considered during the determination of the linear fit (Eq. 4.10). A reduction of the coverage ratio (Fig. A.18) to 50 % is deemed to be tolerable with regard to a trade-off between the available range-bins for the statistical comparison and the error that may be induced by the strong wind speed gradients that are present in the proportionately small area of the jet-stream (blue colour, 09:35 - 09:50 and 6 - 10 km). The overall negative wind speeds (blowing away from the A2D LOS) and additionally the location of the jet-stream agree with the wind direction that can be expected from the meteorological situation discussed in the frame of Fig. 4.18.

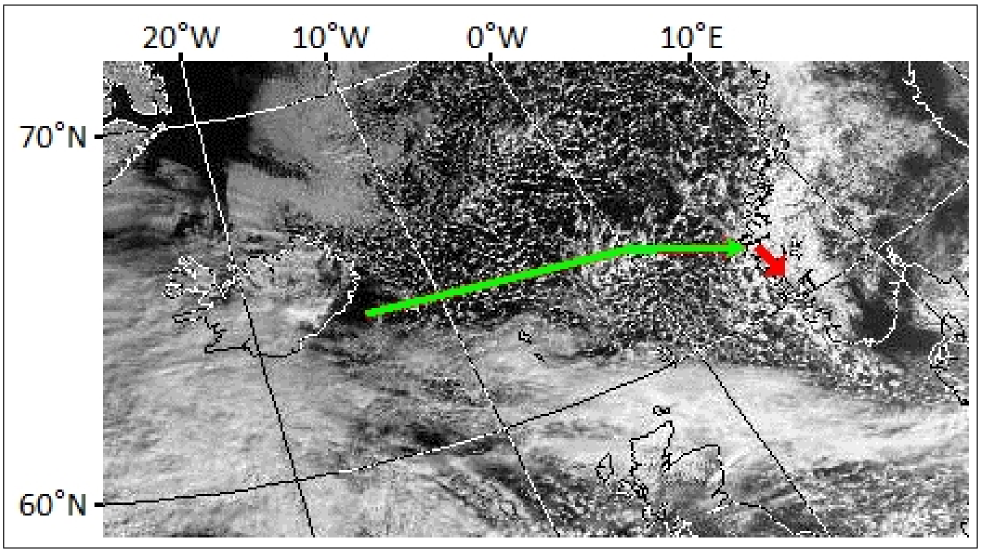

Figure 4.18.: This image from channel 1 (visible, 0.58 µm - 0.68 µm) of the AVHRR instrument hosted by the NOAA-17 satellite was taken at 11:15 UTC on 2009/10/01 and shows the North Atlantic region between Iceland (left) and Norway (right). Clouds are associated with white to dark grey colour. Cloud free areas are shown in black. The green and red arrows indicate the wind measurement section and the MOUSR measurement (subsec. 3.4.6), respectively. (AVHRR image from NERC Satellite Receiving Station, Dundee University, Scotland, `http://www.sat.dundee.ac.uk`)

Fig. 4.20 shows the comparison of A2D Rayleigh and Mie winds against the winds measured by the 2-µm Lidar. Due to the impact of the telescope overlap in the near-field, only the Rayleigh winds between range-gates #9 (mean altitude of upper border: 7937 m) and #21 are used for the statistical comparison (Tab. 4.5). In contrast, all winds available from the A2D Mie channel were used. Comparable to the wind measurement from 2009/09/26 (Fig. 4.12) the measured Rayleigh wind speeds seem to show an altitude dependent systematic error. While a mean bias of about 6 m/s is obtained from the winds measured in the range-gates #5 to #8, the entirety of the remaining winds down to range-gate #21 shows a bias of only -0.5 m/s (blue). Although the bias changes, the slopes derived from the two regions stay close to 1.0. For the linear fit procedure different errors were assumed for the A2D Rayleigh winds (2 m/s) and the 2-µm winds (1 m/s) yielding a slope of 1.06 with an uncertainty of 2 % (Tab. 4.5). No altitude dependency is found for the Mie channel (Fig. 4.20, right). The standard deviation of 1.54 m/s found for the Mie channel is much smaller than the 2.53 m/s and both values are comparable to the standard deviations obtained for 2009/09/26 (Tab. 4.3). With the 2-µm Lidar operating in LOS mode during this wind measurement section, both Lidars were sampling the same atmospheric volumes. Consequently, the error associated with spatial representativeness can be assumed negligible. The fact that the wind retrieval was performed with a mean flight altitude, despite the Falcon declining by about 250 m during the measurement time, might contribute to the overall error.

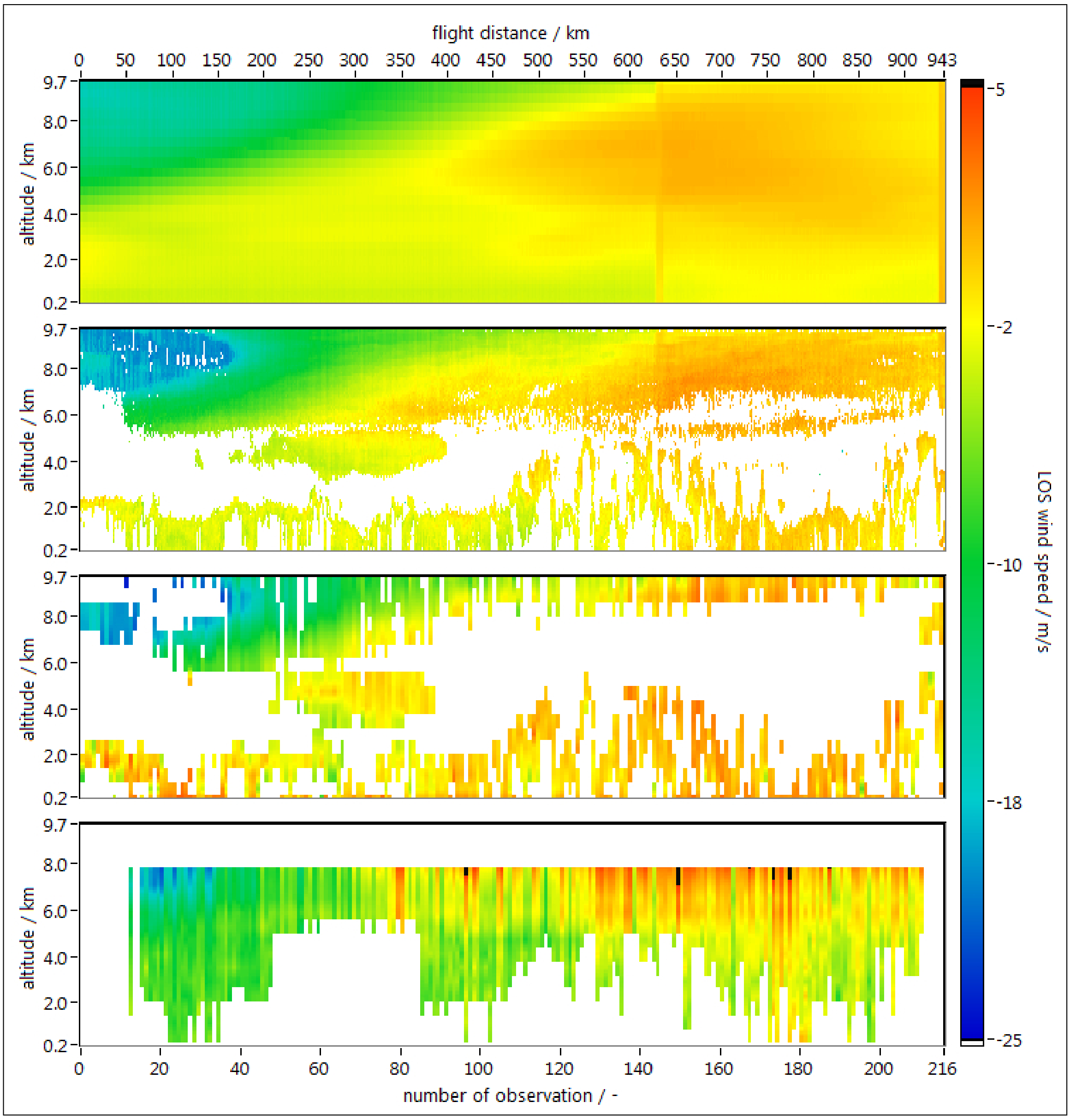

Figure 4.19.: LOS wind speeds as obtained on 2009/10/01 from ECMWF analyses (top) and measurements of the 2-µm Lidar (2nd from top), the A2D Mie channel (3rd from top) and the A2D Rayleigh channel (bottom). The altitudes of 9.7 km and 0.2 km approximately correspond to the upper/lower borders of the A2D range-gates #6 / #21, respectively. White colour represents invalid winds due to low aerosol signal (Mie channel) or to exclusion below clouds and in the region of the telescope overlap (Rayleigh channel). Measured LOS wind speed ranges from minimum -25 m/s to maximum more than 20 m/s (black, Rayleigh channel).

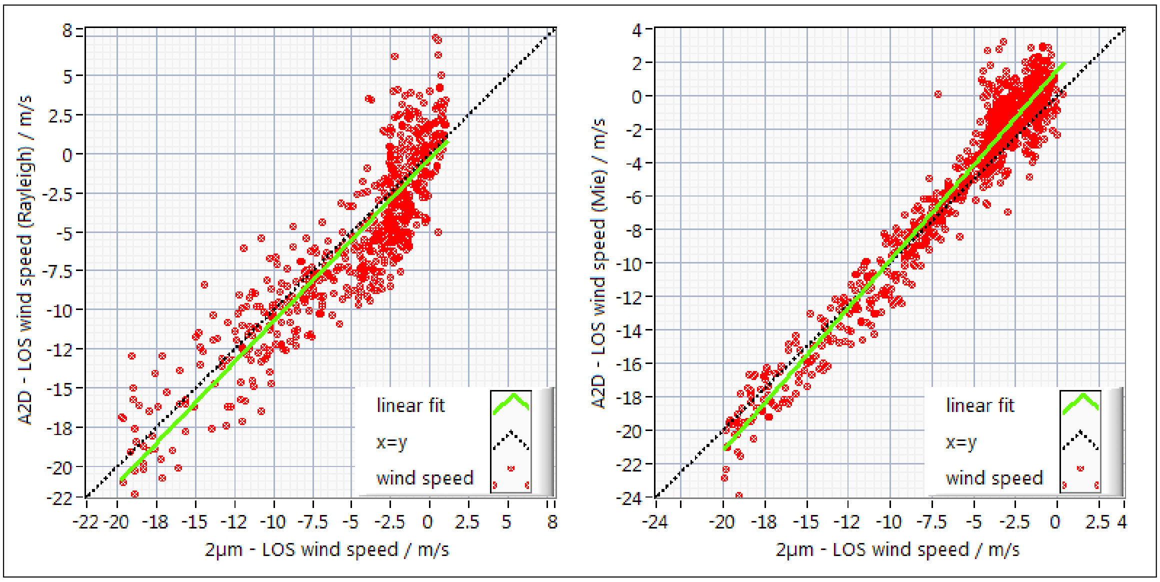

Figure 4.20.: Left: Scatterplot of winds measured by the 2-µm Lidar and the A2D Rayleigh channel (according to case f)) within range-gates #9 - #21 (Internal Reference = #4) processed with the 2nd calibration from 2009/09/21. Right: Scatterplot of winds measured by the 2-µm Lidar and the A2D Mie channel within range-gates #6 - #21 (Internal Reference = #4) processed with the 2nd calibration from 2009/09/21 and corrected for the Rayleigh background (subsec. 3.4.6). The linear fit lines (green) and the ideal x=y lines (dashed, black) are indicated.

Table 4.5.: Results of statistical comparisons of winds measured by the A2D and the 2-µm Lidar on the 2009/09/29 between 09:35.02 - 10:39.48 UTC. The Rayleigh winds were calculated with the 2nd calibration according to case h) (subsection 4.2.3). A coverage ratio of 50% was applied. The Internal Reference is located in range-gate #4. The uncertainties of the slope and intercept for the Mie channel were estimated according to Eq. 4.12 by allocating an error of 1.5 m/s and 1.0 m/s to the A2D and 2-µm winds, respectively.

		Rayleigh ⇔ 2-µm	Mie ⇔ 2-µm
range-gates		#9 - #21	#5 - #21
slope		1.04 ± 0.02	1.14 ± 0.01
slope error	/ %	4 ± 0.02	14 ± 0.01
intercept	/ m/s	-0.33 ± 0.09	1.75 ± 0.07
µ(mean bias)	/ m/s	-0.52	0.75
median	/ m/s	-0.72	0.78
σ(std. dev.)	/ m/s	2.53	1.54
r (correlation coeff.)		0.89	0.97
# of compared winds		596	932

As can be seen in Fig. 4.19 and as found from a corresponding statistical comparison (Fig. 4.21), the winds measured by the 2-µm Lidar agree well with the winds modelled by the ECMWF (difference is shown in Fig. A.20). A standard deviation of 1.58 m/s and a mean bias of 0.12 m/s are obtained, despite the simplified assumption of a linear interpolation in time between the two ECMWF analyses, which likely induces additional uncertainty because the temporal evolution of the wind field might have been more complex. Comparing the wind speeds in the region of the jet-stream (blue) it can be confirmed that the ECMWF model is prone to an underestimation of the high wind speed in a jet-stream (Weissmann and Cardinali (2007), Cardinali et al. (2004)). A small region of LOS wind speeds of up to -20 m/s according to the 2-µm Lidar are slightly offset in Fig. 4.21, illustrating the sharp boundary of the jet-stream. The wind measurements after the turn of the aircraft at 10:16 UTC (Fig. A.20), which results in a change in LOS direction, are recognisable by an offset in the region with wind speeds higher than -4 m/s.

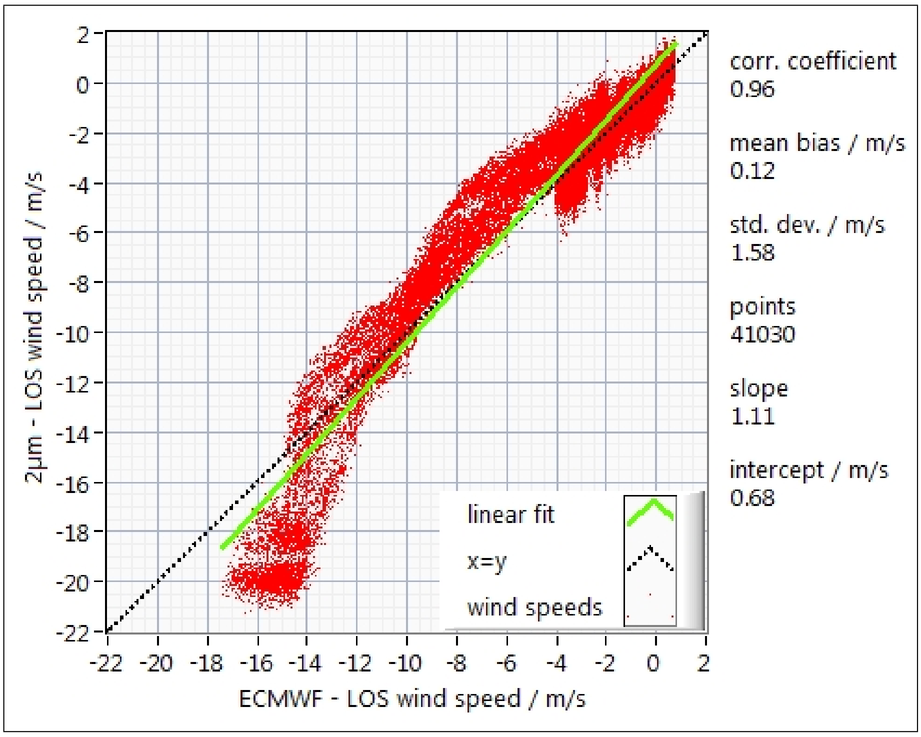

Figure 4.21.: Summarised results of a statistical comparison of winds measured by the 2-µm Lidar and provided by the ECMWF model for 2009/10/01 between 09:35 - 10:39 UTC. According to the measurement grid of the 2-µm Lidar, the scatterplot compares 41,030 range-bins (red dots) between the sea surface and an altitude of 10 km. The linear fit line (green) and the ideal x=y line (dashed, black) are also indicated.

4.5. Discussion of expected wind retrieval errors

Although it is only a single quantity, the derivation of reliable wind speed from measurements of a direct-detection Lidar such as the A2D is challenging. In particular the high accuracy needed regarding the ratio of the Doppler frequency shift to the absolute frequency and the novel arrangement of the spectrometers contribute to the complexity of this task. Eq. 3.26 is the basic formulation for the LOS wind speed measured by the A2D. After combining this equation with Eqs. 3.4, 3.5 and 3.25 it is still valid for both Mie and Rayleigh channel. Additionally considering Eqs. 3.17a and 3.20 yields Eq. 4.14 which is specific for the Rayleigh channel and illustrates the numerous potential contributors to the error in the LOS wind speed v_{los}.

$$
\begin{aligned}
v_{\mathrm{los}} = & \left(\frac{\frac{I_{\mathrm{A,ATM}}-I_{\mathrm{B,ATM}}}{I_{\mathrm{A,ATM}}+I_{\mathrm{B,ATM}}} - \gamma_{\mathrm{ATM}} - \alpha_{\mathrm{ATM}}}{\beta_{\mathrm{ATM}}} - \frac{\frac{I_{\mathrm{A,INT}}-I_{\mathrm{B,INT}}}{I_{\mathrm{A,INT}}+I_{\mathrm{B,INT}}} - \gamma_{\mathrm{INT}} - \alpha_{\mathrm{INT}}}{\beta_{\mathrm{INT}}} \right) \cdot \frac{\lambda_0}{2} \\
& - \begin{pmatrix} v_{\mathrm{ac,NS}} \\ v_{\mathrm{ac,EW}} \\ v_{\mathrm{ac,V}} \end{pmatrix} [\boldsymbol{YPR} \cdot \vec{p}_{\mathrm{ac}}] - v_{\mathrm{ZWC}}
\end{aligned}
\tag{4.14}
$$

The variation of λ_0 is given by the accuracy of the WM to about 3 MHz which is negligibly small ($3.5 \cdot 10^{-9}$) compared to the absolute frequency of ≈ 844 THz. The rotation matrices *YPR* contain the information about the roll angle (α), the pitch angle (β) as well as the true heading (γ) of the aircraft. Along with the components $v_{\mathrm{ac,NS}}$, $v_{\mathrm{ac,EW}}$ and $v_{\mathrm{ac,V}}$ of the velocity vector of the aircraft they are provided by the IRS and GPS. The mechanical mounting angles of the A2D are represented by $\vec{p}_{\mathrm{ac}}$. The corresponding accuracies are not quantified and can only be estimated unless a dedicated measurement procedure is developed. Regarding the 2-µm Lidar the errors in the measured wind speed induced by such uncertainties in the mounting angles are corrected with a dedicated procedure. Experiences show that the systematic error is in the order of 1° and the variation from campaign to campaign of about 0.2°. These numbers itself are uncertain in the way that they depend on the varying temporal and mechanical stress affecting the aircraft structure during the flights. If applied, the ZWC value v_{ZWC} bears a high error potential since this value itself already implies the whole processing chain. Depending on how the ZWC is performed, whether as a mean value over several observation (as it is used in this thesis) or directly for every single observation, it becomes noticeable in v_{los} as a systematic or random error, respectively. Accuracies for the quantities α_{ATM}, β_{ATM}, γ_{ATM}, α_{INT}, β_{INT} and γ_{INT} that describe the atmospheric and the internal response functions on a frequency interval of ± 500 MHz are given in Tab. 3.6. The intensities I_{A} and I_{B} are derived according to Eqs. 3.17b and 3.17c. Thereby, the value of I_{DCO} can be regarded to be very accurate especially after applying the outlier control. In consequence of a long integration time also the values of I_{BKG} are assumed as very accurate. Thus, the raw signal I_{raw} itself is suspected to be the largest contributor to the uncertainties in the measured wind speed. In this respect a noise level was found which is about a factor of 10 larger than expected from Poisson-distributed photon noise and which appears not only on the atmospheric signals but also on the Internal

Reference (subsec. 3.4.5). The reason for such enhanced noise will be investigated in the near future. Only if the source of this noise is understood and significantly reduced, the effects of other noise sources will become apparent and allow further improvement of the overall A2D performance. An overview of the single contributors to the error of the A2D LOS wind speed v_{los} is given in Tab. 4.6.

Table 4.6.: Contributors to the error in the Rayleigh wind retrieval and a rough assessment of their impact.

quantity	accuracy	influence onto A2D error	assessed impact	comment
λ_0	3 MHz	random	minor	accuracy of wavelength meter
α	0.1°	random	minor	IRS[8] Falcon
β	0.1°	random	minor	IRS[8] Falcon
γ	0.4°	random	medium	IRS[8] Falcon
α_{INT}	± 0.06	systematic	major	enhanced noise also on INT
β_{INT}	$\pm 0.02 \cdot 10^{-4}$/MHz	systematic	medium	important for high wind speeds
γ_{INT}	$<$ 8 MHz	systematic	major	reduced if corrected for non-linearity
α_{ATM}	± 0.15	systematic	major	associated with overlap function
β_{ATM}	$\pm 0.052 \cdot 10^{-4}$/MHz	systematic	medium	important for high wind speeds
γ_{ATM}	$<$ 16 MHz	systematic	major	reduced if corrected for non-linearity
$v_{\mathrm{ac,NS}}$	≈ 0.1 m/s	random	minor	GPS (see Weissmann et al. (2005))
$v_{\mathrm{ac,EW}}$	≈ 0.1 m/s	random	minor	GPS (see Weissmann et al. (2005))
$v_{\mathrm{ac,V}}$	-	random	medium	
$I_{\mathrm{raw,INT}}$	1 % - 10 %	random	major	larger than Poisson noise
$I_{\mathrm{raw,ATM}}$	1 % - 15 %	random	major	larger than Poisson noise
I_{DCO}	$<$ 0.5 LSB	random	minor	after outlier correction
I_{BKG}	≈ 3 LSB	random	minor	16 pixel mean, exhibits outliers
$\vec{p}_{\mathrm{ac}}$	$\approx 0.2°$	systematic	minor	experience from 2-µm Lidar
v_{ZWC}	≈ 1 m/s	systematic	major	strong ground return needed

Regarding the atmospheric path of the Rayleigh channel the angular sensitivity in interaction with the alignment jitter is implicitly contained in the variation of $I_{\mathrm{raw,ATM}}$ in Tab. 4.6. Another error source which is not considered in Eq. 4.14 and Tab. 4.6 is the neglect of the differences in the atmospheric state, i.e. pressure and temperature, between the calibration and the wind measurement. The shape of the Rayleigh-Brillouin spectrum is mainly governed by the temperature and the largest difference with respect to the wind measurement on 2009/09/26 was found to be 15°C at an altitude of 7 km. Such temperature differences would induce a systematic wind speed error in the order of several tenths of a metre as assessed by, for instance, Korb et al. (1992), Flesia and Korb (1999), Reitebuch et al. (2010) and Witschas et al. (2010). An error that affects both Rayleigh and Mie channel is mutual contamination of signals caused by the sequential arrangement of the two spectrometers (subsec. 2.3.2). A correction of Rayleigh measurements for contamination by Mie signal is suggested by Dabas et al. (2008) but was not applied within this thesis. However, in cases where reasonably strong Mie scattering is present,

---

[8] `http://www.dlr.de/fb/desktopdefault.aspx/tabid-3718/5796_read-8414/`

the winds retrieved from the A2D Mie channel will generally be preferred over the ones from the Rayleigh channel because of their better accuracy (sec. 4.4).

Regarding the Mie channel, the Rayleigh responses of the form $(I_\mathrm{A} - I_\mathrm{B})/(I_\mathrm{A} + I_\mathrm{B})$ must be substituted for the corresponding responses $R_\mathrm{M}(f)$ (Eq. 3.18). Accordingly, Tab. 3.4 must be considered for the values of α, β and γ and their variations. Thereby, the accuracy of the measured pixel index $R_\mathrm{M}(f)$ is governed by the Downhill Simplex Algorithm (ch. A.1) whose accuracy was examined, for instance, by Paffrath (2006) with simulated signals indicating a systematic and a random error both in the order of 0.1 m/s. Additionally, a mutual influence onto the measured signals is present due to the combined arrangement of the Mie and Rayleigh spectrometers, i.e. the Rayleigh background on the Mie channel (Fig. 3.24) and the sensitivity of the Rayleigh channel with respect to aerosol signal (subsec. 2.3.2).

For the interpretation of the results of the statistical comparisons it is noted that a common use of slope and intercept is preferred over the statement of a single value of a systematic bias. This is a consequence of the present slope errors which render the bias of a specific wind measurement dependent on the magnitude of the wind speed itself. The parametrisation of slope, intercept and standard deviation was also used by Cohn and Goodrich (2002) who compared the radial velocities of a radar wind profiler and a Doppler Lidar.

While the ZWC value changed by roughly 5 m/s between 2009/09/26 and 2009/09/29 for the Rayleigh channel in consequence of the high sensitivity of the FPI's to the incidence angles (Witschas et al. (2012b)), it stayed constant at about 2 m/s for the Mie channel (Fig. A.16 and Fig. A.17). The reason for the fact that the Mie ZWC value is different from zero might be found in the correction of the Rayleigh background (subsec. 3.4.6) or by atmospheric contamination of the range-gate containing the ground return.

The random, systematic and wind speed dependent errors for ADM-Aeolus are given with respect to the projection of the measured wind speed onto the horizontal plane, i.e. with respect to the horizontal line-of-sight (HLOS). Thus, an according projection must be considered for the requirements of the ADM-Aeolus mission on the LOS direction. In order to fulfil the requirement of about 2 m/s accuracy with respect to the HLOS, the LOS wind speed measurements of the satellite would have to exhibit a random error of about 1.2 m/s $(2\,\mathrm{m/s} \cdot \sin(37.5°))$. As the random error of the LOS wind speeds of the A2D Rayleigh channel is in the order of 2.0 m/s - 2.5 m/s and the viewing angle of 20° is less favourable than for ADM-Aeolus, the requirements posed onto the satellite mission cannot be met by the A2D in its current state. This result should be viewed with regard to simulations by Paffrath et al. (2009) who showed that the signal intensities for ADM-Aeolus can be expected to be approximately 10 times lower than for the A2D airborne measurements. A better performance of the A2D is most likely prevented by the alignment jitter and the enhanced noise, which is much higher than currently assumed for the ADM-Aeolus mission.

4.6. Summary

In three case studies the first wind profiles retrieved from A2D measurements in an airborne configuration were presented and validated. A bi-linear interpolation algorithm was developed in order to spatially match the different grids of the A2D, the 2-µm Lidar and the ECMWF analyses. By deriving weights for single A2D winds and by allocating dedicated errors to both A2D and 2-µm winds, parameters as slope and intercept along with respective uncertainties could be derived from statistical comparisons. A sequence of statistical comparisons by successively applying the developed corrections, quality controls and the two calibrations illustrated their impact onto the error in the measured A2D wind speeds. Random errors of less than 2.5 m/s and 1.5 m/s were found for the Rayleigh and the Mie channel, respectively. An altitude dependent systematic offset in wind speed seems to be present in the Rayleigh channel. The procedure of a ZWC was successfully applied taking into account a mismatch of the axes of the A2D telescope and laser beam. Moreover, the A2D and 2-µm Lidar observations were analysed in the context of ECMWF analyses, a radiosonde and recordings of the MODIS, AVHRR and QuickScat instruments. The occurrence of a katabatic wind at the east coast of Greenland, high altitude jet-streams and structures of isolated convection cells over the between Iceland and Norway were highlighted.

5. Conclusion and outlook

Conclusion

According to the World Meteorological Organisation measurements of wind profiles on a global scale are considered to be crucial for numerical weather prediction and climate studies. In order to fulfil this demand the European Space Agency ESA implemented the Earth Explorer Mission ADM-Aeolus whose launch is scheduled for 2015. For the purpose of pre-launch validation, an airborne prototype of the satellite instrument was developed, the ALADIN Airborne Demonstrator (A2D). In September 2009 two Doppler wind Lidars, the A2D along with a coherent 2-µm instrument, were deployed onto the DLR Falcon 20 aircraft during an airborne campaign over Greenland, Iceland and the North Atlantic region and they provided an unprecedented data set. For the first time worldwide wind profiles were obtained from an airborne direct-detection Doppler Lidar operating in the UV spectral range at 355 nm and measuring Mie backscatter from aerosols or clouds and Rayleigh backscatter from molecules simultaneously. In the frame of this thesis, the observations of 10 flights including 33 flight hours were analysed, thereby developing new retrieval algorithms and validating the measurements of the A2D.

Unique features of the A2D are the Fizeau interferometer applying the fringe imaging technique, the sequential arrangement of two Fabry-Pérot interferometers (FPI) for the double-edge technique, the combined arrangement of the Fizeau and the FPI as well as the usage of a novel Accumulation Charge Coupled Device (ACCD) as detector. Benefiting from a cross-coupling between adjacent range-gates based on the principle of the ACCD, algorithms were developed that allow the reliable detection of ground and clouds as well as their discrimination. In turn, this enabled the derivation of a response calibration function for the ground return and a comparison of its properties to those related to the emitted laser pulse. Moreover, the principle of Zero Wind Correction, which aims at correcting wind speeds from the error induced by unknown mispointing, could successfully be applied, thereby showing the need, adequacy and limits of this procedure. It was found that the extension of the interval of the response calibration from 1 GHz (as foreseen for ADM-Aeolus) to 1.7 GHz permits the consideration of the non-linearity of the response function and hence a reduction of random and systematic errors. Therefore, a 5th order polynomial fit proved to be a very accurate approximation. Further corrections have been applied regarding the Rayleigh background on the Mie channel, the aircraft induced LOS velocity and the measurement of the absolute laser frequency. Quality controls in terms of outlier detection and exclusion as well as signal variation, signal-to-noise-ratios and cloud masks were implemented.

During the airborne campaign two simultaneously operating wind Lidar instruments were flown on the same aircraft for the first time worldwide. Employing the coherent technology the wind measurements provided by the well established coherent 2-µm DWL are characterised by low random ($< 0.5\,\mathrm{m/s}$ for 1 s averaging) and systematic ($< 0.1\,\mathrm{m/s}$) errors and a high spatial resolution compared to the A2D. These properties rendered the 2-µm lidar an independent and ideal reference for the characterisation of the errors present in the A2D wind speed measurements. A bi-linear interpolation algorithm was developed and allowed a statistical comparison of the measured wind speeds by using weighted linear fits.

Considering the questions raised in the introduction, random errors of maximum 2.5 m/s and 1.5 m/s were found on different flight tracks for the Rayleigh and the Mie channel. Comparisons of single altitude layers revealed errors of less than 2 m/s and 1 m/s and a slight dependence on altitude. Additionally, a systematic error in the order of $\pm\,1\,\mathrm{m/s}$ for both channels and wind speed dependent errors of several percent are present. The enhanced noise present on the signal of the Internal Reference as well as on atmospheric signals, the uncertainty in the offset of the atmospheric response calibration functions and the uncertainty in the laser pointing direction were found to be the major contributors to the error in the wind speed. By developing a new correction method with respect to the non-linearity of the response calibration function and by applying a Zero Wind Correction, these contribution could partly be accounted for. The newly developed algorithm of summation of ground return signals enabled a more accurate detection of the altitude of the surface and, in comparison to a DEM, a distinction between clouds and ground signal. Two methods that were developed in this thesis, the summation of ground return signal and the non-linearity correction, are currently being tested for integration into the operational L1B processor of the ADM-Aeolus mission. It was shown that with the present random error of 2.0 m/s - 2.5 m/s on the LOS wind speeds of the A2D Rayleigh channel the requirements posed onto the satellite mission cannot be met by the A2D in its current state due to the enhanced instrument noise. A meteorological analysis of the A2D measurements in the context of data from a radiosonde station, flight data of the Falcon aircraft and satellite imagery of the MODIS, AVHRR and QuickScat instruments revealed the occurrence of katabatic winds at the east coast of Greenland, high altitude jet-streams and structures of isolated convection due to breakouts of cold air from the Arctic. Moreover, A2D and 2-µm winds and wind directions were compared to ECMWF analyses highlighting a discrepancy in the location of a jet stream between model and measurements and confirming the underestimation of the velocities in a jet-stream by the ECMWF model.

New retrieval algorithms were developed and their application along with additional quality control schemes, mainly for other geographical locations (e.g. Tropics) or atmospheric conditions (e.g. aerosol-rich air masses), yielded wind speeds that agreed well with data from independent sources (see aim [(1)]). A thorough investigation of the performed calibrations and the respective response functions as well as the detailed examination of the error sources gave insights into the characteristics of the instrument performance [(2)]. Regarding the high quality response calibration functions derived from the airborne observations, the validation of the measurement principle of the A2D, in particular the calibration strategy in downward viewing geometry over ice surfaces, could be achieved [(3)]. The consistency of the results of the wind speed comparisons and the analysis of the A2D wind speeds in the context of satellite imagery and numerical models validated the A2D wind measurement results [(4)].

Outlook

Future airborne campaigns will provide the possibility to perform additional response calibrations allowing a more detailed assessment of the influences onto their variability, in particular regarding the Rayleigh channel (Fig. 4.10). An extended database of wind measurements will foster the enhancement of the retrieval algorithms and quality control schemes. These could greatly profit from the implementation of a cross-observational grouping of measurements, which is the accumulation of signals according to whether or not, for instance a cloud has been hit, as it is currently studied in the frame of the operational L2B processor at ECMWF. Most importantly, the A2D is considered as the core instrument for the validation of the ADM-Aeolus mission after the launch of the satellite. Integrated onto an aircraft which will follow the ground track of the satellite, the A2D will perform crucial collocated measurements. The ALADIN instrument is only tested under laboratory environments and will not perform measurements with realistic atmospheric signal patterns before the launch. Thus, it is expected that much effort will be required in order to consolidate the initial ADM-Aeolus products. In this respect, the A2D can provide wind measurements throughout the lifetime of the ADM-Aeolus mission and contribute to the survey of the long-term stability of the satellite instrument.

Apart from being the most suitable instrument for validation of the ADM-Aeolus mission, the A2D also constitutes a promising tool for the study of atmospheric processes on spatial scales of a few kilometers that are not accessible to the satellite with its horizontal resolution of about 100 km for a single observation. In contrast to heterodyne Lidars, the A2D entails the great advantage of providing wind speed measurements in regions without aerosol by exploiting the molecular backscatter. For example, spatial structures, such as the exact location of weather fronts or jet-streams, can be identified more precisely compared to numerical weather forecasts, especially in regions of sparse data coverage. Measurements of the albedo of various ground surfaces can contribute to the extension of databases in the UV spectral region (Manninen (2012)). Combined with the determination of terrain slopes by using a more accurate DEM, bi-directional reflectance functions can be derived.

A new laser for the A2D will be delivered in 2013. Due to its higher power and pulse repetition frequency it will permit more accurate wind measurements. Recent studies investigated the integration of a scanning device that would allow to retrieve 3-dimensional wind velocity vectors (Klisa (2012)). If deployed on the new DLR aircraft HALO (High Altitude and Long Range Research Aircraft), which outmatches the Falcon 20 aircraft particularly in terms of maximum flight altitude and range, such an A2D configuration will be an even more powerful tool for studying the dynamics of the atmosphere as foreseen for the planned campaigns using the HALO aircraft in the framework of T-NAWDEX (The Observing System Research and Predictability Experiment - North Atlantic Waveguide and Downstream Impact Experiment).

Bibliography

Abreu, V. J. (1979). Wind measurements from an orbital platform using a lidar system with incoherent detection: an analysis. *Applied Optics*, 18(17):2992–2997.

Abreu, V. J., Barnes, J. E., and Hays, P. B. (1992). Observations of winds with an incoherent lidar detector. *Applied Optics*, 31(22):4509–4514.

Amediek, A., Fix, A., Ehret, G., Caron, J., and Durand, Y. (2009). Airborne lidar reflectance measurements at 1.57 μm in support of the A-SCOPE mission for atmospheric CO2. *Atmospheric Measurement Techniques*, 2(2):755–772.

Ansmann, A., Wandinger, U., LeRille, O., Lajas, D., and Straume, A. G. (2007). Particle backscatter and extinction profiling with the spaceborne high-spectral-resolution Doppler lidar ALADIN: methodology and simulations. *Applied Optics*, 46(26):6606–6622.

Baker, W. E., Emmitt, G. D., Robertson, F., Atlas, R. M., Molinari, J. E., Bowdle, D. A., Paegle, J., Hardesty, R. M., Post, M. J., Menzies, R. T., Krishnamurti, T. N., Brown, R. A., Anderson, J. R., Lorenc, A. C., and McElroy, J. (1995). Lidar-Measured Winds from Space: A Key Component for Weather and Climate Prediction. *Bulletin of the American Meteorological Society*, 76(6):869–888.

Baumgarten, G. (2010). Doppler Rayleigh/Mie/Raman lidar for wind and temperature measurements in the middle atmosphere up to 80 km. *Atmospheric Measurement Techniques*, 3(6):1509–1518.

Behrendt, A., Nakamura, T., Onishi, M., Baumgart, R., and Tsuda, T. (2002). Combined Raman Lidar for the Measurement of Atmospheric Temperature, Water Vapor, Particle Extinction Coefficient, and Particle Backscatter Coefficient. *Applied Optics*, 41(36):7657–7666.

Belmonte, A. (2008). Uncertainty Analysis in Doppler Wind Lidars based on Fizeau wedges. In *Proceedings at the 24th International Laser Radar Conference*, pages 164–164, Boulder, Colorado, USA.

Benedetti-Michelangeli, G., Congeduti, F., and Fiocco, G. (1972). Measurement of Aerosol Motion and Wind Velocity in the Lower Troposphere by Doppler Optical Radar. *Journal of the Atmospheric Sciences*, 29(5):906–910.

Bilbro, J., Fichtl, G., Fitzjarrald, D., Krause, M., and Lee, R. (1984). Airborne Doppler Lidar Wind Field Measurements. *Bulletin of the American Meteorological Society*, 65(4):348–359.

Bu, L., Shan, K., Huang, X., Liu, J., Zhou, J., and Chen, W. (2008). Direct-detection wind lidar system based on Fizeau interferometer. In *Proceedings at the 24th International Laser Radar Conference*, pages 64–67, Boulder, Colorado, USA.

Cardinali, C., Rukhovets, L., and Tenenbaum, J. (2004). Jet Stream Analysis and Forecast Errors Using GADS Aircraft Observations in the DAO, ECMWF, and NCEP Models. *Monthly Weather Review*, 132(3):764–779.

Chanin, M. L., Garnier, A., Hauchecorne, A., and Porteneuve, J. (1989). A Doppler lidar for measuring winds in the middle atmosphere. *Geophysical Research Letters*, 16(11):1273–1276.

Chintawongvanich, P., Olsen, R., and Biltoft, C. A. (1989). Intercomparison of Wind Measurements from Two Acoustic Doppler Sodars, a Laser Doppler Lidar, and In Situ Sensors. *Journal of Atmospheric and Oceanic Technology*, 6(5):785–797.

Cohn, S. A. and Goodrich, R. K. (2002). Radar Wind Profiler Radial Velocity: A Comparison with Doppler Lidar. *Journal of Applied Meteorology*, 41(12):1277–1282.

Cosentino, A., D'Ottavi, A., Sapia, A., and Suetta, E. (2012). Spaceborne Lasers Development for ALADIN and ATLID Instruments. In *Proceedings at the International Geoscience and Remote Sensing Symposium*, pages 5673–5675, Munich, Germany.

Dabas, A., Denneulin, M. L., Flamant, P., Loth, C., Garnier, A., and Dolfi-Bouteyre, A. (2008). Correcting winds measured with a Rayleigh Doppler lidar from pressure and temperature effects. *Tellus A*, 60(2):206–215.

Delaval, A., Flamant, P. H., Loth, C., Garnier, A., Vialle, C., Bruneau, D., Wilson, R., and Rees, D. (2000). Performances Validation of Direct Detection and Heterodyne Detection Doppler WIND Lidars; Final Report VALID 2. Technical report, CNRS/IPSL.

Demoz, B., Gentry, B., Bacha, T., Vermeesch, K., Chen, H., Venable, D., Koch, G., Singh, U., Boquet, M., Sauvage, L., and Joseph, E. (2010). A Wind Lidar Comparison Experiment at The Howard University Beltsville Atmospheric Observatory. In *Proceedings at the 25th International Laser Radar Conference*, pages 324–327, St.Petersburg, Russia.

Demoz, B., Vermeesch, K., Gentry, B., Chen, H., Bacha, T., Koch, G., Singh, U., and Sauvage, L. (2012). Evaluation of wind lidar instrument at the Howard University Beltsville Research Site. In *Proceedings at the 9th International Symposium on Tropospheric Profiling*, page Session F, L'Aquila, Italy.

Doppler, C. (1842). Über das farbige Licht der Doppelsterne und einiger anderer Gestirne des Himmels. *Aus den Abhandlungen der k. böhm. Gesellschaft der Wissenschaften*, Folge V, Band 2:19.

Doyle, J. D. and Shapiro, M. A. (1999). Flow response to large-scale topography: the Greenland tip jet. *Tellus A*, 51(5):728–748.

Durand, Y., Chinal, E., Endemann, M., Meynart, R., Reitebuch, O., and Treichel, R. (2006). ALADIN airborne demonstrator: a Doppler Wind lidar to prepare ESA's ADM-Aeolus Explorer mission. In *Proceedings at the SPIE (Earth Observing Systems XI)*, volume 6296, page 62961D.

Durand, Y., Meynart, R., Culoma, A. J., Morancais, D., and Fabre, F. (2004). Results of the pre-development of ALADIN, the direct detection Doppler wind lidar for ADM-Aeolus.

In *Proceedings at the SPIE (Sensors, Systems, and Next-Generation Satellites VIII)*, volume 5570, pages 93–104.

Durand, Y., Meynart, R., Endemann, M., Chinal, E., Morancais, D., Schröder, T., and Reitebuch, O. (2005). Manufacturing of an airborne demonstrator of ALADIN: The direct detection Doppler wind lidar for ADM-Aeolus. In *Proceedings at the SPIE (Lidar Technologies, Techniques and Measurements for Atmospheric Remote Sensing)*, volume 5984, page 598401.

EADS-Astrium (2003). ALADIN Instrument PDM - MSPA Tests Report. Technical report, EADS-Astrium. 30/06/2003.

EADS-Astrium (2004). ALADIN Instrument PDM - RSP Tests Report. Technical report, EADS-Astrium. 13/01/2004.

EADS-Astrium (2005). End-to-End Simulator Detailed Processing Model. Technical report, EADS-Astrium. 14/02/2005.

EADS-Astrium (2006). ALADIN Airborne Demonstrator - Acceptance Tests Report. Technical report, EADS-Astrium. 07/02/2006.

EADS-Astrium (2011). Level 1B Master Algorithm Document. Technical report, EADS-Astrium. 02/2011.

EADS-Astrium (2012). End to End Simulator - Instrument input parameters. Technical report, EADS-Astrium. 04/07/2012.

Endemann, M., Dubock, P., Ingmann, P., Wimmer, R., Morancais, D., and Demuth, D. (2004). The ADM-Aeolus Mission - the first wind lidar in space. In *Proceedings at the 22nd International Laser Radar Conference*, ESA Special Publication SP-561, pages 953–956, Matera, Italy.

ESA (1999). The four candidate Earth Explorer core missions: 4. Atmospheric Dynamics Mission. Technical Report SP-1233(4), European Space Agency.

ESA (2004). Intercomparison of ACE and SRTM30 global digital elevation model at global and regional scale. Technical report, European Space Agency.

ESA (2008). ADM-Aeolus Science Report. Technical Report SP-1311, European Space Agency.

Esselborn, M. (2008). *Lidar-Messungen der Extinktion des atmosphärischen Aerosols am Beispiel der Feldstudie SAMUM-1*. PhD thesis, Ludwig-Maximilians-Universität München.

Fiedler, J., Baumgarten, G., and Lübken, F.-J. (2009). NLC observations during one solar cycle above ALOMAR. *Journal of Atmospheric and Solar-Terrestrial Physics*, 71:424 – 433.

Fiocco, G. and Smullin, L. D. (1963). Detection of Scattering Layers in the Upper Atmosphere (60-140 km) by Optical Radar. *Nature*, 199(4900):1275–1276.

Flamant, P., Cuesta, J., Denneulin, M.-L., Dabas, A., and Huber, D. (2008). ADM-Aeolus retrieval algorithms for aerosol and cloud products. *Tellus A*, 60(2):273–288.

Flesia, C. and Korb, C. L. (1999). Theory of the Double-Edge Molecular Technique for Doppler Lidar Wind Measurement. *Applied Optics*, 38(3):432–440.

Flesia, C., Korb, C. L., and Hirt, C. (2000). Double-edge molecular measurement of lidar wind profiles at 355 nm. *Optics Letters*, 25(19):1466–1468.

Fricke, K. and von Zahn, U. (1985). Mesopause temperatures derived from probing the hyperfine structure of the D2 resonance line of sodium by lidar. *Journal of Atmospheric and Terrestrial Physics*, 47:499 – 512.

Fry, E. S., Hu, Q., and Li, X. (1991). Single frequency operation of an injection-seeded Nd:YAG laser in high noise and vibration environments. *Applied Optics*, 30(9):1015–1017.

Garnier, A. and Chanin, M. L. (1992). Description of a Doppler Rayleigh lidar for measuring winds in the middle atmosphere. *Applied Physics B: Lasers and Optics*, 55:35–40.

Gentry, B., McGill, M., Machan, R., Reed, D., Cargo, R., Wilkens, D. J., Hart, W., Yorks, J., Scott, S., Wake, S., Hardesty, M., and Brewer, A. (2010). Flight Testing of the TWiLiTE airborne molecular Doppler Lidar. In *Proceedings at the 25th International Laser Radar Conference*, pages 265–268, St.Petersburg, Russia.

Gentry, B. M., Chen, H., and Li, S. X. (2000). Wind measurements with 355-nm molecular Doppler lidar. *Optics Letters*, 25(17):1231–1233.

Gentry, B. M. and Korb, C. L. (1994). Edge technique for high-accuracy Doppler velocimetry. *Applied Optics*, 33(24):5770–5777.

Gentry, B. M., McGill, M., Schwemmer, G., Hardesty, M., Brewer, A., Wilkerson, T., Atlas, R., Sirota, M., Lindemann, S., and Hovis, F. (2008). New technologies for direct detection Doppler lidar - Status of the TWiLiTE airborne molecular Doppler lidar project. In *Proceedings at the 24th International Laser Radar Conference*, pages 239–243, Boulder, Colorado, USA.

Günther, B., Xiong, X., Salomonson, V., Barnes, W., and Young, J. (2002). On-orbit performance of the Earth Observing System Moderate Resolution Imaging Spectroradiometer; first year of data. *Remote Sensing of Environment*, 83:16–30.

Hardesty, R. M., Brewer, A., Nardell, C. A., Gentry, B. W., Yoe, J. G., and Ryan, J. M. (2001). Intercomparison of heterodyne and direct detection Doppler Lidars during the 2000 Bartlett, N.H., Measurement Campaign. In *Proceedings at the 11th Coherent Laser Radar Conference*, pages 115–118, Malvern, UK.

Hayakawa, Y. S., Oguchi, T., and Lin, Z. (2008). Comparison of new and existing global digital elevation models: ASTER G-DEM and SRTM-3. *Geophysical Research Letters*, 35(17):L17404.

Heese, B., Flentje, H., Althausen, D., Ansmann, A., and Frey, S. (2010). Ceilometer lidar comparison: backscatter coefficient retrieval and signal-to-noise ratio determination. *Atmospheric Measurement Techniques*, 3(6):1763–1770.

Heinemann, G. and Klein, T. (2002). Modelling and observations of the katabatic flow dynamics over Greenland. *Tellus A*, 54(5):542–554.

Hildebrand, J., Baumgarten, G., Fiedler, J., Hoppe, U.-P., Kaifler, B., Lübken, F.-J., and Williams, B. P. (2012). Combined wind measurements by two different lidar instruments in the Arctic middle atmosphere. *Atmospheric Measurement Techniques Discussions*, 5(3):4123–4156.

Hoffman, R. N. and Leidner, S. M. (2005). An Introduction to the Near-Real-Time QuikSCAT Data. *Weather Forecasting*, 20(4):476–493.

Huffaker, R., Jelalian, A., and Thomson, J. (1970). Laser-Doppler system for detection of aircraft trailing vortices. *IEEE Transactions on Geoscience and Remote Sensing*, 58(3):322–326.

Irgang, T. D., Hays, P. B., and Skinner, W. R. (2002). Two-Channel Direct-Detection Doppler Lidar Employing a Charge-Coupled Device as a Detector. *Applied Optics*, 41(6):1145–1155.

Johnson, C., Berry, P., and Hilton, R. (2001). Report on ACE Version1 Generation. Technical report, De Montfort University, Leicester, U.K.

King, M., Menzel, W., Kaufman, Y., Tanre, D., Gao, B.-C., Platnick, S., Ackerman, S., Remer, L., Pincus, R., and Hubanks, P. (2003). Cloud and aerosol properties, precipitable water, and profiles of temperature and water vapor from MODIS. *IEEE Transactions on Geoscience and Remote Sensing*, 41(2):442–458.

Klisa, T. (2012). Laserscanner for an airborne UV Doppler Wind Lidar. Master's thesis, Munich University of Applied Sciences.

Korb, C. L., Gentry, B. M., and Li, S. X. (1997). Edge technique Doppler lidar wind measurements with high vertical resolution. *Applied Optics*, 36(24):5976–5983.

Korb, C. L., Gentry, B. M., Li, S. X., and Flesia, C. (1998). Theory of the Double-Edge Technique for Doppler Lidar Wind Measurement. *Applied Optics*, 37(15):3097–3104.

Korb, C. L., Gentry, B. M., and Weng, C. Y. (1992). Edge technique: theory and application to the lidar measurement of atmospheric wind. *Applied Optics*, 31(21):4202–4213.

Kox, S. (2008). Development and validation of a multilayer cloud detection algorithm for the airborne demonstrator of the direct detection Doppler lidar on ADM-Aeolus. Master's thesis, Ludwig-Maximilians-Universität München.

Köpp, F., Rahm, S., and Smalikho, I. (2004). Characterization of Aircraft Wake Vortices by 2-μm Pulsed Doppler Lidar. *Journal of Atmospheric and Oceanic Technology*, 21(2):194–206.

Käsler, Y., Rahm, S., Simmet, R., and Kuehn, M. (2010). Wake Measurements of a Multi-MW Wind Turbine with Coherent Long-Range Pulsed Doppler Wind Lidar. *Journal of Atmospheric and Oceanic Technology*, 27(9):1529–1532.

LeRille, O., Endemann, M., Culoma, A., and Wernham, D. (2012). ADM-Aeolus: ESA's high spectral resolution Doppler Wind Lidar Mission - Recent achievements and future prospects.

In *Proceedings at the 26th International Laser Radar Conference*, pages 643–646, Porto Heli, Greece.

Li, T., Fang, X., Liu, W., Gu, S.-Y., and Dou, X. (2012). Narrowband sodium lidar for the measurements of mesopause region temperature and wind. *Applied Optics*, 51(22):5401–5411.

Li, Z., Lemmerz, C., Paffath, U., Reitebuch, O., and Witschas, B. (2010). Airborne lidar experimental measurement of the sea surface reflectance. In *Proceedings at the 25th International Laser Radar Conference*, St.Petersburg, Russia.

Li, Z., Lemmerz, C., Paffrath, U., Reitebuch, O., and Witschas, B. (2009). Airborne Doppler Lidar Investigation of Sea Surface Reflectance at a 355-nm Ultraviolet Wavelength. *Journal of Atmospheric and Oceanic Technology*, 27(4):693–704.

Liu, Z., Wu, S., Liu, B., Li, Z., and Wang, Z. (2008). Direct detection wind lidar development for meteorological applications at Qingdao. In *Proceedings at the 24th International Laser Radar Conference*, Boulder, Colorado, USA.

Manninen, A. (2012). Characterization of returns from ice and land surfaces acquired with an airborne ultraviolet LiDAR. Master's thesis, Technical University Munich.

Marksteiner, U. (2006). Study concerning the significance of solar background radiation for a space-borne H2O-Dial system in the spectral region around 940 nm. Diploma thesis, University Stuttgart.

Marksteiner, U. (2009). Aeolus Simulator and Ground Processor Enhancement. Technical report, ESA-ESTEC.

Marksteiner, U., Reitebuch, O., Rahm, S., Nikolaus, I., Lemmerz, C., and Witschas, B. (2011). Airborne direct-detection and coherent wind lidar measurements along the east coast of Greenland in 2009 supporting ESA's Aeolus mission. In *Proceedings at the SPIE*, page 81820J.

Marseille, G. J. and Stoffelen, A. (2003). Simulation of wind profiles from a space-borne Doppler wind lidar. *Quarterly Journal of the Royal Meteorological Society*, 129(594):3079–3098.

McGill, M. J., Skinner, W. R., and Irgang, T. D. (1997a). Analysis techniques for the recovery of winds and backscatter coefficients from a multiple-channel incoherent Doppler lidar. *Applied Optics*, 36(6):1253–1268.

McGill, M. J., Skinner, W. R., and Irgang, T. D. (1997b). Validation of wind profiles measured with incoherent Doppler lidar. *Applied Optics*, 36(9):1928–1932.

McKay, J. A. (1998a). Modeling of Direct Detection Doppler Wind Lidar. I. The Edge Technique. *Applied Optics*, 37(27):6480–6486.

McKay, J. A. (1998b). Modeling of Direct Detection Doppler Wind Lidar. II. The Fringe Imaging Technique. *Applied Optics*, 37(27):6487–6493.

Mie, G. (1908). Beiträge zur Optik trüber Medien, speziell kolloidaler Metalllösungen. *Annalen der Physik*, IV Folge, Band 25:377–445.

Morançais, D. and Fabre, F. (2004). ALADIN: The first European Lidar in Space. In *Proceedings at the 5th International Conference on Space Optics*, page 852, Toulouse, France.

Nelder, J. A. and Mead, R. (1965). A Simplex Method for Function Minimization. *The Computer Journal*, 7(4):308–313.

Nikolaus, I. (2012). Rayleigh channel non-linearity error. Technical note, Physics Solutions. 30/04/2012.

Norm, D. (1970). Luftfahrtnorm 9300, Flugmechanik.

Paffrath, U. (2006). *Performance assessment of the Aeolus Doppler wind lidar prototype.* PhD thesis, Technische Universität München.

Paffrath, U., Lemmerz, C., Reitebuch, O., Witschas, B., Nikolaus, I., and Freudenthaler, V. (2009). The Airborne Demonstrator for the Direct-Detection Doppler Wind Lidar ALADIN on ADM-Aeolus. Part II: Simulations and Rayleigh Receiver Radiometric Performance. *Journal of Atmospheric and Oceanic Technology*, 26(12):2516–2530.

Pavolonis, M. J. and Heidinger, A. K. (2004). Daytime Cloud Overlap Detection from AVHRR and VIIRS. *Journal of Applied Meteorology*, 43(5):762–778.

Press, W. H., Vetterling, W. T., Teucholsky, S. A., and Flannery, B. P. (1992). *Numerical Recipies in C - The Art of Scientific Computing.* Cambridge University Press.

Rahm, S. (2001). Precursor experiment for an active true airspeed sensor. *Optics Letters*, 26(6):319–321.

Rahm, S., Leike, I., Nagel, E., and Werner, C. (2001). Test results of an optical true-airspeed sensor. In *Proceedings at the 11th Coherent Laser Radar Conference*, pages 119–122, Malvern, UK.

Rahm, S., Simmet, R., and Wirth, M. (2003). Airborne two micron coherent Lidar wind profiles. In *Proceedings at the 12th Coherent Laser Radar Conference*, pages 94–97, Bar Harbor, Maine, USA.

Rees, D. and McDermid, I. S. (1990). Doppler lidar atmospheric wind sensor: reevaluation of a 355-nm incoherent Doppler lidar. *Applied Optics*, 29(28):4133–4144.

Reitebuch, O. (2012). *in Schumann, U. (Editor): Atmospheric Physics: Background - Methods - Trends / Wind Lidar for Atmospheric Research*, book 30, pages 487–505. Springer Berlin Heidelberg.

Reitebuch, O., Briegel, J., Marksteiner, U., Freudenthaler, V., and Wiegner, M. (2012a). A2D Mie Radiometric Performance. Technical note, DLR. 31/05/2012.

Reitebuch, O., Chinal, E., Durand, Y., Endemann, M., Meynart, R., Morancais, D., and Paffrath, U. (2004). Development of an airborne demonstrator for ADM-Aeolus and campaign activities. In *Proceedings at the 22nd International Laser Radar Conference*, pages 1007–1010, Matera, Italy.

Reitebuch, O., Endemann, M., Engelbart, D., Freudenthaler, V., Lehmann, V., Lemmerz, C., Nagel, E., Paffrath, U., Rahm, S., and Witschas, B. (2008). Pre-Launch Validation of ADM-Aeolus with an airborne direct-detection wind lidar. In *Proceedings at the 24th International Laser Radar Conference*, pages 41–44, Boulder, Colorado, USA.

Reitebuch, O., Huber, D., and Leike, I. (2012b). ADM-Aeolus Algorithm Theoretical Basis Document ATBD Level1B Products. Technical report, DLR.

Reitebuch, O., Lemmerz, C., Marksteiner, U., Rahm, S., and Witschas, B. (2012c). Airborne lidar observations supporting the adm-aeolus mission for global wind profiling. In *Proceedings at the 26th International Laser Radar Conference*, pages 759–762, Porto Heli, Greece.

Reitebuch, O., Lemmerz, C., Nagel, E., Paffrath, U., Durand, Y., Endemann, M., Fabre, F., and Chaloupy, M. (2009). The Airborne Demonstrator for the Direct-Detection Doppler Wind Lidar ALADIN on ADM-Aeolus. Part I: Instrument Design and Comparison to Satellite Instrument. *Journal of Atmospheric and Oceanic Technology*, 26(12):2501–2515.

Reitebuch, O., Marksteiner, U., and Lemmerz, C. (2012d). ADM-Aeolus Airborne Campaigns Results. Technical note, DLR. 24/02/2012.

Reitebuch, O., Paffrath, U., and Nikolaus, I. (2010). ADM-Aeolus Ground Campaigns Results. Technical note, DLR. 26/02/2010.

Reitebuch, O., Werner, C., Leike, I., Delville, P., Flamant, P. H., Cress, A., and Engelbart, D. (2001). Experimental Validation of Wind Profiling Performed by the Airborne 10-μm Heterodyne Doppler Lidar WIND. *Journal of Atmospheric and Oceanic Technology*, 18(8):1331–1344.

Schmitt, N. P., Rehm, W., Pistner, T., Zeller, P., Diehl, H., and Navé, P. (2007). The AWIATOR airborne LIDAR turbulence sensor. *Aerospace Science and Technology*, 11(7â€“8):546 – 552.

Schröder, T., Lemmerz, C., Reitebuch, O., Wirth, M., Wührer, C., and Treichel, R. (2007). Frequency jitter and spectral width of an injection-seeded Q-switched Nd:YAG laser for a Doppler wind lidar. *Applied Physics B: Lasers and Optics*, 87:437–444.

Schumann, U., Weinzierl, B., Reitebuch, O., Schlager, H., Minikin, A., Forster, C., Baumann, R., Sailer, T., Graf, K., Mannstein, H., Voigt, C., Rahm, S., Simmet, R., Scheibe, M., Lichtenstern, M., Stock, P., Rüba, H., Schäuble, D.and Tafferner, A., Rautenhaus, M., Gerz, T., Ziereis, H., Krautstrunk, M., Mallaun, C., Gayet, J.-F., Lieke, K., Kandler, K., Ebert, M., Weinbruch, S., Stohl, A., Gasteiger, J., Groß, S., Freudenthaler, V., Wiegner, M., Ansmann, A., Tesche, M., Olafsson, H., and Sturm, K. (2011). Airborne observations of the Eyjafjalla volcano ash cloud over Europe during air space closure in April and May 2010. *Atmospheric Chemistry and Physics*, 11:2245–2279.

She, C.-Y., Yue, J., Yan, Z.-A., Hair, J. W., Guo, J.-J., Wu, S.-H., and Liu, Z.-S. (2007). Direct-detection Doppler wind measurements with a Cabannes-Mie lidar: A. Comparison between iodine vapor filter and Fabry-Perot interferometer methods. *Applied Optics*, 46(20):4434–4443.

Souprayen, C., Garnier, A., and Hertzog, A. (1999a). Rayleigh-Mie Doppler wind lidar for atmospheric measurements. II. Mie scattering effect, theory, and calibration. *Applied Optics*, 38(12):2422–2431.

Souprayen, C., Garnier, A., Hertzog, A., Hauchecorne, A., and Porteneuve, J. (1999b). Rayleigh-Mie Doppler wind lidar for atmospheric measurements. I. Instrumental setup, validation, and first climatological results. *Applied Optics*, 38(12):2410–2421.

Stoffelen, A., Marseille, G. J., Bouttier, F., Vasiljevic, D., de Haan, S., and Cardinali, C. (2006). ADM-Aeolus Doppler wind lidar Observing System Simulation Experiment. *Quarterly Journal of the Royal Meteorological Society*, 132(619):1927–1947.

Stoffelen, A., Pailleux, J., Källén, E., Vaughan, J. M., Isaksen, L., Flamant, P., Wergen, W., Andersson, E., Schyberg, H., Culoma, A., Meynart, R., Endemann, M., and Ingmann, P. (2005). The Atmospheric Dynamics Mission for global wind field measurement. *Bulletin of the American Meteorological Society*, 86(1):73–87.

Sun, D., Zhong, Z., Zhou, J., Hu, H., and Kobayashi, T. (2005). Accuracy Analysis of the Fabry-Perot Etalon Based Doppler Wind Lidar. *Optical Review*, 12:409–414. 10.1007/s10043-005-0409-z.

Tan, D. G. H. and Anderson, E. (2005). The ADM-Aeolus satellite to measure wind profiles from space. In *ECMWF Newsletter No.103*. ECMWF.

Tan, D. G. H. and Andersson, E. (2005). Simulation of the yield and accuracy of wind profile measurements from the Atmospheric Dynamics Mission (ADM-Aeolus). *Quarterly Journal of the Royal Meteorological Society*, 131(608):1737–1757.

Tan, D. G. H., Andersson, E., de Kloe, J., Marseille, G.-J., Stoffelen, A., Poli, P., Denneulin, M.-L., Dabas, A., Huber, D., Reitebuch, O., Flamant, P., Le Rille, O., and Nett, H. (2008). The ADM-Aeolus wind retrieval algorithms. *Tellus A*, 60(2):191–205.

Thomas, S. M., Heidinger, A. K., and Pavolonis, M. J. (2004). Comparison of NOAA's Operational AVHRR-Derived Cloud Amount to Other Satellite-Derived Cloud Climatologies. *Journal of Climate*, 17(24):4805–4822.

Vaughan, J. M. (2002). *The Fabry-Perot interferometer.* Adam Hilger, Institute of Physics Publishing, London.

Vaughan, J. M., Geddes, N. J., Flamant, P., and Flesia, C. (1998). Establishment of a backscatter coefficient and atmospheric database. Technical report, ESA report ESA-CR 12510/97/NL/RE.

Vogelmann, H., Sussmann, R., Trickl, T., and Borsdorff, T. (2011). Intercomparison of atmospheric water vapor soundings from the differential absorption lidar (DIAL) and the solar FTIR system on Mt. Zugspitze. *Atmospheric Measurement Techniques*, 4(5):835–841.

Weissmann, M., Busen, R., Dörnbrack, A., Rahm, S., and Reitebuch, O. (2005). Targeted Observations with an Airborne Wind Lidar. *Journal of Atmospheric and Oceanic Technology*, 22(11):1706–1719.

Weissmann, M. and Cardinali, C. (2007). Impact of airborne Doppler lidar observations on ECMWF forecasts. *Quarterly Journal of the Royal Meteorological Society*, 133(622):107–116.

Witschas, B. (2007). Characterization of beam profile and frequency stability of an injection-seeded Nd:YAG laser for a Doppler wind lidar system. Master's thesis, Munich University of Applied Sciences.

Witschas, B. (2011a). Analytical model for Rayleigh-Brillouin line shapes in air. *Applied Optics*, 50(3):267–270. + errata AO(50):5758.

Witschas, B. (2011b). *Experiments on spontaneous Rayleigh-Brillouin scattering in air.* PhD thesis, Friedrich-Schiller-Universität Jena.

Witschas, B., Lemmerz, C., and Reitebuch, O. (2012a). Horizontal lidar measurements for the proof of spontaneous Rayleigh-Brillouin scattering in the atmosphere. *Applied Optics*, 51(25):6207–6219.

Witschas, B., Lemmerz, C., and Reitebuch, O. (2013). Daytime measurements of tropospheric temperature profiles (2-15 km) by Lidar utilizing Rayleigh-Brillouin scattering. *submitted to Optical Society of America*.

Witschas, B., Nikolaus, I., Reitebuch, O., and Lemmerz, C. (2012b). A2D Rayleigh spectrometer alignment sensitivity. Technical note, DLR. 12/01/2012.

Witschas, B., Vieitez, M. O., van Duijn, E.-J., Reitebuch, O., van de Water, W., and Ubachs, W. (2010). Spontaneous Rayleigh–Brillouin scattering of ultraviolet light in nitrogen, dry air, and moist air. *Applied Optics*, 49(22):4217–4227.

World Meteorological Organisation (2012). Statements of Guidance for Global NWP. available from http://www.wmo.int/pages/prog/www/OSY/GOS-RRR.html.

Xia, H., Sun, D., Yang, Y., Shen, F., Dong, J., and Kobayashi, T. (2007). Fabry-Perot interferometer based Mie Doppler lidar for low tropospheric wind observation. *Applied Optics*, 46(29):7120–7131.

Zwally, H., Schutz, B., Abdalati, W., Abshire, J., Bentley, C., Brenner, A., Bufton, J., Dezio, J., Hancock, D., Harding, D., Herring, T., Minster, B., Quinn, K., Palm, S., Spinhirne, J., and Thomas, R. (2002). ICESat's laser measurements of polar ice, atmosphere, ocean, and land. *Journal of Geodynamics*, 34(34):405 – 445.

A. Appendix

A.1. Downhill simplex algorithm

The Fizeau interferometer of the A2D images the incident light as a linear fringe onto an ACCD area of 16 x 16 pixels. A summation of the signal over 16 rows yields an array of signals on 16 pixels representing a single Mie peak. The amplitude, position and width of the Mie peak reflects the amount of aerosol in the targeted atmospheric volume as well as its mean velocity and velocity distribution. The accuracy of the determination of the lateral position of the centroid of this Mie peak governs the accuracy of the derived wind speed. A quality criterion with respect to the width of the Mie peak can be applied, excluding measurements that exhibit spectrally broad peaks as a result of large velocity variations within the sampled volume.

A Lorentzian function L (Eq. A.1) can be used to approximate the shape of the Mie peak and was selected for the analysis of Mie signals of the A2D (Paffrath (2006)) and the ADM-Aeolus mission (EADS-Astrium (2005)). Whereas x is the selected pixel position, x_p is the position of the peak value and Δf_FWHM the full width at half maximum, all in units of pixel. The scaling factor for adapting the amplitude s and the constant offset C, which takes into account the remaining background signal, are determined from fitting the Lorentzian function to the Mie signal.

$$L(x) = \frac{s \cdot \Delta f_\mathrm{FWHM}^2}{4 \cdot \left[(\frac{\Delta f_\mathrm{FWHM}}{2})^2 + (x - x_\mathrm{p})^2 \right]} + C \tag{A.1}$$

An effective method for the minimisation of a function of n (with $n > 1$)) independent variables was introduced by Nelder and Mead (1965). The term *simplex* refers to a geometrical body with $n+1$ vertices in an n-dimensional space. By evaluating the function at the $n+1$ vertices, the vertice with the largest value is determined. Subsequently, it is tried to move this single vertex either by a reflection at the opposite face of the simplex or by a contraction or expansion of the simplex to a lower position. Taking the new simplex and repeating the procedure of evaluation and movement, allows finding the minimum (at least local) of the function.

With respect to the task to find the optimal shape and position of the Lorentzian function to describe the Mie signal, a Downhill Simplex Algorithm (DSA) was implemented according to Press et al. (1992). Whereas s and C are adopted from the initial fit of the Lorentzian function, Δf_FWHM and x_p (Eq. A.1) are considered as the independent variables. Hence, a simplex that exhibits $n = 3$ vertices, i.e. a triangle, moves in a space of $n = 2$ dimensions. Best-guess starting values for the two variables are assumed and a simplex is generated by incrementing according to:

$$\begin{bmatrix} \Delta f_{\mathrm{FWHM}} & ; \; x_{\mathrm{p}} \\ \Delta f_{\mathrm{FWHM}} + \mathrm{d}\Delta f_{\mathrm{FWHM}} & ; \; x_{\mathrm{p}} \\ \Delta f_{\mathrm{FWHM}} & ; \; x_{\mathrm{p}} + \mathrm{d}x_{\mathrm{p}} \end{bmatrix}$$

The Lorentz function is evaluated for these three vertices and compared to the distribution of the measured Mie signal by computing a residual error which is defined as the sum of the squared differences of the respective pixel intensities. Subsequently, the worst vertex is moved to a lower point and the next iteration of evaluation and comparison is started. A termination criterion is defined by taking into account the difference between the currently lowest and highest value of the three vertices. The FWHM and the position of the Mie peak found by the DSA is used in an outer loop to determine new values for the offset C and the scaling factor s, which are in turn again input to the DSA for the next iteration. If the residual error falls below a defined threshold, the outer loop is terminated and the final estimate of the peak location x_{p} is used to determine the wind speed.

A.2. Median filter for 2-µm LOS data

During several flight sections of the airborne campaign the 2-µm Lidar was operating in LOS mode. The provided wind profiles have not been subject to a quality control. Therefore, a median filter is applied to the winds of the 2-µm Lidar before they are compared to A2D winds (sec. 4.4). The filter acts as a quality control and extracts the valid range-bins according to selectable parameters (Tab. A.1).

Table A.1.: Parameters for the median filter with values as applied to the 2-µm LOS wind speed data in sec. 4.4.

size of evaluation area	5 by 5 range-bins 0.5 km (vertical) by 1.0 km (horizontal)
wind speed upper thresh.	30 m/s
wind speed lower thresh.	-30 m/s
max. acceptable difference to median	± 1 m/s
min. fraction of good values	0.35

For the analysis of wind speeds measured during the airborne campaign in Greenland and Iceland, in particular regarding the case study on 2009/10/01 (sec. 4.4), an evaluation area of 5 time 5 range-bins was chosen. This equals 500 m in the vertical and about 1000 m in horizontal direction when assuming a mean aircraft velocity of 210 m/s. The 25 wind speeds within the 5 by 5 area decide about the validity of the wind speed of the central range-bin. In a first step, each of the 25 wind speeds which does not fall within the threshold range of ± 30 m/s are excluded. From the remaining bins the bin with the highest absolute difference to the current mean value is successively deleted until the maximum absolute difference value falls below the acceptance threshold of ± 1 m/s. Then, the value of the current wind bin is considered to be valid. Additionally, the current range-bin is only accepted if the ratio of good range-bins remaining within the acceptance threshold to all 25 range-bins exceeds a fraction of 35 %.

The effect of the median filter that is applied to 2-µm LOS wind speed data from the 2009/09/29 is presented in Fig. A.1. Within the vertical region from 0.2 km - 7.7 km a number of 70950 range-bins could have been possibly measured. The 2-µm data set provided 60036 LOS measurements, out of which 33269 have passed the quality control of the median filter. These remaining valid wind speeds are input to the bi-linear interpolation algorithm discussed in subsec. 4.1.1.

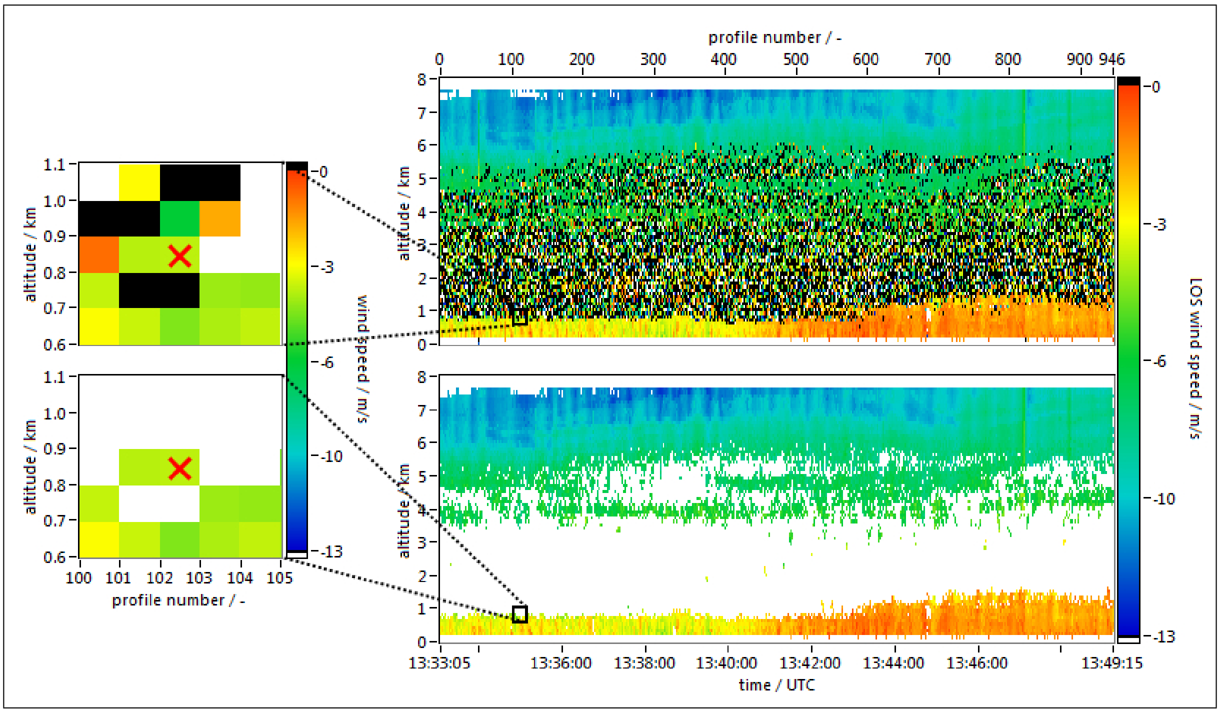

Figure A.1.: The effect of the median filter shown for the measurement period on 2009/09/29 from 09:35 - 09:51 UTC. Right: LOS wind speed measurements of the 2-µm Lidar before (top) and after the application of the median filter (bottom). Left: Zoom into an example section comparing the unfiltered (top) and filtered data (bottom). Since the fraction of good values with the 5 by 5 evaluation area exceeds 0.35, the central bin (marked with a red cross) is considered valid and passes the quality control of the median filter. Invalid wind speeds are indicated in white. White colour within the first 200 m and above 7 km marks regions where no data is available. In the unfiltered data black and white colour symbolise wind speeds that are out of the chosen range of 0 to -13 m/s. The original algorithm was provided by Stephan Rahm (DLR).

A.3. Alternative non-linearity correction

For ADM-Aeolus it is suggested to derive the wind speed by taking into account the sensitivity, the offset and, additionally, the NL. The latter is considered as a function of response, unlike in subsec. 3.4.4 and subsec. 3.5.1, where the NL is used as a function of frequency. So far, a correction for the NL is based on a next neighbour approach (EADS-Astrium (2011)). Due to the equally spaced commanded TLE frequency steps of 25 MHz, the NL with respect to frequency (Fig. 3.17) is well defined over the calibration interval, which assures a bijective function. This is not necessarily the case when considering the NL with respect to the respective responses. Fig. A.2 shows the NL displayed versus the response for the two airborne calibrations.

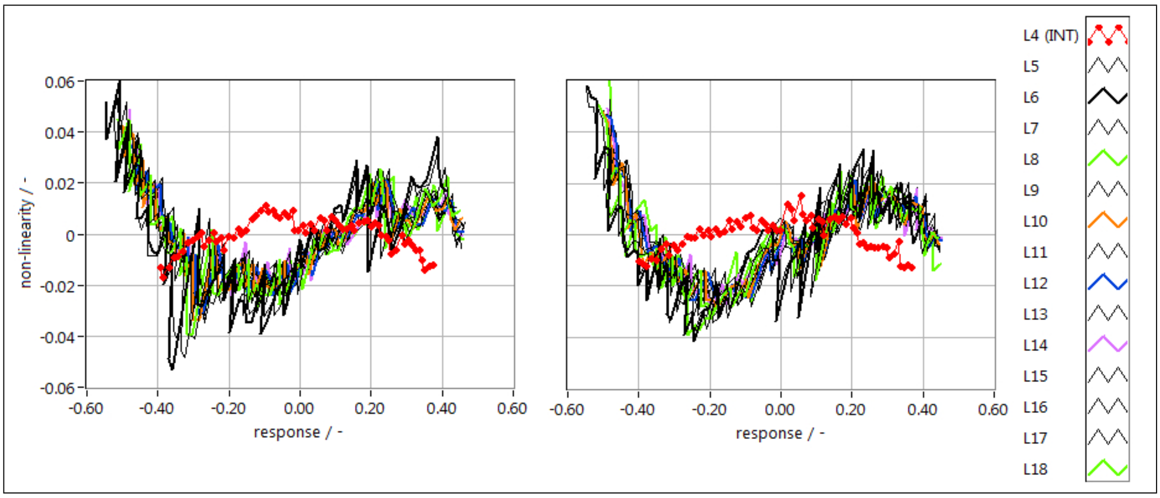

Figure A.2.: The non-linearities of the measured Rayleigh response curves from the 1st (left) and 2nd (right) response calibration for a frequency interval of ± 850 MHz. Non-linearities from response curves of the Internal Reference (INT) and the atmospheric range-gates (L5 - L18) are shown.

As can be seen from the outliers at around (-0.35, 0.05) in the 1st calibration and around (0, 0.03) in the 2nd calibration, an allocation of the NL to the corresponding response value does not necessarily yield a bijective function. Thus, the NL $\gamma_R(R)$ should not be used directly as measured but should be modelled, e.g. by a polynomial fit. In contrast to Eq. 3.21, the response function is then represented by Eq. A.2.

$$R_R(f) = \alpha_R + \beta_R \cdot f + \gamma_R(R) \tag{A.2}$$

The implicit structure of Eq. A.2 requires a slightly different approach for the wind retrieval as sketched in Fig. A.3 compared to Fig. 3.25.

From a measured response R_{meas} obtained in the wind measurement mode, the NL value is determined via the relationship between $\gamma_R(R)$ and the response. Thereafter, the NL value is subtracted from the measured response. The resulting response R_{lin} is used to determine the

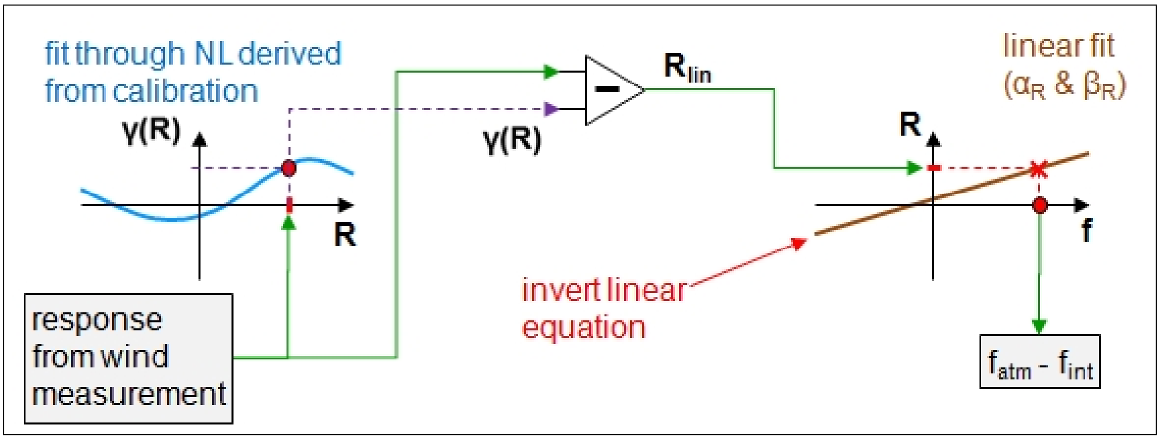

Figure A.3.: Sketch of the wind retrieval scheme incorporating the NL as a function of the response.

relative frequency from the linear (index *lin*) relationship to the frequency, which is defined by the offset α_{R} and the sensitivity β_{R} (Eqs. A.3). Here $\gamma_{\mathrm{RR,i}}$ is the i^{th} coefficient of the polynomial fit through the NL as a function of the response (second index R).

$$R_{\mathrm{lin}} = \alpha_{\mathrm{R}} + \beta_{\mathrm{R}} \cdot f \tag{A.3a}$$

$$f = \frac{R_{\mathrm{meas}} - \gamma(R_{\mathrm{meas}}) - \alpha_{\mathrm{R}}}{\beta_{\mathrm{R}}} \tag{A.3b}$$

$$f = \frac{R_{\mathrm{meas}} - \sum_i \left(\gamma_{\mathrm{RR,i}} \cdot R^i_{\mathrm{meas}}\right) - \alpha_{\mathrm{R}}}{\beta_{\mathrm{R}}} \tag{A.3c}$$

A.4. Additional figures

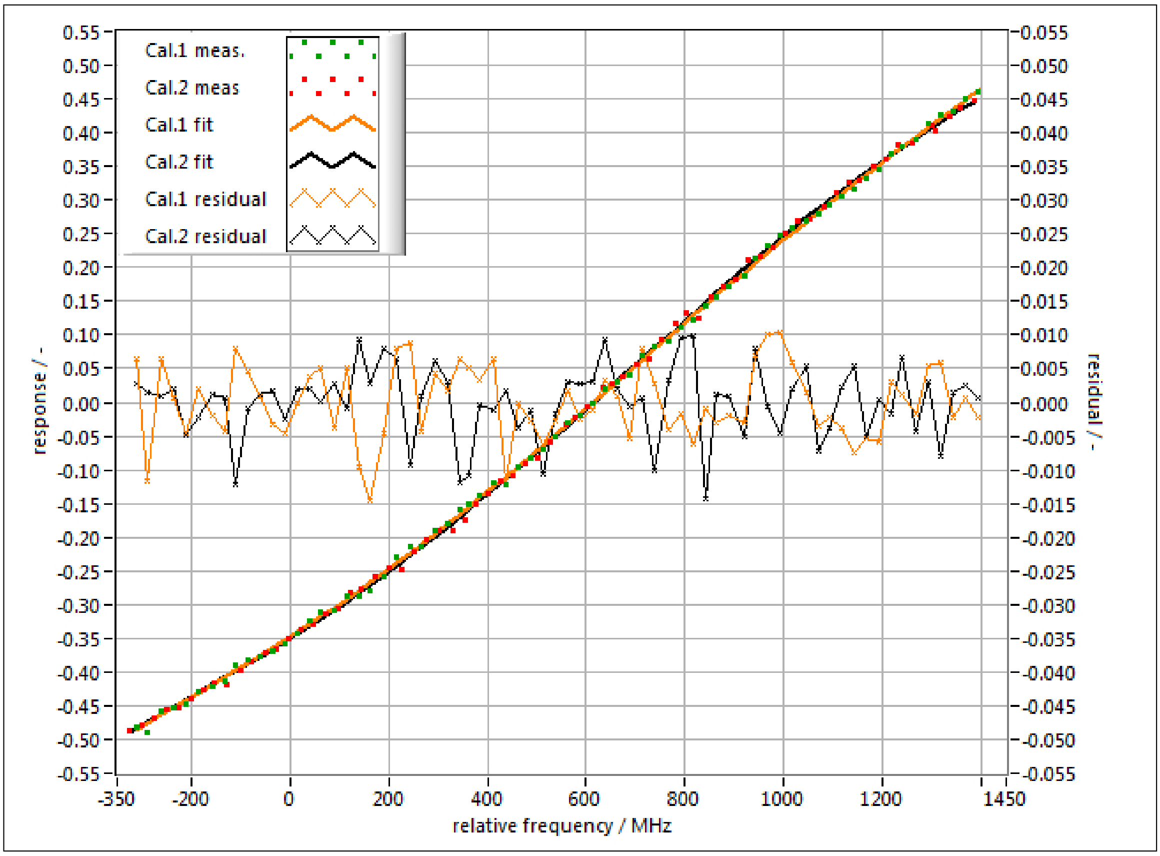

Figure A.4.: The responses of range-gate #15 for the 1st (green dots) and the 2nd (red dots) calibration, the respective 5th order polynomial fits (bold solid orange and bold solid black line) and the corresponding residuals (thin orange and black line with crosses). The frequencies are relative to $844.750000 \cdot 10^{12}$ Hz. The standard deviations $\sigma_{\mathrm{c,ATM}}$ (Tab. 3.5) are $5.45 \cdot 10^{-3}$ (1st calibration) and $5.43 \cdot 10^{-3}$ (2nd calibration).

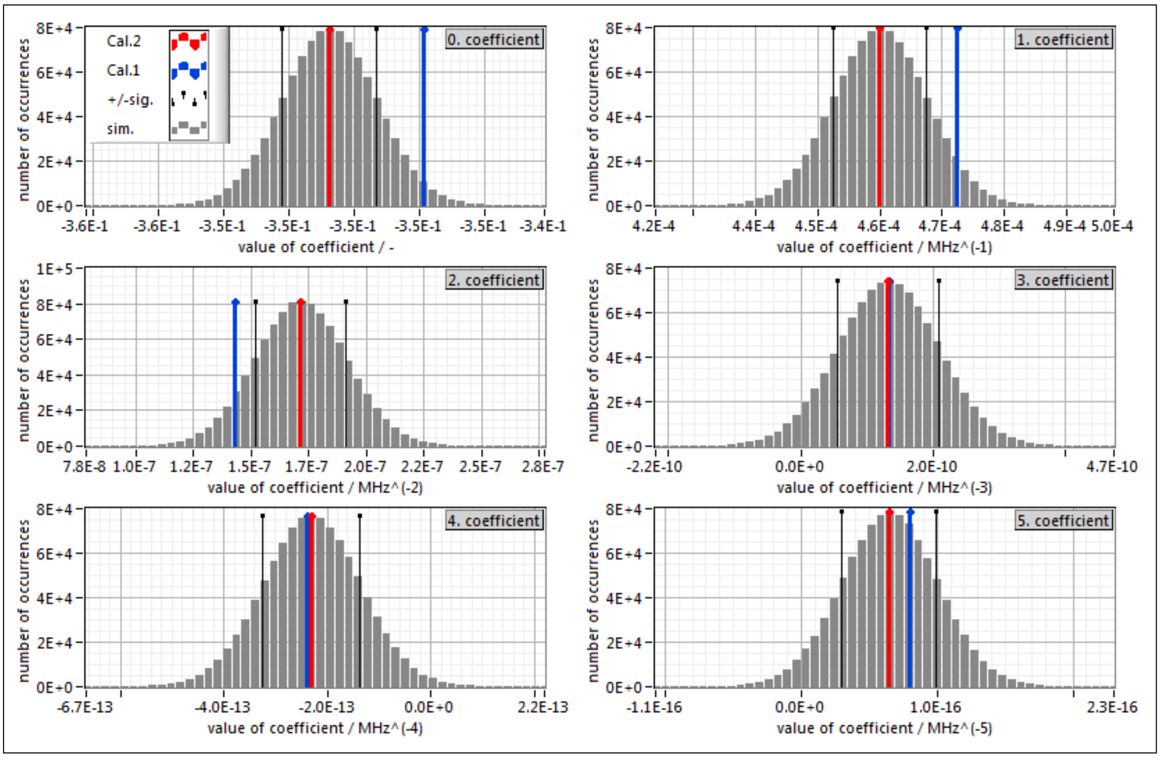

Figure A.5.: Distribution of the six coefficients (grey, according to Eq. 3.21b) obtained from 10^6 simulations of a response function using random noise according to σ_c and the coefficients derived from the 5th order polynomial fit for 2nd (red) calibration for range-gate #15. The intervals of ± 1 standard deviation of the coefficients of the 2nd calibration are marked in black. The coefficients derived from the 5th order polynomial fit for 1st calibration are indicated in blue.

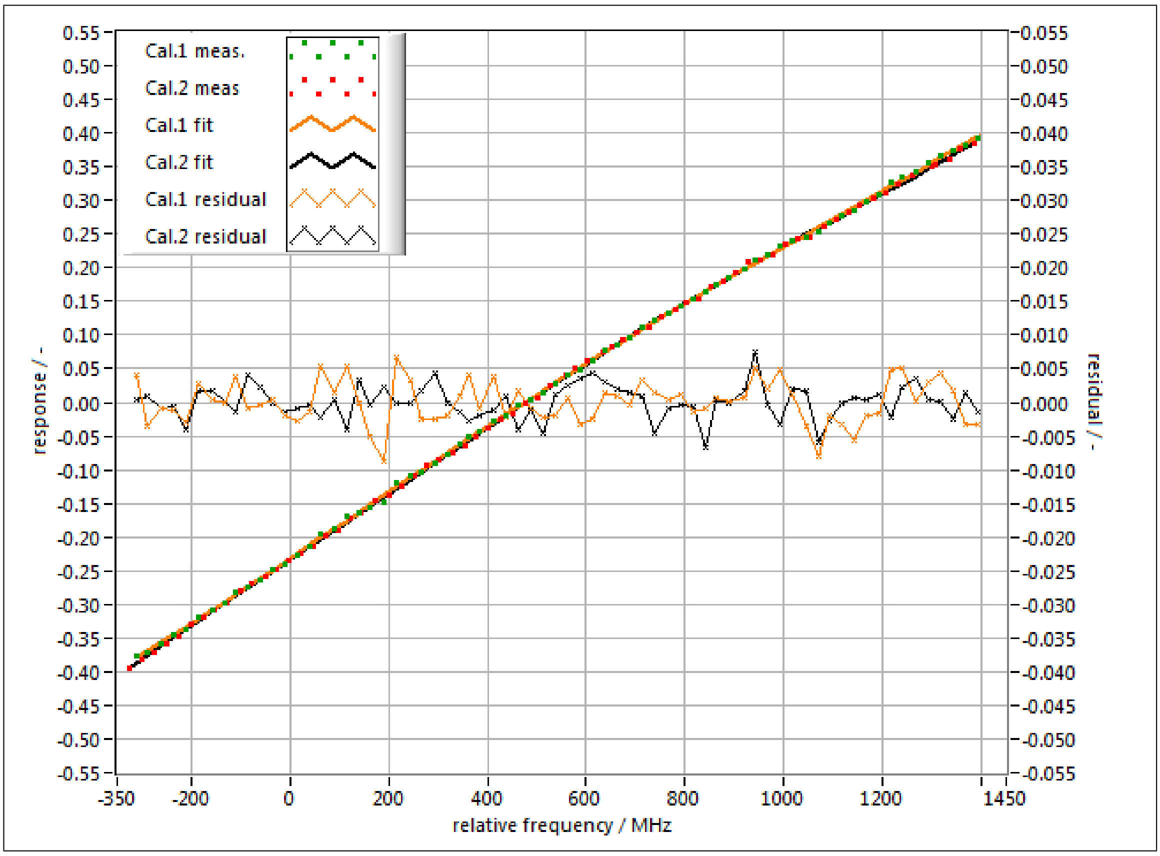

Figure A.6.: The responses of the ground return for the 1st (green dots) and the 2nd (red dots) calibration, the respective 5th order polynomial fits (bold solid orange and bold solid black line) and the corresponding residuals (thin orange and black line with crosses). The frequencies are relative to $844.750000 \cdot 10^{12}$ Hz. The standard deviations $\sigma_{\mathrm{c,GR}}$ (Tab. 3.5) are $3.20 \cdot 10^{-3}$ (1st calibration) and $2.54 \cdot 10^{-3}$ (2nd calibration).

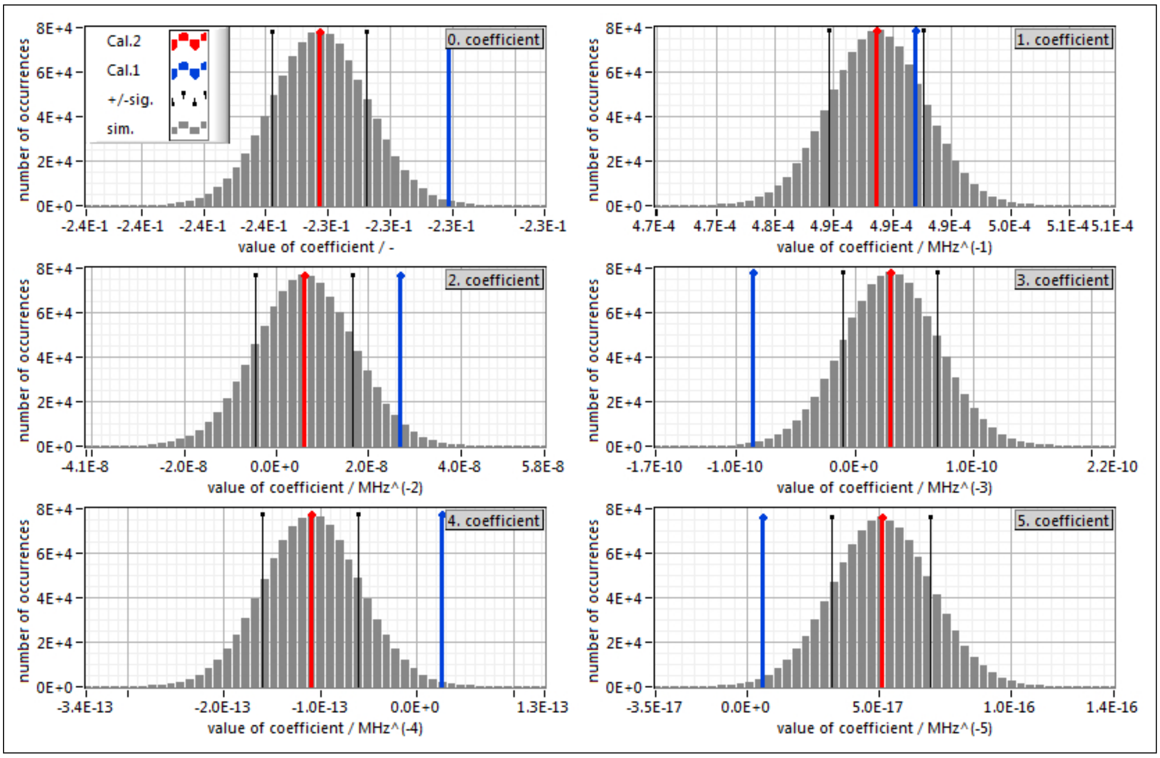

Figure A.7.: Distribution of the six coefficients (grey, according to Eq. 3.21b) obtained from 10^6 simulations of a response function using random noise according to σ_c and the coefficients derived from the 5th order polynomial fit for 2nd calibration (red) for range-gate #15. The intervals of ± 1 standard deviation of the coefficients of the 2nd calibration are marked in black. The coefficients derived from the 5th order polynomial fit for 1st calibration are indicated in blue.

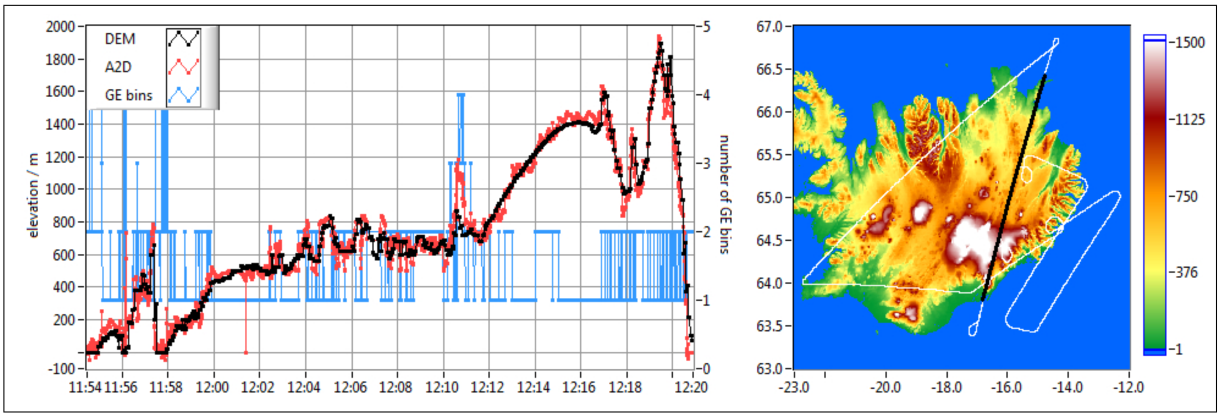

Figure A.8.: Left: Elevation of calculated intersection points of the DEM and the A2D LOS (black) compared with the elevation of the ground return derived from A2D intensities on the Mie channel (red) per observation for flight #09 (Tab. 3.2) on 2009/09/29. The ground returns detected within one observation are mostly spread within 1 - 2 range-gates (blue). The mean absolute deviation of DEM and A2D ground elevation for this section is about 60 m (standard deviation 86 m). Times are in UTC. / Right: Flight track (white) and the analysed flight section (black) shown with elevations above sea level (longitude and latitude scales in units of degree).

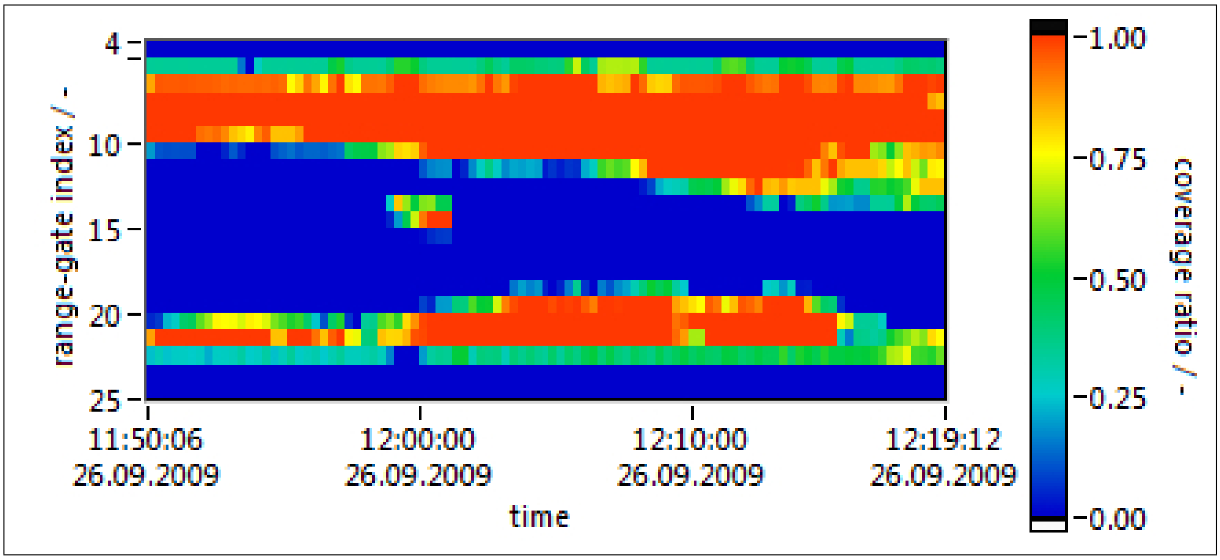

Figure A.9.: Aerial coverage ratios of valid 2-µm wind data on A2D range-bins for the flight section along the east coast of Greenland between 11:50 - 12:19 UTC (comprising 97 observations) on 2009/09/26. The uppermost range gate (#4) corresponds to the Internal Reference and is not covered by 2-µm data (coverage ratio = 0).

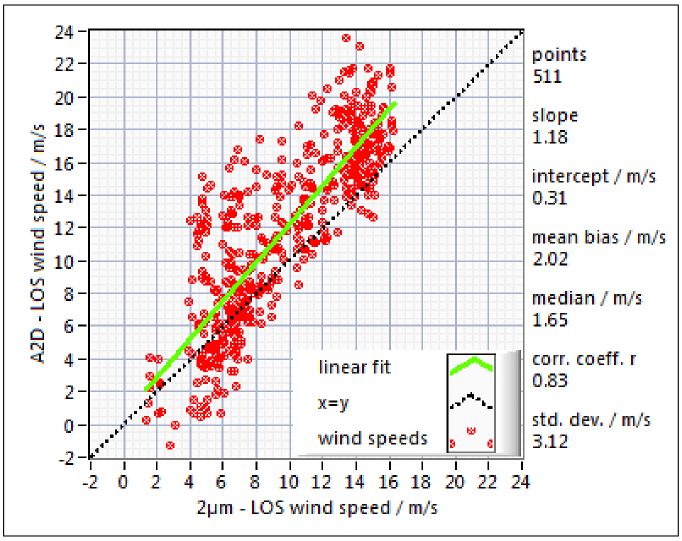

Figure A.10.: Scatterplot for winds measured on 2009/09/26 by the A2D Rayleigh channel and the 2-µm Lidar (red dots) within range-gates #7 - #21 (Internal Reference = #4) processed with the 1st calibration from 2009/09/21, using a coverage ratio of 85 % and the correction scheme of case i) from Tab.4.2. The linear fit line (green) and the ideal x = y line (dashed, black) are also indicated.

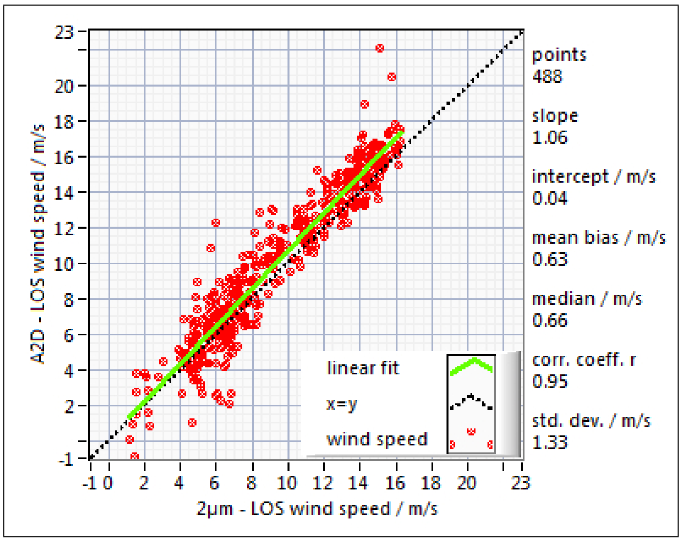

Figure A.11.: Scatterplot for winds measured on 2009/09/26 by the A2D Mie channel and the 2-µm Lidar (red dots) within range-gates #7 - #21 (Internal Reference = #4) processed with the 1st calibration from 2009/09/21, using a coverage ratio of 85 %. The linear fit line (green) and the ideal x = y line (dashed, black) are also indicated.

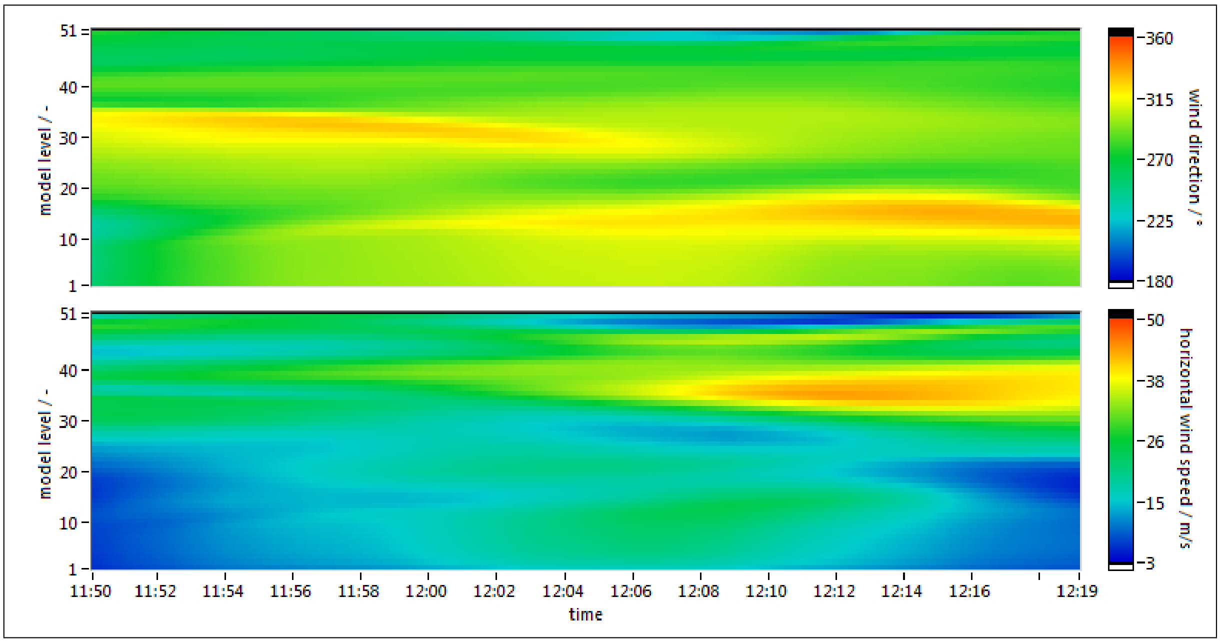

Figure A.12.: Wind direction (top) and horizontal wind speed (bottom) from ECMWF analysis for 12:00 UTC on 2009/09/26. Model level 0 and 51 refer to altitudes of 0 km and 14.4 km, respectively. Falcon flight level corresponds approximately to level 40 with 10.5 km

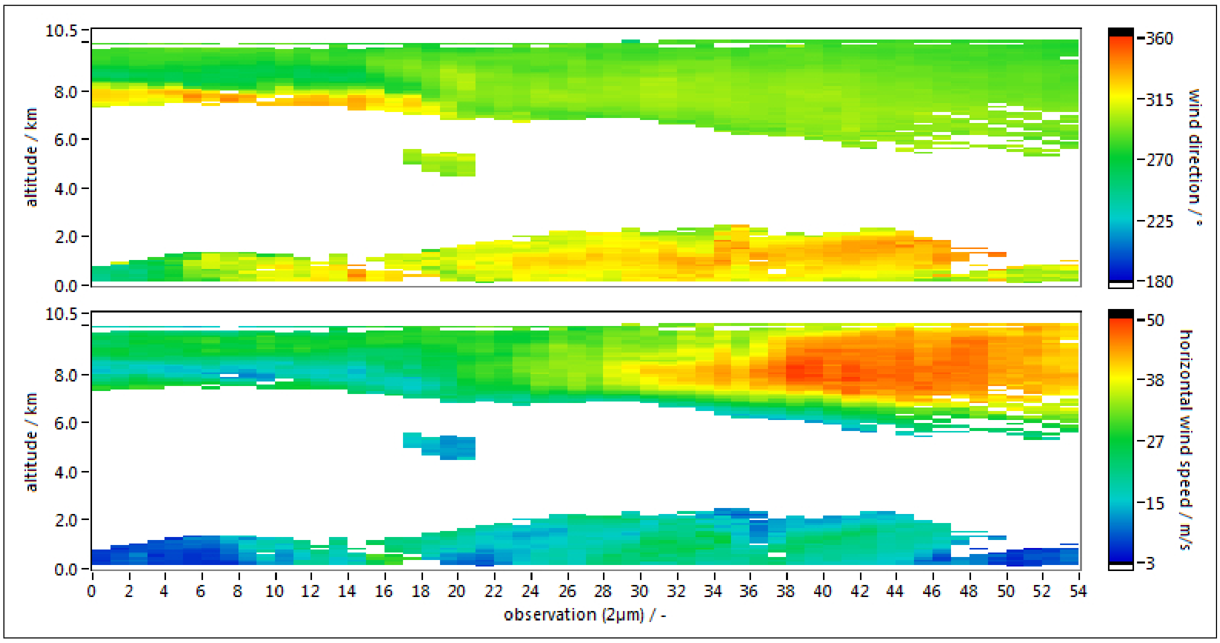

Figure A.13.: Wind direction (top) and horizontal wind speed (bottom) from 2-µm measurements between 11:50 - 12:19 UTC on 2009/09/26. White colour represents invalid measurements due to low aerosol signal.

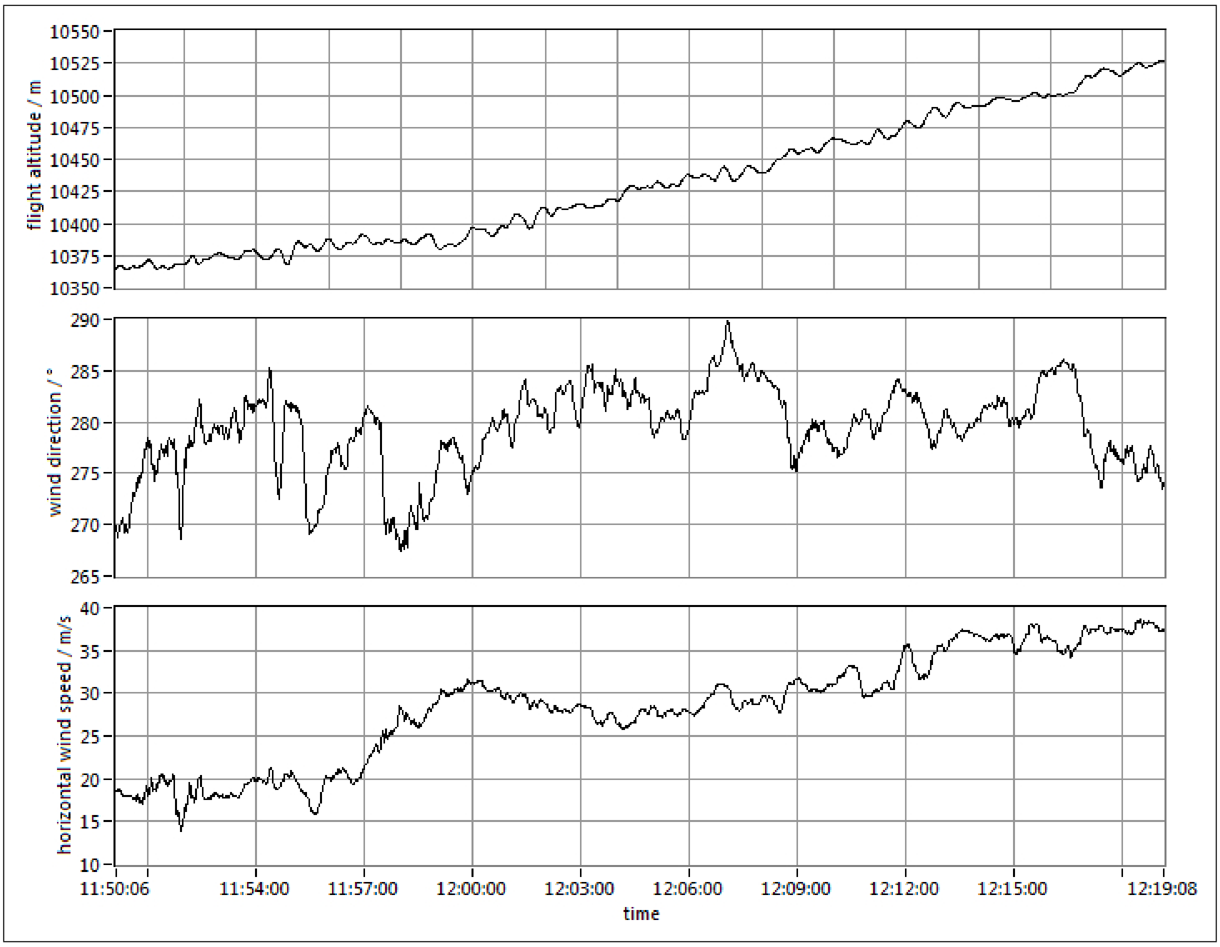

Figure A.14.: Flight altitude (GPS) of the Falcon aircraft (top) and wind direction (middle) and wind speed (bottom) measured by the Falcon nose-boom on 2009/09/26 between 11:50 - 12:19 UTC.

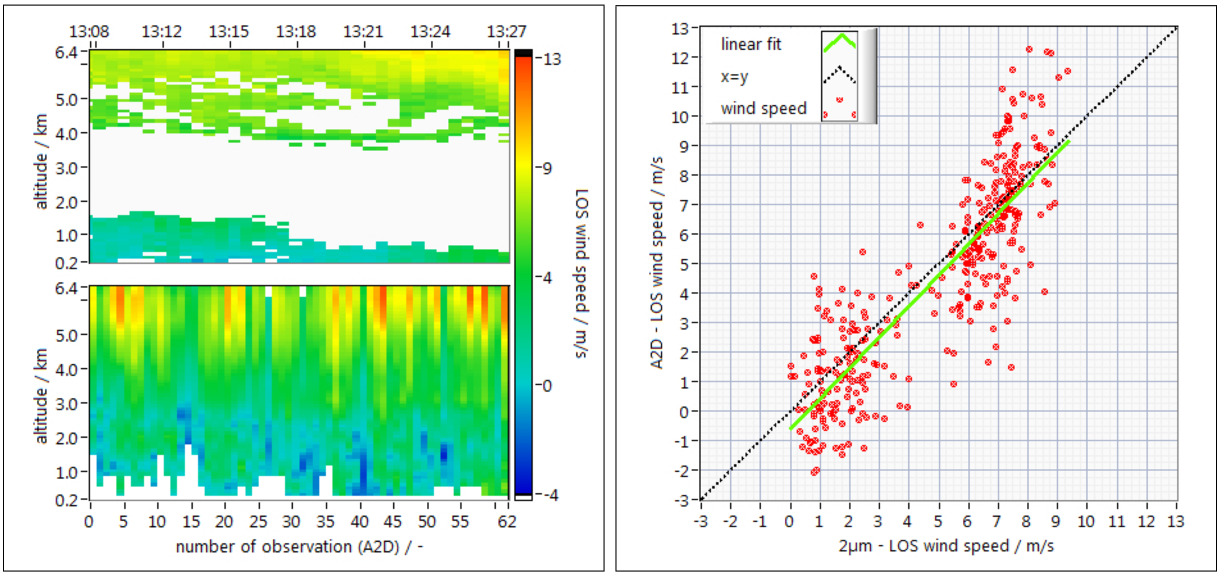

(a) *(b)*

Figure A.15.: (a) LOS wind speeds obtained from the A2D Rayleigh channel (bottom) and the 2-µm Lidar operating in scanning mode (top) on 2009/09/29 between 13:08 - 13:27 UTC. The A2D winds are corrected with a ZWC value of 5.4 m/s. The 62 observations correspond to 197 km horizontal distance. With a mean flight height of the Falcon of 8091 m, the altitude range from 0.2 to 6.4 km approximately comprises the A2D range-gates #7 to #21. Rayleigh wind measurements below ground and clouds are indicated in white. / (b) Scatterplot for winds measured by the A2D Rayleigh channel and the 2-µm Lidar (red dots) within range-gates #7 to #21 (Internal Reference in range-gate #4) processed with the 2^{nd} calibration from 2009/09/21, using a coverage ratio of 50 % and the correction scheme of case f) from Tab. 4.2. The linear fit line (green) and the ideal x=y line (dashed, black) are also indicated.

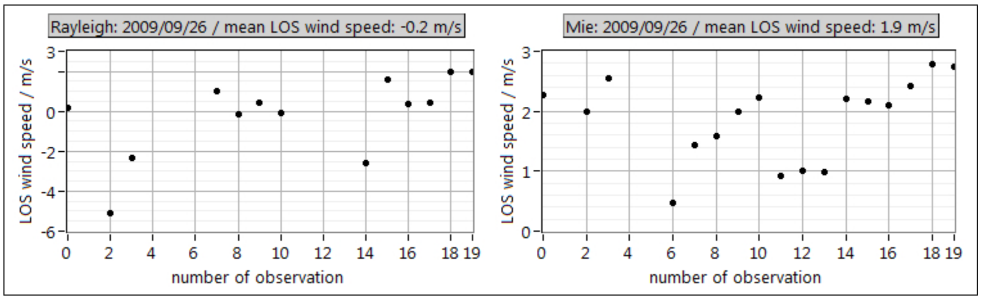

Figure A.16.: The ZWC values of -0.2 m/s for the Rayleigh channel and 1.9 m/s for the Mie channel were determined from LOS velocity measurements of the ground return on 2009/09/26 between 12:57.49 - 13:03.47 UTC. The number of 20 observations corresponds to the 700 measurements in Fig. 3.27 (right).

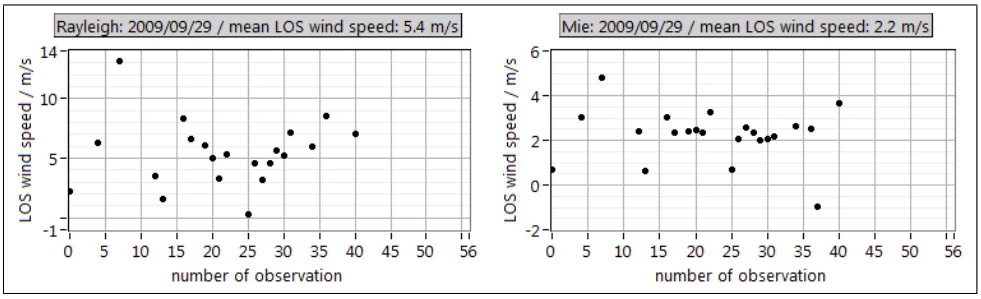

Figure A.17.: The ZWC values of 5.4 m/s for the Rayleigh channel and 2.2 m/s for the Mie channel were determined from LOS velocity measurements of the ground return on 2009/09/29 between 12:07.15 - 12:24.24 UTC. The number of 57 observations corresponds to the 1995 measurements in Fig. 3.27 (left).

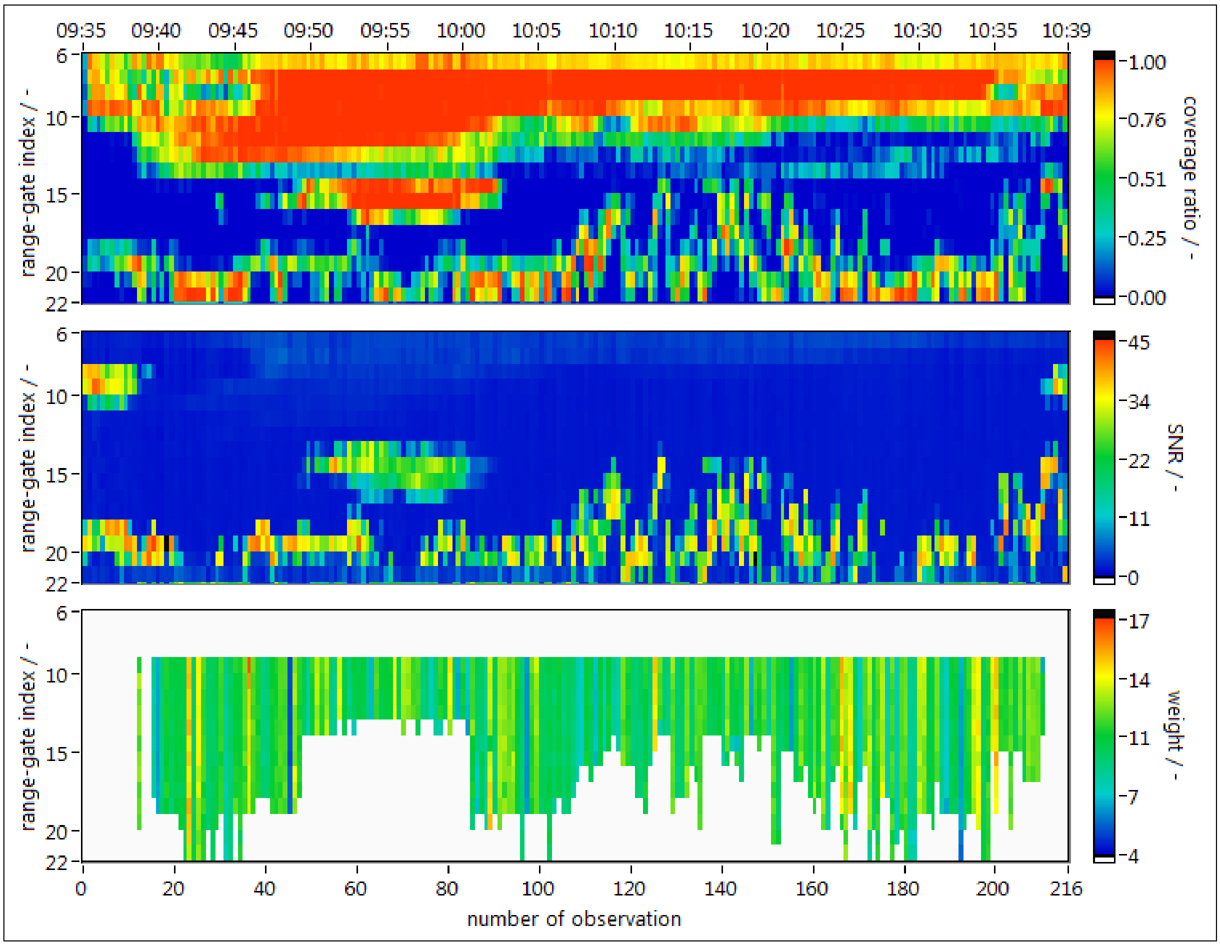

Figure A.18.: Aerial coverage ratios (top, according to Eq. 4.1) of A2D range-bins with valid 2-µm wind data for the flight section between Iceland and Norway on 2009/10/01. During 09:35 - 10:40 UTC the Falcon covered a distance of 943 km comprising 215 A2D observations. The mean upper/lower borders of range-gates #6/#21 are located at 9715 m and 236 m, respectively. The distribution of the SNR values (middle) of the Mie channel according to Eq. 3.29 reflect the broken cloud scenery. Strong Mie backscatter occurred at the start of the measurement section above range-gate #9 in the region of the jet-stream. Low particle concentrations seem to be present below the aircraft in the range-gates #6 and #7 along the whole scene. The weights according to Eq. 4.11a (bottom) are used for the statistical comparison of the Rayleigh winds against the 2-µm winds. A cloud mask (Fig. 3.8a) was applied and range-bins below clouds (white colour) are excluded.

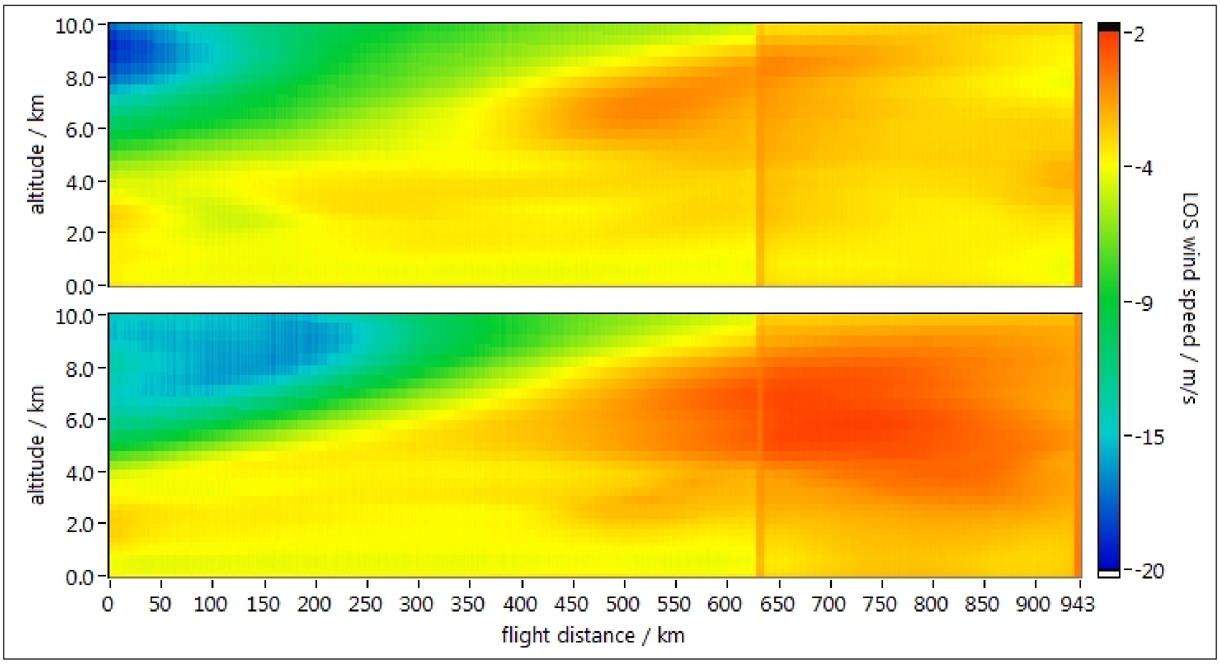

Figure A.19.: Wind speeds with respect to the A2D LOS calculated from ECMWF data for the 943 km flight track between Iceland and Norway on 2009/10/01. ECMWF data of horizontal wind speed and wind direction from the analyses for 06:00 UTC (top) and 12:00 UTC (bottom) were used and interpolated onto the measurement grid of the 2-µm Lidar. On the upper left side the jet-stream is visible in blue colour. The vertical streaks at 630 km and 940 km are due to short curves flown by the Falcon aircraft and hence a change in LOS direction.

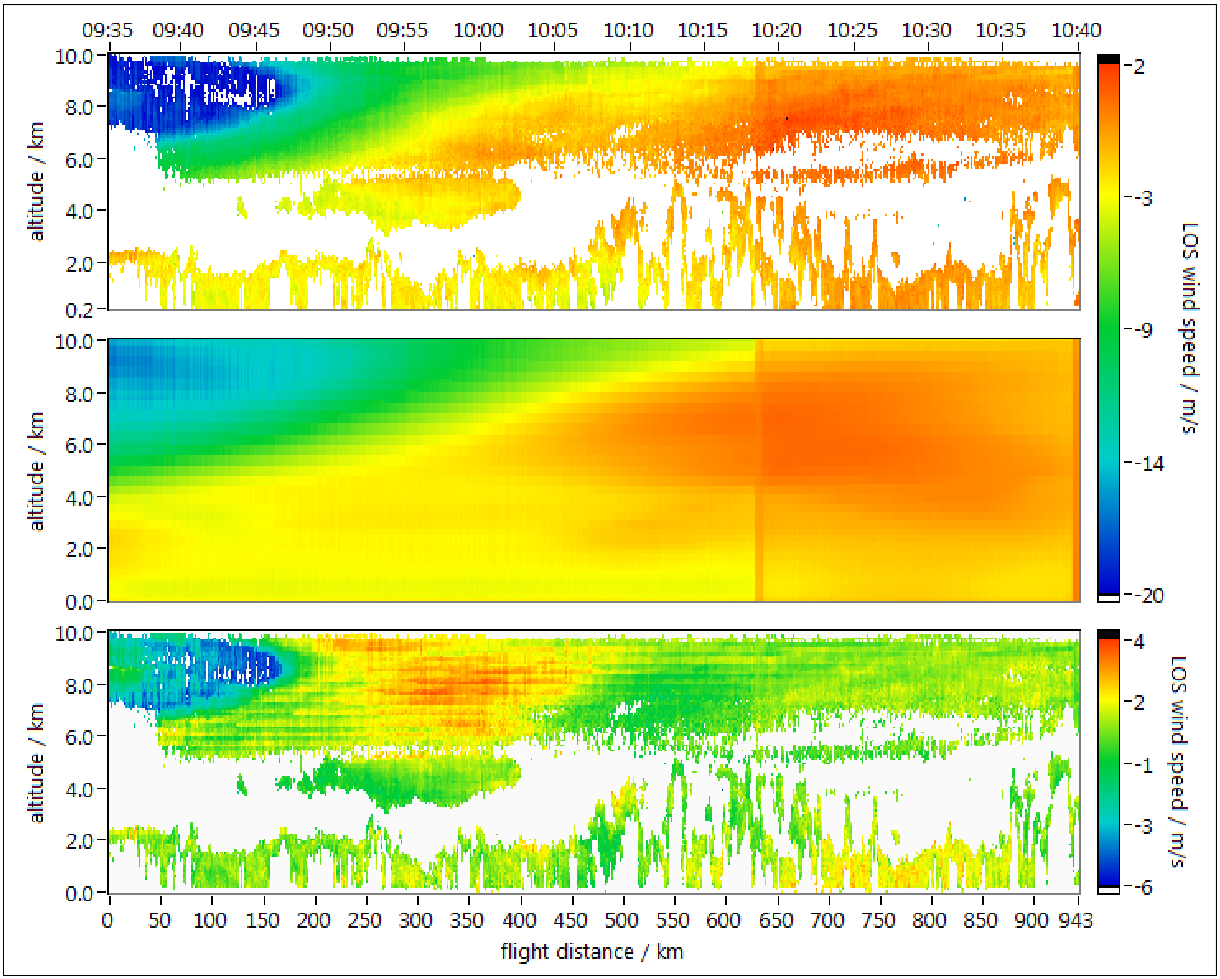

Figure A.20.: Top: Wind speeds as measured by the 2-µm Lidar in LOS mode on 2009/10/01 between 09:35 - 10:40 UTC. Middle: The wind speeds derived from the ECMWF model are linearly interpolated between the analyses for 06:00 UTC and 12:00 UTC according to the measurement time of each profile and subsequently projected onto the LOS of the 2-µm Lidar and interpolated onto the measurement grid of the 2-µm Lidar. The vertical streaks at 630 km and 940 km are due to short curves flown by the Falcon aircraft and hence a change in LOS direction. Bottom: Differences in LOS wind speed between ECMWF and 2-µm Lidar.

A.5. Acronyms, abbreviations and symbols

Acronyms and abbreviations

A2D	Aladin Airborne Demonstrator
ACCD	Accumulation Charge Coupled Device
ADM	Atmospheric Dynamics Mission
ALADIN	Atmospheric LAser Doppler INstrument
AOCS	Attitude and Orbit Control System
ASL	Above Sea Level
AVHRR	Advanced Very High Resolution Radiometer
CALIPSO	Cloud-Aerosol Lidar and Infrared Pathfinder Satellite Observation
CCD	Charge Coupled Device
COS	Coordinate System
DCO	Detection Chain Offset
DIAL	Differential Absorption Lidar
DLR	Deutsches Zentrum für Luft- und Raumfahrt
DSA	Downhill Simplex Algorithm
DWL	Doppler Wind Lidar
ECMWF	European Centre for Medium-range Weather Forecasts
EADS	European Aeronautic Defence and Space company
EOM	Electro Optical Modulator
ESA	European Space Agency
FOV	Field-Of-View
FPI	Fabry-Pérot Interferometer
FSR	Free Spectral Range
FWHM	Full-Width at Half-Maximum
GPS	Global Positioning System
HLOS	Horizontal Line-Of-Sight
IR	InfraRed
ICESat	Ice Cloud and land Elevation Satellite
LASER	Light Amplification by Stimulated Emission of Radiation
LIDAR	LIght Detection And Ranging
LITE	Lidar-In-space Technology Experiment
LOS	Line-Of-Sight
LSB	Least Significant Bit
MODIS	MODerate resolution Imaging Spectroradiometer
MOUSR	Mie Out of Useful Spectral Range
NASA	National Aeronautics and Space Administration
NOAA	National Oceanographic and Atmospheric Administration
NL	Non-Linearity

NWP	Numerical Weather Prediction
PLL	Phase Locked Loop
QuikSCAT	Quick Scatterometer
RADAR	Radio Detection and Ranging
RLH	Reference Laser Head
SNR	Signal-to-Noise Ratio
TLE	Transmit Laser Electronics
UTC	Universal Time Coordinated
UV	UltraViolet
VAD	Velocity Azimuth Display
WM	Wavelength-Meter
WMO	World Meteorological Organization
ZWC	Zero Wind Correction

Symbols

Table A.3.: Symbols

Symbol	Meaning	Unit
A	telescope area	m^2
a	intercept	m s^{-1}
a_{w}	intercept under consideration of weights	m s^{-1}
a_{B}	intercept for errors on both axes	m s^{-1}
b	slope	-
b_{w}	slope under consideration of weights	-
b_{B}	slope for errors on both axes	-
C	offset of the Lorentzian function	-
c	speed of light (299,792,458)	m s^{-1}
$c_{\mathrm{ATM,i}}$	i$^{\mathrm{th}}$ polynom. coeff. of Rayleigh atm. resp. func.	-
$c_{\mathrm{INT,i}}$	i$^{\mathrm{th}}$ polynom. coeff. of Rayleigh int. resp. func.	-
c_{i}	i$^{\mathrm{th}}$ polynom. coeff. of Rayleigh response function	-
d	relative vertical extent of range gate contribution	-
$\vec{d}$	vector of vertical weights	-
d_{r}	length of a range-gate	m
d_{v}	vertical thickness of a range-gate	m
E_{l}	pulse energy	kg m^2 s^{-2}
f	frequency	Hz
f_0	frequency emitted by the laser (source)	Hz
f_1	Doppler shifted frequency as perceived by moving scatterer	Hz
f_2	twice Doppler shifted frequency as perceived by the Lidar	Hz
f_{a}	center frequency of atmospheric backscatter	Hz
f_{ATM}	relative frequency of atmospheric signal	Hz
f_{b}	beat frequency	Hz
f_{D}	Doppler frequency shift	Hz
f_{INT}	relative frequency of internal signal	Hz
f_{lo}	frequency of local oscillator	Hz
$f_{\mathrm{M,ATM}}$	relative frequency of atmospheric signal (Mie)	Hz
$f_{\mathrm{M,INT}}$	relative frequency of internal signal (Mie)	Hz
f_{off}	applied frequency offset for heterodyne detection	Hz
f_{p}	frequency of the emitted laser pulse	Hz
$f_{R,ATM}$	relative frequency of atmospheric signal (Rayleigh)	Hz
$f_{R,INT}$	relative frequency of internal signal (Rayleigh)	Hz
g	index for ground return range-gates	-
$g_{\mathrm{M,R}}$	radiometric gain for Mie/Rayleigh channel	LSB e^{-1}
h	altitude above sea level of range-gate centre	m
h	Planck constant ($= 6.62606957 \cdot 10^{-34}$)	kg m^2 s^{-1}

... continued on next page

Table A.3 – continued from previous page

Symbol	**Meaning**	**Unit**
h_{ac}	height above sea level	m
h_{GR}	groud elevation	m
I	intensity	LSB
I_{A}	intensity on Rayleigh channel A (direct)	LSB
$I_{\mathrm{A,B}}$	intensity reaching the respective detector behind filter A or B	W m^{-2}
I_{B}	intensity on Rayleigh channel B (reflected)	LSB
I_{BKG}	intensity of background signal	LSB
I_{DCO}	intensity of detection chain offset	LSB
I_{GR}	intensity of ground return signal	LSB
I_{INT}	intensity of Internal Reference signal	LSB
I_{m}	intensity of a measurement	LSB
I_{max}	maximum intensity	LSB
$I_{\mathrm{M,corr}}$	intensity of corrected Mie signal	LSB
$I_{\mathrm{M,R}}$	intensity of Mie/ Rayleigh observation	LSB
$I_{\mathrm{m,scaled}}$	scaled intensity of a measurement	LSB
I_{raw}	raw intensity	LSB
I_{Ray}	intensity of Rayleigh background on Mie channel	LSB
i	index referring to range gate, pixel or counter	-
j	index	-
k	Lidar ratio (extinction-to-backscatter ratio)	sr
k_{c}	conversion factor from frequency to wind speed	MHz m^{-1} s
L	Lorentzian function	-
m	index referring to number of measurement	-
N	index or number of measurements per obs.	-
N_{ACCD}	number of photons on ACCD	-
N_{det}	number of detected photons	-
N_{em}	number of emitted photons	-
$\vec{n}$	unit vector	-
n	index, index referring to range-bin	-
O	overlap function of the fields of view of telescope and laser	-
$\boldsymbol{P}$	rotary matrix referring to the pitch angle of the aircraft	-
$P_{\mathrm{valid,i}}$	fraction of valid measurements	-
p	index referring to number of pulse	-
$\vec{p}_{\mathrm{ac}}$	A2D LOS vector in the aircraft-fixed coordinate system	-
$\vec{p}_{\mathrm{los}}$	A2D LOS vector in the geodetic coordinate system	-
q_{eff}	quantum efficiency of detector	-
R	response	-
$\boldsymbol{R}$	rotary matrix referring to the roll angle of the aircraft	-
$R_{\mathrm{los,ac}}$	response correction due to aircraft induced LOS velocity	-
R_{R}	Rayleigh response	-

... continued on next page

Table A.3 – continued from previous page

Symbol	**Meaning**	**Unit**
R_{M}	Mie response	pixel
$R_{\mathrm{M,ATM}}$	Mie response for atmospheric signal	pixel
$R_{\mathrm{M,INT}}$	Mie response for internal signal	pixel
$R_{\mathrm{R,ATM}}$	Rayleigh response for atmospheric signal	-
$R_{\mathrm{R,INT}}$	Rayleigh response for atmospheric signal	-
r	range, distance	m
r	correlation coefficient	-
$r_{\mathrm{cvg,i}}$	coverage ratio of i$^{\mathrm{th}}$ range-bin	-
r_{l}	location/range to/of Lidar	m
r_{r}	range from instrument to centre of a range-bin	-
r_{t}	location/range to/of target	m
r_{v}	vertical distance of a range-gate	m
S	system constant describing properties of the Lidar	sr
S_{i}	intensity spectrum of atmospheric backscatter	W m^{-3}
SNR	signal to noise ratio	-
s	scaling factor	-
T	filter transmission function	-
$T_{\mathrm{A,B}}$	transmission function of the respective filter A or B	-
T_{p}	maximum of transmission function, constant	-
t	integration time	s
t	relative horizontal extent of range gate contribution	-
$\vec{t}$	vector of horizontal weights	-
v	velocity or wind speed	m s^{-1}
$\boldsymbol{V}$	matrix containing 2-µm wind velocities	-
$v_{2\mu\mathrm{m}}$	wind velocity measured by 2-µm Lidar	m s^{-1}
$v_{2\mu\mathrm{m,LOS}}$	2-µm wind projected onto A2D LOS	m s^{-1}
$\vec{v}_{2\mu\mathrm{m}}$	3D wind vector measured by 2-µm Lidar	-
$\vec{v}_{\mathrm{A2D,LOS,u}}$	temporal mean of the A2D LOS unit vector	-
$v_{2\mu\mathrm{m,N}}$	north component of 2-µm wind vector	m s^{-1}
$v_{2\mu\mathrm{m,E}}$	south component of 2-µm wind vector	m s^{-1}
$v_{2\mu\mathrm{m,Z}}$	vertical component of 2-µm wind vector	m s^{-1}
$v_{\mathrm{A2D,Nu}}$	north component of A2D LOS unit vector	m s^{-1}
$v_{\mathrm{A2D,Eu}}$	south component of A2D LOS unit vector	m s^{-1}
$v_{\mathrm{A2D,Zu}}$	vertical component of A2D LOS unit vector	m s^{-1}
$\overline{v}_{2\mu\mathrm{m}}$	mean 2-µm wind from ECMWF aerial interpolation	m s^{-1}
$\vec{v}_{\mathrm{ac}}$	velocity vector of the Falcon aircraft	-
$v_{\mathrm{ac,EW}}$	east-west component of Falcon velocity vector	m s^{-1}
$v_{\mathrm{ac,NS}}$	north-south component of Falcon velocity vector	m s^{-1}
$v_{\mathrm{ac,V}}$	vertical component of Falcon velocity vector	m s^{-1}
$v_{\mathrm{los,ac}}$	aircraft induced LOS velocity	m s^{-1}

... continued on next page

Table A.3 – continued from previous page

Symbol	**Meaning**	**Unit**
v_{meas}	relative velocity between aircraft and target	m s^{-1}
v_{los}	true LOS wind speed of target	m s^{-1}
v_{ZWC}	zero wind correction velocity	m s^{-1}
$v_{2\mu\mathrm{m,i}}$	i$^{\mathrm{th}}$ 2-µm wind for ECMWF aerial interpolation	m s^{-1}
$\overline{v}_{\mathrm{A2D}}$	mean A2D wind from ECMWF aerial interpolation	m s^{-1}
$v_{\mathrm{A2D,i}}$	i$^{\mathrm{th}}$ A2D wind for ECMWF aerial interpolation	m s^{-1}
w	weight	-
$w_{\mathrm{i,Ray}}$	weight for i$^{\mathrm{th}}$ Rayleigh range-bin	-
$w_{\mathrm{i,Mie}}$	weight for i$^{\mathrm{th}}$ Mie range-bin	-
x	position	pixel
x_{i}	single non-linearity value	-
x_{i}	placeholder for 2-µm wind speed	m s^{-1}
x_{p}	position of the centroid of the Mie peak	pixel
$\boldsymbol{Y}$	rotary matrix referring to the yaw angle of the aircraft	-

Table A.4.: Greek Symbols

Symbol	**Meaning**	**Unit**
α	roll angle	degree
α_{ac}	roll angle of Falcon aircraft	degree
α_{aer}	aerosol extinction coefficient	m^{-1}
α_{i}	integration angle of A2D with respect to roll axis of aircraft	degree
α_{M}	offset of Mie response calibration function	pixel
$\alpha_{\mathrm{M,INT}}$	offset of Mie response calibration function for Internal Ref.	pixel
$\alpha_{\mathrm{M,GR}}$	offset of Mie response calibration function for Ground Return	pixel
α_{mol}	molecular extinction coefficient	m^{-1}
α_{R}	offset of Rayleigh response calibration function	-
α_{tot}	total extinction coefficient	m^{-1}
β	pitch angle	degree
β_{ac}	pitch angle of the Falcon aircraft	degree
β_{aer}	aerosol backscatter coefficient	$\mathrm{m}^{-1}\ \mathrm{sr}^{-1}$
β_{i}	integration angle of A2D with respect to pitch axis of aircraft	degree
β_{M}	offset of Mie response calibration function	$\mathrm{MHz\ pixel}^{-1}$
$\beta_{\mathrm{M,INT}}$	offset of Mie response calibration function for Internal Ref.	$\mathrm{MHz\ pixel}^{-1}$
$\beta_{\mathrm{M,GR}}$	offset of Mie response calibration function for Ground Return	$\mathrm{MHz\ pixel}^{-1}$
β_{mol}	molecular backscatter coefficient	$\mathrm{m}^{-1}\ \mathrm{sr}^{-1}$
β_{R}	sensitivity of Rayleigh response calibration function	MHz^{-1}
$\beta_{\mathrm{R/M,a/g}}$	sensitivity according to index	-
β_{tot}	total backscatter coefficient	m^{-1}
γ	yaw angle	degree
γ_{ac}	yaw angle of Falcon aircraft	degree
γ_{M}	integration angle of A2D with respect to yaw axis of aircraft	degree
γ_{R}	non-linearity of Rayleigh response calibration function	-
$\gamma_{\mathrm{R,i}}$	non-linearity of Rayleigh response calibration function for atmospheric range gate i	-
$\gamma_{\mathrm{R,INT}}$	non-linearity of Rayleigh response calibration function for Internal Reference	-
$\gamma_{\mathrm{R,GR}}$	non-linearity of Rayleigh response calibration function for atmospheric range gate i	-
Δ	difference	-
Δf_{FWHM}	full width at half maximum of a transmission curve	Hz
Δf_{FSR}	free spectral range of a Fabry-Pérot interferometer	Hz
Δt	window of integration time	s
λ	wavelength	m
λ_0	wavelength emitted by the laser	m
λ_1	wavelength, lower integration limit	m
λ_2	wavelength, upper integration limit	m

... continued on next page

Table A.4 – continued from previous page

Symbol	**Meaning**	**Unit**
λ_l	wavelength emitted by the laser	m
μ	mean value	-
μ	systematic error (or bias)	m s^{-1}
ω	off-nadir angle	degree
σ	standard deviation	-
$\sigma_{2\mu\mathrm{m}}$	standard deviation of 2-µm winds	m s^{-1}
$\sigma_{2\mu\mathrm{m,A2D}}$	cross correlation between A2D and 2-µm data	m^2 s^2
σ_A2D	standard deviation of A2D winds	m s^{-1}
σ_α	variation of offset	-
σ_β	variation of sensitivity	-
σ_a	uncertainty in the estimation of the intercept	m s^{-1}
σ_b	uncertainty in the estimation of the slope	-
σ_i	standard deviation of signal for i^th range-gate	LSB
σ_NL	standard deviation of non-linearity	-
$\tau(r,\lambda)$	transmission	-
χ^2	chi-square value, costs	-
${\chi^2}_\mathrm{w}$	chi-square value, costs considering weights	-

A.6. Acknowledgements

At this point my thanks go to everyone, who contributed to the success of this thesis. I would like to express my particular gratitude to:

- Prof. Dr. Richard Bamler, for supervising me as a PhD student, for the detailed review of this thesis, for continuously giving valuable advice and for providing effective organisational support.
- Prof. Dr. Markus Rapp for acting as an expert in the examination board and for providing very adjuvant comments regarding this thesis.
- Prof. Dr. Ulrich Schumann for giving valuable advices.
- Dr. Gerhard Ehret for his continuous support during my time at the DLR.
- Dr. Oliver Reitebuch for being an excellent mentor, for his tireless help & endless patience, for his ever present readiness for discussions, for his guidance and encouragement and for being such a marvellous team leader arranging a distinguished working atmosphere.
- Dr. Benjamin Witschas, Christian Lemmerz and Engelbert Nagel for putting the A2D into the condition that it provided the wind measurements I was allowed to evaluate, for their constructive comments & support in every aspect and most of all for just being such excellent team members.
- Dr. Stephan Rahm for processing the 2-µm data and providing the resulting wind profiles.
- Prof. Dr. Ulrike Paffrath for giving me a detailed initial introduction to the A2D and the basic evaluation routines as well as for her continued interest in my work.
- Prof. Dr. Ines Leike for providing crucial assistance regarding the retrieval algorithms and for giving invaluable insights into LabView programming during the last three years.
- Dorit Huber for being of great support before and throughout the time of this thesis, for providing the essential assistance in C++ programming and for the stimulating and helpful discussions.
- Dr. Andreas Schäfler for the conditioning of the ECMWF data, the provision of the AVHRR and MODIS satellite recordings and his meteorological expertise.
- Jürgen Streicher for his countless little assistances and for being an easily bearable office mate always open to discuss about Lidar topics and more.
- the Lidar department for being great colleagues in an inspiring working atmosphere.
- all the participants of the A2D-Progress Meetings, especially Martin Endemann, Herbert Nett, Anne-Grete Straume, Olivier LeRille (all ESA/ESTEC), Alain Dabas (Météo-France) and Michael Vaughan for invaluable advices, ideas and fruitful discussions and in particular also Ad Stoffelen (KNMI) for his detailed help.
- the members of the Atmospheric Dynamics Mission Advisory Group (ADMAG) for allowing me to attend some of their outstandingly interesting and exciting meetings.
- Dr. Oliver Reitebuch, Dr. Benjamin Witschas, Sonja Fehling, Dr. Naomi Murdoch and Gurmeet Pawar for spending so much effort in proofreading my thesis in times when they surely had better things to do.
- my family, Brigitte, Rainer & Kristin, and last but not least to my ♡ Sonja Fehling for their constant practical and emotional support, understanding and love.